"Higgs boson interaction with the top quark : CP properties at the LHC"

Demartin, Federico

Abstract

It is astonishing how the variety of Nature, from all the living species to oceans, mountains and stars, results from different rearrangements of the same few building blocks, the elementary particles. The standard model (SM) of particle physics has been incredibly effective so far in describing the interactions among our fundamental constituents, which ultimately determine significant properties of ourselves and our universe. The 2012 discovery of the Higgs boson at the LHC experiments has marked the completion of the SM picture, and the beginning of a new journey: the quest for new physics beyond the current paradigm. This quest can be pursued in many directions, including the search for deviations from the SM predictions in the interactions among the Higgs boson and the other elementary particles. In this thesis I address the interaction between the Higgs boson and the top quark, the two heaviest known elementary particles, which are at the centre of the LHC research. I promote pr...

Document type : *Thèse (Dissertation)*

Référence bibliographique

Demartin, Federico. *Higgs boson interaction with the top quark : CP properties at the LHC.* Prom. : Maltoni, Fabio

Université catholique de Louvain

Secteur des sciences et technologies
Institut de recherche en mathématique et physique
Centre for Cosmology, Particle Physics and Phenomenology

Higgs boson interaction with the top quark: CP properties at the LHC

Doctoral dissertation presented by

Federico Demartin

in fulfilment of the requirements for the degree of Doctor in Sciences

Jury de thèse

Prof. Jean-Marc Gérard (*président*)	UCL, Belgium
Prof. Fabio Maltoni (*promoteur*)	UCL, Belgium
Prof. Giacomo Bruno	UCL, Belgium
Prof. Jorgen d'Hondt	VUB, Belgium
Prof. Michael Krämer	RWTH Aachen, Germany

---

24 February 2017

“a questa tanto picciola vigilia
d’i nostri sensi ch’è del rimanente
non vogliate negar l’esperïenza
[...] *fatti non foste a viver come bruti*
ma per seguir virtute e canoscienza”

Dante – Inferno, Canto XXVI, 114-116; 119-120

“Hunc igitur terrorem animi tenebrasque necessest
non radii solis neque lucida tela diei
discutiant, sed naturae species ratioque.
Principium cuius hinc nobis exordia sumet,
nullam rem e nihilo gigni divinitus umquam.
[...] *Huc accedit uti quicque in sua corpora rursum*
dissoluat natura neque ad nihilum interemat res.
[...] *Quod nunc, aeterno quia constant semine quaeque,*
donec vis obiit, quae res diverberet ictu
aut intus penetret per inania dissoluatque,
nullius exitium patitur natura videri.
[...] *quia multa modis multis mutata per omne*
ex infinito vexantur percita plagis,
omne genus motus et coetus experiundo
tandem deveniunt in talis dispositura,
qualibus haec rerum consistit summa creata”

Titus Lucretius Carus – De Rerum Natura, Liber I,
146-150; 215-216; 221-224; 1024-1028

Thanks!

First and foremost, I sincerely thank you for reading this thesis and expressing interest in my work!

Then, I'd like to explicitly thank many people, starting from the members of my PhD jury, Jean-Marc, Giacomo, Jorgen, Michael and Fabio. Not only because you patiently read the manuscript, but also for asking interesting questions that broadened my point of view on the subject, and for your kind remarks.

Thank you Fabio for giving me the opportunity to pursue this PhD, which has been a unique experience under many points of view. I have grown up as a scientist and as a human being, both in its satisfying and rewarding moments and during the tough and frustrating ones. Thank you Giacomo for the humanity and support you showed me during my struggle.

Thanks to my collaborators Kentarou, Marco and Benedikt for our work together and some fun we have shared, and to the MG5 team (Olivier, Rikkert, Valentin, Paolo and Pierre) for their feedback and technical support. Thanks to Kentarou and then to Alberto for hosting me at VUB during many occasions. And thanks again to Kentarou for your lessons on patience and perseverance.

Thanks to all the colourful people I've met during this experience, who made me feel well and at home everywhere I was. My dear Lucia and Antonio, thanks for being there during most of my PhD, in good and bad times, and for the rare but close moments we shared after you left. Thanks Davide for your friendly support, both moral and technical, and the interesting discussions we had spacing from physics to pop culture. Thanks David for your kind encouragements. Thanks Elisa, Ludivine, Thomas, Mihailo, Nataly, Marcello, Michele, Ioannis, Ambresh, Manoj, Alessia, Pieter, Luca, Riccardo, Ken, Bram, Robin and Jože for the laughs we shared. Thanks to all the other CP3 people who supported me, in particular to our secretaries Ginette and Carinne. A second round of thanks to my italian collagues, especially Elisa, Lucia and Davide, for the many lunches we shared. Thanks to Sofia, Giovanna, Marco, Lorenzo, and especially to Sara, for our exchanges about art, music, food and drinks, and the fun we had together. Thanks Rubens for our many coffees and talks together. Special thanks to my fellow paranymph Andrea, and again to Antonio and Lucia, for our irreverent conversations; had we all shared the same office, I wonder how it would have turned out...

Many thanks also to the people who were there whenever I went back to Italy, and made me feel as if I've never left. Thanks to my long-time friends Danilo (and to his beloved cars that carried us around many trips), the two Giacomo's (even though one currently lives in the other hemisphere), the three Matteo's, Davide, Giovanni, Andrea, Federica, Stefania and Monica. Thanks to Erika for our discussions about the PhD and life in general, while always eating something. Special thanks to aunt Anna, uncle Sandro and Simona.

The most important thanks go to the people who stayed closest to me during these years. Thanks Marta for your love, our cultural exchanges, the great moments we shared, the difficult ones and the lessons we have learned together. Thanks to my parents Franco and Lina and to my grandma Sandra, for being always there with continuous affection, support and encouragements, and to my brother Ale for opening up to me.

Last but not least, thanks to the people who inspired me to pursue my studies. First my father, who since I was a kid encouraged me to be curious, taught me the scientific culture, and has never stopped after all these years (sometimes joking about our different academic specialisations). Then Paola, who made me appreciate physics at high school, and finally Stefano and Alessandro at university, with whom I've developed my passion (also in the Latin sense) for theoretical physics.

Without you, this accomplishment would have been impossible.

Federico

Abstract

It is astonishing how the variety of Nature, from all the living species to oceans, mountains and stars, results from different rearrangements of the same few building blocks, the elementary particles. The standard model (SM) of particle physics has been incredibly effective so far in describing the interactions among our fundamental constituents, which ultimately determine significant properties of ourselves and our universe. The 2012 discovery of the Higgs boson at the LHC experiments has marked the completion of the SM picture, and the beginning of a new journey: the quest for new physics beyond the current paradigm. This quest can be pursued in many directions, including the search for deviations from the SM predictions in the interactions among the Higgs boson and the other elementary particles.

In this thesis I address the interaction between the Higgs boson and the top quark, the two heaviest known elementary particles, which are at the centre of the LHC research. I promote predictions accurate at next-to-leading order (NLO) in perturbation theory for processes relevant to study this interaction at the LHC. I show how NLO accuracy is decisive in order to reduce systematic uncertainties in the theoretical computations, such as the scale dependence or the number of light quarks (flavour scheme). It is essential to control these uncertainties if we want to spot signs of new phenomena in deviations from the SM. I also discuss several observables sensitive to new physics that can be measured at the LHC. In particular, I focus on hypothetical CP-violating effects in the Higgs-top interaction, which could help to explain the imbalance between matter and antimatter observed in the universe.

Contents

Introduction

A thorough exploration of the physics at the electroweak energy scale has been a major goal in high energy physics during the last few decades, and a key motivation to build the gargantuan Large Hadron Collider (LHC) at CERN, the largest European laboratory for particle physics. This unprecedented scientific endeavour, which involves thousands of scientists from all over the world, reached its peak of visibility during summer 2012, when the discovery of the long-sought Higgs boson was announced on the 4th of July by two independent and competing experimental collaborations, ATLAS and CMS [1, 2]. The discovery of the Higgs boson granted many prestigious awards to the scientists involved in this decades-long effort, including the 2013 Nobel Prize to Peter Higgs and François Englert, who, together with Robert Brout, first proposed in 1964 the mechanism implying the existence of the newly-found particle [3–6].[1] The Brout-Englert-Higgs mechanism was later implemented by Weinberg in the Standard Model (SM) of fundamental interactions, the currently-accepted theory of particle physics, to generate the masses of the elementary particles [8]. The results from the LHC experiments have so far supported the idea that this mechanism is indeed the one realized in Nature. Being the last fundamental particle predicted by the Standard Model yet to be discovered, the Higgs boson has required formidable efforts from both the theoretical and experimental communities in high energy physics, and has drawn a lot of attention as well from the general public in the form of media announcements and scientific outreach.

Notwithstanding this early success, the LHC scientific mission is far from being completed. In fact, a detailed study of the Higgs boson is one of the main pillars of the LHC physics programme at current and future runs of the collider, which will require many more years of data taking. Accurate measurements of the Higgs boson properties are crucial both to validate various aspects of

---

[1] This mechanism has been explored at the time also by Guralnik, Hagen and Kibble [7], in an article published a few months later.

the Standard Model, as well as to possibly discover new physics (BSM) if deviations from the SM predictions are detected. The first run of the LHC (data taking in proton–proton collisions during 2011 and 2012) has already collected compelling evidence that the particle discovered is indeed consistent with the SM Higgs boson. In particular, its spin-0 nature has been proven [9–11] – being the first known elementary particle to feature this property – together with a measurement of its interactions with the electroweak bosons [12]. A limited exploration of the Higgs Yukawa interactions with fermions has been carried out as well, with direct evidence limited to tau leptons, and indirect evidence for the top quark; a more precise assessment is foreseen at the ongoing Run II (started in 2015), and at future LHC runs with even higher statistics.

Another main pillar of the LHC research programme is the study of the top quark. Discovered at the Fermilab Tevatron collider in 1995 [13, 14], the top quark was the last quark predicted by the Standard Model to be found, and is produced copiously in LHC collisions. Being the heaviest known elementary particle, the top quark also plays an outstanding role in Higgs boson phenomenology. In particular, the main production channel for the Higgs boson at the LHC – namely gluon fusion – entails a top-quark loop, while very soon Run II will be sensitive to on-shell top–anti-top pair production in association with a Higgs boson, a process that will bring key information on the properties of the top-quark Yukawa interaction. Rarer Higgs production channels in association with a single top quark are also very interesting due to their sensitivity to deviations from the Standard Model paradigm, which results in (sometimes spectacularly) enhanced event rates. Furthermore, the top-Higgs interaction drives the quantum stability of the SM vacuum state at high energies, which could affect the lifetime of our universe if no new physics is realized below the Planck scale.

This thesis fits in the context outlined above, and in particular is devoted to study the phenomenology of the top-quark Yukawa interaction with the Higgs boson at the LHC. To this aim, we promote precise and accurate predictions in the Standard Model for the relevant processes at the LHC, as well as point out observables that are sensitive to new fundamental interactions, beyond the physics encompassed in the SM paradigm. A description of the thesis structure follows.

Chapters 1 and 2 introduce the reader to the background of the work, discussing some key technical details and the state of the art. In particular, Chapter 1 briefly surveys the main ideas behind the description of high-energy processes at hadron colliders such as the LHC, and the simulation of hadronic events accurate at next-to-leading order (NLO) in QCD, including matching to parton shower programs (NLO+PS). Chapter 2 reviews some important properties of the two fundamental particles at the centre of this thesis, the Higgs boson and the top quark. The status of Higgs precision measurements and the path forward are discussed; we introduce the Higgs Characterisation framework, used to explore the properties of the top Yukawa coupling throughout this thesis.

Chapters from 3 to 6 are devoted to the presentation of the original research results. In particular, in Chapter 3 we study the production of a Higgs boson plus one and two jets via gluon fusion, in the heavy-top approximation, pointing out observables that are sensitive to the CP properties of the top Yukawa. In Chapter 4 we repeat the CP study for the associated production of a Higgs and a top-quark pair. In Chapter 5 we address two of the three Higgs production channel in association with a single top quark, t-channel and s-channel tH. We promote state-of-the-art predictions in the SM not only for event generation and differential distributions, but also for total cross sections, performing a detailed study of the residual theoretical uncertainties. Then, the inclusion of these results in the official predictions for the LHC Higgs Cross Section Working Group (HXSWG) is discussed. Finally, we characterise CP-mixing in the top Yukawa employing the dominant t-channel production mode. In Chapter 6 we discuss the third Higgs plus single top channel, namely tWH production. Similarly to the previous chapter, we first study the process in the SM, and then move to CP-mixing. A large preliminary discussion is devoted to the separation of the $t\bar{t}H$ and the tWH processes at NLO; since the same problem affects the analogous processes without a Higgs, *i.e.* $t\bar{t}$ and tW, we perform a critical analysis of tW simulations as well. All the processes outlined above are studied at NLO+PS accuracy in QCD. The key results of the research are summarised in the Outlook.

A few appendices follow, collecting complementary numerical results, or technical details whose discussion is postponed to avoid excessive dispersal in the main body of the thesis. In Appendix A we review the Standard Model of fundamental interactions, and the Brout-Englert-Higgs mechanism to generate the masses of elementary particles. In Appendix B we present the complete Higgs Characterisation model at NLO, used to perform the CP-mixing studies in this thesis. In Appendix C we discuss gluon fusion at NLO in the approximation of a heavy top quark. In Appendices D and E we collect some additional numerical results for t-channel and s-channel tH production. Finally, in Appendix F we perform a separate study of the tWb channel, the one where tW production at NLO overlaps with $t\bar{t}$, and we repeat a similar study for the $tWbH$ channel in tWH production at NLO, which overlaps with the $t\bar{t}H$ process.

The original results presented in this thesis are based on the following publications on peer-reviewed journals [15–18]

- P. Artoisenet, P. de Aquino, F. Demartin, R. Frederix, S. Frixione et al., *A framework for Higgs characterisation*, *JHEP* **1311** (2013) 043, [`1306.6464`];
- F. Demartin, F. Maltoni, K. Mawatari, B. Page and M. Zaro, *Higgs characterisation at NLO in QCD: CP properties of the top-quark Yukawa interaction*, *Eur.Phys.J.* **C74** (2014) 3065, [`1407.5089`];
- F. Demartin, F. Maltoni, K. Mawatari and M. Zaro, *Higgs production in association with a single top quark at the LHC*, *Eur. Phys. J.* **C75** (2015) 267, [`1504.00611`];
- F. Demartin, B. Maier, F. Maltoni, K. Mawatari and M. Zaro, *tWH associated production at the LHC*, *Eur. Phys. J.* **C77** (2017) 34, [`1607.05862`].

on parts of the fourth technical report of the LHCHXSWG [19]

- LHC Higgs Cross Section Working Group collaboration, D. de Florian et al., *Handbook of LHC Higgs Cross Sections: 4. Deciphering the Nature of the Higgs Sector*, `1610.07922`;

and on the following conference proceedings [20, 21]

- F. Demartin, E. Vryonidou, K. Mawatari and M. Zaro, *Higgs characterisation: NLO and parton-shower effects*, in *2nd Toyama International Workshop on Higgs as a Probe of New Physics (HPNP2015) Toyama, Japan, February 11-15, 2015*, 2015. `1505.07081`;
- F. Demartin and B. Maier, *Single top, W and Higgs associated production*, *PoS* **TOP2015** (2016) 080.

The Higgs Characterisation Feynman rules at NLO are coded in the HC_NLO_X0 UFO model, which is publicly available online [22].

Chapter 1

Event generation at hadron colliders

Going from the Lagrangian formulation of a fundamental theory to phenomenological predictions of results in particle experiments is a long and complex effort. In this chapter we review some ideas and techniques behind the simulation of high-energy processes at hadron colliders, and we briefly discuss event generation at NLO matched to parton showers, which has been used to produce many results collected in this thesis. In particular, we stress two key points:

1. the separation of short-distance physics, which is directly related to the Lagrangian of the theory describing fundamental interactions (either the SM or a BSM theory), and long-distance physics, which is universal for all processes, ruled by QCD and expressed in terms of initial-state parton distributions and final-state shower/hadronisation;
2. how the inclusion of perturbative corrections in QCD reduces the dependence of predictions on the choice of μ_R and μ_F scales.

A deeper review of the topics under discussion can be found in textbooks such as *Ellis, Stirling & Webber* [23], and in the latest Review of Particle Physics [24].

We remind that, after the first prototypes of particle accelerators appeared in the late 1920s and in the 1930s, these machines have gradually become an essential instrument in modern particle physics. The experimental inquiry over the last decades has been mostly centred around collider experiments, where two beams of particles are accelerated to a very high kinetic energy and then brought into collision. Examples include the CERN SPS ($p\bar{p}$), LEP (e^+e^-) and LHC (pp), the Fermilab Tevatron ($p\bar{p}$) and the DESY HERA (ep) colliders. Sophisticated detectors are placed around the collision points in order to study the fundamental interactions that occur in these high-energy collisions, which can lead among other things to the creation of new particles, such as the Higgs boson and the top quark, by transforming kinetic energy into mass.

In a nutshell, collider physics relies on counting the number of recorded events with certain features, and then comparing to the corresponding number predicted by the theory (this is of course process-specific). The number N of expected events can be computed from the equation

$$N = L\,\sigma\,, \tag{1.1}$$

where σ is the cross section for the process under investigation, and the proportionality factor L is the luminosity accumulated by the collider. The luminosity has dimensions of an inverse area, $[L] = [\mathrm{m}]^{-2}$, and is related to the capability of the particle accelerator to make particles interact. It depends only on the machine performance, through parameters such as the transverse beam size, the number of particles per beam, the collision frequency and the time spent running; for more details, see *e.g.* [23] and references therein. On the other hand, the cross section expresses the effective area of interaction between two particles via the specific process under inquiry, $[\sigma] = [\mathrm{m}]^2$, and does not depend on the machine parameters except the particle energy. Therefore, the investigation of high energy physics at particle colliders boils down to computing cross sections, once a model of fundamental interactions (*i.e.* a Lagrangian) is given; we will discuss how this can be done in Section 1.2. Here we remind that cross sections can be inclusive, namely the total rate for producing a given particle such as the Higgs boson, or differential over some physical observable, *e.g.* the transverse momentum of the Higgs. Also, it is customary to express cross sections in units of *barns* instead of squared meters, where $1\ \mathrm{b} = 100\ \mathrm{fm}^2 = 10^{-28}\ \mathrm{m}^2$ is an appropriate area when studying interactions at the nuclear scale; for rare high-energy LHC processes, submultiples such as picobarns (pb) or femtobarns (fb) are typically used.

1.1 Strong interactions at high energy

Quantum chromodynamics (QCD) has been formulated in the 1970s [25, 26], and its tremendous experimental success has established it as the currently-accepted theory of strong interactions. It is an $SU(3)$ gauge theory that describes the interactions among hadrons in terms of fundamental (point-like) constituents, the quarks and the gluons, and together with the electroweak (EW) theory it forms the Standard Model (SM) of fundamental interactions (fore more details, see Appendix A.3.1). QCD plays a paramount role at hadron colliders such as the LHC, where strong interactions affect all the theoretical predictions of physical quantities, also called *observables*, and determines many properties of the final-state objects analysed by the experimental detectors.

A major property of QCD is *asymptotic freedom*, which means that at sufficiently high energies we can use perturbation theory to solve the path-integral formulation of quantum field theory, and compute the scattering probability from a given initial state to some wanted final state in terms of correlation functions. Perturbative QCD is expressed as a power series of the strong coupling $\alpha_s = g_s^2/4\pi$, where g_s is the (bare) coupling parameter in the QCD Lagrangian (see Eq. (A.56) in Appendix A). Techically, when performing perturbative calculations of a physical observable $O(Q, \alpha_s)$, divergences may arise from corrections such as quantum loops, and some energy scale μ needs to be introduced as a mathematical regulator. Typically, one gets logarithmic divergences where ratios of physical scales Q and regulator scales μ appear, namely $\log(Q^2/\mu^2)$ with $\mu \to 0$. One thus needs to separate the divergent part in the log from the physical scale dependence by introducing a renormalisation scale μ_R: $\log(Q^2/\mu^2) = \log(Q^2/\mu_R^2) + \log(\mu_R^2/\mu^2)$. This procedure ensures that we can define a measurable quantity combining the constant parameters in the Lagrangian, such as $\alpha_s = g_s^2/4\pi$, and the divergent part of quantum corrections in the limit $\mu \to 0$; the resulting renormalised parameter $\alpha_s(\mu_R)$ is not a constant anymore, showing instead scale dependence. We end up with fixed-order predictions for a renormalised physical observable $O_R = O_R\big(Q, \mu_R/Q, \alpha_s(\mu_R)\big)$.

Clearly, as μ_R is not a Lagrangian parameter, nor a property of the experimental setup, but instead an arbitrary scale introduced in the intermediate steps of our computation, physical observables ought not to depend on it. This leads to the renormalisation group equations (RGEs)

$$\frac{d}{d\log(\mu_R^2)}\,O_R = \left(\frac{\partial}{\partial\log(\mu_R^2)} + \frac{\partial\,\alpha_s}{\partial\log(\mu_R^2)}\frac{\partial}{\partial\,\alpha_s}\right)O_R = 0 \tag{1.2}$$

which predict how renormalised quantities like $\alpha_s(\mu_R)$ should change with the scale in order to compensate the explicit dependence from $\log(Q^2/\mu_R^2)$ left in physical observables. We have

$$\frac{\partial}{\partial\log(\mu_R^2)}\,\alpha_s(\mu_R) \equiv \beta(\alpha_s) = -\big(\beta_0\alpha_s^2 + \beta_1\alpha_s^3 + \mathcal{O}(\alpha_s^4)\big)\,, \tag{1.3}$$

where β_0 is computed from one-loop corrections to the gluon propagator, β_1 from two loops, and so on. Since $\beta_0 = (11C_A - 4T_F n_f)/12\pi = (33 - 2n_f)/12\pi$,

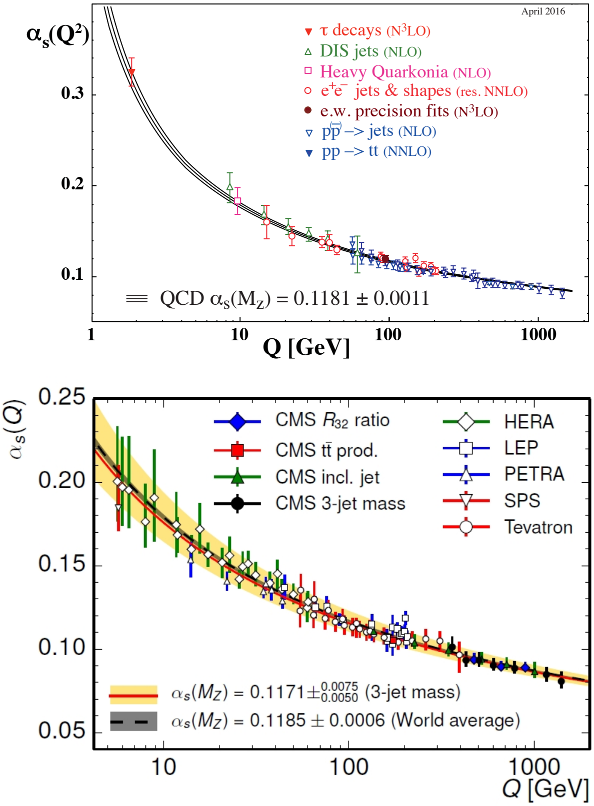

Figure 1.1: Top: values of the strong coupling α_s at different energies; the RGE running predicted by QCD starting from $\alpha_s(m_Z)$ is shown with solid lines. Taken from [24]. Bottom: a similar result from a CMS analysis [27].

the beta function is negative as long as the number n_f of active flavours, *i.e.* of quarks with $m_q \ll \mu_R$, is less than 17. This causes the decreasing of α_s at increasing energies, and thus asymptotic freedom

$$\alpha_s(\mu_R) = \frac{\alpha_s(Q_0)}{1 + \alpha_s(Q_0)\,\beta_0 \log(\mu_R^2/Q_0^2)} \left(1 + \mathcal{O}(\alpha_s)\right). \tag{1.4}$$

While the value of α_s cannot be computed from first principles, once it is measured in an experiment at a certain reference scale Q_0[1], then we are able to use QCD to predict how it will evolve at different scales, as long as we remain in the perturbative regime. The running of α_s at different energies is a key prediction of QCD which has been extensively tested, see Fig. 1.1, and in general

---

[1] The most common reference value is $\alpha_s(m_Z) \simeq 0.12$.

of renormalisable theories like the SM. At scales below about 1 GeV, instead, the theory becomes strongly interacting, and the strong coupling diverges at $\Lambda_{\rm QCD} \sim 200$ MeV.[2] As a consequence, quarks and gluons cannot propagate at distances larger than about 10^{-15} m, and stay confined inside hadrons.

In summary, on the one hand the renormalisation scale is unphysical, but on the other hand we need it in order to ensure the predictability of perturbative calculations at different energies, giving meaning to our physical theory.

1.2 The factorisation of hadronic cross sections

A consequence of asymptotic freedom is that highly energetic collisions between two protons do not involve each proton as a whole, but instead can be described in terms of their fundamental (point-like) constituents, namely quarks and gluons, which are collectively called partons. Such energetic collisions are pictured employing the *factorisation theorem*, according to which the cross section for a given high-energy process can be expressed as[3]

$$\begin{aligned} \sigma_{pp\to\mathcal{F}}(P_1,P_2) = \sum_{i_1,i_2} \int dx_1\, dx_2\, f_1(x_1,\mu_F)\, f_2(x_2,\mu_F) \\ \sigma_{i_1 i_2\to\mathcal{F}}\big(p_1,p_2,\alpha_s(\mu_R),\mu_F\big)\,. \end{aligned} \tag{1.5}$$

Here $\mathcal{F}$ is the desired final state of the pp collision (including possible extra QCD radiation) and P_1 and P_2 are the momenta of the incoming protons; the indices i_1 and i_2 run over the possible partons (massless quarks and gluons) that can initiate the fundamental process $i_1 i_2 \to \mathcal{F}$, whose momenta are, respectively, $p_1 = x_1 P_1$ and $p_2 = x_2 P_2$. The distribution of such momenta is described by the parton distribution functions (PDFs), where $f_i(x)\,dx$ is the probability of finding a parton i with momentum fraction x inside the proton. In other words, highly energetic protons (or hadrons) can be seen as a broad band of partons with different momenta. The cross section $\sigma_{i_1 i_2\to\mathcal{F}}$ describes the hard scattering among partons in terms of fundamental interactions, and can be computed at a fixed order in perturbation theory, after truncating the expansion in powers

---

[2] Sometimes $\mu = \Lambda_{\rm QCD}$ is considered as the regulator of the theory; in this case one says that renormalisation absorbs logarithmic terms $\log(\mu_R/\Lambda)$ into the definition of $\alpha_s(\mu_R)$.

[3] Factorisation is strictly proven [28] only for a few processes, such as deep inelastic scattering (lepton-hadron collisions) and Drell-Yan (vector boson W, Z, γ^* production), in the limit of massless partons and up to power-suppressed effects $\mathcal{O}(\Lambda^2_{\rm QCD}/Q^2)$. At present there is no rigorous proof for generic hadron-hadron collisions, and Eq. (1.5) is an ansatz *assumed* to be valid, especially when computing non-inclusive observables and generating events.

of the strong interaction parameter α_s, which becomes small at high energies

$$\sigma_{i_1 i_2 \to \mathcal{F}} = \alpha_s^{k_0} \sum_{n=0}^{\infty} \sigma_n \, \alpha_s^n \,. \tag{1.6}$$

The coefficients σ_n of the perturbative series need to be computed taking into account the fundamental interactions that can connect the initial and final states, including possible extra QCD radiation. Different processes will start at a different power $\alpha_s^{k_0}$, that can be factored out; for example, W boson production starts at α_s^0, while top-quark pair production at α_s^2. The term σ_0 is called leading order (LO), or Born approximation, and is the first contribution to the series; σ_1 is the next-to-leading-order (NLO) correction, σ_2 is the NNLO term, and so forth. We will discuss more details in Section 1.3.

Note that the cross section in Eq. (1.5) does not encompass all the hadronic processes that can take place in particle experiments. In fact, the greatest part of the proton-proton total cross section comes from low-energy strong interactions, that we cannot factorise and describe with perturbation theory. However, these interactions produce final states almost collinear with the proton beams, that are not analysed by particle detectors such as ATLAS and CMS. As we said, the factorisation theorem describes instead the structure of high-energy processes, which are of great interest because we are able both to detect them in the experimental apparata, and to compute them in the SM (or in a BSM theory) using the perturbative expansion. A very important point to stress here is that we have been able to separate a *universal* contribution to the hadronic cross section, related to the low-energy structure of the proton, which is determined by QCD and expressed in terms of PDFs, and a *process-specific* high-energy contribution related to the partonic scattering, which directly depends on the fundamental interactions in the SM (or BSM) Lagrangian.

In a way analogous to the renormalisation of α_s described in Section 1.1, we need to introduce a factorisation scale μ_F to separate the divergent part of the collinear emissions from initial-state partons into the PDF definition, obtaining a measurable parton distribution $f(x, \mu_F)$ that is scale dependent.[4] The corresponding RGE equations for the parton distributions are the so-called DGLAP[5] equations, which show how the quark and gluon distributions change

---

[4] One can again consider $\mu = \Lambda_{QCD}$ as the regulator of the splitting, and say in this sense that log terms $\log(\mu_F/\Lambda_{QCD})$ are absorbed into the definition of the PDFs.

[5] Dokshitzer [29], Gribov and Lipatov [30], Altarelli and Parisi [31].

with scale due to collinear emissions and splittings

$$\frac{\partial}{\partial t}\, q(x,\mu_F) = \int_x^1 \frac{dz}{z}\left[P_{qq}\Big(\frac{x}{z},\alpha_s\Big)\, q(z,\mu_F) + P_{qg}\Big(\frac{x}{z},\alpha_s\Big)\, g(z,\mu_F)\right], \tag{1.7}$$

$$\frac{\partial}{\partial t}\, g(x,\mu_F) = \int_x^1 \frac{dz}{z}\left[P_{gq}\Big(\frac{x}{z},\alpha_s\Big)\, q(z,\mu_F) + P_{gg}\Big(\frac{x}{z},\alpha_s\Big)\, g(z,\mu_F)\right], \tag{1.8}$$

where $t = \log(\mu_F^2)$, and the splitting functions $P_{ji}(z)$ describe the probability that a parton i emits a parton j carrying a fraction of momentum z. This is another successfully tested prediction of QCD, see Fig. 1.2.

While the key idea of RGE is that observable quantities must depend only on the physical scales of the process and not on the choice of μ_R or μ_F, in practice when we use perturbation theory to perform computations this statement is true only within the perturbative accuracy achieved. If the series is truncated at order α_s^m, a residual dependence on μ_R and μ_F of $\mathcal{O}(\alpha_s^{m+1})$ is present in the result, due to incomplete cancellations in the neglected higher orders; *i.e.* the RGEs like Eq. (1.2) become $\frac{d}{d\log\mu^2}\, O_R = \mathcal{O}(\alpha_s^{m+1})$. This leads to two common practices:

1. choose $\mu_{R,F}$ close to the physical scale Q of the hard scattering, and
2. estimate the residual scale dependence, varying the value of $\mu_{R,F}$ (conventionally by a factor 2).

Since unphysical scales will always appear as ratios to physical ones, namely as terms like $Q^2/\mu_{R,F}^2$, the first point is necessary to ensure that large logarithms of such ratios do not appear at all orders, which may hamper the convergence of the perturbative series or even spoil it completely. Sometimes it can be useful to do a wide-range exploration of how results change with scale before choosing appropriate reference values for μ_R and μ_F, as we do for tH production in Chapter 5, Fig. 5.4. The second point allows to determine whether residual scale dependence is under acceptable control, or if we need to improve our predictions by computing higher orders in the perturbative series. Note that, while this procedure can provide information on the scale-dependent terms in the missing higher orders, it cannot say anything about the neglected contributions that do not depend on $\mu_{R,F}$. A known worst-case scenario is the gluon-fusion production of colourless heavy states such as the Higgs and the Z bosons, where colour factors and soft gluon emission enhance the full NLO corrections significantly beyond the LO uncertainty band obtained from scale variation [34–37]. In general, when doing precision physics it is desirable to in-

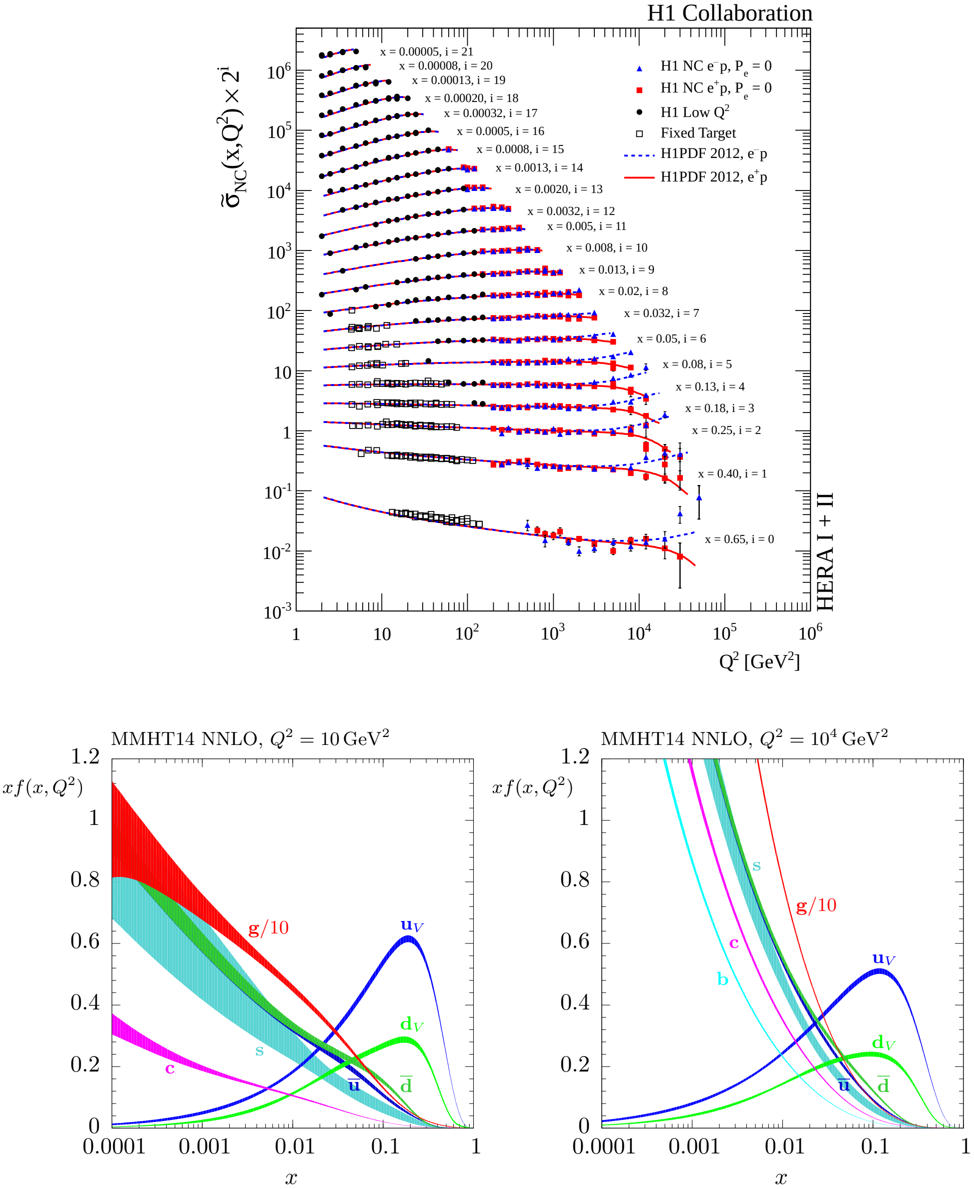

Figure 1.2: Top: neutral-current differential cross sections at the HERA *ep* collider [32], as a function of x and the exchanged energy Q^2, which are directly sensitive to the proton PDFs. Bottom: PDFs extracted by the MMHT global fit at NNLO [33] at the scale $\mu_F = 3.1$ GeV (left), and evolved via the DGLAP equations up to the scale $\mu_F = 100$ GeV (right).

clude at least NLO corrections, in order to improve the accuracy and precision of the computed observables, and to reduce their residual scale dependence.[6]

1.3 NLO computations

To obtain fully differential distributions, two key ingredients are needed in the computation of the partonic cross section: all the relevant amplitudes to compute, up to a given perturbative order, the scattering matrix element (*i.e.* probability) to obtain the desired final state, and a procedure to take care of all the infrared (IR) singularities.

If we are interested in a final state containing at least n particles, $\mathcal{F} = o_1 \dots o_n$, then the partonic cross secton is given by

$$\begin{aligned} 2s\,\sigma_{i_1 i_2 \to o_1 \dots o_n} &= \int d\phi_n \left|\mathcal{A}_{2\to n}\right|^2 \;+\; \int d\phi_{n+1} \left|\mathcal{A}_{2\to n+1}\right|^2 \\ &\quad + \int d\phi_{n+2} \left|\mathcal{A}_{2\to n+2}\right|^2 \;+\; \dots\,, \end{aligned} \tag{1.9}$$

where $2s = 2(p_1+p_2)^2$ is the flux of incoming partons. The scattering probability is given by $|\mathcal{A}|^2$, where the amplitudes $\mathcal{A}$ are computed from the Feynman diagrams of the process; $\mathcal{A}_{2\to n}$ consists of a sum of all the tree-level, one-loop, two-loop, etc. diagrams with n particles in the final state, $\mathcal{A}_{2\to n+1}$ will contain the analogous set of amplitudes with $n+1$ final-state legs, and so on. Different subsets of diagrams will contain different powers of the strong coupling g_s, and therefore will contribute at different perturbative orders. To compute the LO term σ_0 in Eq. (1.6), only the $2 \to n$ amplitudes with the lowest power of g_s are relevant; typically these are tree-level diagrams, but also loop-induced processes exist, such as Higgs production via gluon fusion. The NLO correction σ_1 encompasses the interference of LO diagrams with $2 \to n$ diagrams featuring one extra loop (virtual QCD radiation), and also the squared $2 \to n+1$ lowest-order diagrams (real QCD radiation). For NNLO, $2 \to n$ diagrams with two extra loops, $2 \to n+1$ diagrams with one extra loop, and lowest-order $2 \to n+2$ diagrams are needed, and so forth. The factorial growth in the number of relevant Feynman diagrams, and the need to integrate over multiple quantum loops, means that higher-order calculations rapidly become

---

[6] For example, at LO no explicit dependence on μ_R appears in the expression of the hard scattering $\sigma_{i_1 i_2}$, thus μ_R affects physical observables only implicitly through α_s; formally, two choices $\alpha_s(\mu_{R,1})$ and $\alpha_s(\mu_{R,2})$ differ only by higher-order corrections, so they are equivalent at LO accuracy. In practice, however, the numerical value of α_s can vary significantly with μ_R, leading to a large, uncompensated scale dependence at LO.

unfeasible. At present, state-of-the-art automatic tools can compute arbitrary tree-level and one-loop amplitudes, to provide fully-differential predictions up to NLO; various processes up to $n = 3$ have been computed at NNLO using *ad hoc* techniques, while N^{3}LO results have been obtained only for a $2 \to 1$ process, the production of a heavy and colourless spin-0 particle in gluon fusion (either the Higgs or a pseudoscalar boson).

The scattering probability $|\mathcal{A}|^2$ is integrated over all possible configurations of the final-state momenta, given by the Lorentz-invariant phase space element

$$d\phi_n = (2\pi)^4 \delta^{(4)}(p_1 + p_2 - k_1 \ldots - k_n) \prod_{i=1}^{n} \frac{d^3\vec{k}_i}{(2\pi)^3 2E_i} \,, \tag{1.10}$$

where $E_i = k_i^0$ is the energy of particle i, and momentum conservation is ensured by the $\delta^{(4)}$. Analytic results exist if very few particles are present in the final state, while in general numeric integration (using Monte Carlo techniques) is needed for large phase-space dimensionality. Featuring a different number of final-state particles, virtual and real NLO corrections need to be integrated separately. However, both results are separately divergent, and only suitable combinations are finite and meaningful; this is due to the aforementioned IR singularities. In fact, QCD real emissions satisfy the following relation with respect to the Born amplitudes

$$\lim_{\theta_i \to 0,\, E \to 0} d\phi_{n+1} \, |\mathcal{A}_{n+1}|^2 \;=\; d\phi_n \, |\mathcal{A}_n|^2 \, \frac{\alpha_s}{\pi} \, C_i \, \frac{d\theta_i^2}{\theta_i^2} \frac{dE}{E} \,, \tag{1.11}$$

where $E = k_{n+1}^0$ is the energy of the QCD radiation, θ_i is the angle it forms with any parton i already present at LO, namely $\cos\theta_i = \vec{k}_{n+1} \cdot \vec{k}_i / |\vec{k}_{n+1}||\vec{k}_i|$, and C_i is the emission colour factor ($C_q = 4/3$, $C_g = 3$). Infrared singularities arise because Eq. (1.11) features non-integrable divergences when the QCD real emission is *soft*, namely when its momentum goes to zero ($k_{n+1} \to 0$), or is *collinear* with another parton ($\theta_i \to 0$), or both. While initial-state collinear singularities can systematically be subtracted and reabsorbed into the definition of PDFs, the remaining IR singularities genuinely belong to the partonic scattering. Loop corrections to the Born process present IR singularities of similar origin, that cancel against the real-emission ones. In fact, this must happen in any meaningful physical observable, since the picture we perceive of the world depends on the resolution of the instrument we use to look at it (eyes or detectors). Any finite resolution will act as a regulator; for example, it is impossible to distinguish the $(n+1)$-particle case of a gluon emitted with arbitrarily small energy, to the n-particle case where no such emission took place. Similarly, a collinear system quark+gluon with momenta l and k is degenerate with a single quark with momentum $l + k$, if these particle are massless.

This argument is formalised in the KLN theorem [38,39], which guarantees the cancellation of IR singularities in any sufficiently inclusive observable. Other than total rates, examples of IR-safe observables include fully-differential *jet* cross sections, where QCD radiation is clustered in jets of finite size by suitable IR-safe algorithms; a popular jet definition, which we use throughout this thesis, is given by the anti-k_T algorithm [40]. The term *jet* originates from the fact that the same algorithms are used to cluster collimated jets of hadrons that hit the detectors in collider experiments, as we will see in the next section.

An important point related to Eq. (1.11) is that one can predict the structure of IR divergences and deal with them for any given process. In fact, one can introduce suitable counterterms, parametrised as the Born phase space times a $1 \to 2$ radiation splitting $\phi_n \otimes \phi_2$, to regularise the IR divergences and ensure a numerically efficient cancellation of the infinities. The phase space needs to be sliced in different parts accordingly to the structure of soft and collinear singularities, but schematically we can write

$$\begin{aligned}\sigma_{\mathrm{NLO}} = &\int d\phi_n \left[\mathrm{B}(\phi_n) + \mathrm{V}(\phi_n) + \int d\phi_2\, \mathcal{S}_{\mathrm{IR}}(\phi_{n+1}) \right] \\ &+ \int d\phi_{n+1} \left[\mathrm{R}(\phi_{n+1}) - \mathcal{S}_{\mathrm{IR}}(\phi_{n+1}) \right], \qquad (1.12)\end{aligned}$$

where B is the Born, V is the virtual and R is the real contribution, while $\mathcal{S}_{\mathrm{IR}}$ is the subtraction term introduced to make each integral separately finite. The two contributions will depend on the specific subtraction term $\mathcal{S}_{\mathrm{IR}}$ that we have introduced, however their sum in IR-safe observables does not. Notable schemes to deal with IR divergences at NLO are the FKS subtraction [41], the CS dipole [42] and the antenna subtraction [43–45].

1.4 From partons back to the low-energy world

Parton-level events can be obtained by generating a random phase-space point (*i.e.* a set of final-state momenta) and computing the scattering probability associated to it. Once a statistically significant sample of events is simulated, one can extract predictions about any desired differential distribution. To obtain a realistic description of the physics at hadron colliders, however, this is not sufficient. As we said before, partons describe the physics at scales above a few GeV, and are confined within distances of about 10^{-15} m, so experimental detectors cannot see them directly. What detectors see are instead bunches of hadrons, *i.e.* bound states; even though hadrons tend to be collimated in the directions of the original high-energy partons (see Fig. 1.3), we need to complete the picture by including the evolution of the partonic event down to the low-energy hadronic final state. This is important not only to describe accurately differential distributions, but already when measuring total rates, because experimental detectors have finite acceptance which cannot cover the whole solid angle around the collision, nor measure particles with too-low transverse momentum. When performing this task, it is often necessary to cover, within some approximation, QCD effects that are enhanced at all orders in perturbation theory, and thus are not adequately taken into accout by simple fixed-order results.

A primary example is the enhancement of matrix elements in the limit of a collinear emission; in this approximation, the enhanced part factorises from the rest of the matrix element, and the corresponding emission probability is described by the splitting functions P_{ji} introduced in Eqs. (1.7) and (1.8). One can introduce the Sudakov form factor for each external hard parton i

$$\Delta_i(Q_0, Q_1) = \exp\left[- \int_{Q_0^2}^{Q_1^2} \frac{dt}{t} \int_{\zeta = Q_0^2/2Q_1^2}^{1-\zeta} dz \, \frac{\alpha_s(t)}{2\pi} \, P_{ji}(z) \right] , \tag{1.13}$$

which describes the probability that such a parton, starting from the scale Q_0, survives without undergoing a *resolvable* QCD splitting before the scale Q_1. Note that a logarithmic divergence would be present in the exact collinear limit (and would cancel against the corresponding virtual contribution), while resolvable but quasi-collinear emissions come with a logarithmic enhancement at all orders in α_s, which provides our approximation to the exact matrix element. The non-emission probability is essentially 1 for hard scales close to the partonic scattering, while it rapidly decreases at softer scales, also due to the increasing strong coupling; this leads to the *parton shower* picture, where multiple QCD emissions occur at lower energies and “dress” the hard-scattering event. Another example of enhanced QCD effect is the emission of soft gluons, which under certain assumptions can also factorise and contribute to the Sudakov form factor.

The approximate description of extra $q \to qg$, $g \to q\bar{q}$ and $g \to gg$ branchings outlined above is at the core of parton shower Monte Carlo generators, such as PYTHIA [48–50], HERWIG [51, 52] and SHERPA [53]. The purpose of these programs is in fact to evolve a parton-level event down to low energy observable states. First, they dress the hard event with additional QCD radiation, distributed accordingly to the Sudakov form factor. Starting from a high-energy scale typical of the hard partonic scattering, and following some scale ordering, the non-emission probability decreases with the scale until some resolvable emission occurs. This will be the starting point for generating a new emission at a lower scale, and the process continues until the non-perturbative

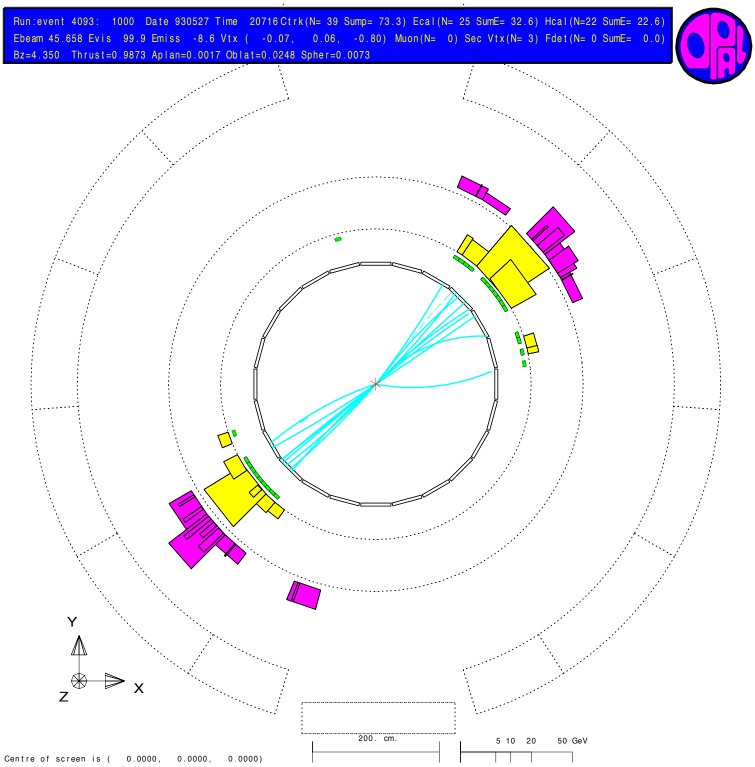

Figure 1.3: Production of two jets of hadrons at the LEP e^+e^- collider. The transverse section in the OPAL detector of an $e^+e^- \to q\bar{q}$ event is shown. The e beams are orthogonal to the page (central red star), and the cyan lines represent the tracks of hadrons originated from the back-to-back $q\bar{q}$ pair. Electrically charged hadrons curve into the detector's magnetic field. Taken from [46].

scale of hadronisation is reached, typically around 1 GeV. The scale ordering ensures that each emission is disentangled from the subsequent ones, and can be generated independently. At the end of the shower, a realistic partonic structure has been obtained, with broadened jets with respect to the original few high-energy parton seeds. Effectively, the parton shower performs a leading-log (LL) resummation of collinear and soft QCD emissions, which is needed to accurately describe events where multiple scales appear; for example, the differential transverse momentum (p_T) distribution of a heavy particle (such as the top quark or the H, W and Z bosons) will receive important QCD corrections in the low-p_T region, see Fig. 1.5.

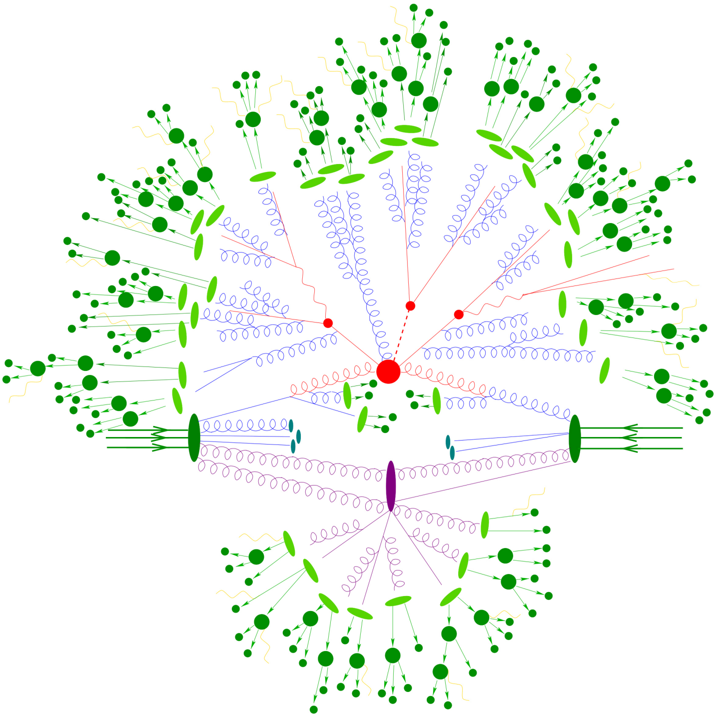

Figure 1.4: Pictorial representation of a hadron-hadron collision at high energy. The hard scattering ($t\bar{t}H$ event) is depicted by red lines, the initial- and final-state parton shower by blue lines, the underlying event by violet lines, and non-perturbative hadronisation by green bubbles. Taken from [47].

After the QCD shower, and possibly a modelling of the low-energy interactions among the proton remnants (underlying event), partons are clustered into hadronic bound states. This is a non-perturbative process, poorly understood from the theoretical point of view. Therefore, it is described by means of some phenomenological modelling of hadronisation that is fitted to experimental data (mainly from hadron productions in e^+e^- collisions), similarly to what happens for the PDFs, and then reused to describe hadron-hadron collisions. After shower and hadronisation, we obtain a realistic low-energy event, which contains the actual particles that are measured in the experimental apparatus. It is important once again to stress that, like the parton distributions, the shower and hadronisation are governed by QCD interactions at lower energy than the partonic scattering; the latter is the only part of the pp scattering that can be affected by possible new physics.

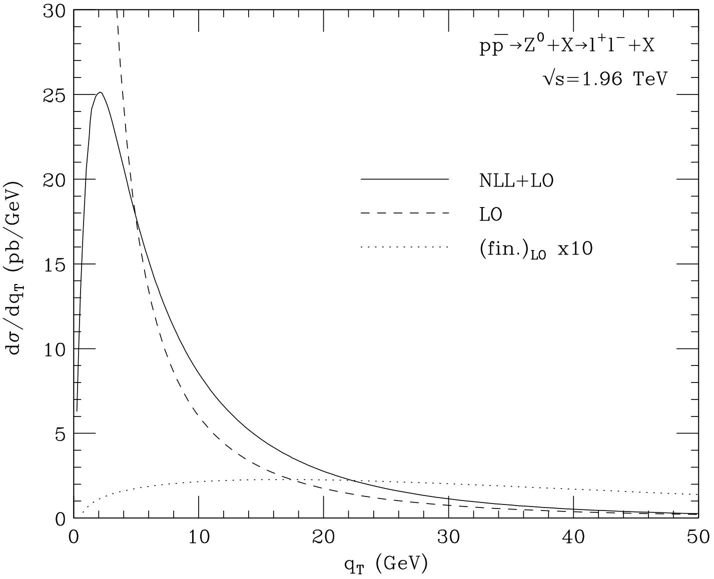

Figure 1.5: Transverse momentum of the Z boson at the Tevatron $p\bar{p}$ collider. The dashed line shows the fixed-order prediction (LO), obtained from the production process $pp \to Z + 1$ parton, which diverges for $p_T \to 0$; the solid line shows instead the resummed result (NLL+LO), which is finite and has an important effect on the shape at low p_T. Taken from [54].

Difficulties can arise when interfacing fixed-order computations in perturbative QCD to parton showers. While at LO the inclusion of PS is straightforward, at higher orders one needs a *matching* procedure to avoid double counting QCD radiation in the shower and in the real-emission matrix element of the hard scattering. At NLO this problem has been solved, and two different methods are available: the MC@NLO [55] matching and the POWHEG [56] matching.

The results presented in this thesis have been obtained employing the MadGraph5_aMC@NLO framework [57]. This framework allows to generate tree-level and one-loop matrix elements automatically, once the Feynman rules for a given theory are provided in the form of a UFO model [58]. It performs the phase space integration using the FKS subtraction [59] at NLO, and it can match parton-level events to Pythia or HERWIG using the MC@NLO prescription. A notable feature present in MadGraph5_aMC@NLO, among many others, is the possibility to decay heavy particles, such as the top quark, keeping spin correlations between the production and decay amplitudes [60]; such task is performed by the MadSpin module [61].

In summary, this is the skeleton of the framework we have employed for producing the results presented in this thesis:

$$\textbf{UFO} \;\rightarrow \textbf{MG5\_aMC} \rightarrow \textbf{NLO+PS events} \rightarrow \textbf{observables} \;,$$

where the UFO model can be either the LOOP_SM, that comes by default with MG5_aMC@NLO in order to do NLO computations in the Standard Model, or the HC_NLO_X0 model [22], that we use whenever we want to simulate non-SM Higgs interactions (for further details, see Chapter 2 and Appendix B).

Chapter 2

Higgs boson and top quark phenomenology

In this Chapter we review some key properties of the Higgs boson and the top quark, whose interplay is of central interest at the LHC research programme, and is also the central topic of this thesis. We summarize the status of the Higgs measurements after the LHC Run I. Then, we introduce the Higgs Characterisation Lagrangian, which provides a framework to study the fundamental top-Yukawa interaction and how it can be affected by BSM physics. At the end, we briefly mention how some properties of the top Yukawa can be investigated in other non-LHC experiments, in particular by means of low-energy and high-precision probes such as EDMs.

For a deeper review of the top quark and, in particular, the Higgs boson and its properties, we refer to the reader to the latest Review of Particle Physics [24], to Ref. [62] and to the technical reports of the LHCHXSWG [19,63–65].

2.1 The unique features of the top quark

Before introducing the Higgs boson in the next Section, here we review some of the properties of the other particle central to this thesis, the top quark.

The top quark was discovered at the Fermilab Tevatron $p\bar{p}$ collider in 1995 by the CDF and DZero experiments [13,14], after almost 20 years of searches. A crucial prediction of the SM electroweak theory is the existence of complete families of particles consisting of a quark doublet (up-type and down-type) and a lepton doublet (charged and neutrino), so that each generation must contain four members. In its first 1960s version the EW theory postulated only two generations of particles. Evidence for the first generation was there before the formulation of the EW theory, while the search for the second generation was completed in 1974 with the discovery of the charm quark, at the SLAC LBL detector in e^+e^- collisions [66], and at BNL in proton collisions against a fixed target [67]. Even before then, however, a third generation of particles had already been hypothesized to explain CP violation in the EW interactions [68]. The first evidence for this third generation was collected with the discovery of the tau lepton from $e^\pm\mu^\mp$ events at the same SLAC LBL experiment [69]. Soon after, in 1977, the bottom quark was discovered at Fermilab [70] analysing proton collisions against a fixed target. These discoveries prompted the search for the two missing partners: the tau neutrino – discovered by the DONUT experiment at Fermilab only in 2000 due to its elusive nature [71] – and the top quark, which, being far heavier than the other elementary fermions, required an accelerator more powerful and advanced than the ones built in the 1970s.

In fact, the top quark is the heaviest known point-like particle: $m_t \simeq 173$ GeV, about 180 times heavier than the proton and 25 times heavier than the bottom quark. This large mass determines many of its peculiar properties, making it a unique particle among the other quarks. First, it is the only quark massive enough to undergo a two-body decay to a bottom and a W boson. At first approximation, the width of this decay reads [74]

$$\Gamma_{t\to Wb} = |V_{tb}|^2 \, \frac{\sqrt{2}G_\mu}{16\pi} \, m_t^3 \left(1 - \frac{m_W^2}{m_t^2}\right)^2 \left(1 + 2\frac{m_W^2}{m_t^2}\right) \simeq 1.5 \text{ GeV}\,, \qquad (2.1)$$

while higher-order QCD corrections reduce this value by about 10%; in other words, the top decays to Wb after approximately $5\cdot 10^{-25}$ s. Such a large decay width, greater than Λ_{QCD}, means that the top quark is not expected to undergo hadronisation[1] during its short lifetime, and offers a unique chance to study a "naked" quark directly from its decay products. For example, the $t \to Wb$ decay can be used to directly test the left-handed structure of electroweak interactions among quarks. We remark that the top quark tends not to couple to the other generations' quarks, namely $V_{tb} \simeq 1$ while V_{td}, $V_{ts} \ll 1$, therefore it almost always decays to the final state considered above. This means that the final state of the top decay is determined by the W decay channel, either to a charged lepton and its neutrino or to hadronic jets. For $t\bar{t}$ events there are three possible combinations: all jets, lepton plus jets (semi-leptonic), and

---

[1] An exception is the possibility to form loosely bound $t-\bar{t}$ states (toponium) if a top pair is produced very close to threshold, *i.e.* almost at rest [75, 76].

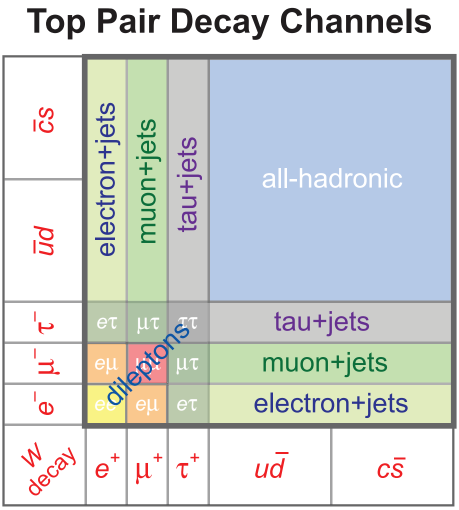

Figure 2.1: Combinations of top decay modes in $t\bar{t}$ production [72].

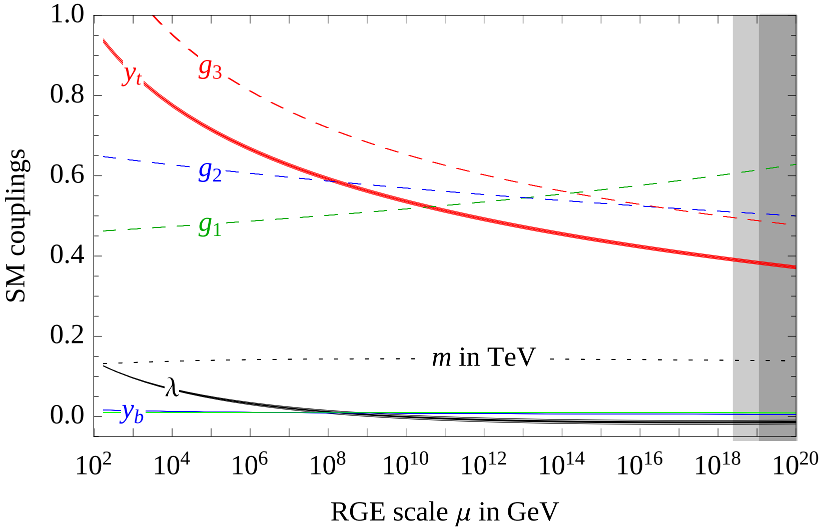

Figure 2.2: Running of the SM couplings up to the Planck scale. The top Yukawa y_t is the second-largest coupling up to about 10^8 GeV, and is significantly higher than any other Yukawa coupling. The λ coupling becomes smaller at high energy, and possibly negative, disrupting the SM vacuum state [73].

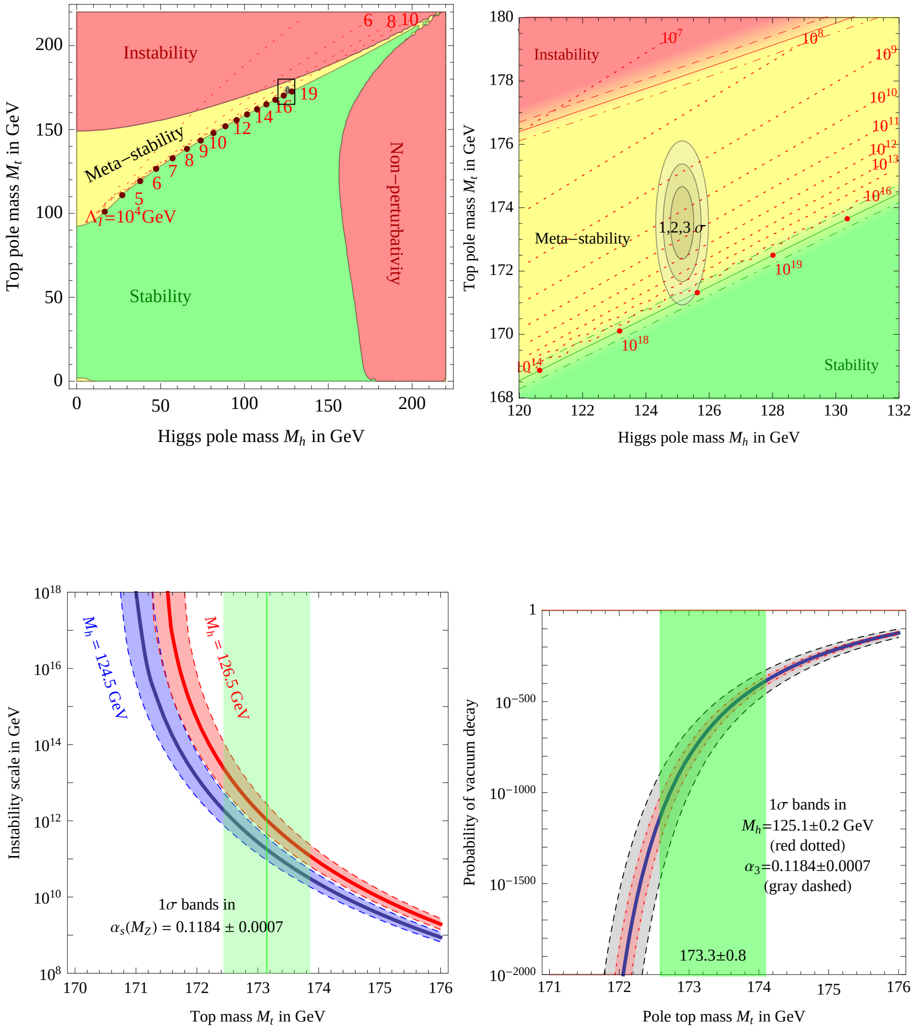

Figure 2.3: Top: stability of the SM as a function of the Higgs and top-quark masses (the right plot is a zoom of the black rectangle on the left). Bottom: Instability scale as a function of the top mass (left), and probability that the universe has decayed to a different vacuum state in our past light cone (right). Taken from [73].

two leptons, see Fig. 2.1. Their relative occurrence probability is roughly 4/9, 4/9 and 1/9, respectively; if we take into account the fact that tau leptons are much more difficult to reconstruct than electrons or muons, the effective fraction of leptonic channels in experimental analyses is smaller.

Second, the top is the only fermion with a Yukawa coupling to the Higgs boson close to unity, its mass being of the same order of the electroweak scale. This has lead to speculation in BSM theories about a special role of the top, ranging from the determination of the electroweak scale itself, to the existence of top-quark partners "behind the corner" of energy frontier. As a consequence, many searches of new physics are based on signatures from top-quark related processes. Regardless of BSM theories, the top quark plays a special role already in the SM, notably in Higgs phenomenology. It is thanks to its large Yukawa coupling, together with the abundance of initial-state gluons at the relevant energies, that gluon fusion is the main Higgs production mechanism at the LHC. Moreover, processes where the Higgs is produced in association with top quarks are the subject of extensive research at the ongoing LHC Run II, and will continue to be a main topic of research at future runs, too. The top Yukawa coupling provides also an important contribution to the running of the λ parameter in the SM potential, and can ultimately determine the stability of the SM vacuum state at high energies if no new physics appears before then, see Fig. 2.2. In fact, the current measurements favour a scenario where the SM vacuum is metastable, with decay time much larger than the current age of the Universe [73]. Nonetheless, we seem to live around a critical point in the SM phase diagram, and a very precise measurement of the top quark mass is needed in order to have the last word on the fate of the SM at high energy: a variation of just about 1 GeV in m_t would make the a difference of orders of magnitude in the stability of the SM, see Fig. 2.3. The top mass is also a crucial parameter in precision fits of the Standard Model; for example, already before its discovery in 2012, the Higgs boson mass range was constrained by the precise measurements of the top and W masses, as we will remark in the next section.

The mass of the top quark is extracted from $t\bar{t}$ events at the Tevatron or the LHC, combining different techniques, which are optimised for the specific decay channel analysed. Current analyses of the fully-hadronic and semi-leptonic channels are based on fitting template distributions with different top masses, while reducing at the same time the systematics associated to the jet energy scale. Alternative multivariate analyeses can be pursued, especially in the dileptonic channels; for example, in "matrix element" techniques the scattering probability is computed event-by-event as a function of the top mass, and then m_t is extracted maximising the likelihood of data. Despite the high level of sophistication reached by present analyses at hadron colliders, they all suffer from a common definition systematic, that makes difficult to interpret the m_t value extracted from the experiment as the actual top mass, with an accuracy better than 1 GeV or so [77, 78]. In fact, what the experiments measure is the so-called Monte Carlo mass, *i.e.* the input parameter in Monte Carlo event simulations at hadron colliders. This quantity roughly corresponds to the propagator pole mass, which is itself affected by theoretical ambiguities of about 100 MeV [78], entangled in addition with the systematics effects related to Monte Carlo event generators, which are the dominant source of uncertainty. To improve the knowledge of the top mass to 100 MeV or better, an e^+e^- collider is needed: a fine scan of the $t\bar{t}$ threshold at such a machine allows to extract a value of m_t free of the aforementioned ambiguities [79].

2.2 The SM Higgs boson after the LHC Run I

Phenomenology of the Standard Model Higgs boson

The primary goal of the Brout-Englert-Higgs (BEH) mechanism is to allow a mass term for the weak vector bosons, without spoiling the mathematical properties of the underlying gauge theory, notably the ones that guarantee a consistent renormalisation procedure [80,81], and also unitarity at high energy. Soon after it was proposed in the 1960s, this mechanism became a cornerstone in the electroweak theory, a composite $SU(2)\otimes U(1)$ gauge theory which aimed at unifying (at high energy) the apparently different (at low energy) electromagnetic and weak interactions. In a nutshell, the BEH mechanism introduces a complex scalar doublet in the EW Lagrangian, and three of its degrees of freedom are used to give mass to the vector bosons $W^\pm$ and Z that mediate charged and neutral weak interactions. This explains why weak interactions are relevant only at subnuclear scales, while the massless photon γ can mediate electromagnetic interactions at longer distances. The remaining fourth degree of freedom results in a massive scalar particle, the Higgs boson H. The existence of this particle is a key prediction of the BEH mechanism, a feature that can experimentally single it out for being the actual mechanism realised in nature, among competing alternatives. For more details, see Appendix A.2.

The first phenomenological studies of the Higgs boson appeared in the 1970s [82], while most of the physicists were still busy unravelling the fundamental nature of weak interactions. The observation of neutral weak currents at the CERN Gargamelle experiment in 1973 [83], and the discovery of the $W^\pm$ (charged) and Z (neutral) mediators of weak interactions at the CERN SPS collider in

1983 [84,85], marked a series of successful predictions of the electroweak theory, which emerged as the undisputed Standard Model (together with QCD). After these discoveries, the Higgs boson attracted more and more attention as the only missing piece of the SM puzzle, until the climax was reached in July 2012, when the LHC experiments finally announced its observation.

The only free parameter of the SM before the Higgs discovery was its own mass. However, bounds on this mass could be given already before the construction of the LHC started. Stringent lower bounds were obtained from direct searches, first at LEP I in the $Z \to Hf\bar{f}$ decay channel, then at LEP II looking for ZH associated production, which ultimately set the limit $m_H > 114.4$ GeV (at 95% c.l.). Before its discovery in 2012, the SM Higgs boson was also constrained to have $m_H < 152$ GeV (at 95% c.l.) from precision fits of the Standard Model to the measured top and W masses, since these three parameters are correlated through electroweak loop corrections, see Fig. 2.4. A loose upper bound $m_H < 1$ TeV can be also derived from general and purely theoretical arguments, imposing perturbative unitarity in weak boson scattering. The observation of a Higgs boson with a mass of 125 GeV, exactly in the window allowed by precision fits, has marked another success of the Standard Model.

The discovery of the Higgs is not the last word on this quest, but the beginning of a new exploration. All the SM predictions on the structure of gauge boson interactions have been successfully tested with high precision since the 1990s, at the CERN LEP collider, the Fermilab Tevatron, the LHC and elsewhere. The scalar sector is the only part of the SM that hasn't yet been probed with the same degree of accuracy. Therefore, a thorough testing of the Higgs particle is mandatory to reveal the innermost nature of the BEH mechanism, to ascertain if the 125 GeV Higgs is fully responsible for the masses of the other elementary particles, or to find signs of possible new physics (BSM) in deviations from the Standard Model paradigm. For instance, the SM predicts precise properties and interactions of the Higgs boson, which are deeply related to how the other known elementary particles acquire mass within this theory. The SM Higgs boson must be a scalar ($J^P = 0^+$) particle, *i.e.* with spin 0 and CP-even interactions with the electroweak bosons; the intensity of this interaction must be proportional to the square of their mass. In terms of mass eigenstates, the relevant part of the SM Lagrangian is

$$\mathcal{L}_{HV} = \left(m_W^2 \, W^{+\mu} W^-_\mu \; + \; \frac{1}{2} m_Z^2 \, Z^\mu Z_\mu \right) \left(1 + \frac{H}{v} \right)^2 , \tag{2.2}$$

which, on top of the mass terms for the W and the Z, implies also the interaction vertices reported in Fig. 2.5a and 2.5b.

Given its minimalistic nature, the SM exploits the same Higgs complex scalar doublet not only to give masses to the weak bosons, but also to generate the masses of fermions via Yukawa interactions. In term of mass eigenstates, these interactions read

$$\mathcal{L}_{Hf} = -\sum_{i=1}^{3} \left(m_{\ell_i} \bar{\ell}_i \ell_i + m_{d_i} \bar{d}_i d_i + m_{u_i} \bar{u}_i u_i \right) \left(1 + \frac{H}{v} \right) , \tag{2.3}$$

where $\ell_i = (e, \mu, \tau)$, $d_i = (d, s, b)$ and $u_i = (u, c, t)$. Similarly to the weak bosons case, an immediate consequence is that not only we get the mass terms for fermions, but also interaction vertices like the one in Fig. 2.5c, with intensity directly proportional to the fermion masses. We can see that the SM Higgs consistently features the same $J^P = 0^+$ properties also in its interaction with fermions. On top of that, once the (arbitrary) overall phase in the coupling with EW bosons is fixed, then also the one with fermions is determined; in other words, the SM Higgs has a well-defined relative sign between the HVV and $Hf\bar{f}$ interactions, which is important in processes such as $H \to \gamma\gamma$ decay or, as we will see in Chapter 5, Higgs production with a single top quark.

The tendency to couple to massive particles leads to a very rich phenomenology, and can be exploited to find its signature in collider experiments. On top of the possible decay signatures in pairs of heavy particles, there are also the loop-induced interactions with two photons (or a photon and a Z) of Fig. 2.6, or with two gluons. In Fig. 2.7 we report the decay branching ratios as a function of the Higgs mass. In fact, having a mass of about 125 GeV, the Higgs cannot decay to a pair of top quarks, and decays predominantly to bottom quarks; other fermions (tau, charm, etc.) follow in order of decreasing mass. While a direct decay to a pair of heavy bosons is kinematically forbidden as well, the final state with four light fermions, mediated by off-shell weak bosons, is another important decay mode. In fact, together with the rare decay to two photons, the four-fermion channel has proven crucial for the Higgs discovery at the LHC, where the $b\bar{b}$ final state is more challenging because of the huge QCD background. Since it cannot decay directly to the heaviest particles in the SM, the Higgs width is relatively small compared to its mass; it approximately amounts to 4 MeV (below the mass resolution of the LHC experiments), which corresponds to a lifetime of about $1.6 \cdot 10^{-22}$ s.

The single Higgs production modes studied at the LHC, and their relative cross sections, are presented in Fig. 2.8. The loop-induced interaction with gluons does not only provide a relatively important contribution to its decay modes; in fact, gluon fusion (GF) is the main Higgs production mechanism at the LHC, thanks both to the large top Yukawa coupling and to the abundance of initial-state gluons at the relevant energies. Important production mechanisms

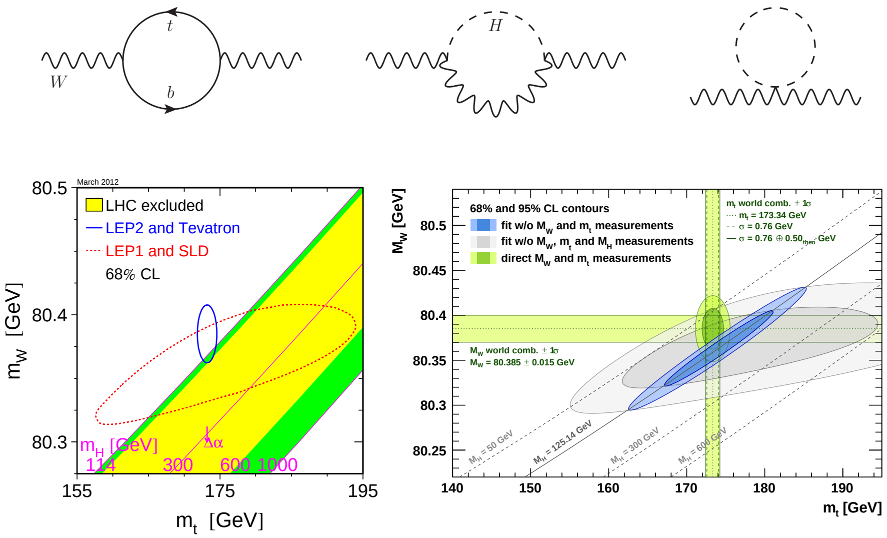

Figure 2.4: Top: examples of loop corrections correlating the masses of the Higgs, the top and the W. Bottom: constraints on m_H from electroweak precision fits, before (left, 2012 [86]) and after (right, 2014 [87]) the direct Higgs mass measurement.

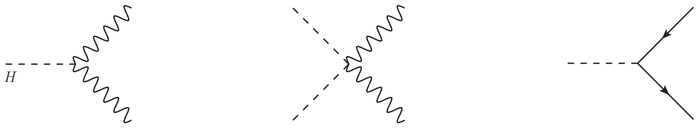

(a) (b) (c)

Figure 2.5: Interaction vertices between Higgs and weak bosons (a) and (b), and between Higgs and massive fermions (c).

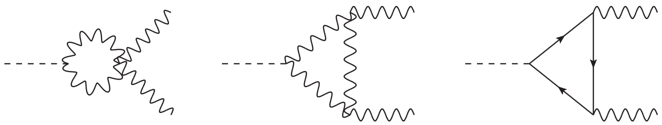

Figure 2.6: Loop-induced interactions with two photons, or a photon and a Z.

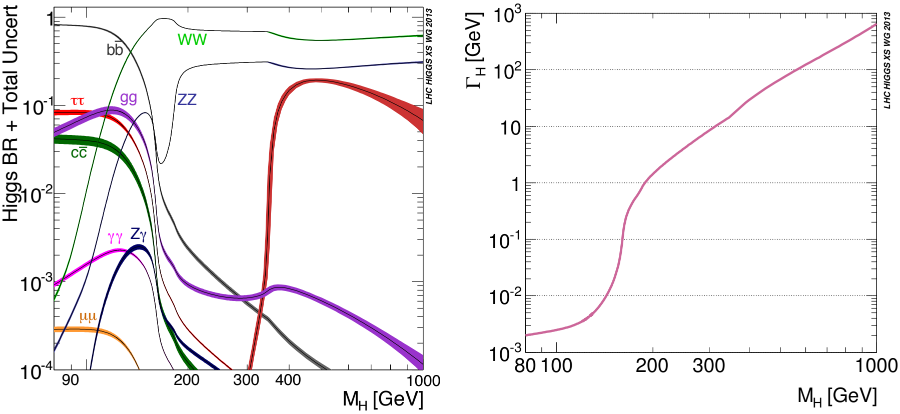

Figure 2.7: Higgs decay branching ratios (left) and total decay width (right), as a function of its mass. Taken from the CERN TWiki of the LHCHXSWG [88].

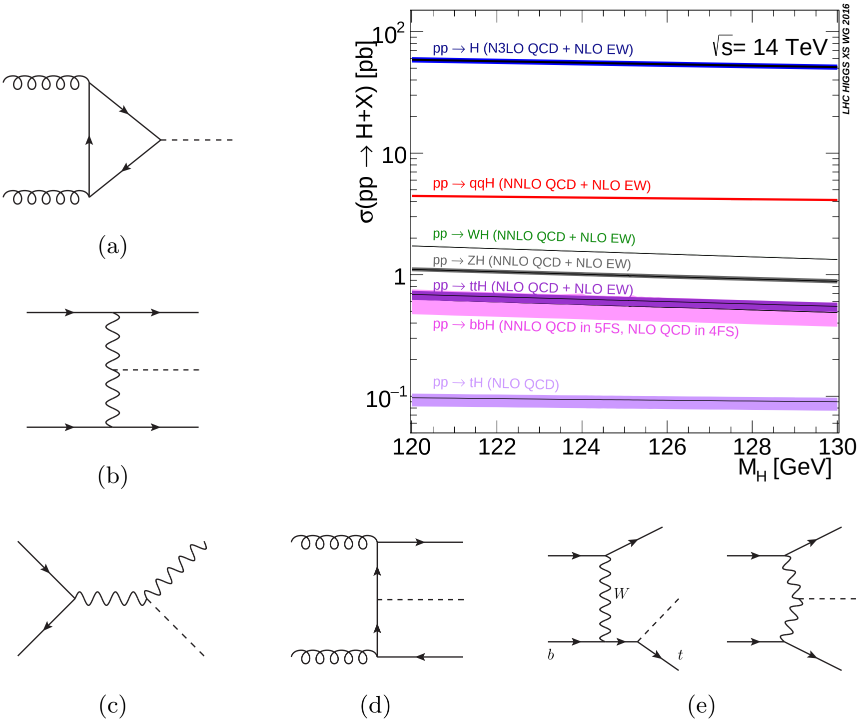
(a)

(b)

(c)

(d)

(e)

Figure 2.8: Sample diagrams for single Higgs production at the LHC, and corresponding cross sections [88] at $\sqrt{s} = 14$ TeV: gluon fusion (a), weak vector boson fusion (b) and associated production (c), associated production with a heavy-quark pair (d) and with a single top (e).

Production process	Measured significance (σ)	Expected significance (σ)
VBF	5.4	4.6
WH	2.4	2.7
ZH	2.3	2.9
VH	3.5	4.2
ttH	4.4	2.0
Decay channel		
$H \to \tau\tau$	5.5	5.0
$H \to bb$	2.6	3.7

Table 2.1: Observation significance of various Higgs boson production and decay modes in the combination of ATLAS and CMS data from Run I. Gluon fusion production (indirectly) and $H \to \gamma\gamma$, WW^*, ZZ^* decays have been clearly observed by each experiment, and are not included. Taken from [12].

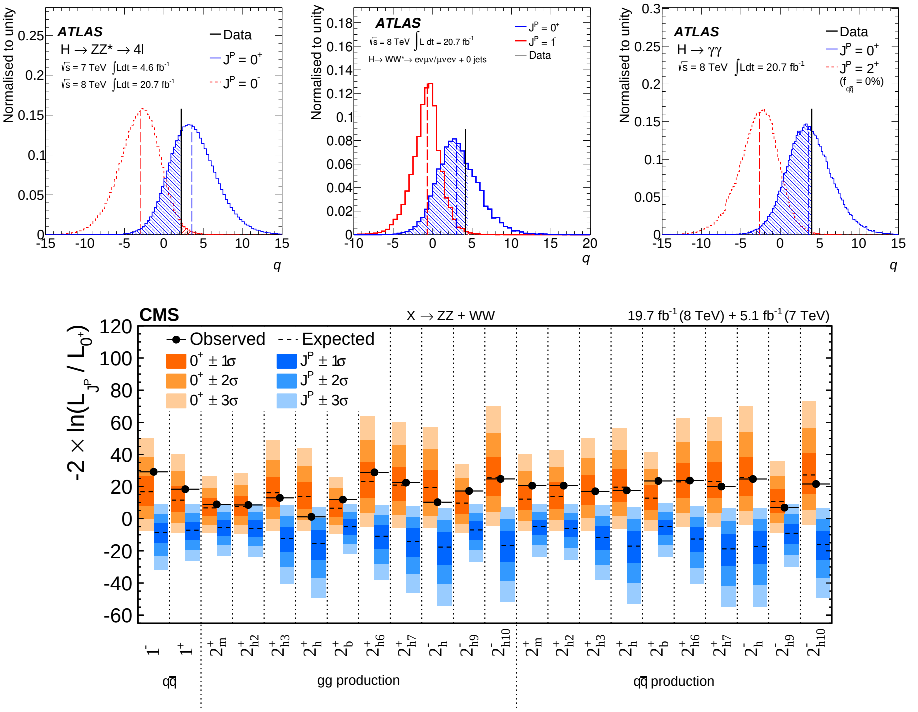

Figure 2.9: Top: ATLAS likelihood tests of the spin and parity properties of the Higgs boson [10]. The data (black line) favour the SM $J^P = 0^+$ hypothesis (in blue) against the 0^- (left), 1^- (centre) and 2^+ (right) alternatives (in red). Bottom: Analogous plots produced by CMS [11], seen from above, testing the SM (in orange) against a variety of spin-1 and spin-2 scenarios (in blue).

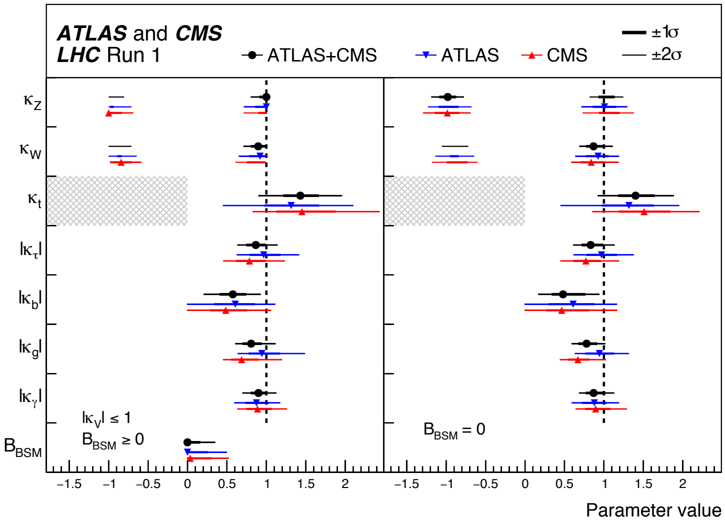

Figure 2.10: Measured intensity of the interaction between the Higgs boson and other SM particles, in terms of coupling strength modifiers κ's and hypothetical BSM interactions. Taken from [12].

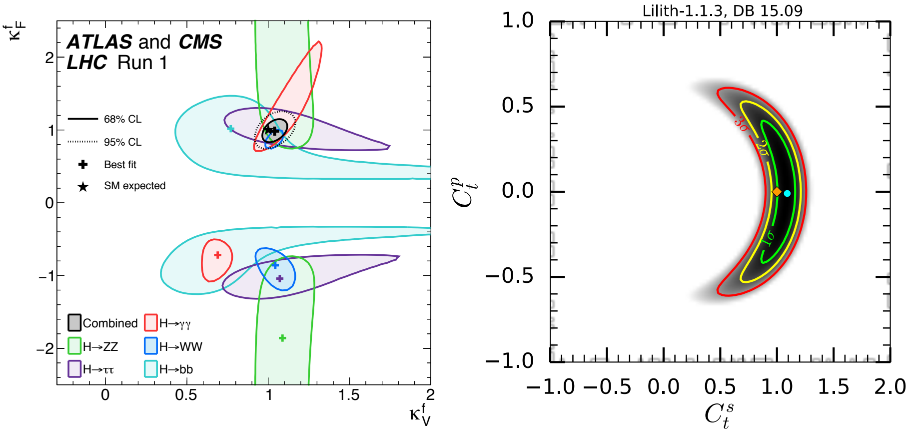

Figure 2.11: Left: Fit of the coupling strength with weak bosons $\kappa_W = \kappa_Z \equiv \kappa_V$ and with fermions $\kappa_t = \kappa_b = \kappa_\tau \equiv \kappa_F$, in the various Higgs final states (f) [12]. Right: Constraints on a CP-violating top quark Yukawa coupling from Run I, assuming the other interactions as in the SM [89]. The plane shows the allowed intensity of the scalar ($C_t^s = \kappa_t$) and pseudoscalar (C_t^p) coupling between the Higgs and the top; this plane is orthogonal to the $\kappa_V - \kappa_F$ one in the left plot, and corresponds to the line $\kappa_V = 1$.

that allow to test the Higgs coupling to the electroweak bosons are the vector boson fusion (VBF) and associated production (VH). Higgs production in association with a pair of heavy quarks (top or bottom) allows to directly probe their Yukawa couplings, while the rare Higgs production in association with a single top quark is sensitive to the relative phase between the HVV and $Hf\bar{f}$ interactions, together with the di-photon decay channel and the loop-induced $gg \to ZH$ production.

Properties of the Higgs boson measured at the LHC Run I

During the LHC Run I, the ATLAS and CMS experiments have collected data corresponding to about 5 fb^{-1} of luminosity at 7 TeV and 20 fb^{-1} at 8 TeV. This has allowed to gather clear evidence for the GF and VBF production processes, and for the Higgs decay to the $\gamma\gamma$, WW^*, ZZ^* and $\tau^+\tau^-$ final states, as reported in Table 2.1.

Thus far, all the observed Higgs properties are consistent with the SM expectations. We have already shown above that its mass of about 125 GeV is consistent with SM precision fits. Its spin and parity have been tested in the $H \to \gamma\gamma$, WW^* , ZZ^* decays, studying correlations among the decay products. As illustrated in Fig. 2.9, data favour a $J^P = 0^+$ scenario over alternative hypotheses with definite parity ($J^P = 0^-$, $1^\pm$, $2^\pm$). The intensity of the Higgs interactions with the other fundamental particles is in agreement with the Standard Model as well, see Fig. 2.10, albeit Yukawa interactions having opposite sign with respect to the SM are not yet ruled out by the Run I data. In fact, the Yukawa sector has just started to being probed, with only direct evidence of Higgs coupling to τ leptons. The experiments are not sensitive to $H \to b\bar{b}$ with Run I data, while the Yukawa coupling with the top quark has been constrained only indirectly, measuring the gluon fusion production and di-photon decay rates and assuming only SM particles in the loops. In particular, at Run I only the $H \to \gamma\gamma$ decay can provide some discrimination on the sign of the top Yukawa coupling; one can see that the left plot in Fig. 2.11 is not symmetric with respect to $\kappa_F = 0$ in this channel. The other Yukawas provide too tiny corrections to the di-photon channel, while $H \to f\bar{f}$ decays are sensitive only to the absolute magnitude of the coupling. Decisive information on the Yukawa sector is going to be extracted at the LHC Run II and beyond, where the energy and luminosity will allow to study direct production of the Higgs in association with top quarks, thus a direct extraction of the top Yukawa coupling, including its sign. Higgs decay to bottom quarks is also expect to be unambiguously observed and measured.

2.3 Investigating the top Yukawa properties

For a thorough discussion on how to provide a sufficiently general parametrisation of BSM physics, how to maximise the extraction of information from LHC data in a way that is as little model-dependent as possible, and how to interpret the experimental results in order to constrain or find new physics, we refer to the fourth LHCHXSWG report [19], in particular Chapters II and III. In this Section we give a brief survey in order to introduce the Higgs Characterisation framework, and we focus on the part related to the top Yukawa interaction. This framework has been employed to produce many of the original results presented in this thesis, that are going to be discussed in the next Chapters. At the end, we also briefly address constraints on the top Yukawa from non-LHC experiments.

Effects of new physics on the Higgs-top interaction

With Run I data, the ATLAS and CMS experimental collaborations have constrained deviations from the SM paradigm in the so-called κ framework [65,90], where the SM interactions in Eq. (2.2) and (2.3) are simply rescaled by a constant factor κ. This is a convenient approach, where the path towards increasingly precise measurements of the strength of a Yukawa coupling is relatively straightforward. However, it is certainly not the most general way to look for deviations from the SM; an exploration of hypothetical contributions from interactions with a structure different to the SM case is considerably more open.

For instance, CP violations in the SM and beyond are an active topic of research. Since such effects are tiny in the SM, new sources of CP violation from BSM physics are needed in order to explain the imbalance between baryonic matter and antimatter observed in the universe. Therefore, it is interesting to investigate whether there is room for CP violation in the Yukawa sector; namely, if the Higgs is not exactly a CP-even 0^+ state, but can couple to both scalar and pseudoscalar fermionic currents, notably with the top quark. In this perspective, one could add to the Lagrangian a new pseudoscalar interaction between the Higgs and the top, given by the operator

$$C_t^p \left(-i \frac{m_t}{v} \bar{\psi}_t \gamma_5 \psi_t H \right) , \tag{2.4}$$

and ask how much this BSM interaction is constrained by data. This question expands the fit parameter space beyond the usual κ framework, adding a new parameter C_t^p. The right plot of Fig. 2.10 shows the result of such a phenomenological study, that constrains CP-mixing in the top Yukawa interaction (*i.e.* the other interactions are assumed to be the SM ones, and only two parameters enter the fit), employing the public LHC data.

A consistent top-down approach to BSM interactions needs to assume a UV-complete theory that extends the SM Lagrangian, for example a two Higgs doublet model (2HDM). In fact, the SM employs one $SU(2)$ doublet to generate the masses of both gauge bosons and fermions; while this is certainly an elegant and economic solution, we can add more than one Higgs doublet to the Lagrangian (the simplest step forward being two). Given the larger parameter space, in practice there can be different realisations of the 2HDM, see [91] for a thorough review. In all realisations the particle spectrum is enriched with more scalar particles; one of them can resemble the SM Higgs boson for appropriate parameter choices, but in general its interactions with the other SM particles can be different. Depending on the actual parameters of the 2HDM, deviations from the SM paradigm can sometimes be striking, for example resulting in fermion Yukawa couplings with similar magnitude but opposite sign than in the SM [92]. In typical realisations of the 2HDM, flipped-sign Yukawa couplings of up-type quarks such as the top are challenged by the combination of LHC data and precise measurements on B hadrons in flavour physics, since the latter significantly constrain the allowed parameter space, or even rule out this scenario entirely [93]. On the other hand, flipped-sign Yukawa couplings of down-type quarks such as the bottom are still allowed, but are much harder to probe at the LHC (the major effect comes from the interference between t and b loops in gluon fusion).

Perhaps more importantly, the 2HDM allows for new sources of CP violation, which is the historical reason behind its proposal [94] and motivates our initial question about the CP properties of the top Yukawa. In fact, if no additional symmetries are imposed with respect to the SM, CP mixing can occur in the top Yukawa interaction (among others). However, this comes also with flavour-changing neutral currents (FCNCs) involving the Higgs boson and the top quark, mediated by Htu and Htc vertices; other FCNCs in the Yukawa sector are typically suppressed by the masses of lighter fermions. Recently, CMS and ATLAS have put experimental limits on top-Higgs FCNCs in the $t \to Hq$ decay [95, 96], which leaves room for $\mathcal{O}(10\%)$ deviations from the SM; accordingly, there can be as well some small room for CP-mixing effects in the top Yukawa.

While the 2HDM provides a popular benchmark for investigating possible BSM physics in many directions, there are many more theories that extend the SM and predict some effect in the properties of the Higgs boson and its interactions with the other SM particles. For example, deviations in the Higgs boson couplings could also result from a composite Higgs scenario, see Section VII.6.3 in [24].

On the one hand, despite the limits of 2HDMs or other models, we can see that there is theoretical motivation to investigate at the LHC both the reversed-sign scenario and the possibility of CP mixing in the top-quark Yukawa interaction. On the other hand, the lack (so far) of clear signs of new physics from the LHC at the EW scale discourages a top-down approach in Higgs physics, because there is no guideline to which BSM theory should be preferred in order to interpret the experimental results. A bottom-up approach is more convenient in this case, and a theoretically consistent formulation is given by the effective field theory (EFT) framework.

The EFT consists in adding to the SM Lagrangian all the higher-dimensional operators in the SM fields, namely the operators with dimension $d > 4$. Dimensional analysis dictates that the couplings in front of these operators must contain some inverse power of a scale Λ^{4-d}, typically associated to new physics, such as the mass of a BSM particle mediating the interaction

$$\mathcal{L}_{\mathrm{SMEFT}} = \mathcal{L}_{\mathrm{SM}} + \sum_{d>4} \frac{c_i}{\Lambda^{d-4}} \mathcal{O}_i^{(d)} . \tag{2.5}$$

In general, the EFT description is helpful to capture the low-energy effects of a new high-energy theory, whose new particles are too heavy to be produced. In this case, higher-dimensional operators are suppressed by the new physics scale Λ, so, they provide small effects. Moreover, only the operators with lowest dimension become relevant, and one can typically ignore those with dimension higher than six. In short, at scales smaller than Λ the EFT becomes predictive and can be employed as a consistent formulation of the physics. Such an approach has proven to be extremely successful in modelling weak interactions such as β decay at energies much smaller than the EW scale, namely in the Fermi theory. In this case, physics is described by a four-fermion interaction vertex, derived from a dimension-six operator, with a dimensionful coupling that depends on the masses of the weak boson mediator $G_\mu \sim 1/m_W^2$. Since no BSM particle has yet been discovered at the LHC, and no strong deviations from the SM have been found so far, the EFT approach looks suitable to quantify and constrain deviations from the SM at the electroweak scale, in a way that is rather general and model independent. Moreover, higher-order corrections in the SM interactions, notably those coming from QCD, can be consistently included for the purpose of precision physics at the LHC.

The major drawback of the EFT approach is that a considerable amount of new parameters is added to the theory. As a matter of fact, the SM is described in terms of 18 parameters, while the dimension-six operators add 2499 parameters to the SM EFT Lagrangian, way too many to be tackled at once. Even if we consider only operators that directly affect Higgs physics, we are still left with 65 parameters to constrain, which are still quite a lot. Moreover, the validity of the EFT is limited to small deviations from the SM paradigm, and so is the interpretation of experimental results. In summary, on the one hand the EFT is more general than the κ framework because it allows to investigate a broader range of interactions than simply the SM ones. On the other hand, however, it cannot easily allow to explore scenarios such as a reversed-sign top Yukawa coupling, which is not a small deviation because it entails a BSM effect twice as large as the SM one (and with opposite sign).

Higgs Characterisation of the top Yukawa

The Higgs Characterisation (HC) framework [15] fits in the bottom-up strategy outlined above, and aims to provide a practical approach to study and constrain the Higgs properties at the LHC. It is a hybrid model that combines the κ framework, allowing for an arbitrary rescaling of the SM interactions, and a simplified EFT, where only the higher-dimensional operators most relevant for single-Higgs processes are included, thus the number of parameters to fit is more manageable. In practice, this model extends the κ framework, allowing to investigate the effects of new physics that cannot be described by a simple rescaling of the SM interactions, such as those related to CP violation. As we will see in the next chapters, BSM physics entails in general new Lorentz structures that can affect the shape of distributions. For example, it can experimentally result in harder p_T tails, or different angular and rapidity correlations. Therefore, at variance with the κ framework, the HC framework allows not only to measure the Higgs properties resulting from total cross sections, but also to include the information carried by differential shapes. Clearly, this is important in order to maximise the information extracted from Higgs data, especially since new physics may manifest itself only in some corners of the phase space, and not in the bulk of Higgs events.

The complete HC Lagrangian, including the higher-dimensional interactions with EW bosons, is reported in Appendix B. Since we are interested in exploring the top-quark Yukawa interaction, here we report just the relevant operator, that is

$$\mathcal{L}_0^t = -\bar{\psi}_t\big(c_\alpha \kappa_{Htt} g_{Htt} + i s_\alpha \kappa_{Att} g_{Att}\, \gamma_5\big)\psi_t\, X_0\,. \tag{2.6}$$

Here X_0 labels a generic spin-0 particle with CP-violating couplings, $c_\alpha \equiv \cos\alpha$ and $s_\alpha \equiv \sin\alpha$ are related to the CP-mixing phase α, $\kappa_{Htt,Att}$ are real dimensionless rescaling parameters, and $g_{Htt} = g_{Att} = m_t/v\,(= y_t/\sqrt{2})$, with $v \simeq 246$ GeV. While obviously redundant (only two independent real quantities are needed to parametrise the most general CP-violating interaction), this parametrisation has several practical advantages, among which the possibility of easily interpolating between the CP-even ($c_\alpha = 1, s_\alpha = 0$) and CP-odd ($c_\alpha = 0, s_\alpha = 1$) assignments, as well as to easily recover the SM case when $\alpha = 0$ and $\kappa_{Htt} = 1$. We can see that κ_{Htt} rescales the SM Higgs-top interaction, while the pseudoscalar contribution comes from the dimension-six operator

$$\frac{c_t}{\Lambda^2}\,(\phi^\dagger\phi)\,\big(Q_L\tilde{\phi}\big)\,t_R \,+\, \text{h.c.} \tag{2.7}$$

with c_t complex, and then setting two $\phi = v$, which is suitable for single-Higgs processes. The EFT hypothesis is satisfied if deviations from the SM are not too large, *i.e.* $c_\alpha\kappa_{Htt} \simeq 1$ and $s_\alpha\kappa_{Att} \simeq 0$, but of course one can actually explore a wider range of scenarios, such as the reversed-sign top Yukawa coupling when $\alpha = 0$ and $\kappa_{Htt} = -1$. We have discussed above how the exploration of CP mixing or a flipped-sign Yukawa coupling can be motivated (at least theoretically) and interpreted in the light of a 2HDM. Interestingly, in the HC framework a flipped-sign top Yukawa can be seen as the result of two continuous, but physically different transformations: either a rescaling of the SM interaction from $\kappa_{Htt} = 1$ to $\kappa_{Htt} = -1$ (as in the κ framework), or a rotation in the CP-mixing plane from $\alpha = 0$ to $\alpha = \pi$.

The nature of the top quark Yukawa coupling directly affects the loop-induced Higgs coupling to gluons[2], which in the limit of a heavy top quark can be described by

$$\mathcal{L}_0^g = -\frac{1}{4}\,\big(c_\alpha\kappa_{Hgg}g_{Hgg}\,G^a_{\mu\nu}G^{a,\mu\nu} \,+\, s_\alpha\kappa_{Agg}g_{Agg}\,G^a_{\mu\nu}\widetilde{G}^{a,\mu\nu}\big)X_0\,, \tag{2.8}$$

where $g_{Hgg} = -\alpha_s/(3\pi v)$ and $g_{Agg} = \alpha_s/(2\pi v)$. For further information on the Higgs interactions with gluons, see Appendix C. In the parametrisation given above, the strength of the coupling between Higgs and gluons can be rescaled independently of the top quark Yukawa coupling. Assuming that the top quark dominates the gluon-fusion (GF) process at the LHC energies, then $\kappa_{Hgg} \to \kappa_{Htt}$ and $\kappa_{Agg} \to \kappa_{Att}$.

These interactions have been implemented in the public code of the UFO model HC_NLO_X0 [22], together with the NLO UV counterterms for these new interactions, as well as the R_2 terms needed to compute loop integrals with the OPP method [97]. This model can be loaded from MadGraph5_aMC@NLO

---

[2] The loop-induced couplings to $\gamma\gamma$ and $Z\gamma$ are affected as well by an anomalous top Yukawa, but not reported here. Note that in this case there is also the numerically dominant W loop.

and used to generate simulations of single-Higgs processes at state-of-the-art NLO+PS accuracy. In fact, high precision and accuracy both in SM and BSM predictions are needed to be sensitive to new physics effects. The discussion of results obtained within this framework largely constitutes the core of original results presented in this thesis, which encompasses Chapter 3 to Chapter 6. Here we also remark that HC_NLO_X0 has been the first model allowing to generate processes at NLO within MadGraph5_aMC@NLO, beyond the built-in SM (loop_sm). For this reason, it has provided a key feedback to develop and improve the flexible MadGraph5_aMC@NLO framework, especially in its early versions.

Low-energy probes of the Yukawa interactions

While experiments at the high-energy frontier, provided by the LHC collisions, are a natural and direct way to investigate the Higgs boson's properties and interactions, the quest of finding new physics is much more wide-ranging. For instance, it is actively pursued also in experiments at lower energies, but at the intensity and precision frontiers, which can provide indirect but complementary and valuable constraints on the SM and on BSM effects. Thus, before moving to the LHC results of this thesis in the next Chapters, we would like to briefly recall a few results from low-energy probes of the Yukawa sector.

An important example of low-energy probe, and the only one we discuss here, is given by electric dipole moments (EDMs). The EDMs of long-lived particles (ordinary matter) can be measured with astounding accuracy, which can be sensitive to new-physics effects in higher-order loop corrections. For example, in Fig. 2.12 we show some two-loop diagrams contributing to the EDM of the electron and the neutron, that give corrections proportional to the top-quark Yukawa interaction. While on the one hand the current precision of EMD experiments does not allow to constrain the intensity of a SM-like top Yukawa coupling (*i.e.* a scalar interaction in the κ framework), on the other hand they can be very sensitive to a CP-violating Yukawa interaction. In fact, the EDM of the electron and neutron in the SM are extremely small and out of the reach of current experiments, while a pseudoscalar contribution to the top Yukawa would result in an effect larger by many orders of magnitude, and experimentally accessible. As we can see from Fig. 2.13, these probes, in particular the electron EDM, put a very stringent constraint on a CP-mixed top Yukawa, much more than LHC data. The only critical assumption to obtain this constraint is that the Higgs Yukawa interaction with first-generation fermions must be exactly the SM one, and CP-violating effects are limited to the third generation. If one lifts this assumption, then only the neutron EDM

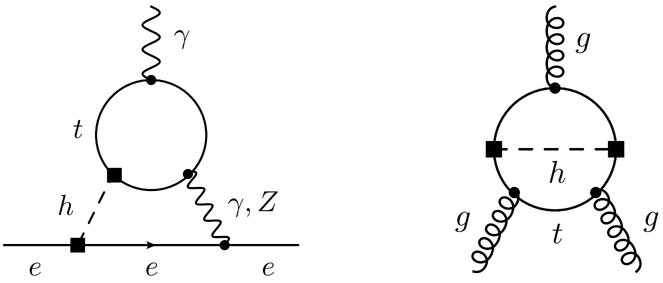

Figure 2.12: Left: Barr-Zee [98] diagram contributing to the EDM of the electron. Similar diagrams with the up and down quarks affect the EDM of the neutron, while inserting gluons in the place of photons one gets the chromoelectric contribution (CEDM). Right: Weinberg [99] diagram contributing the the EDM of the neutron.

remains sensitive to the top Yukawa through the right diagram in Fig. 2.12, and the constraining power from EDMs is degraded considerably, becoming significantly worse than the one from LHC data, see Fig. 2.14. Nevertheless, future-generation experiments on the neutron EDM can provide competitive constraints, complementary to the ones from the LHC.

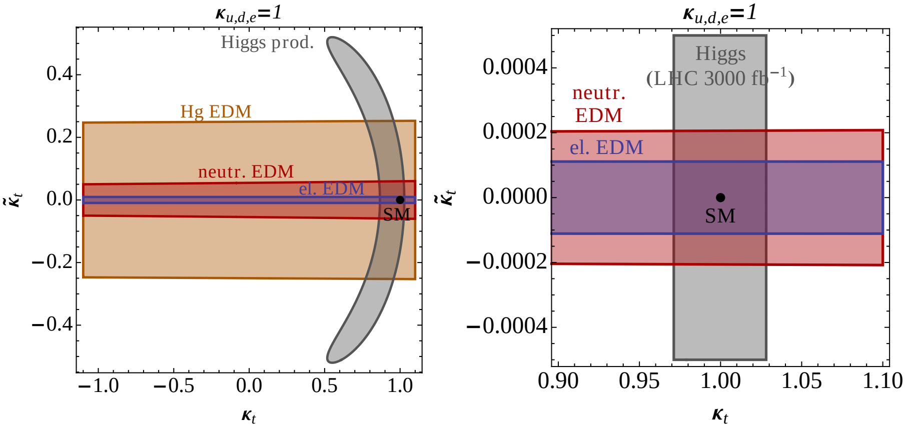

Figure 2.13: EDM constraints on CP-violation in the top-quark Yukawa interaction, assuming the SM Higgs interactions with first-generation fermions (left), and projected sensitivity of future-generation experiments (right). Taken from [100].

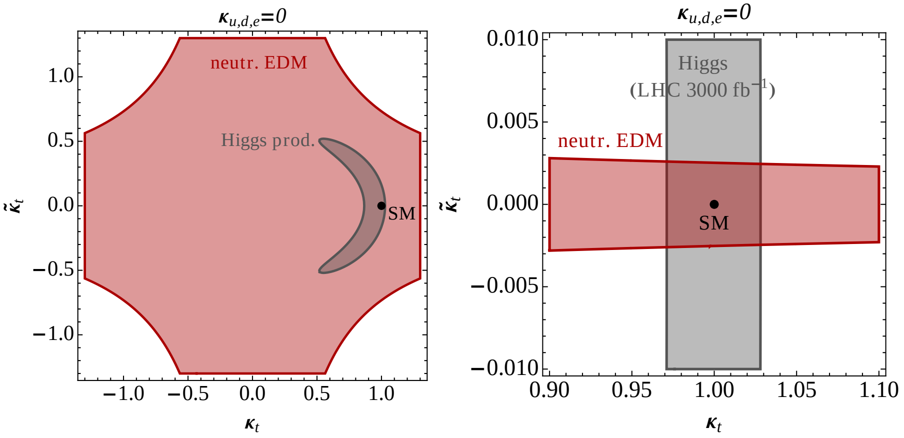

Figure 2.14: Same as Fig. 2.13, but after lifting the assumption of a SM Yukawa interaction with the first-generation fermions.

Chapter 3

Higgs plus two jet production via gluon fusion

In this chapter we study Higgs plus two jet production ($H + 2j$) via the gluon fusion (GF) mechanism, at NLO accuracy in QCD and also matching short-distance events to a parton shower (NLO+PS). In particular we investigate observables which provide indirect probes to the CP properties of the top-quark Yukawa interaction; in the heavy-top limit, these properties are inherited by the effective interactions between the Higgs and the gluons in the corresponding EFT. We also perform a comparison to vector boson fusion (VBF) results in the same observables, in order to assess possible overlap and contamination between these two processes.

The chapter is organised as follows: in section 3.1 we describe the setup and input parameters for NLO simulations, including parton-shower matching. In section 3.2 we present total rates for gluon-fusion Higgs production plus one and two jets, both at fixed order and after shower effects. In section 3.3 we discuss differential distributions for Higgs plus two jets at NLO+PS accuracy, focusing in particular on the CP-sensitive observables (in the lab frame), and performing a comparison between the gluon fusion and the vector boson fusion processes. The main results presented in this chapter are summarised in section 3.4.

We remark here that as GF is the dominant Higgs production mechanism, enormous theoretical efforts to achieve more precise computation have been made over the last two decades, and we refer to the reports by the LHC Higgs Cross Section Working Group (LHCHXSWG) [19, 63–65] for more details. State-of-the-art predictions (in the EFT) for the single-Higgs inclusive cross section have been computed at N^{3}LO accuracy [101], while Higgs plus one jet has been recently computed at NNLO by various groups (see *e.g.* [102] and references therein).

The original results we present in this chapter are NLO prediction, in the large top-mass limit, for GF production at the LHC of a generic (mixed) scalar/pseudoscalar state in association with one or two jets, also matching to parton shower; they have been published in [16]. These NLO+PS predictions represent the state-of-the-art accuracy for Higgs plus two (or more [103]) jet calculations, whose feasibility has greatly improved thanks to the present automatic tools for computing tree-level and one-loop amplitudes.

Previously to [16], Higgs production plus two (three) jets through GF has been computed at LO in refs. [104, 105] (refs. [106, 107]), where the full top-mass dependence was retained. The results cited above justify the use of the Higgs–gluon EFT, showing that it is a very good approximation as long as the transverse momentum of the jets is not sensibly larger than the top mass. At NLO, the resulting analytic expressions for GF $H + 2j$ in the $m_t \to \infty$ limit have been implemented in MCFM [108], and at NLO+PS in the POWHEG BOX [109] and SHERPA [110]. Independent NLO+PS predictions in SHERPA plus GOSAM [111] and in MADGRAPH5_AMC@NLO [57] were also available. All the above results were computed for the SM Higgs boson, *i.e.* the CP-even state, while the CP-odd state $A+2j$ production has been available only at LO, yet with the exact top-mass dependence [112].

3.1 Setup of the NLO+PS simulation

We generate events at the LHC with centre-of-mass energies $\sqrt{s} = 8$ and 13 TeV, and we set the spin-0 particle's mass to $m_{X_0} = 125$ GeV, while we match the effective operators in Eq. (2.8) to the SM heavy-top-quark limit (with the other five quarks massless), see Appendix C.

In MADGRAPH5_AMC@NLO the code and the events for X_0 plus two jets in the GF channel can be automatically generated by issuing the following commands (note the `/ t` syntax to forbid diagrams containing top loops):

```
> import model HC_NLO_X0-heft
> generate p p > x0 j j / t [QCD]
> output
> launch
```

where the `-heft` suffix in the model name refers to the corresponding model restriction. As a result, all the amplitudes featuring the Higgs–gluon effective vertices in the heavy-top limit are generated, including corrections up to NLO in QCD. Analogous commands can be issued to generate events for X_0 plus zero and one jet at NLO. Since our interest is geared towards QCD effects in production distributions, we do not include Higgs decays in our studies.

Parton distribution functions (PDFs) are evaluated by using the NNPDF2.3 (LO/NLO) parametrisation [113] in the five-flavour scheme (5FS), through the LHAPDF interface [114]. For NLO predictions, the PDF uncertainty is computed together with the uncertainty in the strong coupling constant $\alpha_s(m_Z)$

$$\alpha_s^{(\mathrm{NLO})}(m_Z) = 0.1190 \pm 0.0012 \ (68\,\%\ \text{c.l.})\,, \tag{3.1}$$

as described in [115] (the confidence interval is taken accordingly to the 2010 PDF4LHC recommendations [116, 117]). For LO predictions we compute the sole PDF uncertainty[1], with $\alpha_s^{(\mathrm{LO})}(m_Z) = 0.130$ [118, 119].

Central values μ_0 for the renormalisation and factorisation scales $\mu_{R,F}$ are set to

$$\mu_0^{(\mathrm{GF})} = H_T/2 \tag{3.2}$$

for X_0(+jets) production in the GF channel, and to

$$\mu_0^{(\mathrm{VBF})} = m_W \tag{3.3}$$

for X_0jj production in the VBF channel, where $m_T \equiv \sqrt{m^2 + p_T^2}$ is the transverse mass of a particle, and H_T is the sum of the transverse masses of the particles in the final state. Uncertainties coming from missing higher orders are estimated varying μ_R and μ_F, independently, by a factor 2 around μ_0,

$$1/2 < \mu_{R,F}/\mu_0 < 2\,. \tag{3.4}$$

We define the total theoretical uncertainty of an observable as the linear sum of two terms: the PDF+α_s uncertainty on the one hand, and the overall scale dependence on the other.

For parton showering and hadronisation we employ HERWIG6 [51]. Jets are reconstructed with the anti-k_T algorithm [40] as implemented in FastJet [120], with distance parameter $R = 0.4$ and requiring

$$p_T(j) > 30\ \text{GeV}\,, \quad |\eta(j)| < 4.5\,. \tag{3.5}$$

GF J^P scenario	HC parameter choice	
0^+(SM)	$c_\alpha = 1\,,$	$\kappa_{Hgg} = 1$
0^-	$c_\alpha = 0\,,$	$\kappa_{Agg} = 1$
$0^\pm$	$c_\alpha = 1/\sqrt{2}\,,$	$\kappa_{Hgg,Agg} = 1$

Table 3.1: Benchmark scenarios for $H + 2j$ production via GF.

VBF J^P scenario	HC parameter choice		
0^+(SM)	$c_\alpha = 1\,,$	$\kappa_{SM} = 1$	
0^+(HD)	$c_\alpha = 1\,,$	$\kappa_{HZZ,HWW} = 1\,,$	$\Lambda = 1$ TeV
0^-(HD)	$c_\alpha = 0\,,$	$\kappa_{AZZ,AWW} = 1\,,$	$\Lambda = 1$ TeV
$0^\pm$(HD)	$c_\alpha = 1/\sqrt{2}\,,$	$\kappa_{HZZ,HWW,AZZ,AWW} = 1\,,$	$\Lambda = 1$ TeV

Table 3.2: Benchmark scenarios for VBF, used for comparison to GF.

In Table 3.1 we list the representative scenarios that we later use for illustration, with the X_0 couplings to fermions as described by Eq. (2.6), and the effective couplings to gluons as described by the corresponding gluonic operators in Eq. (2.8). The first scenario, which we label 0^+(SM), corresponds to the SM (in the heavy-top limit). The second scenario, which we label 0^-, describes a pure pseudoscalar state. The third scenario, $0^\pm$, represents a CP-mixed case, where the spin-0 boson is a scalar/pseudoscalar state in equal proportions.

To compare between $H + 2$ jets in GF and in VBF, we collect in Table 3.2 some of the physics scenarios considered in the HC paper on VBF [121]. The first scenario corresponds to the SM. The second scenario, 0^+(HD), represents a scalar state interacting with the weak bosons in a custodial invariant way through the higher-dimensional (HD) operators in Eq. (B.3) with $\kappa_{HZZ,HWW}$ coefficients (see Appendix B). The third scenario, 0^-(HD), is the analogous of a pure pseudoscalar state, while the fourth scenario is representative of a CP-mixed case, with equal contributions from the scalar and pseudoscalar components.

---

[1] At the time when [16] was prepared, there was no PDF set allowing the correct assessment of PDF+α_s uncertainty at LO.

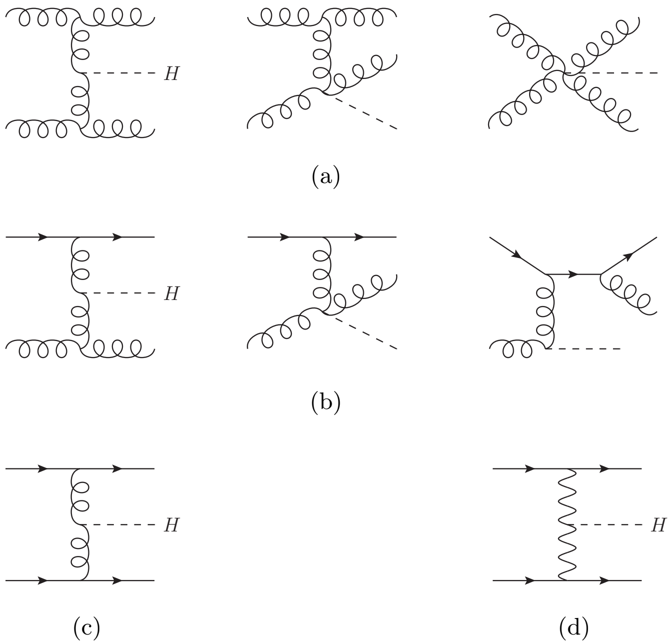

(a) (b) (c) (d)

Figure 3.1: Examples of LO Feynman diagrams for Higgs plus two jet production, via gluon fusion in the gg (a), qg (b) and qq (c) channels (after integrating out the top-quark loop), and via weak boson fusion (d). In the pseudoscalar case the gg-channel diagram on the right is zero, see appendix C.

3.2 Total rates

In this section we discuss inclusive results, showing total cross sections for Higgs plus two jet production in the gluon-fusion channel. Unlike the VBF case, which starts at LO with two jets in the final state, requiring the presence of jets in the GF final state entails imposing cuts at the generation level, and also after the event generation in the case of NLO+PS simulations[2]. As a consequence, the total cross section depends on the jet definition, both in terms of reconstruction algorithm and in terms of cuts; in this case, the anti-k_T algorithm is employed, and the acceptance cuts in Eq. (3.5) are imposed. Also note that, since reconstructed jets after parton shower and hadronisation are different from the fixed-order partonic jets, the PS-matched cross section can be different from the fixed-order prediction. In particular, the shower is unitary

---

[2] When generating events to be passed to a parton shower, we have checked that the preliminary (technical) cuts imposed at the parton-level generation were loose enough not to affect the final NLO+PS rates and distributions.

J^P	$\sigma_{\rm LO}$ [pb$\pm\delta_\mu^\%\pm\delta_{\rm PDF}^\%$]	$\sigma_{\rm NLO}$ [pb$\pm\delta_\mu^\%\pm\delta_{{\rm PDF}+\alpha_s}^\%$]	K	$\sigma_{\rm NLO+PS}$ [pb$\pm\delta_\mu^\%\pm\delta_{{\rm PDF}+\alpha_s}^\%$]	R
		LHC 8 TeV			
0^+	$4.002(4)\,^{+46.8}_{-29.6}\pm3.3$	$5.484(7)\,^{+17.0}_{-16.8}\pm1.2$	1.37	$4.618\,^{+21.8}_{-18.8}\pm1.2$	0.84
0^-	$9.009(9)\,^{+46.8}_{-29.6}\pm3.3$	$12.34(2)\,^{+17.1}_{-16.8}\pm1.2$	1.37	$10.38\,^{+21.7}_{-18.8}\pm1.2$	0.84
$0^\pm$	$6.511(6)\,^{+46.8}_{-29.6}\pm3.3$	$8.860(14)\,^{+16.9}_{-16.8}\pm1.2$	1.36	$7.474\,^{+21.7}_{-18.8}\pm1.2$	0.84
		LHC 13 TeV			
0^+	$10.67(1)\,^{+41.7}_{-27.5}\pm2.6$	$14.09(2)\,^{+16.2}_{-14.9}\pm1.1$	1.32	$12.08\,^{+19.8}_{-16.7}\pm1.0$	0.86
0^-	$24.01(2)\,^{+41.7}_{-27.5}\pm2.6$	$31.67(6)\,^{+16.2}_{-14.9}\pm1.1$	1.32	$27.14\,^{+20.3}_{-16.4}\pm1.0$	0.86
$0^\pm$	$17.36(2)\,^{+41.7}_{-27.5}\pm2.6$	$22.83(3)\,^{+16.2}_{-14.9}\pm1.1$	1.32	$19.59\,^{+19.5}_{-16.6}\pm1.0$	0.86

Table 3.3: LO and NLO cross sections in pb, and corresponding QCD K factors, for $pp \to X_0 j$ production (GF channel) at the LHC, under the three J^P scenarios defined in Table 3.1. We report the integration error in the last digit(s) in parentheses, and the relative scale and PDF($+\alpha_s$) uncertainties in % units. In addition to fixed-order results, the PS-matched NLO cross sections and the ratios $R \equiv \sigma_{\rm NLO+PS}/\sigma_{\rm NLO}$ are also shown.

J^P	$\sigma_{\rm LO}$ [pb$\pm\delta_\mu^\%\pm\delta_{\rm PDF}^\%$]	$\sigma_{\rm NLO}$ [pb$\pm\delta_\mu^\%\pm\delta_{{\rm PDF}+\alpha_s}^\%$]	K	$\sigma_{\rm NLO+PS}$ [pb$\pm\delta_\mu^\%\pm\delta_{{\rm PDF}+\alpha_s}^\%$]	R
		LHC 8 TeV			
0^+	$1.351(1)\,^{+67.1}_{-36.8}\pm4.3$	$1.702(6)\,^{+19.7}_{-20.8}\pm1.7$	1.26	$1.276\,^{+29.4}_{-23.9}\pm1.7$	0.75
0^-	$2.951(3)\,^{+67.2}_{-36.8}\pm4.4$	$3.660(15)\,^{+19.1}_{-20.6}\pm1.7$	1.24	$2.755\,^{+29.8}_{-24.1}\pm1.8$	0.75
$0^\pm$	$2.142(2)\,^{+67.1}_{-36.8}\pm4.4$	$2.687(10)\,^{+19.6}_{-20.8}\pm1.7$	1.25	$2.022\,^{+29.7}_{-24.1}\pm1.8$	0.75
		LHC 13 TeV			
0^+	$4.265(4)\,^{+61.5}_{-34.9}\pm3.3$	$5.092(23)\,^{+15.4}_{-17.9}\pm1.2$	1.19	$4.025\,^{+23.9}_{-21.3}\pm1.2$	0.79
0^-	$9.304(9)\,^{+61.6}_{-34.9}\pm3.4$	$11.29(4)\,^{+16.0}_{-18.2}\pm1.2$	1.21	$8.701\,^{+24.6}_{-21.6}\pm1.3$	0.77
$0^\pm$	$6.775(6)\,^{+61.5}_{-34.9}\pm3.3$	$8.055(35)\,^{+15.8}_{-18.2}\pm1.2$	1.19	$6.414\,^{+24.4}_{-21.5}\pm1.2$	0.80

Table 3.4: Same as Table 3.3, but for $pp \to X_0 jj$ production (GF).

and tends to soften the jets, thus we expect it to reduce the overall rate with respect to fixed-order cross sections; we shall comment more on this point in a moment, when we discuss NLO+PS results.

Before addressing $H + 2j$, it is instructive to look at results for $H + 1j$ production. Table 3.3 collects the LO and NLO total cross sections and the corresponding K factors for $pp \to X_0 j$ at the 8- and 13-TeV LHC, together with uncertainties, for the three scenarios defined in Table 3.1. The figure in parentheses is the integration error in the last digit(s). The first uncertainty (in units of percent) corresponds to the envelope obtained by varying independently the renormalisation and factorisation scales by a factor 2 around the central value, $\mu_0 = H_T/2$. The second one corresponds to the PDF($+\alpha_s$) uncertainty (as mentioned in sect. 3.1, the full PDF+α_s uncertainty is computed only at NLO). We can see that both the scale dependence and PDF+α_s uncertainties are independent of the scenarios, and as expected they are significantly reduced going from LO to NLO; the residual scale dependence is the dominant source of uncertainty in the GF channel. The NLO K factors are essentially independent on the J^P scenario as well. We also note that $\sigma(0^-)$ is larger than $\sigma(0^+)$ by a factor 9/4 at LO (and to a good approximation even at NLO) due to the different coupling normalisation (see Table B.1 in Appendix B), and $\sigma(0^\pm)$ is equal to the average of $\sigma(0^+)$ and $\sigma(0^-)$. This last point means that there is no net interference effect between scalar and pseudoscalar components in the total rate for this process.

In addition to the fixed-order results, we also show the NLO cross sections matched with parton shower $\sigma_{\mathrm{NLO+PS}}$. The ratios to the fixed-order NLO rates, $R \equiv \sigma_{\mathrm{NLO+PS}}/\sigma_{\mathrm{NLO}}$ are shown in the last column. These ratios are smaller than one because, as we anticipated before, extra radiation generated by the parton shower tends to spread the energy of the original hard partons, some of which may fall outside the reconstructed jet; this affects the jet spectra, leading in turn to fewer events that pass the cuts. The survival rate after showering increases a bit with the collider energy, after incrementing it from 8 to 13 TeV. Finally, we note that the ratios can slightly depend on the parton-shower program [122], and these differences shall be considered as PS-matching systematics. Another effect of the parton shower that we can observe is a slightly increased scale dependence in the results, compared to the corresponding fixed-order predictions.

After having looked at $H+1j$, we can now turn to the results for $pp \to X_0 + 2j$ production in Table 3.4. The features of the cross sections and uncertainties are qualitatively similar to the 1-jet case in Table 3.3, while rather different quantitatively. As one increases the number of extra jets, the cross section becomes smaller as expected, yet moderately (not by an entire order of magnitude, as one would naively presume from the extra power of α_s). The K factors, which mildly depend on the scenario, are also reduced. On the other hand, the scale dependence increases – especially at LO, while just mildly at NLO – as more powers of α_s enter the matrix element. We also note that the LO ratio $\sigma(0^-)/\sigma(0^+)$ slightly deviates from 9/4 because of the missing $ggggA$ vertex, as well as the different helicity structure of the amplitudes [123].

The most important feature is that the ratios $R \equiv \sigma_{\text{NLO+PS}}/\sigma_{\text{NLO}}$ are smaller than in the 1-jet case, as we now require *two* jets passing the acceptance cuts. This means that a modelling of the QCD radiation not only in the hard scattering, but also including the parton-shower effects, is crucial to provide a realistic description of this process.

3.3 Distributions

In the previous section we have seen that if the strength of the scalar and pseudoscalar couplings in the Higgs-top interaction is similar (*i.e.* $\kappa_{Htt} = \kappa_{Att}$ in Eq. (2.6)), then total Higgs production rate in GF is sensitive to the CP mixing of the Higgs boson; this is true already at the inclusive level, *i.e.* $pp \to X_0$ production. However, if $\kappa_{Att} = 2/3\,\kappa_{Htt}$, then the total production rate is the same for any value of the CP-mixing angle α. Therefore, in a global analysis of the Higgs properties, it is also important to include observables which can discriminate between different CP scenarios regardless of the total rate of events. To this purpose, in this section we address differential distributions, where in particular the shapes of GF jet–jet correlations (computed at LO) have been known for some time to be sensitive to the Higgs CP properties [112,124–129]. It is important to confirm with an NLO(+PS) simulation that these correlations are not disrupted by higher-order effects in QCD, and can effectively be employed in CP studies of the top-quark Yukawa interaction.

In the following, all the distributions will be shown for the LHC at 13 TeV. For these studies, we require the presence of at least two reconstructed jets in the final states. The jets are ordered by decreasing transverse momentum.

We start by showing the invariant mass distribution m_{jj} of the two leading jets in Fig. 3.2, where GF and VBF are compared for the various scenarios defined in Tables 3.1 and 3.2. In the VBF HD scenarios we fix the cutoff scale to $\Lambda = 1$ TeV. GF is dominant in the small di-jet mass region, while VBF tends to produce a jet pair with higher invariant mass [105]. This is because, for Hjj production via GF, the gg and qg initial states are dominant, hence the Higgs

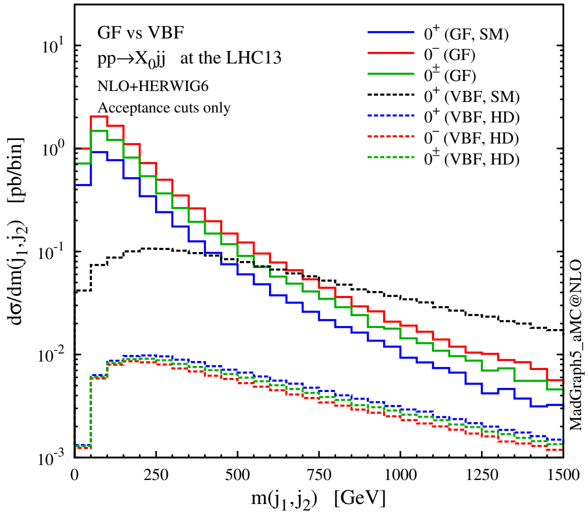

Figure 3.2: Invariant mass of the two hardest jets in $pp \to X_0 jj$ production through GF (solid lines) and VBF (dashed) at the 13-TeV LHC. The different hypotheses are defined in Tables 3.1 and 3.2.

can be radiated off the initial or final gluon legs, leading to more central jets (when just the acceptance cuts are applied). The VBF process, on the other hand, produces the Higgs only through the t-channel weak-boson exchange, leading to the forward hard jets which are a typical signature of this process. Based on this fact, we usually require a minimum m_{jj} as a cut to minimise the GF contribution, in order to extract the VBF information.

At this point, we notice two instructive facts. First, the shapes of the m_{jj} spectra are similar among the different CP scenarios within the same channel. This means that, apart from the difference between GF and VBF, the invariant mass cut acts in a similar way on every CP scenario in a given channel; more details for the VBF case can be found in ref. [121]. Second, the $qq \to X_0 qq$ subprocess in GF features VBF-like t-channel gluon exchange (see Fig. 3.1), and it is not suppressed by the m_{jj} cut since the jets tend to be produced in the forward region, similarly to the VBF case [128]. Moreover, even for the dominant gg- and qg-induced subprocesses, the t-channel contribution becomes relatively important afert imposing the invariant mass cut. In other words, the VBF cut maximises not only the VBF/GF ratio, but also the GF contributions featuring a t-channel gluon exchange, which are the most sensitive to the CP properties of the Higgs [125].

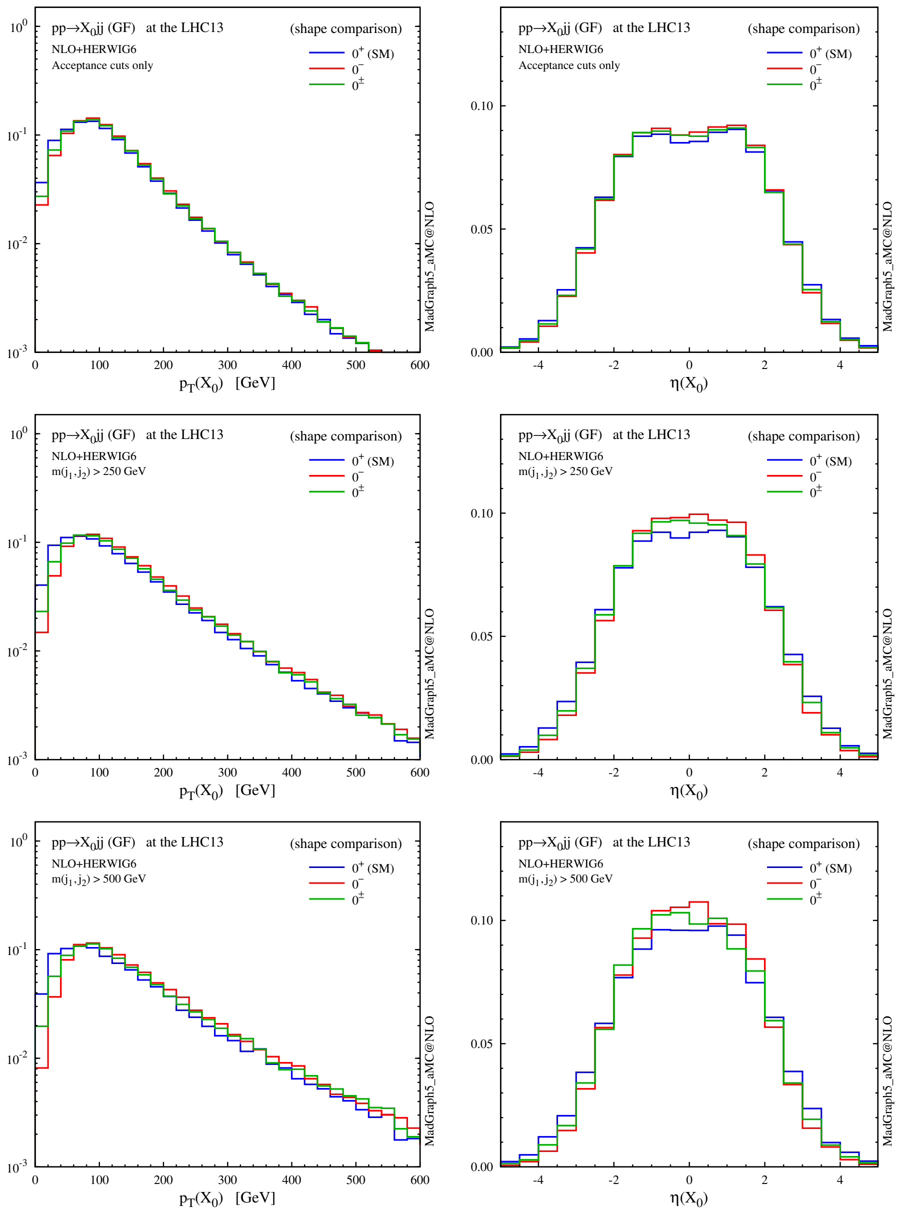

Figure 3.3: Normalised distributions (shape comparison) in p_T and η of the X_0 particle, with the acceptance cuts for jets (top), plus $m(j_1, j_2) > 250$ GeV (centre) and 500 GeV (bottom). The three spin-0 scenarios are defined in Table 3.1.

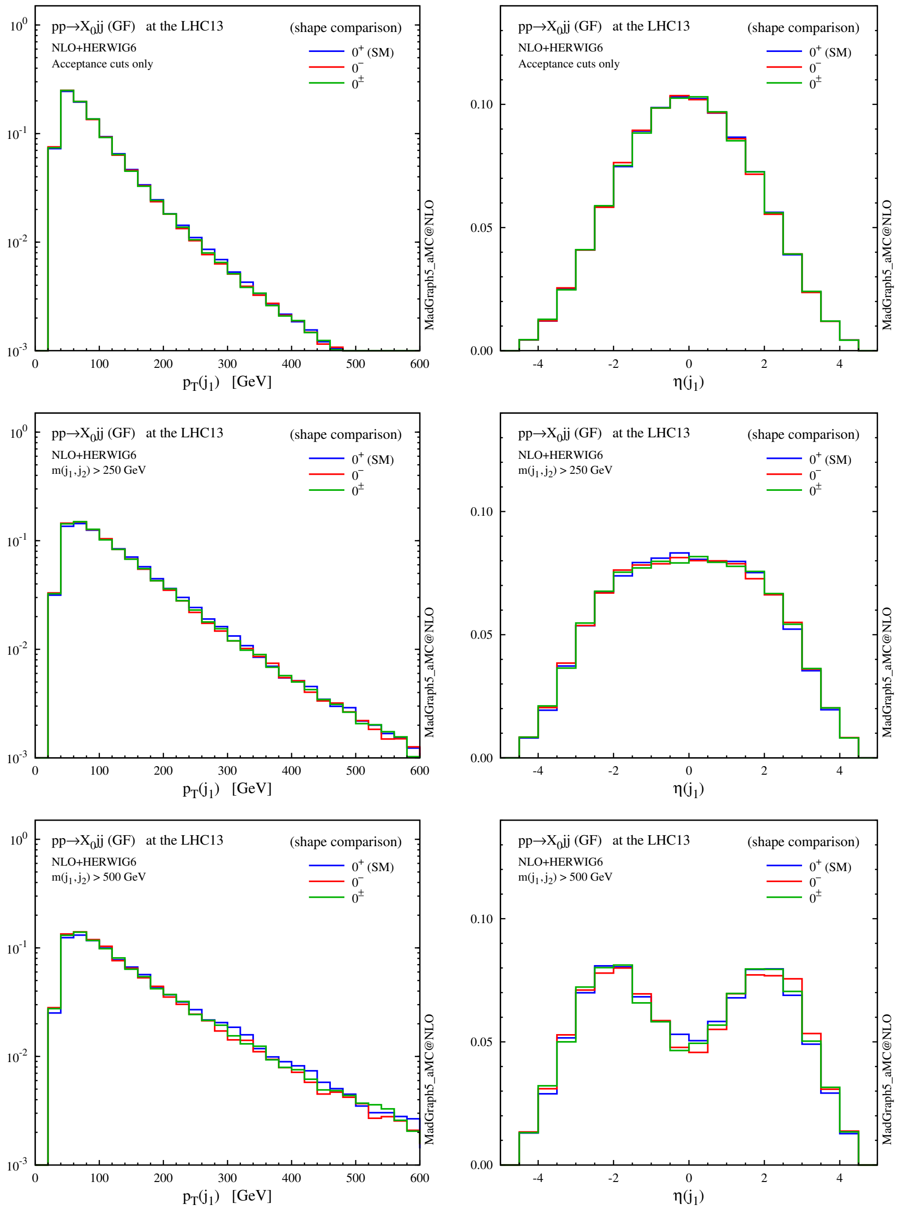

Figure 3.4: Same as Fig. 3.3, but for the leading jet.

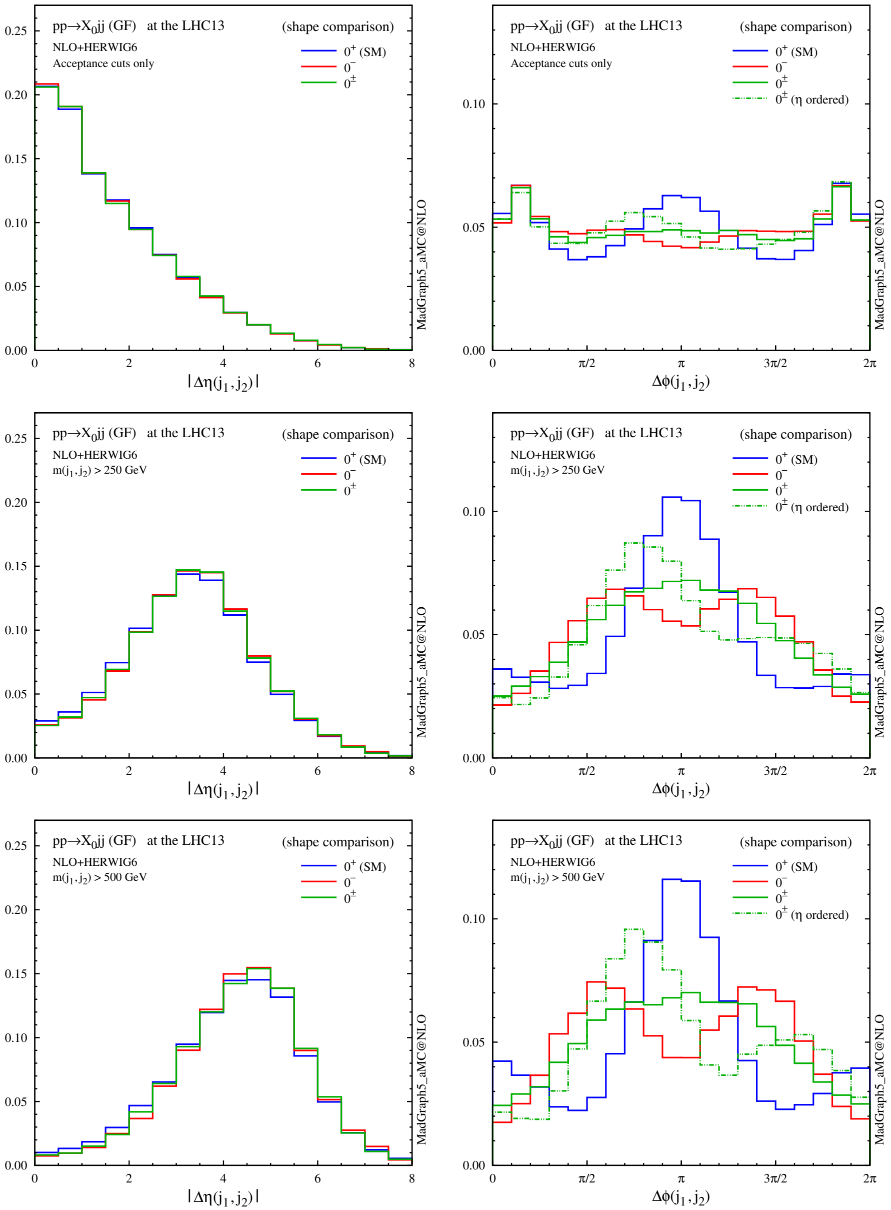

Figure 3.5: Same as Fig. 3.3, but for $\Delta\eta$ and $\Delta\phi$ distributions between the two tagging jets. In the case of $\Delta\phi$, the distribution with the additional η jet ordering is also shown by a dash-dotted line for the $0^{\pm}$ scenario.

To illustrate how the CP-sensitive observables change with the VBF selection, on top of the acceptance cuts we impose an increasing invariant mass cut

$$m(j_1, j_2) > 250,\ 500 \text{ GeV}\,. \tag{3.6}$$

We do not require a minimum rapidity separation, although this is another common VBF cut, since $\Delta\eta_{jj}$ itself is an observable that has been considered for studying the CP properties of X_0 in VBF [128,130], and we want to address its sensitivity to CP mixing in the GF case.

Figs. 3.3 and 3.4 show the effect of the invariant mass cut on the p_T and η distributions for the resonance X_0 and the leading jet. Imposing larger m_{jj} cuts leads to harder transverse momenta for both the X_0 and the jets; as a result, the X_0 is produced more centrally, while the jets are shifted to the forward regions, and the difference in the low-$p_T(X_0)$ region between the various CP scenarios becomes more pronounced. This behaviour is due to the fact that, at larger m_{jj}, topologies featuring the emission of the Higgs boson from a t-channel gluon line are enhanced, similarly to the typical VBF topology.

A possible concern is to what extent the EFT approach, where the top-quark loop has been integrated out, is valid. In fact the heavy-top-quark effective Lagrangian in Eq. (2.8) is known to be a good approximation for the inclusive production of a single light Higgs boson. At the differential level, the EFT closely reproduces the m_{jj} spectrum of the loop computation even in the very high invariant mass region [105]. However, this approximation fails when the transverse momenta of the jets are much larger than the top mass [104], overestimating the exact prediction in the $p_T(j_1) > m_t$ region. Since the events are generated predominantly in the small $p_T(j_1)$ region, we choose not to apply any rejection of events with large jet p_T in the following analysis. For a more quantitative assessment of this approximation, see also Appendix C.

The most sensitive observables for the CP nature of the Higgs boson couplings to the top quark in this channel are di-jet correlations, shown in Fig. 3.5. As already seen in Fig. 3.4, the invariant mass cut effectively suppresses the central jet activity, although the different CP scenarios can hardly be distinguished employing the rapidity separation $\Delta\eta_{jj} \equiv \eta(j_1) - \eta(j_2)$. On the other hand, the azimuthal angle between the two jets $\Delta\phi_{jj} \equiv \phi(j_1) - \phi(j_2)$ is well known to be very sensitive to the CP mixing, and our results confirm that this is still the case also after including NLO corrections (for a LO vs. NLO comparison see Fig. 3.6).

A remarkable observation is that the $\Delta\phi_{jj}$ distribution is more sensitive to the CP-mixed state when the two leading jets (ordered by p_T) are reordered in

$m_{jj} >$ GF scenario		250 GeV	500 GeV	500 GeV + jet veto
LHC 8 TeV	0^+	22.7 %	6.6 %	5.0 %
	0^-	21.4 %	5.7 %	4.5 %
	$0^\pm$	21.5 %	6.2 %	4.6 %
LHC 13 TeV	0^+	26.3 %	9.0 %	6.4 %
	0^-	25.4 %	8.6 %	6.2 %
	$0^\pm$	25.6 %	8.6 %	6.2 %

Table 3.5: Selection efficiencies with different di-jet invariant mass cuts for $pp \to X_0 jj$. A jet veto defined in Eq. (3.7) is also applied in the last column.

pseudorapidity[3] (dash-dotted green), compared to the case with vanilla p_T jet ordering (solid green). This is especially true for the maximal mixing scenario, *i.e.* $0^\pm$: after η reordering of the two hardest jets, the $\pi/4$ phase shift generated by quantum interference between the CP-even and CP-odd components is clearly visible. With simple p_T ordering, on the other hand, this $\pi/4$ phase shift is cancelled between $+\Delta\phi_{jj}$ and $-\Delta\phi_{jj}$ [124], and the distribution for $0^\pm$ without η reordering is just the weighted average of the 0^+ and 0^- cases.

The NLO computation allows also to investigate the effect of applying a veto on additional jets in the event, a procedure that is known to suppress the central QCD activities and to enhance the VBF signal [131, 132]. We implement it by vetoing events containing a third jet laying in pseudorapidity between the forward and backward tagging jets,

$$\min\{\eta(j_1), \eta(j_2)\} < \eta(j_{\text{veto}}) < \max\{\eta(j_1), \eta(j_2)\}\,. \tag{3.7}$$

Table 3.5 shows the selection efficiencies, with respect to the acceptance cuts only, on the NLO+PS samples after $m_{jj} > 250$ GeV and 500 GeV cuts, and $m_{jj} > 500$ GeV plus the central jet veto. As already seen in Fig. 3.2, the efficiencies are very similar among the different scenarios. The additional jet veto could be useful to enhance the sensitivity to CP-mixing, especially for the 13-TeV run. Indeed, we have checked that the different modulations in the $\Delta\phi_{jj}$ distribution of Fig. 3.5 become slightly more pronounced. The related jet binning uncertainties have been discussed in detail in ref. [133].

---

[3] This definition is equivalent to Eq. (4.1) in ref. [124].

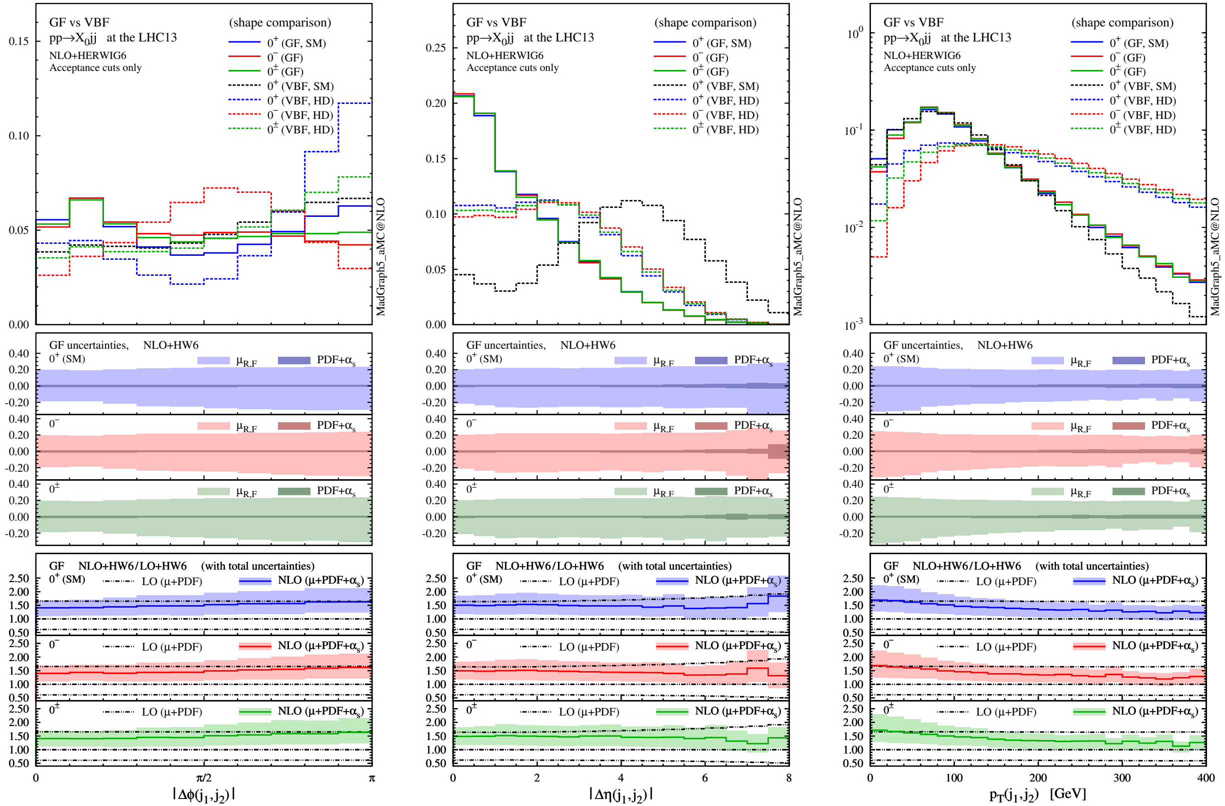

Figure 3.6: Normalised $\Delta\phi$ (left) and $\Delta\eta$ (centre) distributions between the two tagging jets, and p_T of the di-jet system (right) for GF (solid lines) and VBF (dashed), after acceptance cuts. For each GF scenario, the middle panels show the scale and PDF+α_s uncertainties, while the bottom ones give the ratio of NLO+PS to LO+PS with their total uncertainties.

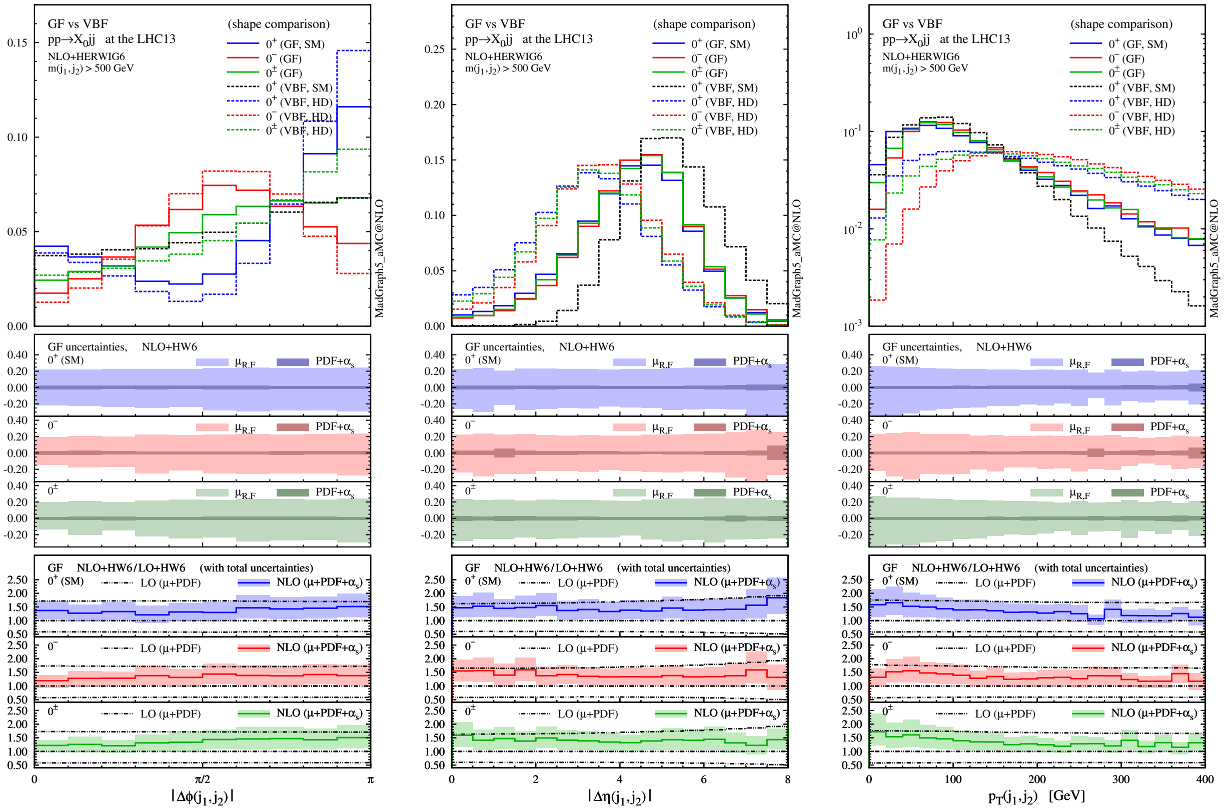

Figure 3.7: Same as Fig. 3.6, but after applying the $m(j_1, j_2) > 500$ GeV cut.

Finally, we discuss the theoretical uncertainties for some CP-sensitive observables. Fig. 3.6 displays, from left to right, normalised distributions of the azimuthal and pseudorapidity difference between the two tagging jets, and the transverse momentum of the di-jet system (which is equivalent to $p_T(X_0)$ only at LO), for $pp \to X_0 + 2$ jets in GF (solid lines) at the 13-TeV LHC. The acceptance cuts and the invariant mass cut $m_{jj} > 500$ GeV are imposed. The middle panels show the scale and PDF+α_s uncertainties for each scenario, while the bottom ones give the ratio of NLO+PS to LO+PS results with the total theoretical uncertainties. The total uncertainty is defined as the linear sum of the scale and PDF+α_s uncertainties. The scale uncertainty is dominant, as already observed in Table 3.4, and both the scale and PDF+α_s uncertainties change mildly over the phase space. In all cases NLO corrections are relevant and cannot be described by an overall K factor.

In the main panel, we also draw a comparison with the VBF contributions (dashed lines). The $p_T(j_1, j_2)$ and $\Delta\eta(j_1, j_2)$ distributions show that in the SM VBF case the Higgs boson is produced more centrally, while the tagging jets are more forward than in GF production. For the three HD VBF cases, conversely, the jets are more central. We recall that similar dimension-five operators $X_0 V_{\mu\nu} V^{\mu\nu}$ and $X_0 V_{\mu\nu} \widetilde{V}^{\mu\nu}$ describe the physics in both GF and HD VBF. We track down the difference between GF and HD VBF in the $\Delta\eta_{jj}$ distribution to the mass of the t-channel vector boson propagator, *i.e.* massless gluons vs. massive weak bosons. On the other hand, the modulation of the $\Delta\phi_{jj}$ distribution is slightly less pronounced in GF due to the additional presence of the gg- and qg-initiated channels [125, 128]. We note that the interference between GF and VBF can be safely neglected [134, 135].

3.4 Summary

In this chapter we have presented NLO-QCD accurate predictions, including parton-shower effects, for the gluon-fusion hadroproduction of a spin-0 particle featuring a CP-mixed coupling to the top quark, in association with one and two jets. These results are based on the work published in [16], where they have been presented for the first time in the literature. They have direct relevance and application to the LHC physics programme, since they can be employed to study the CP properties of the recently-discovered Higgs boson, in particular in the fermionic Yukawa sector.

We have shown that NLO corrections are crucial to reduce the notoriously large theoretical uncertainties in gluon fusion, in particular the scale dependence.

NLO+PS effects are needed in order to accurately predict the distributions of the final-state objects and perform precision Higgs physics.

We have confirmed that di-jet correlations in Higgs plus two jet production via gluon fusion can be employed effectively as CP-mixing probes of the Higgs-top interaction, since their sensitivity is not spoiled by the inclusion of extra QCD radiation. In particular, the azimuthal difference between the two tagging jets ($\Delta\phi_{jj}$) is very sensitive to CP-mixing effects. Other observables, such as the low-p_T distribution of the Higgs (or the recoiling di-jet system), are moderately sensitive as well and can provide additional information.

Finally, we have performed a comparison with results for Higgs plus two jet production through weak vector boson fusion (VBF). The gluon-fusion contribution to this final state entails a contamination in VBF analyses, which can be important even after applying VBF cuts. It needs to be taken into account not only as a background to extract the VBF signal, but also in a reliable study of the Higgs properties. For example, the VBF process in the SM produces a mild slope in the $\Delta\phi_{jj}$ distribution, while a pronounced sinusoidal shape can be the sign of BSM interactions between the Higgs and the weak bosons. However, an analogous modulation is present already in the SM gluon fusion contribution, due to the different structure of the interaction [125], and can become more pronounced after VBF cuts. Therefore, it is crucial to model all these possible scenarios when generating events for Higgs plus two jets, and use global analyses that include other processes in order to constraint (or extract) BSM interactions between the Higgs and the weak bosons on the one hand, and the Higgs and the top quark on the other hand. The HC_NLO_X0 UFO model is a convenient and effective tool that can be employed to this purpose.

Chapter 4

Higgs production in association with a pair of top quarks

In this chapter we study the production of a Higgs boson in association with a top-quark pair ($t\bar{t}H$), at NLO accuracy in QCD and also matching short-distance events to a parton shower. This is the most abundant channel where the Higgs is produced directly together with top quarks, hence it can provide crucial information on the interaction between these two particles. In particular, we investigate effective lab-frame observables which provide direct probes to the CP properties of the top-quark Yukawa interaction; we also study the discriminating power of these observables after a minimum cut on the Higgs transverse momentum $p_T > 200$ GeV is imposed ("boosted Higgs"), as it is required in $H \to b\bar{b}$ analyses such as [136], to extract the signal over the copious backgrounds given by $t\bar{t}$+jets, V+jets, $t\bar{t}V$ and tW.

The chapter is organised as follows: in section 4.1 we describe the setup and input parameters for NLO simulations, including parton-shower matching. In section 4.2 we present total rates for Higgs production in association with at top-quark pair, both at fixed order and after shower effects. In section 4.3 we discuss differential distributions at NLO+PS accuracy, focusing in particular on the CP-sensitive correlations that can be constructed from the top-quark decay products, employing simple lab-frame observables. The main results of this chapter are summarised in section 4.4.

The results collected in this chapter are based on the work published in [16], where in particular we have studied for the first time the general case of a CP-mixed spin-0 particle ($0^{\pm}$) including NLO-QCD corrections, parton-shower effects and spin-correlated top decays. Previously to [16], NLO-QCD corrections to this process have been known for quite some time [137, 138], while matching to parton shower has been done only recently in MG5_aMC@NLO [139] for both CP eigenstates 0^+ and 0^-, and in the Powheg Box [140] for the CP-even case only. The spin-correlation effects of the top–antitop decay products have been studied at the NLO+PS level with the help of MadSpin [61, 141]. The phenomenology of a CP-mixed Higgs coupling to the top quark at the LHC has been studied at LO in ref. [142].

Recently, probably also in view of the ongoing LHC Run II, a large number of $t\bar{t}H$ studies have been published; in particular, electroweak corrections have been reported in refs. [143–145]. For a more exhaustive list of references, we refer again to the LHCHXSWG reports [19, 63–65].

As a final remark, we note that here we only address the CP properties in the case of flavour-diagonal Higgs–top-quark interactions, which can be parametrised in full generality as in Eq. (2.6). At the dimension-six level, other operators appear that lead to effective three-point and four-point Higgs–top-quark interactions of different type [146–150], including flavour changing neutral ones [146, 151, 152].

4.1 Setup of the NLO+PS simulation

The code and events for $t\bar{t}X_0$ hadroproduction can be automatically generated by issuing the following commands in MadGraph5_aMC@NLO:

```
> import model HC_NLO_X0(-no_b_mass)
> generate p p > x0 t t~ [QCD]
> output
> launch
```

The top quarks are subsequently decayed passing the event file (in the Les Houches format [153]) to MadSpin [61], which follows a procedure [60] that keeps intact production and decay spin correlations. We do not include a particular Higgs decay channel in our studies, keeping it stable, but we investigate what happens when the Higgs boson is required to have a large transverse momentum ("boosted Higgs"), as demanded in the decay channel to bottom quarks, by imposing a minimum p_T cut of 200 GeV.

$t\bar{t}H$ J^P scenario	HC parameter choice	
0^+(SM)	$c_\alpha = 1\,,$	$\kappa_{Htt} = 1$
0^-	$c_\alpha = 0\,,$	$\kappa_{Att} = 1$
$0^\pm$	$c_\alpha = 1/\sqrt{2}\,,$	$\kappa_{Htt,Att} = 1$

Table 4.1: Benchmark scenarios for $t\bar{t}H$ hadroproduction.

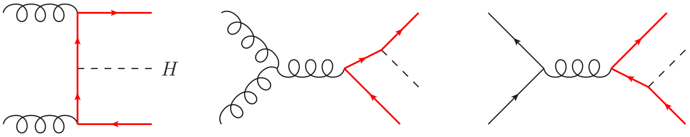

Figure 4.1: Examples of LO Feynman diagrams for Higgs production in association with a top-quark pair (the heavy quark line is coloured in red).

The setup and inputs for the $t\bar{t}H$ simulation at NLO+PS are mostly the same ones used in the $H + 2j$ simulation, see section 3.1: we set the Higgs mass to $m_{X_0} = 125$ GeV and the LHC energy to $\sqrt{s} = 8$ and 13 TeV, employing NNPDF2.3 parton distributions (in the 5FS) with $\alpha_s^{(\mathrm{LO})}(m_Z) = 0.130$ and $\alpha_s^{(\mathrm{NLO})}(m_Z) = 0.1190 \pm 0.0012\,.$ On the other hand, the top-quark mass is set to $m_t = 173$ GeV, and the central scale to

$$\mu_0^{(t\bar{t}H)} = \sqrt[3]{m_T(t)\, m_T(\bar{t})\, m_T(X_0)} \tag{4.1}$$

where $m_T \equiv \sqrt{m^2 + p_T^2}$ is the transverse mass of a final-state particle. Scale uncertainties are estimated varying μ_R and μ_F, independently, by a factor 2 around μ_0 as in Eq. (3.4), and the total theoretical uncertainty is computed as the linear sum of scale and PDF+α_s uncertainties. As for $H + 2j$, we employ the HERWIG6 parton shower, and we define jets via the anti-k_T algorithm with parameters $R = 0.4\,,$ $p_T(j) > 30$ GeV and $|\eta(j)| < 4.5\,,$ see Eq. (3.5). A jet is b-tagged if a b hadron is found among its constituents in the event-record information, and we ideally assume 100% b-tagging efficiency.

In Table 4.1 we list the representative scenarios that we later use for illustration. They are completely analogous to the GF ones collected in Table 4.1: 0^+(SM) corresponds to the SM coupling to top quarks in Eq. (2.6), 0^- to a pure pseudoscalar state, and $0^\pm$ describes a CP-mixed state in equal proportions.

J^P	σ_{LO} [fb$\pm\delta_\mu^\%\pm\delta_{\mathrm{PDF}}^\%$]	σ_{NLO} [fb$\pm\delta_\mu^\%\pm\delta_{\mathrm{PDF}+\alpha_s}^\%$]	K	$\sigma_{\mathrm{NLO+PS}}^{\mathrm{dilep}}$ [fb$\pm\delta_\mu^\%\pm\delta_{\mathrm{PDF}+\alpha_s}^\%$]	R [%]
		LHC 8 TeV			
0^+	130.3(1) $^{+36.8}_{-24.6}$ ±5.9	134.9(2) $^{+3.2}_{-8.3}$ ±3.0	1.04	3.088 $^{+3.1}_{-8.4}$ ±2.8	2.29
0^-	44.49(4) $^{+42.5}_{-27.6}$ ±10.3	47.07(6) $^{+6.5}_{-11.5}$ ±4.9	1.06	1.019 $^{+5.5}_{-11.0}$ ±4.3	2.16
$0^\pm$	87.44(8) $^{+38.2}_{-25.4}$ ±6.9	90.93(12) $^{+3.9}_{-9.1}$ ±3.4	1.04	2.052 $^{+3.6}_{-9.0}$ ±3.2	2.26
		LHC 13 TeV			
0^+	468.6(4) $^{+32.8}_{-22.8}$ ±4.5	525.1(7) $^{+5.7}_{-8.7}$ ±2.1	1.12	11.52 $^{+5.5}_{-8.7}$ ±2.0	2.19
0^-	196.8(2) $^{+37.1}_{-25.2}$ ±7.5	224.3(3) $^{+6.8}_{-10.5}$ ±3.2	1.14	4.488 $^{+5.6}_{-9.8}$ ±2.8	2.00
$0^\pm$	332.4(3) $^{+34.0}_{-23.5}$ ±5.4	374.1(5) $^{+6.0}_{-9.3}$ ±2.5	1.13	8.022 $^{+5.4}_{-8.9}$ ±2.2	2.14

Table 4.2: LO and NLO cross sections in fb, and corresponding QCD K factors, for $pp \to t\bar{t}X_0$ at the LHC, under the three scenarios defined in Table 4.1. We also report the integration error in the last digit(s) in parentheses, and the relative scale and PDF($+\alpha_s$) uncertainties in % units. In addition to the fixed-order results, the PS-matched NLO cross sections for the di-leptonic decay channel of the top quarks $\sigma_{\mathrm{NLO+PS}}^{\mathrm{dilep}}$ and the ratios $R \equiv 100 \cdot \sigma_{\mathrm{NLO+PS}}^{\mathrm{dilep}}/\sigma_{\mathrm{NLO}}$ are also shown, where the acceptance cuts in Eqs. (4.2) and (4.3) are applied.

4.2 Total rates

In this section we discuss inclusive results for $t\bar{t}H$ production. In Table 4.2 we show total cross sections at LO and NLO accuracy, and the corresponding NLO K factors, at the LHC with 8 and 13 TeV centre-of-mass energy, under the three scenarios defined in Table 4.1. Similarly to Tables 3.3 and 3.4, the uncertainties correspond, in the order, to (i) the integration error in the last digit(s), reported in parentheses, (ii) the envelope obtained by independently varying the renormalisation and factorisation scales by a factor 2 around the central value given in Eq. (4.1), and (iii) the PDF+α_s uncertainty (only PDF at LO).

At variance with the GF process, the pseudoscalar production rate is smaller than the scalar one. Such a difference is proportional to the top-quark mass, as the amplitudes for the scalar and pseudoscalar interactions are identical in the limit where the Yukawa coupling is kept constant but the fermion mass is neglected. In pp collisions at the LHC energies, the contribution of the gg initial state is dominant over $q\bar{q}$ annihilation in all the scenarios. It is rather interesting to observe, however, that for a CP-odd scalar $q\bar{q}$ annihilation contributes at LO to just 16% (10%) of the total cross section at 8 (13) TeV, compared to around 40% (30%) of the SM CP-even case. This difference is such that the CP-odd case exhibits slightly larger scale and PDF uncertainties. Once again, we note that the scale dependence is larger than the PDF+α_s uncertainty, though not as much as in H+jet production via GF; in fact, the different partonic centre-of-mass energy results in larger PDF uncertainties compared to GF, while the scale dependence is decidedly smaller. All the uncertainties are significantly reduced going from LO to NLO, as expected. Increasing the collision energy from 8 to 13 TeV enhances the cross sections by about a factor four, while the K factors grow just slightly. As in the GF case, $\sigma(0^{\pm})$ is equal to the average of $\sigma(0^{+})$ and $\sigma(0^{-})$. We have verified explicitly that at LO the interference between amplitudes corresponding to different parity interactions is exactly zero. At NLO, the interference at the amplitude level is nonzero, yet the total rates do sum up to each of the parity-definite contributions.

To investigate the spin-correlation effects among the decay products from the top quark and antiquark, we present results for the di-leptonic decay channel of the top pair, $t \to b\ell^{+}\nu_{\ell}$ and $\bar{t} \to \bar{b}\ell^{-}\bar{\nu}_{\ell}$ with $\ell = e, \mu$. We require two leptons and two b-tagged jets passing the acceptance cuts

$$p_T(\ell) > 20 \text{ GeV}\,, \quad |\eta(\ell)| < 2.5\,, \tag{4.2}$$

and, respectively,

$$p_T(j_b) > 30 \text{ GeV}\,, \quad |\eta(j_b)| < 2.5\,. \tag{4.3}$$

It is known that dedicated top and Higgs reconstruction are crucial in order to obtain a significant $t\bar{t}H$ signal over the background, at least for the dominant $H \to b\bar{b}$ decay channel. Several proposals have been put forward, from using multivariate analysis like the matrix element method [154], to jet substructure/boosted techniques [155–158]. In this study we are mainly concerned in checking what observables are sensitive to the CP properties, and we do not consider either backgrounds or reconstruction issues. However, in the next section we will consider how CP-sensitive observables are affected by the requirement of a large transverse momentum for the Higgs, *i.e.* a "boosted Higgs".

In Table 4.2, we also report the PS-matched NLO cross sections for the di-leptonic decay channel and the corresponding ratios to the fixed-order NLO prediction, $R \equiv \sigma^{\text{dilep}}_{\text{NLO+PS}}/\sigma_{\text{NLO}}$, where acceptance cuts (assuming 100% efficiencies in bottom and lepton tagging) are taken into account. Given the branching fraction of the di-leptonic mode $(0.213)^2 \simeq 0.045$, the ratios show that parton shower effects and acceptance cuts lead to a decrease in the event rate of about a factor 2. The acceptance is slightly different in the three scenarios because, as we will see in the next section, the top quarks tend to be more forward in the CP-odd case. Increasing the CM energy also results in slightly smaller R ratios. This effect can be compensated if experiments expand their tracker coverage, as planned for example by CMS [159]. Indeed, we have checked that an extension of the tagging capability to cover the region $|\eta| < 4$ increases the event acceptance of about 10% in the 0^+ SM scenario, and up to 20% in the CP-odd 0^- case, with respect to our standard $|\eta| < 2.5$ cut.

4.3 Distributions

In this section we address the potential of $t\bar{t}H$ differential observables, in the laboratory frame, to perform CP studies; we focus in particular on shape differences, which are independent from the total event rates, and show results only at the LHC with centre-of-mass energy $\sqrt{s} = 13$ TeV. In Fig. 4.2 we show differential cross sections for $t\bar{t}X_0$ production as a function of the transverse momentum of the Higgs $p_T(X_0)$. As one can see, the difference between the various scenarios is significant in the low-p_T region, while the high-p_T tail of the distributions, featuring exactly the same shape, are not sensitive to CP mixing [139]. It is also interesting to notice that our normalisation choice $g_{Htt} = g_{Att} = m_t/v\,(= y_t/\sqrt{2})$ leads to exactly the same rates at high p_T, independently of the mixing angle α, which is a known feature of massless spin-0 radiation from a heavy quark [137,160,161]. This raises the important question whether analyses requiring a boosted Higgs can be sensitive to CP properties of the Higgs–top-quark coupling. In the following, we address this question by comparing results before and after imposing a $p_T(X_0) > 200$ GeV cut on the Higgs transverse momentum.

Fig. 4.3 shows some other distributions for the $t\bar{t}X_0$ final state, without and with the $p_T(X_0) > 200$ GeV cut: the pseudorapidity distribution of X_0, and the top-quark transverse momentum and pseudorapidity. Compared to the SM, a CP-odd Higgs tends to be produced more centrally, while the accompanying top quarks are slightly more forward. In Fig. 4.4 we show the correlations between the top and antitop. These correlations are passed to the heavy-quark decay products, namely the b-tagged jets and the charged leptons (in the di-leptonic channel), as shown respectively in Fig. 4.5 and Fig. 4.6.

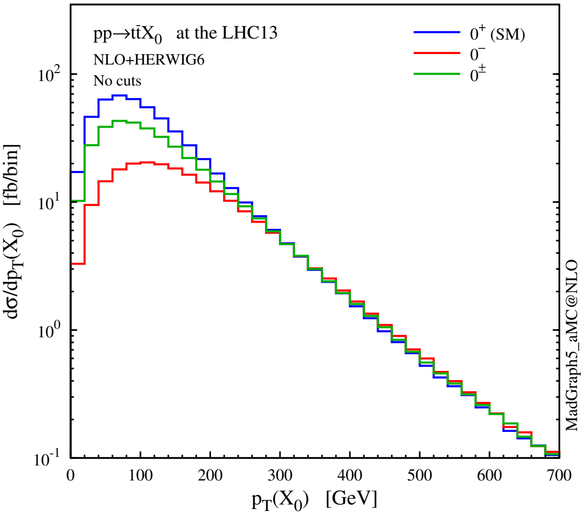

Figure 4.2: Distribution of the transverse momentum of X_0 in $pp \to t\bar{t}X_0$ at the 13-TeV LHC. The different hypotheses are defined in Table 4.1.

One of the most sensitive distribution to CP mixing is the pseudorapidity difference between the top and antitop $\Delta\eta(t,\bar{t}) \equiv \eta(t) - \eta(\bar{t})$. This observable is hardly affected by the $p_T(X_0) > 200$ GeV cut, thus the correlations among the top–antitop decay products are able to provide a good CP-discriminating power also in the boosted regime. The lab-frame angles[1] between the leptons $\theta(\ell^+,\ell^-)$ or between the b jets $\theta(j_{b,1}, j_{b,2})$ can be useful as well in CP studies, but their discriminating power is significantly degraded if a boosted Higgs is required. The azimuthal difference $\Delta\phi$ between the tagging b jets is another observable sensitive to the top-Yukawa CP properties, and it retains its discriminating power even after the boosted Higgs cut. On the other hand, $\Delta\phi$ between the charged leptons is essentially insensitive to CP mixing when just the acceptance cuts are applied, but becomes sensitive in the boosted regime and can be used to obtain complementary information.

We note that, although we have considered only the fully leptonic decay channel, there is no limitation to study the semi-leptonic and fully hadronic top-pair decays by using MadSpin; in particular, the b-jet correlations we have shown here do not depend on the specific decay channel of the top quark.

---

[1] The angular observables in different frames have been studied in ref. [141].

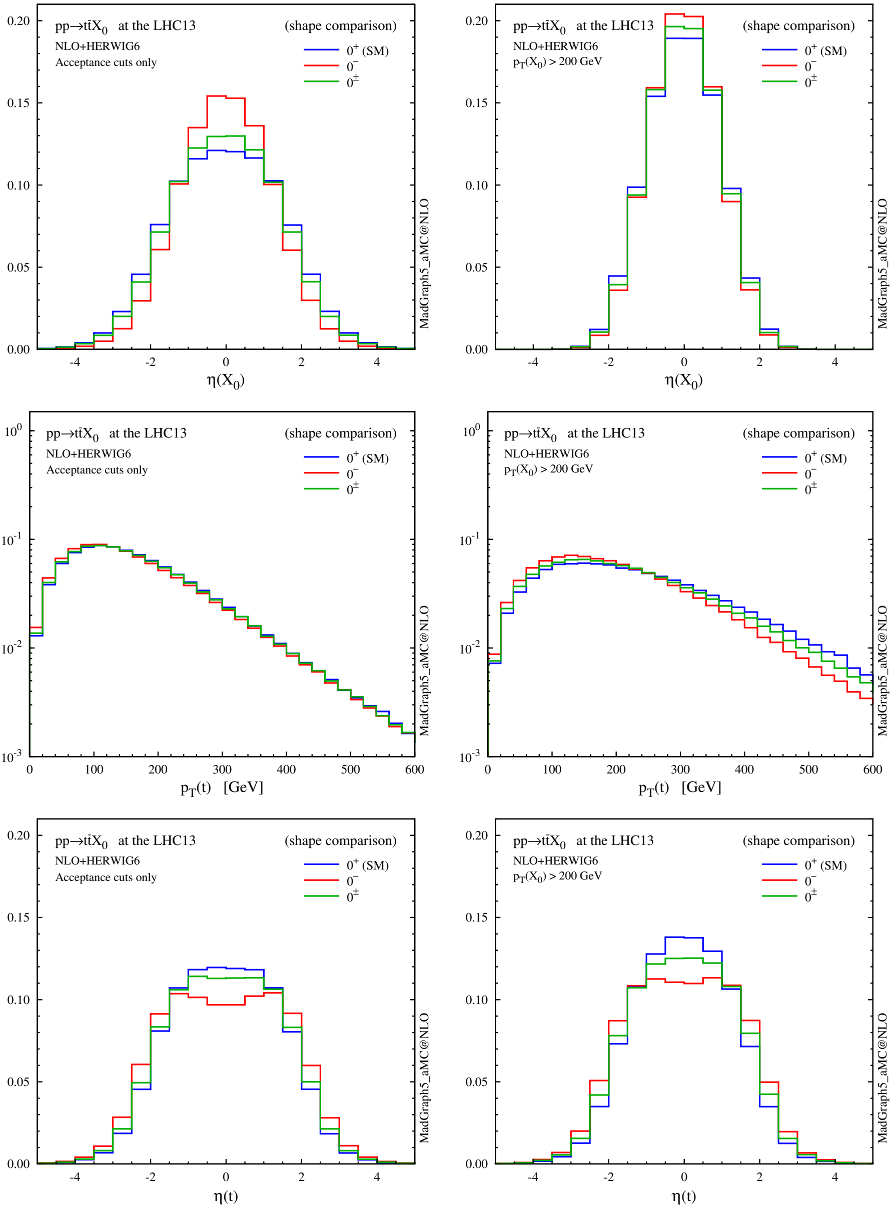

Figure 4.3: Normalised distributions (shape comparison) for the Higgs and the top quark, without cuts (left), while with the $p_T(X_0) > 200$ GeV cut (bottom). The three spin-0 hypotheses are defined in Table 4.1.

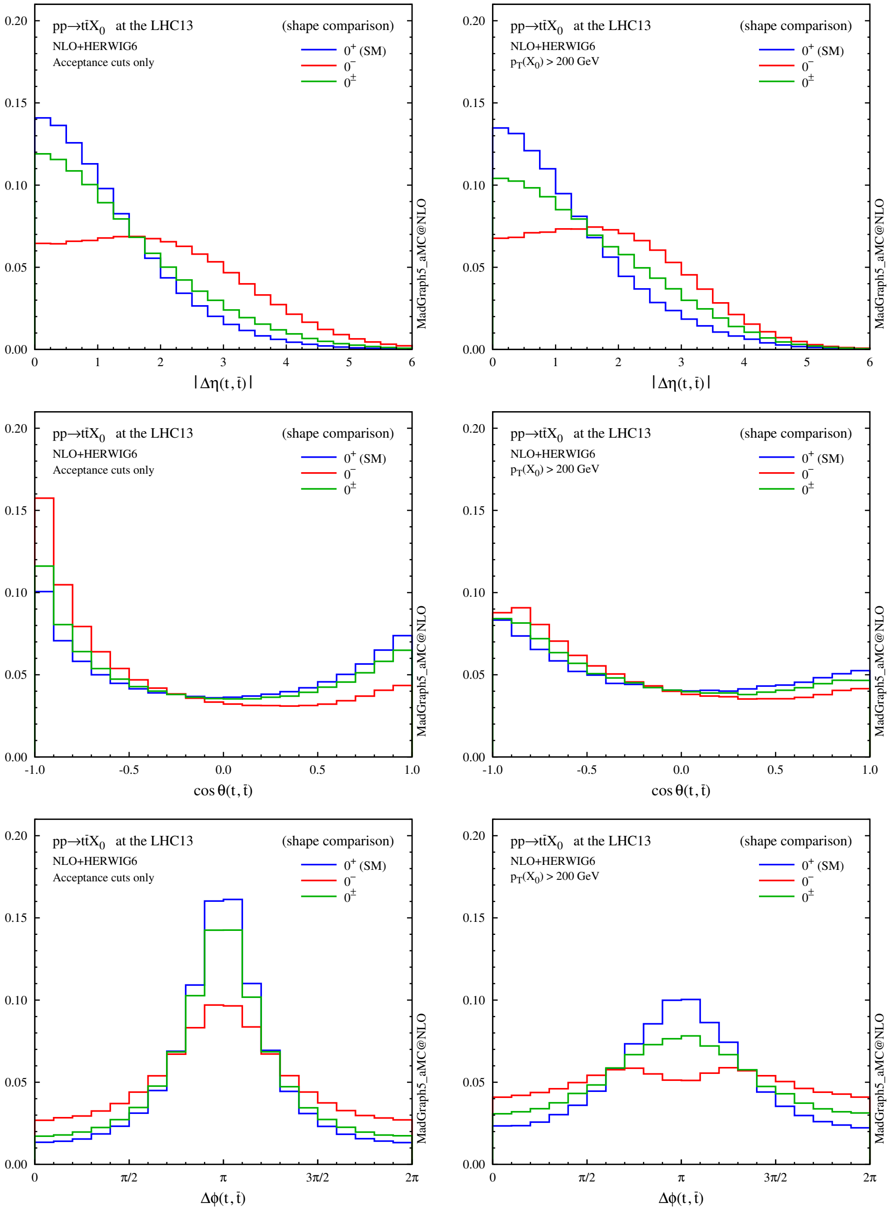

Figure 4.4: Normalised distributions (shape comparison) for the correlations between the top quark and antiquark, with the acceptance cuts (left) plus the $p_T(X_0) > 200$ GeV cut (right).

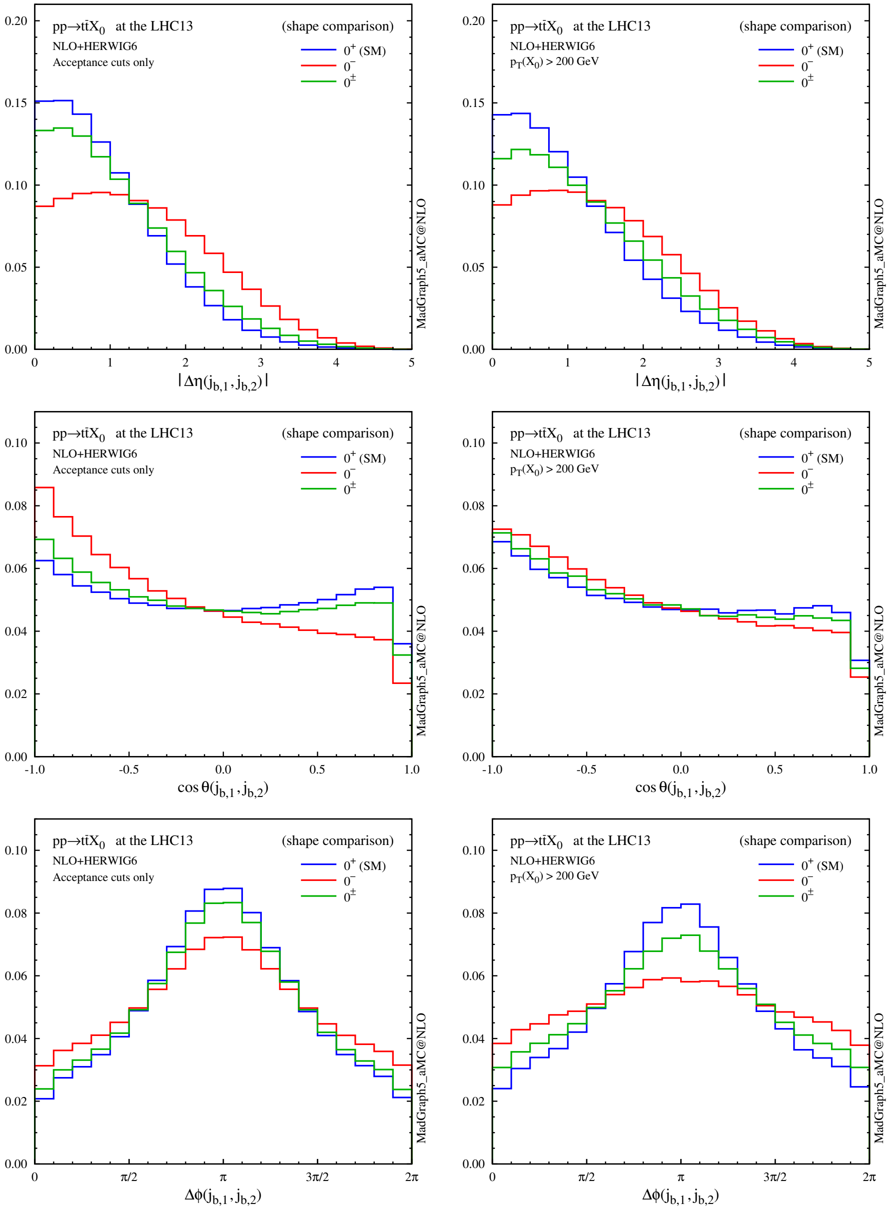

Figure 4.5: Same as Fig. 4.4, but for the b-tagged jets from the top-quark decays.

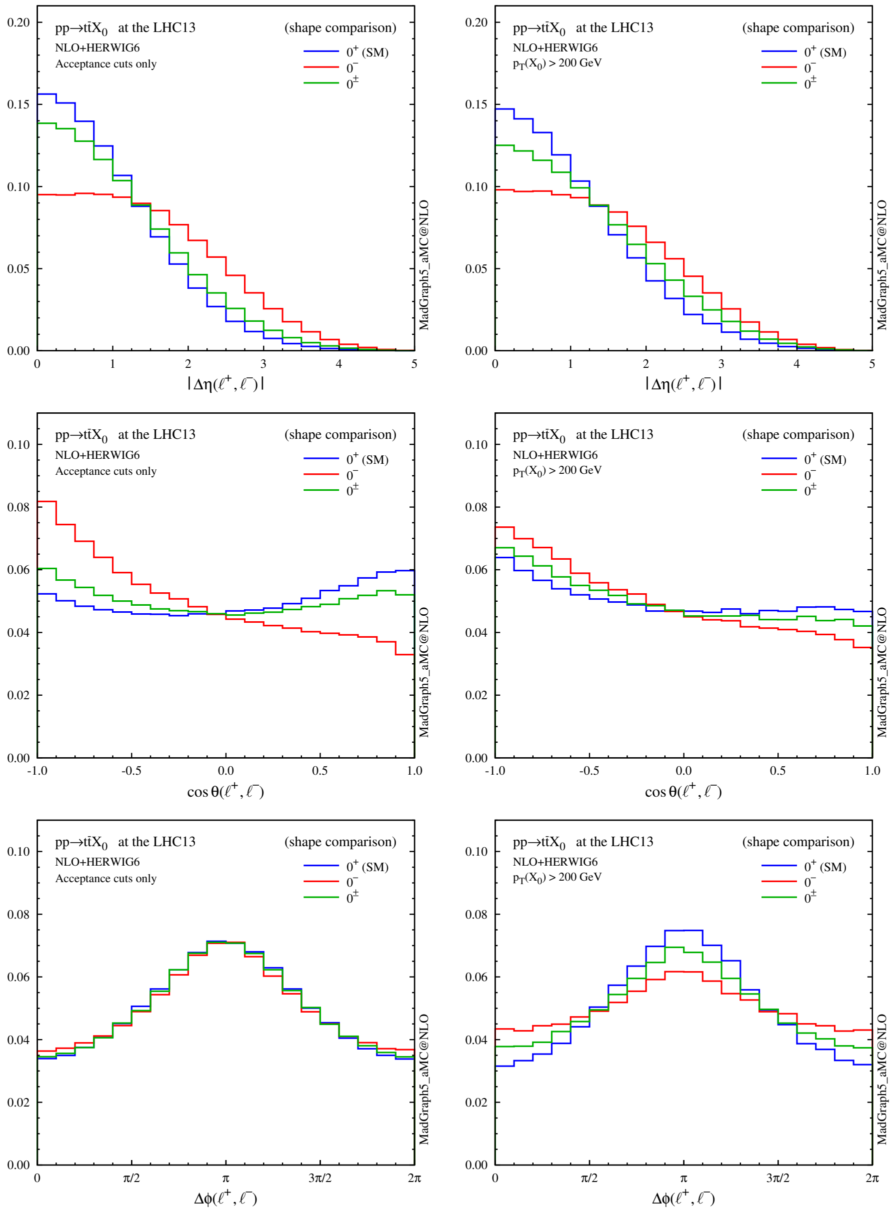

Figure 4.6: Same as Fig. 4.5, but for the charged leptons from the top quarks.

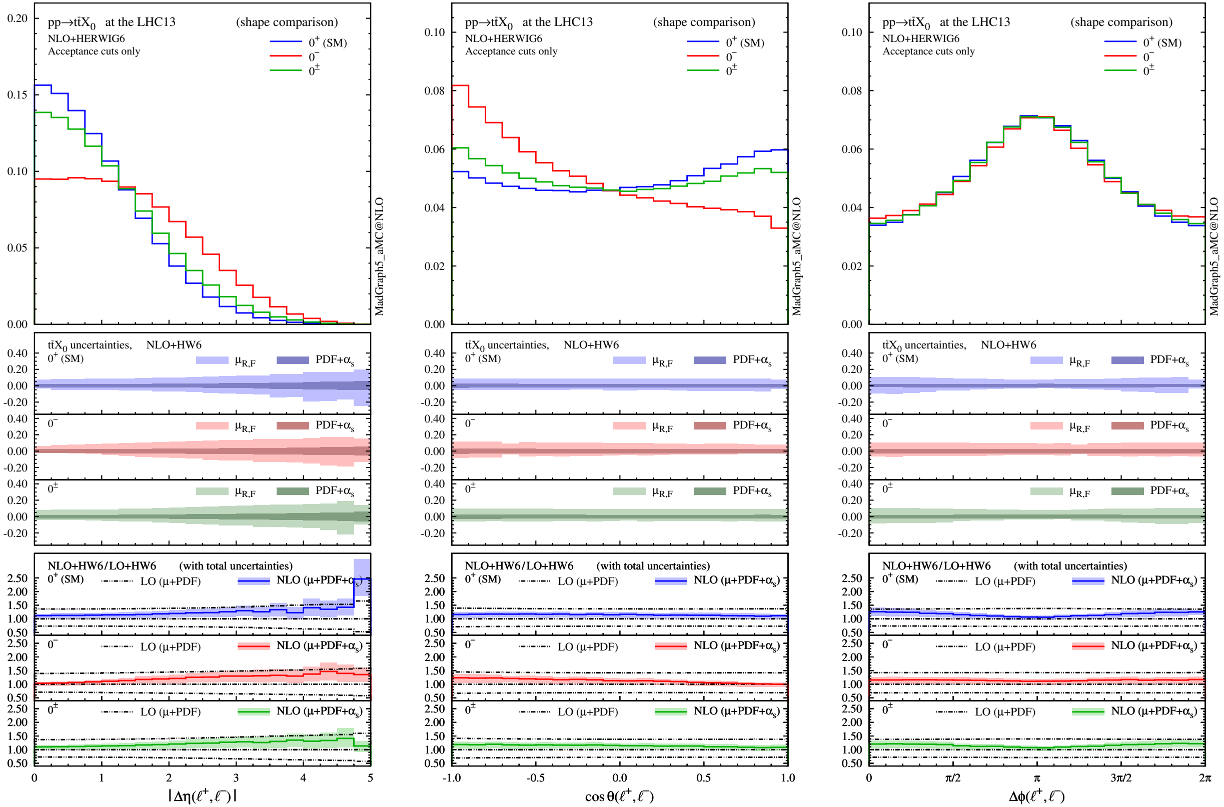

Figure 4.7: Normalised distributions of the $\Delta\eta$ (left), $\cos\theta$ (centre) and $\Delta\phi$ (right) separation between the charged leptons from the top decays, in the lab frame, after acceptance cuts. For each scenario, the middle panels show the scale and PDF+α_s uncertainties, while the bottom ones give the ratio of NLO+PS to LO+PS results, with their total uncertainties.

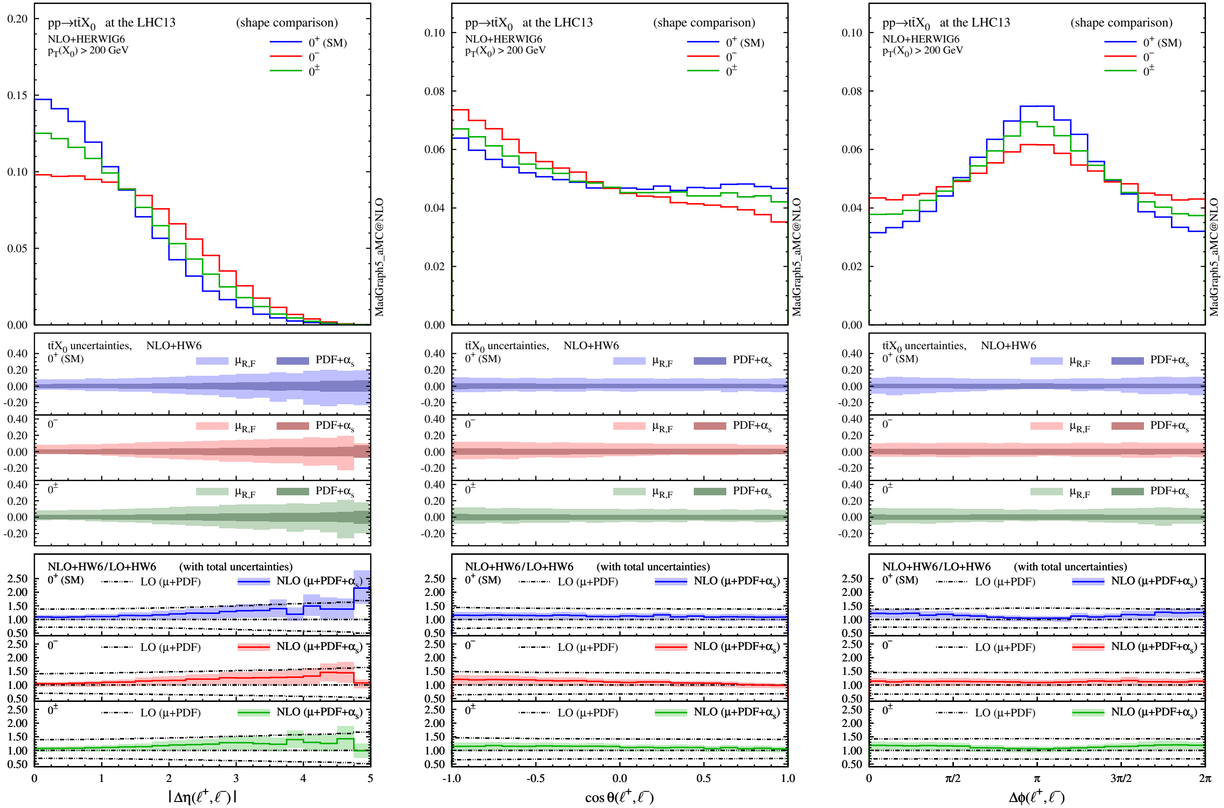

Figure 4.8: Same as Fig. 4.7, but after applying also the $p_T(X_0) > 200$ GeV cut.

Finally, we discuss the theoretical uncertainties. Fig. 4.7 displays, from left to right, the pseudorapidity distance ($\Delta\eta$), the opening angle ($\cos\theta$) and the azimuthal distance ($\Delta\phi$) between the charged leptons coming from the top decays, after applying the acceptance cuts in Eqs. (4.2). In Fig. 4.8 we collect the same plots once the boosted-Higgs cut $p_T(X_0) > 200$ GeV is also applied. The middle panels show the scale dependence and the PDF+α_s uncertainty for each scenario, while the bottom ones report the ratio of NLO+PS to LO+PS results, each one with its total theoretical uncertainty band. As in H+jets via GF, NLO corrections are important, considerably reduce the theoretical uncertainty, and cannot be described by an overall K factor. We can see that, depending on the observable considered, not only the NLO corrections, but also the corresponding uncertainties can change significantly over the phase space.

4.4 Summary

In this chapter we have presented NLO-QCD accurate predictions for the hadroproduction of a spin-0 particle in association with a top-quark pair, assuming a generic CP-mixed Yukawa interaction, and including parton-shower effects and spin-correlated decays of the heavy quarks. These results are based on the work published in [16] and are relevant to the study of the $t\bar{t}H$ process at the ongoing LHC Run II and beyond. In particular, this process is of paramount importance to directly exploring the properties of the Higgs interaction with the top quark, in a way that is rather model independent – unlike gluon fusion, where the heavy particles running in the loop are not accessible in the final state.

We have shown that NLO corrections are a key to reduce the theoretical uncertainties and pave the way to an accurate and precise measurement of the Higgs properties.

Correlations between the top quark and antiquark decay products can be used to extract the CP properties of the top-quark Yukawa interaction, and we have illustrated how many sensitive probes can be constructed from simple lab-frame observables, without the need to fully reconstruct the Higgs or the top momenta with precision (to boost in different frames). In particular, the pseudorapidity distance between the b jets, and also between the leptons in fully leptonic channels, is a promising observable, especially if a "boosted Higgs" cut is required in the analysis.

Chapter 5

Higgs production in association with a single top quark

In this chapter we study the production of a Higgs boson in association with a single top quark (tH), at NLO accuracy in QCD and also matching short-distance events to a parton shower. At variance with the $t\bar{t}H$ process, where top quarks are produced via the strong interaction, the production of a single top quark proceeds through the electroweak interaction; as a consequence, tH is characterised by a much smaller cross section at hadron colliders than $t\bar{t}H$ (and also the other main production modes - GF, VBF, VH). Despite being a rare process, tH is particularly interesting because it features unique aspects, which can offer invaluable complementary information for pinning down the Higgs properties. For this reason, this process will be thoroughly investigated at the ongoing (Run II) and future LHC runs. In particular, it is among the very few processes at the LHC (together with $H \to \gamma\gamma$ and $gg \to ZH$) to be sensitive to the relative size and phase of the Higgs interactions with the top quark and with the weak bosons. For t-channel and W-associated modes, diagrams where the Higgs couples to the top quark interfere destructively with those where the Higgs couples to the W boson (due to the unitarity of the weak interactions in the SM), making cross sections and distributions extremely sensitive to departures from SM Higgs properties [162]. In fact, changing the sign of the top-quark Yukawa results in a large enhancement of the tH cross section, even above the $t\bar{t}H$ rate.

The chapter is organised as follows: in section 5.1 we introduce the main features of Higgs production in association with a single top, in particular the separation among the t-channel, s-channel and W-associated processes. In section 5.2 we collect results for the main t-channel process in the SM. First we present inclusive cross sections at NLO, paying particular attention to evaluate the various sources of theoretical uncertainty; then we discuss NLO+PS differential distributions, focusing on the dominant scale and flavour-scheme uncertainties. These results provide state-of-the-art predictions for Higgs production in association with a single top. In section 5.3 we briefly discuss the s-channel process, which is characterised by a tiny cross section. In section 5.4 we review the inclusion of these SM t- and s-channel tH predictions among the official state-of-the-art results of the LHC Higgs Cross Section Working Group. In section 5.5 we go beyond the SM and explore the impact of an anomalous, CP-mixed top-quark Yukawa on the t-channel process, both at the inclusive and differential level. All the results presented in this chapter are summarised in section 5.6.

The results collected in this chapter are based on the work published in [17], and in the fourth LHCHXSWG report [19]. In particular, we have performed the first thorough study of tH production at NLO accuracy in both the 4FS and 5FS, including the various sources of theoretical uncertainty, and also exploring BSM CP-mixed interactions between the Higgs boson and the top quark. Previously, this process had been studied at NLO accuracy only in the 5FS and for the SM scenario [163, 164], without evaluating the associated theoretical uncertainties (apart from scale variation in [163]).

5.1 Channel separation and flavour schemes

In this section we introduce the main features of Higgs production in association with a single top quark. At LO accuracy in QCD one can effectively organise the various production mechanisms into three groups, based on the virtuality of the W boson that mediates the electroweak creation of a single top: t-channel production features a space-like W propagator, s-channel production a time-like (off-shell) W, and W-associated production an on-shell W boson, see Fig. 5.1 (and also Figs. 5.3, 5.13 and 6.9). One has to bear in mind that while this classification is certainly useful, it is not strictly physical, being an approximation that holds only at LO and in the five-flavour scheme. At higher orders in QCD, or using a different flavour scheme to define the processes, the separation becomes increasingly fuzzy, as it will be clarified at the end of this section.

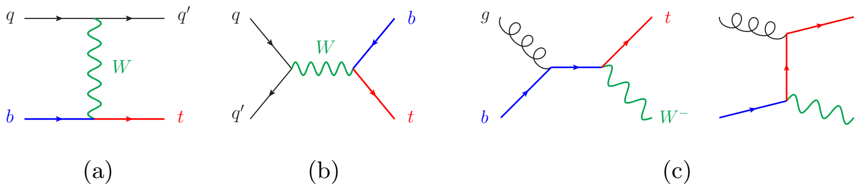

(a) (b) (c)

Figure 5.1: LO Feynman diagrams for single-top production in the 5FS, via the t-channel (a), s-channel (b) and W-associated channel (c).

As in the production of a single top alone in the SM, the Higgs plus single top process is always mediated by a tWb vertex, and therefore it entails the presence of a bottom quark either in the initial (t-channel and W-associated) or in the final state (s-channel). When describing processes featuring initial-state bottom quarks, two different approaches can be followed to perform perturbative calculations: the so-called four-flavour and five-flavour schemes.

In the four-flavour scheme (4FS) one assumes that the typical scale of the hard process Q is not significantly higher than the bottom mass, which in turn is considerably heavier than the fundamental hadronic scale $\Lambda_{\rm QCD}$

$$Q \ \gtrsim \ m_b \ \gg \ \Lambda_{\rm QCD}\,. \tag{5.1}$$

Technically, one constructs an effective theory of QCD with only four light flavours, where heavier quarks (bottom and top), being massive, do not contribute to the initial-state proton wave-function in terms of PDFs, nor to the running of the strong coupling, and they appear only as final-state particles. In so doing, mass effects in the kinematics of heavy-quark production are correctly taken into account already at the lowest order in perturbation theory. In addition, the matching to parton-shower programs is straightforward, the heavy-quark mass acting as an infrared cutoff for inclusive observables. However, limitations might arise when $Q \gg m_b$ and one probes kinematic configurations which are dominated by almost collinear $g \to b\bar{b}$ splittings: in this case the accuracy of predictions can be spoiled by large logarithms $\log(Q^2/m_b^2)$ appearing at all orders in perturbative QCD. Were this the case, such large logarithms would harm the behaviour of a fixed-order expansion in α_s.

This issue can be addressed in the five-flavour scheme (5FS) – and improvements thereof – whose aim is to reorganise the perturbative expansion by resumming such logarithms to all orders. One starts by assuming

$$Q \ \gg \ m_b \ \gtrsim \ \Lambda_{\rm QCD}\,, \tag{5.2}$$

and defines a scheme where power corrections of order m_b^2/Q^2 appear at higher orders in the α_s expansion. In practice, one sets the bottom mass to zero in the

	4FS	5FS
Inclusive level		
$\alpha_s^k \log^n(\mu_F^2/m_b^2)$	computed at fixed order in the full $g \to b\bar{b}$	resummed to all orders in the b PDF at a fixed log accuracy
$\alpha_s^k \, (m_b/Q)^n$	included	neglected
tH channels interference	at NLO in a few channels, but negligible	at NNLO
$tWH - t\bar{t}H$ interference	already at LO	at NLO
Differential level		
additional $g \to b\bar{b}$ aspects like $p_T(b)$	full description, same accuracy as inclusive	one order of accuracy less (neglected at LO, LO accuracy at NLO, ...)

Table 5.1: Differences between the 4FS and 5FS descriptions.

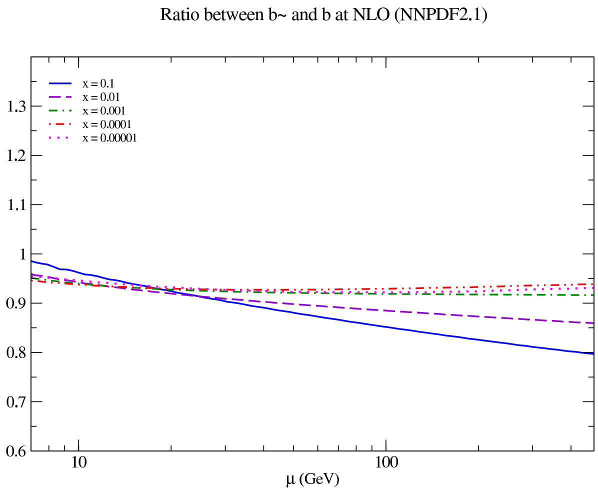

Figure 5.2: Ratio between the logarithms from the $g \to b\bar{b}$ splitting included in the 4FS at NLO accuracy ($b\sim$), and the all-order tower of such logarithms resummed into the b PDF in the 5FS at NLL. Different lines show this ratio as a function of μ_F, at different values of Bjorken-x. Taken from [163].

hard-scattering matrix element and includes bottom quarks in the initial state as proton constituents.[1] In so doing, towers of logarithms $\alpha_s^k \log^n(\mu_F^2/m_b^2)$ associated with the initial-state $g \to b\bar{b}$ splitting are resummed to all orders in perturbation theory by evolving the perturbative bottom-quark PDF via the DGLAP equations. Computations in the 5FS are typically much simpler than the corresponding ones in the 4FS, because of the lesser final-state multiplicity and the simpler phase space. This is for example the reason why single-top production is known at NNLO in the 5FS [168], while only at NLO in the 4FS [169].

Both schemes usually feature complementary advantages and disadvantages, and one may be more suitable than the other depending on the specific process and the collider energy. For a systematic investigation of the differences between the 4FS and 5FS in single b-quark and double b-quark induced processes we refer the reader to [163] and [170], respectively. Given the features outlined above and summarised in Table 5.1, a general guideline is the following: if logarithmic corrections are large, the 5FS should be more reliable; otherwise, the 4FS should be preferred. Bottom-mass power corrections are phase-space suppressed, being important only close to the partonic threshold, thus do not pose particular problems. Concerning logarithrms, in [163] two important results have been shown. The first one is that the impact of 5FS resummation is important only at large Bjorken fractions ($x \gtrsim 0.1$) and factorisation scales ($\mu_F \gtrsim 100$ GeV). Otherwise, the logs included at fixed-NLO in the 4FS already provide an approximation of about 10% or better to the resummed result, see Fig. 5.2. The second one is that the Q^2/m_b^2 argument of the initial-state logarithms is always accompanied by universal phase space factors, therefore the factorisation scale is effectively different from to the naive expectation $\mu_F = Q$. In particular, at typical LHC energies and processes, the phase space for the emission of the spectator b quark is large enough, and kinematical configurations with significantly-transverse splitting get enhanced to the point that the factorisation scale is appreciably smaller than Q. Therefore, if Q is not extremely large, the tower of logs resummed in the 5FS can be approximated rather well by the logs included at fixed-NLO in the 4FS. As a last remark, for electroweak processes like (Higgs plus) single top, one can also argue that the renormalisation scale μ_R of the strong coupling α_s should be chosen accordingly to μ_F, since QCD mostly affects the $g \to b\bar{b}$ splitting.

---

[1] Effects due to the bottom mass can be reinstated explicitly at higher-orders by systematically including it in diagrams that do not feature bottom quarks in the initial state, as in the so-called S-ACOT scheme [165], or more generally with the FONLL matching at various orders [166, 167]. Here, however, we adopt a “pure” 5FS where $m_b = 0$ throughout, thus bottom-mass power corrections are always neglected.

In short, the two schemes mostly differ in what kind of terms are pushed into the missing higher-order corrections, and in general neither power corrections nor logarithms of the bottom mass are typically very large. Therefore, as the perturbative accuracy of the predictions increases, differences between the schemes are expected to decrease. This provides a strong motivation to go at least to NLO accuracy in the computation of the t-channel cross section, in order to reduce the flavour-scheme dependence of the predictions and thus the overall theoretical uncertainty. The final accuracy, however, will depend on the specific observable considered, whose perturbative accuracy can be different in the two schemes (see also differential observables in sect. 5.2.3).

Additionally, in the case of (Higgs plus) single top production at hadron colliders, the 5FS has also an operational advantage: it allows an easy separation of the various production mechanisms into the three channels mentioned at the beginning of this section. In the 5FS the t-channel, s-channel and W-associated production (tWH) are independent up to NLO, and start to interfere only at NNLO; tWH interferes also with $t\bar{t}H$ starting from NLO. In the 4FS, on the other hand, the t-channel at NLO can interfere with the s-channel process (at NNLO) and with W-associated production (if the W decays hadronically), and the W-associated production interferes with $t\bar{t}H$ already at leading order. While the former interferences among single-top channels are very small, and can be safely neglected if the aim is to evaluate the dominant t-channel cross section, the interference of tWH with $t\bar{t}H$ turns out instead to be quite large. The on-shell W-associated production therefore needs a dedicated study, that we defer to Chapter 6.

5.2 SM results in the *t*-channel

In this section we investigate t-channel tH production in the Standard Model, at NLO accuracy in QCD. We provide predictions at the LHC with centre-of-mass energy $\sqrt{s} = 13$ TeV, together with a thorough evaluation of the residual uncertainties coming from scale variation, choice of flavour scheme, parton distributions, strong coupling constant and heavy quark masses. We perform a careful comparison of results obtained in the 4FS and 5FS, pinning down the most relevant differences, especially at the level of differential observables.

This section is divided in three parts: in subsection 5.2.1 we discuss the simulation setup, in 5.2.2 we present results for total cross section at NLO, including the various sources of theoretical uncertainty, and finally in 5.2.3 we address differential distributions at NLO+PS accuracy.

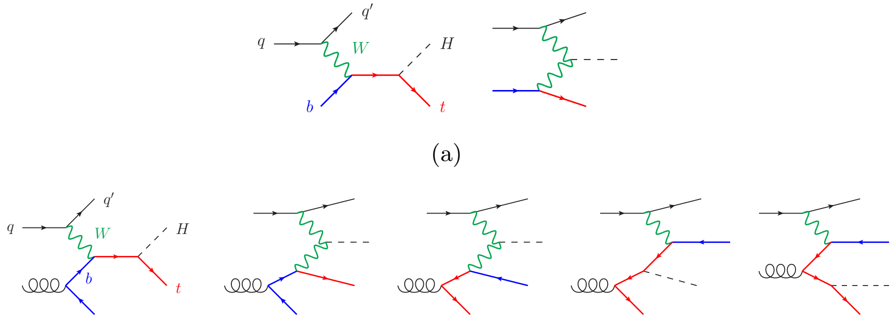

(a)

(b)

Figure 5.3: LO Feynman diagrams for t-channel tH production, in the 5FS (a) and in the 4FS (b).

5.2.1 Setup of the NLO+PS simulation

In MadGraph5_aMC@NLO the code and events for t-channel tH production at hadron colliders in the 4FS can be automatically generated by issuing the following commands:

```
(> import model loop_sm)
 > generate p p > h t b~ j $$ w+ w- [QCD]
 > add process p p > h t~ b j $$ w+ w- [QCD]
 > output
 > launch
```

while the corresponding commands for the 5FS simulation are:

```
 > import model loop_sm-no_b_mass
 > generate p p > h t j $$ w+ w- [QCD]
 > add process p p > h t~ j $$ w+ w- [QCD]
 > output
 > launch
```

Note that the `$$ w+ w-` syntax removes s-channel tH diagrams as well as real-correction diagrams where an on-shell W decays to two light quarks, which belong to WH associated production. The top-quark decays are subsequently performed by MadSpin [61], following a procedure [60] that keeps spin correlations.

In the numerical calculation, the mass of the Higgs boson is set to $m_H = 125.0$ GeV, while the mass of the top quark is set to $m_t = 173.3$ GeV. We renormalise the top quark Yukawa coupling on-shell, setting it to $y_t/\sqrt{2} = m_t/v$, where $v \simeq 246$ GeV is the EW vacuum expectation value.

The on-shell mass of the bottom quark is set to

$$m_b = 4.75 \pm 0.25 \text{ GeV}\,, \tag{5.3}$$

where we take the uncertainty to be of $\mathcal{O}(\Lambda_{\text{QCD}})$, accordingly to the prescription in ref. [171]. On the other hand, we set the bottom-quark Yukawa coupling to zero, because we find that contributions proportional to the Higgs-bottom Yukawa interaction are negligible for this process. We remind that in the 4FS the value of m_b enters the hard-scattering matrix element and the final-state phase space, while in the 5FS it affects only the parton luminosity.

PDFs are evaluated by using three global fits: NNPDF2.3 [113], MSTW2008 [119] and CT10 [172], through the LHAPDF interface. PDF uncertainties are computed for each set of distributions, following the recipes summarised in [116]. A comparison among these three global fits allows to estimate the PDF systematic uncertainties related to the technical details of the fitting procedure employed by each group. We note that the three global fits above provide NLO PDF sets both in the 4FS and 5FS, while only MSTW has published LO PDFs in both schemes.[2]

The reference value for the strong coupling constant we employ here is

$$\alpha_s^{(\text{NLO},\,5\text{FS})}(m_Z) = 0.1190 \pm 0.0012\,, \tag{5.4}$$

where the uncertainty is taken accordingly to the 2010 PDF4LHC recommendation [116, 117], and the central value is chosen such that our 68% confidence interval encompasses the 2014 PDG world average [173] and the best $\alpha_s(m_Z)$ estimates obtained by each of the three PDF global fits [174–176]. We remark that the value in Eq. (5.4) is consistent with the 5FS description. Since the difference between the 4FS and 5FS in the running of α_s is limited to scales above m_b, Eq. (5.4) can be translated into the following condition on $\alpha_s(m_b)$ (running α_s at 2-loop accuracy)

$$\alpha_s^{(\text{NLO})}(m_b) = 0.2189 \pm 0.0042\,, \tag{5.5}$$

which is now flavour-scheme independent (for any $n_f \geq 4$).

---

[2] The present-generation PDF fits CT14 and NNPDF3 provide LO parton distributions in different flavour schemes, too.

CT10 does not provide PDF sets to compute m_b uncertainties in the 5FS, and PDF uncertainties in the 4FS; both CT10 and MSTW2008 do not provide 4FS PDF sets with different $\alpha_s(m_Z)$ values. Thus, it is possible to address all the various sources of uncertainty in both schemes only when using NNPDF2 parton distributions[3], while MSTW2008 and CT10 uncertainty bands can be sometimes underestimated (though just slightly, as we will see later in sect. 5.2.2).

We match short-distance events to the PYTHIA8 [177] parton shower through the MC@NLO method [55], while HERWIG6 [51] has been used for a few comparisons. Jets are reconstructed by means of the anti-k_T algorithm [40] as implemented in FASTJET [120], with distance parameter $R = 0.4$, and required to have

$$p_T(j) > 30 \text{ GeV}\,, \quad |\eta(j)| < 4.5\,. \tag{5.6}$$

A jet is b-tagged if a b hadron (or bottom quark in fixed-order calculations) is found among its constituents, and if the jet satisfies

$$p_T(j_b) > 30 \text{ GeV}\,, \quad |\eta(j_b)| < 2.5\,. \tag{5.7}$$

We assume 100% b-tagging efficiency in this study.

5.2.2 Total rates

In this section we present the total cross section for t-channel production of a Standard-Model Higgs boson together with a single top quark (or antiquark), at NLO accuracy in QCD, at the LHC with $\sqrt{s} = 13$ TeV. The main sources of theoretical uncertainty that we address here are:

1. renormalisation and factorisation scale dependence,
2. 4FS and 5FS dependence,
3. PDF uncertainty,
4. $\alpha_s(m_Z)$ uncertainty,
5. m_b uncertainty.

At the end of this section we will also briefly comment on the impact of the bottom-quark Yukawa coupling, and the parametric dependence on the Higgs and the top-quark masses.

---

[3] NNPDF2.1 for m_b variations in the 5FS, and NNPDF2.3 for everything else.

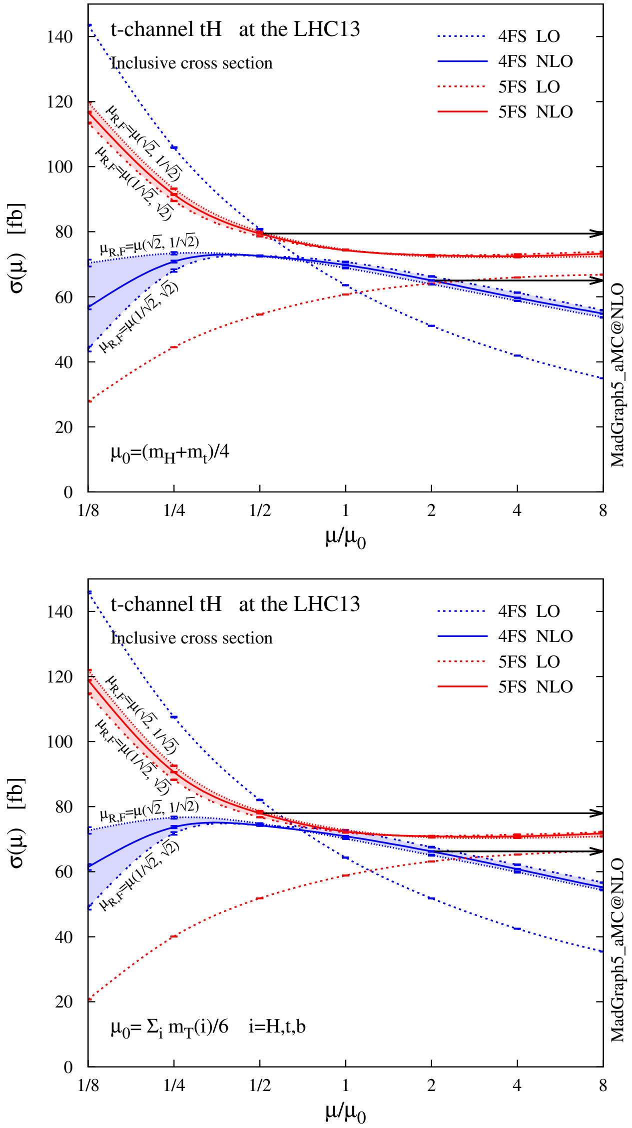

Figure 5.4: Scale dependence of the total cross sections for t-channel tH production at the 13-TeV LHC ($pp \to tHq + \bar{t}Hq$), where the 4FS (blue) and 5FS (red) schemes are compared. LO (dashed) and NLO (solid) predictions with MSTW2008 PDFs are presented for $\mu_R = \mu_F \equiv \mu$, with a static (top) and a dynamic (bottom) scale choice. Two off-diagonal profiles of the scale dependence at NLO are also shown, for ($\mu_R = \sqrt{2}\mu$, $\mu_F = \mu/\sqrt{2}$) and for ($\mu_R = \mu/\sqrt{2}$, $\mu_F = \sqrt{2}\mu$). The black arrows visualise the envelope of the combined scale and flavour-scheme uncertainty defined in Eq. (5.10).

t-channel scheme	$\sigma_{\rm LO}$ [fb]	$\sigma_{\rm NLO}$ [fb]	K
4FS (μ_0^s)	$63.46(8)\ ^{+27.2\%}_{-19.7\%}$	$69.43(7)\ ^{+4.0\%}_{-5.8\%}$	1.09
5FS (μ_0^s)	$60.66(6)\ ^{+5.6\%}_{-10.0\%}$	$73.45(8)\ ^{+7.0\%}_{-2.3\%}$	1.21
4FS (μ_0^d)	$64.31(8)\ ^{+27.6\%}_{-19.5\%}$	$71.29(10)\ ^{+3.8\%}_{-7.1\%}$	1.11
5FS (μ_0^d)	$58.83(5)\ ^{+7.6\%}_{-11.9\%}$	$71.54(7)\ ^{+7.3\%}_{-2.1\%}$	1.22

Table 5.2: LO and NLO cross sections and corresponding K factors for t-channel tH production at the 13-TeV LHC in the 4FS and 5FS. MSTW2008 PDFs have been used. The integration error in the last digit(s) and the scale dependence by a factor 2 around the static and dynamic scale choices in Eqs. (5.8) and (5.9) are also reported.

We start by showing in Fig. 5.4 the renormalisation and factorisation scale dependence of the LO and NLO total cross sections, both in the 4FS and in the 5FS. We compute cross sections with two different scale choices, one static and one dynamic, and we vary $\mu_R = \mu_F \equiv \mu$ around the central scale μ_0, which is given by

$$\mu_0^s = (m_H + m_t)/4 \tag{5.8}$$

in the static case (left figure), and

$$\mu_0^d = H_T/6 = \sum_{i=H,t,b} m_T(i)/6 \tag{5.9}$$

for the event-by-event dynamic choice (right figure), where $m_T \equiv \sqrt{m^2 + p_T^2}$ is the transverse mass of a particle.

We find a pattern similar to the case of the single top production (see Fig. 3 in [169]). At LO the scale dependence in the 4FS is stronger than in the 5F, simply because the 4FS calculation starts already at order α_s. As expected, predictions at NLO are much more stable under the scale variation than at LO. We find that the 4FS and 5FS predictions are in better agreement if μ is chosen to be roughly a factor four (six) smaller than the typical hard scale of the process, *i.e.* $m_H + m_t$ (H_T) for the static (dynamic) scale choice. This is a known and general feature of b-initiated processes at hadron colliders [163]. At such reduced scales the 4FS and 5FS predictions are typically in good agreement, as we have discussed in section 5.1, and this is indeed what we observe taking the reference scale choice μ_0 as in Eqs. (5.8) and (5.9). Table 5.2 shows the corresponding values of the LO and NLO cross sections in Fig. 5.4, where the scale dependence is estimated varying μ by a factor 2 around μ_0.

In Fig. 5.4 we also plot two off-diagonal ($\mu_R \neq \mu_F$) slices of the NLO cross section surface in the plane (μ_R, μ_F), shifted by a factor $\sqrt{2}$ in the direction orthogonal to the diagonal. The effects of off-diagonal scale choices are more pronounced in the 4FS than in the 5F, even though in general they are quite modest, except at very low scales, *i.e.* comparable to m_b. We conclude that, for our choice of μ_0, the diagonal $\mu_R = \mu_F$ is sufficiently representative of the scale dependence of the total cross section, when the scale is varied by the usual factor two. We also observe that the scale value which minimises the flavour-scheme dependence is rather stable under shifts away from the diagonal.

We note that the scale dependence pattern is strongly correlated to the flavour scheme employed. Therefore, after we estimate the scale dependence of both 4FS and 5FS results (varying the scale $\mu_F = \mu_R \equiv \mu$ by a factor 2 around μ_0), we define a combined scale and flavour-scheme uncertainty band by taking the envelope of the extremal values (shown by the black arrows in Fig. 5.4), and the best prediction for the cross section as the central point of this envelope. The total cross section at NLO and its combined scale plus flavour-scheme uncertainty are thus defined by

$$\sigma_{\rm NLO} = (\sigma^+ + \sigma^-)/2\,, \qquad\qquad \delta_{\mu+\rm FS} = (\sigma^+ - \sigma^-)/2\,, \tag{5.10}$$

where

$$\sigma^+ = \max_{\mu\in[\mu_0/2,\,2\mu_0]} \left\{ \sigma^{\rm 4FS}_{\rm NLO}(\mu)\,,\ \sigma^{\rm 5FS}_{\rm NLO}(\mu) \right\}, \tag{5.11}$$

$$\sigma^- = \min_{\mu\in[\mu_0/2,\,2\mu_0]} \left\{ \sigma^{\rm 4FS}_{\rm NLO}(\mu)\,,\ \sigma^{\rm 5FS}_{\rm NLO}(\mu) \right\}. \tag{5.12}$$

Now we turn to the PDF, $\alpha_s(m_Z)$ and m_b uncertainties. In principle these three uncertainties can be correlated. In practice, however, the correlations are very small and can be often neglected in combinations. For example, using NNPDF, we have explicitly checked that the combined PDF+α_s uncertainty computed with full correlations differs from the one without correlations by 0.1% at most. In the 4FS m_b is independent of PDF and α_s, while we confirmed that the uncertainty correlation between PDF and m_b in the 5FS is well below the percent level. Moreover, the correlation between α_s and m_b is tiny and can be neglected as well [171]. We note that neglecting correlations allows us to compare PDF uncertainty bands at a common α_s value, once central predictions (computed with this common α_s) are dressed with their corresponding fractional PDF uncertainty (computed with each group's dedicated set)This is a known fact and it has been extensively used in PDF benchmarks [178].

	t-channel	$\sigma_{\rm NLO}(\mu_0^s)$ [fb]	$\delta^{\%}_{\mu}$	$\delta^{\%}_{{\rm PDF}+\alpha_s+m_b}$	$\delta^{\%}_{\rm PDF}$	$\delta^{\%}_{\alpha_s}$	$\delta^{\%}_{m_b}$
4FS	tH	45.90(7)	$^{+3.6}_{-6.3}$	$^{+2.3}_{-2.3}$	±0.9	$^{+0.6}_{-0.9}$	$^{+2.0}_{-2.0}$
	$\bar{t}H$	23.92(3)	$^{+4.2}_{-6.6}$	$^{+2.5}_{-2.7}$	±1.4	$^{+1.6}_{-1.8}$	$^{+1.4}_{-1.5}$
	$tH+\bar{t}H$	69.81(11)	$^{+3.2}_{-6.6}$	$^{+2.8}_{-2.5}$	±0.9	$^{+1.6}_{-1.7}$	$^{+2.1}_{-1.6}$
5FS	tH	48.80(5)	$^{+7.1}_{-1.7}$	$^{+2.8}_{-2.3}$	±1.0	$^{+1.7}_{-1.1}$	$^{+2.0}_{-1.8}$
	$\bar{t}H$	25.68(3)	$^{+6.8}_{-2.0}$	$^{+3.4}_{-2.9}$	±1.4	$^{+1.9}_{-1.5}$	$^{+2.5}_{-2.0}$
	$tH+\bar{t}H$	74.80(9)	$^{+6.8}_{-2.4}$	$^{+3.0}_{-2.4}$	±1.0	$^{+1.5}_{-1.1}$	$^{+2.4}_{-1.9}$

Table 5.3: NLO cross sections and uncertainties for t-channel tH production at the 13-TeV LHC: $pp \to tHq$, $\bar{t}Hq$, and their sum. The static scale in Eq. (5.8) and NNPDF2.3 PDFs have been employed (NNPDF2.1 for m_b variations in the 5FS). The integration uncertainty in the last digit(s) (in parentheses) as well as the scale dependence and the combined PDF + $\alpha_s + m_b$ uncertainty in Eq. (5.13) (in %) are reported. The separate PDF, α_s and m_b uncertainties are also presented as a reference.

	t-channel	$\sigma_{\rm NLO}(\mu_0^d)$ [fb]	$\delta^{\%}_{\mu}$	$\delta^{\%}_{{\rm PDF}+\alpha_s+m_b}$	$\delta^{\%}_{\rm PDF}$	$\delta^{\%}_{\alpha_s}$	$\delta^{\%}_{m_b}$
4FS	tH	46.67(8)	$^{+4.3}_{-6.1}$	$^{+3.2}_{-1.9}$	±0.9	$^{+1.6}_{-0.4}$	$^{+2.6}_{-1.6}$
	$\bar{t}H$	24.47(5)	$^{+4.4}_{-6.8}$	$^{+2.5}_{-2.3}$	±1.4	$^{+1.4}_{-1.4}$	$^{+1.6}_{-1.2}$
	$tH+\bar{t}H$	71.20(11)	$^{+4.3}_{-6.5}$	$^{+3.0}_{-2.4}$	±0.9	$^{+2.0}_{-1.1}$	$^{+2.0}_{-1.9}$
5FS	tH	47.62(5)	$^{+7.4}_{-2.2}$	$^{+3.0}_{-2.4}$	±1.0	$^{+1.6}_{-0.8}$	$^{+2.4}_{-2.0}$
	$\bar{t}H$	25.07(3)	$^{+7.4}_{-2.1}$	$^{+3.2}_{-2.9}$	±1.4	$^{+1.7}_{-1.8}$	$^{+2.4}_{-1.8}$
	$tH+\bar{t}H$	72.79(7)	$^{+7.4}_{-2.4}$	$^{+2.9}_{-2.3}$	±1.0	$^{+1.2}_{-1.4}$	$^{+2.4}_{-1.6}$

Table 5.4: Same as Table 5.3, but for the dynamic scale choice in Eq. (5.9).

	t-channel	$\sigma_{\rm NLO}(\mu_0^s)$ [fb]	$\delta^{\%}_{\mu+{\rm FS}}$	$\delta^{\%}_{{\rm PDF}+\alpha_s+m_b}$
4FS+5FS	tH	47.64(7)	± 9.7	$^{+2.9}_{-2.3}$
	$\bar{t}H$	24.88(4)	± 10.2	$^{+3.5}_{-2.6}$
	$tH+\bar{t}H$	72.55(10)	± 10.1	$^{+3.1}_{-2.4}$

Table 5.5: Same as Table 5.3, but for the flavour-scheme combined results, according to Eq. (5.10).

	t-channel	$\sigma_{\rm NLO}(\mu_0^d)$ [fb]	$\delta^{\%}_{\mu+{\rm FS}}$	$\delta^{\%}_{{\rm PDF}+\alpha_s+m_b}$
4FS+5FS	tH	47.47(6)	± 7.7	$^{+3.1}_{-1.8}$
	$\bar{t}H$	24.86(3)	± 8.3	$^{+3.3}_{-2.3}$
	$tH+\bar{t}H$	72.37(10)	± 8.0	$^{+2.9}_{-2.3}$

Table 5.6: Same as Table 5.5, but for the dynamic scale choice in Eq. (5.9).

Given that correlations among the uncertainties are very small, as discussed above, and also that not every PDF set allows to take into account all the correlations, we define the combined PDF, α_s and m_b uncertainty by simply summing each uncertainty in quadrature as

$$\delta^{\pm}_{{\rm PDF}+\alpha_s+m_b} = \sqrt{\left(\delta^{\pm}_{\rm PDF}\right)^2 + \left(\delta^{\pm}_{\alpha_s}\right)^2 + \left(\delta^{\pm}_{m_b}\right)^2}\,. \tag{5.13}$$

Finally, we define the total theoretical uncertainty as the linear sum of the upper and lower variations for δ_μ and $\delta_{{\rm PDF}+\alpha_s+m_b}$ in a given flavour scheme.

In Tables 5.3 and 5.4, we report the NLO cross sections and their uncertainties at the 13-TeV LHC, for t-channel tH and $\bar{t}H$ productions separately, and for their sum $tH+\bar{t}H$. Results are shown, using NNPDF2.3, in the 4FS and 5FS for the static and dynamic scale choices in Eqs. (5.8) and (5.9), including the sources of uncertainty discussed above: the scale dependence and the combined PDF, $\alpha_s(m_Z)$ and m_b uncertainty, which are also presented individually. The combinations of 4FS and 5FS results, as defined in Eq. (5.10), are presented in Tables 5.5 and 5.6. The combined scale and flavour-scheme uncertainty $\delta_{\mu+{\rm FS}}$ is the dominant source of theoretical uncertainty, much larger than the $\delta_{{\rm PDF}+\alpha_s+m_b}$ contribution from PDFs, α_s and m_b. We stress that the 4FS+5FS combination is remarkably stable when passing from the static to the dynamic scale choice, while the $\delta_{\mu+{\rm FS}}$ uncertainty becomes slightly smaller.

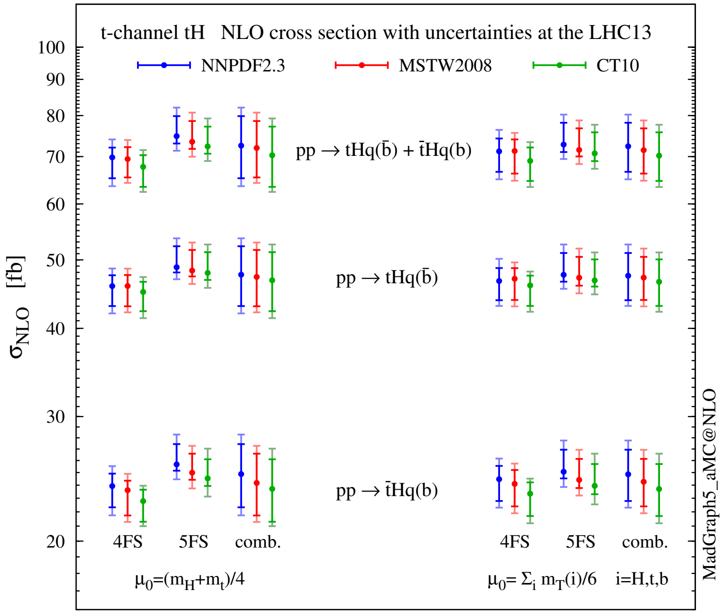

Figure 5.5: Summary plot of the NLO cross sections with uncertainties for Higgs production in association with a single top quark, via the exchange of a t-channel W boson, at the 13-TeV LHC. The inner ticks display the scale (plus combined flavour-scheme) dependence $\delta_{\mu(+\mathrm{FS})}$, while the outer ones include the $\delta_{\mathrm{PDF}+\alpha_s+m_b}$ uncertainty.

Fig. 5.5 summarises the NLO cross sections and the theoretical uncertainties for t-channel tH production, including also the MSTW2008 and CT10 predictions (tables with the corresponding numbers can be found in appendix D). We can see that the differences among the three PDF extraction methods can increase the theoretical systematics by an additional $2-3\%$, *i.e.* they are comparable to the $\delta_{\mathrm{PDF}+\alpha_s+m_b}$ uncertainty computed with a single PDF set.

We conclude this section by commenting on two minor additional sources of uncertainty. The first one is related to the value of the Higgs and top-quark masses. In Table 5.7 we collect results for the t-channel NLO cross section (in the 5FS only) with parametric variations of 1 GeV in m_H and m_t. The variations have a modest impact on the total cross section, at most 1% if both masses are varied in the same direction. After the combination of Tevatron and LHC experimental results [179], and also the more recent LHC analyses [180, 181], the top mass is currently known with a precision better than 1 GeV, while

t-channel $tH+\bar{t}H$		m_t [GeV]		
$\sigma^{\rm 5FS}_{\rm NLO}(\mu_0^s)$ [fb]		172.3	173.3	174.3
	124.0	75.54 (+1.0%)	75.18 (+0.5%)	74.99 (+0.3%)
m_H [GeV]	125.0	75.10 (+0.4%)	74.80	74.43 (−0.5%)
	126.0	74.70 (−0.1%)	74.16 (−0.8%)	73.74 (−1.4%)

Table 5.7: Higgs and top quark mass dependence of the NLO cross sections in the 5FS for $pp \to tHq + \bar{t}Hq$ at the LHC with $\sqrt{s} = 13$ TeV. NNPDF2.3 PDFs have been used with $\mu_0 = (m_H + m_t)/4$. The figures in parentheses are the % variations with respect to the reference cross section, computed with $m_H = 125.0$ GeV and $m_t = 173.3$ GeV.

the combination of the latest ATLAS and CMS measurements of the Higgs mass has a precision better than 0.5 GeV [182]. We conclude that the impact of these uncertainties on the t-channel cross section at the LHC is below 1%. The last source of uncertainty we discuss is the Yukawa coupling of the bottom quark. We have checked that it is completely negligible, both in the 4FS and 5FS, the impact of turning y_b on/off being smaller than the accuracy we achieved in the numeric integration at NLO $(0.1-0.2\%)$. Finally, we remind the reader that EW corrections for this process are presently unknown, and they could have an impact on the accuracy of the present predictions.

5.2.3 Distributions

We now present a selection of kinematical distributions for the combined t-channel $tH + \bar{t}H$ production at the 13-TeV LHC, with NLO corrections and matching to a parton shower (NLO+PS). For the sake of brevity, we do not consider top and anti-top processes separately in this section, and will dub with t both the top quark and its antiquark. Our main interest here is to assess the precision of the predictions for t-channel production, therefore we do not specify any decay mode for the Higgs boson, *i.e.* we leave it stable in the simulation. On the other hand, we consider leptonic top decays, which allows us to compare the distributions of b jets coming from the hard scattering to the one coming from the top quark.

The kinematical distributions are generated using the NNPDF2.3 PDFs and the PYTHIA8 parton shower. We have compared predictions obtained with the MSTW2008 and CT10 PDF sets and found no difference worth to report.

We have also employed the HERWIG6 parton shower to verify that some important conclusions on the difference of the radiation pattern between the 4FS and the 5FS were not dependent on shower programs. We estimate the scale dependence by varying μ_R and μ_F independently by a factor two around the reference dynamic scale $H_T/6$ defined in Eq. (5.9), which for differential distributions returns a smaller scale dependence than the static choice of Eq. (5.8), especially in the high-p_T region.

We start by showing in Fig. 5.6 and 5.7 some differential distributions for the Higgs boson and the top quark (before they decay). The first observation is that NLO distributions in the 4FS and 5FS are in excellent agreement within their respective uncertainty associated to scale variation, *i.e.* within the 10% level. Interestingly, though, differential K factors (information can be found from the ratio plots in the insets) are more pronounced for the 5FS than for the 4FS; the NLO results in the 5FS is typically out of the LO uncertainty band from scale variation. It should be noted that the LO process in the 5FS does not depend on the renormalisation scale, and therefore its smaller uncertainty (especially in the high-p_T region) can be an artefact of the scheme. Results in the 5FS tend to have a scale uncertainty that increases with p_T much more than in the 4FS, but in most cases the differences are not striking. Slightly larger deviations between 4FS and 5FS results appear only very close to the tH threshold, a region where we expect the 4FS to catch the underlying physics already at LO.

In Fig. 5.8 we present distributions for the two hardest jets which are not b-tagged. Jets and b jets are defined in Eqs. (5.6) and (5.7). The contributions from the non-taggable forward b jets ($2.5 < |\eta| < 4.5$) are also denoted by shaded histograms as a reference. The jet with the highest transverse momentum (j_1) tends to be produced in the forward region, very much like in single-top and VBF production. Most of the time this jet can be clearly associated to the light-quark current in the hard scattering; anyway, experimental analyses can benefit from a tracker upgrade that extends the capability to tag heavy flavours, *e.g.* up to $|\eta| < 4$ as planned by CMS [159]. The very good agreement between 4FS and 5FS predictions is manifest. This is expected as this observable should not be too sensitive on the details of heavy-quark current, as colour connections between the two currents are either vanishing or suppressed at the order in QCD we are working. On the other hand, sizeable differences arise for the second-hardest jet (j_2), which shows a much steeper p_T spectrum and tends to be produced centrally. The difference between predictions in the 4FS and 5FS is often much larger than the scale uncertainty band (which is more pronounced in the 5FS in the bulk of the events). We will discuss further this feature when presenting jet multiplicities in the following.

In Fig. 5.9 we show the analogous distributions for the b-tagged jets. These are all the jets containing a bottom hadron and falling inside the acceptance of the tracking system, defined in Eq. (5.7). We consider the two hardest b jets ($j_{b,1}$ and $j_{b,2}$) in the event regardless of their origin and, separately, we study the b jet coming from the top quark decay $j_{b,t}$ (tagged by using Monte Carlo information), which is shown in Fig. 5.10. The p_T spectrum of $j_{b,1}$ has a rather long tail compared to $j_{b,2}$ and, at variance with light jets, all the b jets tend to be produced in the central region. Scale dependence at NLO is rather small in the 4FS, never reaching 10% and being typically around 5%. Differences between 4FS and 5FS predictions are visible, especially in the uncertainty band of $j_{b,2}$ in the 5FS; this is of course expected, given that this observable is described only at LO accuracy in this scheme. Quite remarkably, however, these differences at NLO are often significantly less pronounced than in the case of light jets (especially j_2), while naively one might expect the b-jet observables to be mostly affected by the flavour-scheme choice. On the other hand, at LO the inadequacy of the 5FS to describe b jets is evident.

Comparing the transverse momentum of $j_{b,t}$ (in Fig. 5.10) to the corresponding spectra of $j_{b,1}$ and $j_{b,2}$, it can be inferred that b jets from the top quark mostly contribute to the hardest-b-jet ($j_{b,1}$) spectrum at low p_T. On the other hand, as the p_T tail falls much more rapidly for $j_{b,t}$ than for $j_{b,1}$, gluon splitting in the hard scattering becomes the predominant mechanism at high p_T, *i.e.* the main source of b jets in this region. This observation also explains why the scale dependence in the 5FS is small for low $p_T(j_{b,1})$, but increases sharply in the high-$p_T(j_{b,1})$ region: the first region is dominated by the top decay and thus described at NLO accuracy, while in the second region the physics is dominated by the transverse dynamics of the $g \to b\bar{b}$ splitting, which is described only at LO.

We conclude this section by studying the jet multiplicities, which are sensitive to the flavour scheme as well as to the choice of the shower scale. As argued in [163], the dynamics of $g \to b\bar{b}$ splitting takes place at a scale which is typically lower than the hard scale of the process $m_t + m_H$ or H_T, affecting the choice for the factorisation scale that one should use to describe t-channel production. An analogous argument could be made also for the shower scale choice [170], which in the MadGraph5_aMC@NLO matching procedure is chosen to be of the order of the partonic centre-of-mass energy in the Born process. In Fig. 5.11, we study the dependence of jet rates on the flavour scheme as well as on the shower scale, where two different choices of the shower scale are compared: one is the default value, and the other is the default value divided by a factor four. We can see that reducing the parton-shower scale has only a minor impact on the distributions, while a more interesting pattern arises from the choice of

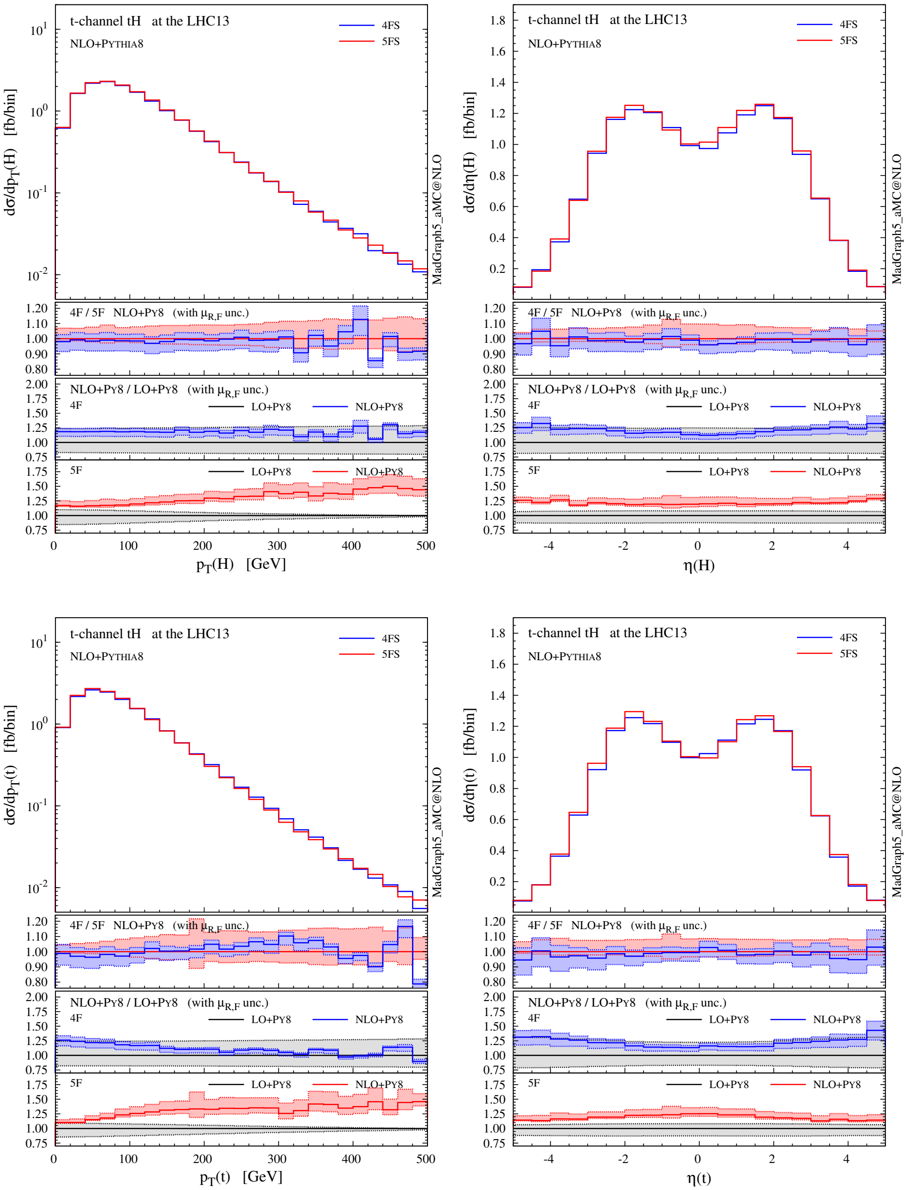

Figure 5.6: Representative differential distributions (in p_T and η) for the Higgs boson and the top quark at NLO+PS accuracy in t-channel tH associated production at the 13-TeV LHC. The lower panels provide information on the differences between 4FS and 5FS as well as the differential K factors in the two schemes.

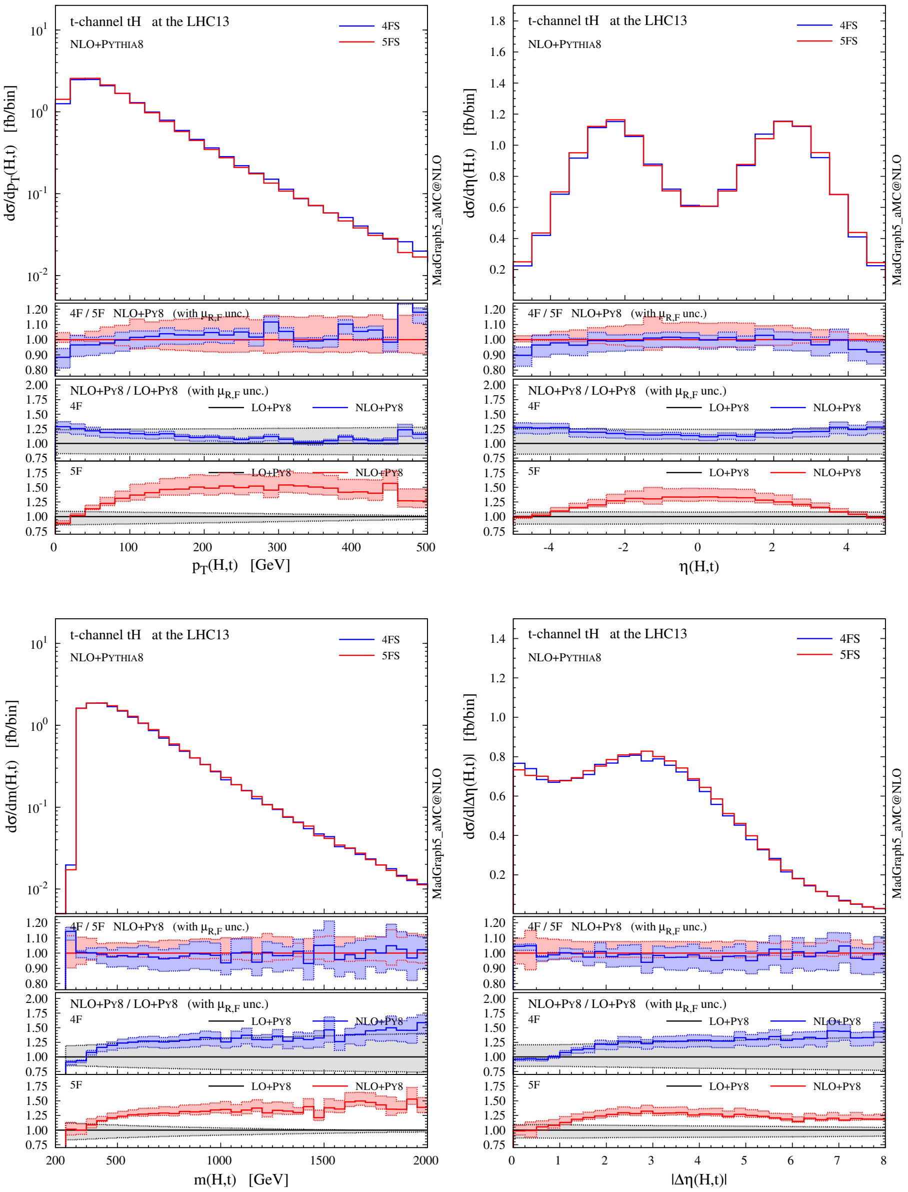

Figure 5.7: Similar to Fig. 5.6, but for the Higgs-top system.

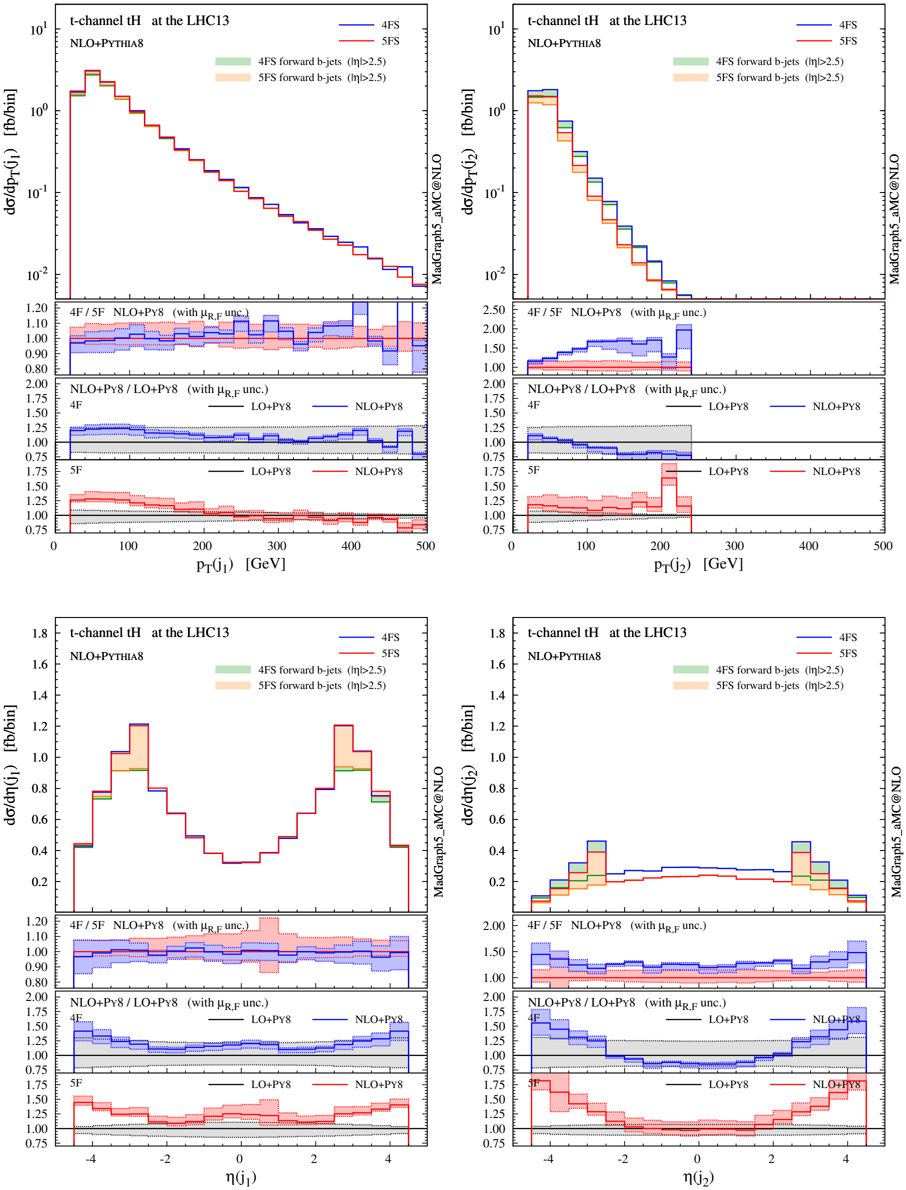

Figure 5.8: Same as Fig. 5.6, but for the two hardest jets. The contributions from non-taggable forward b jets are also shown by shaded histograms, as a reference.

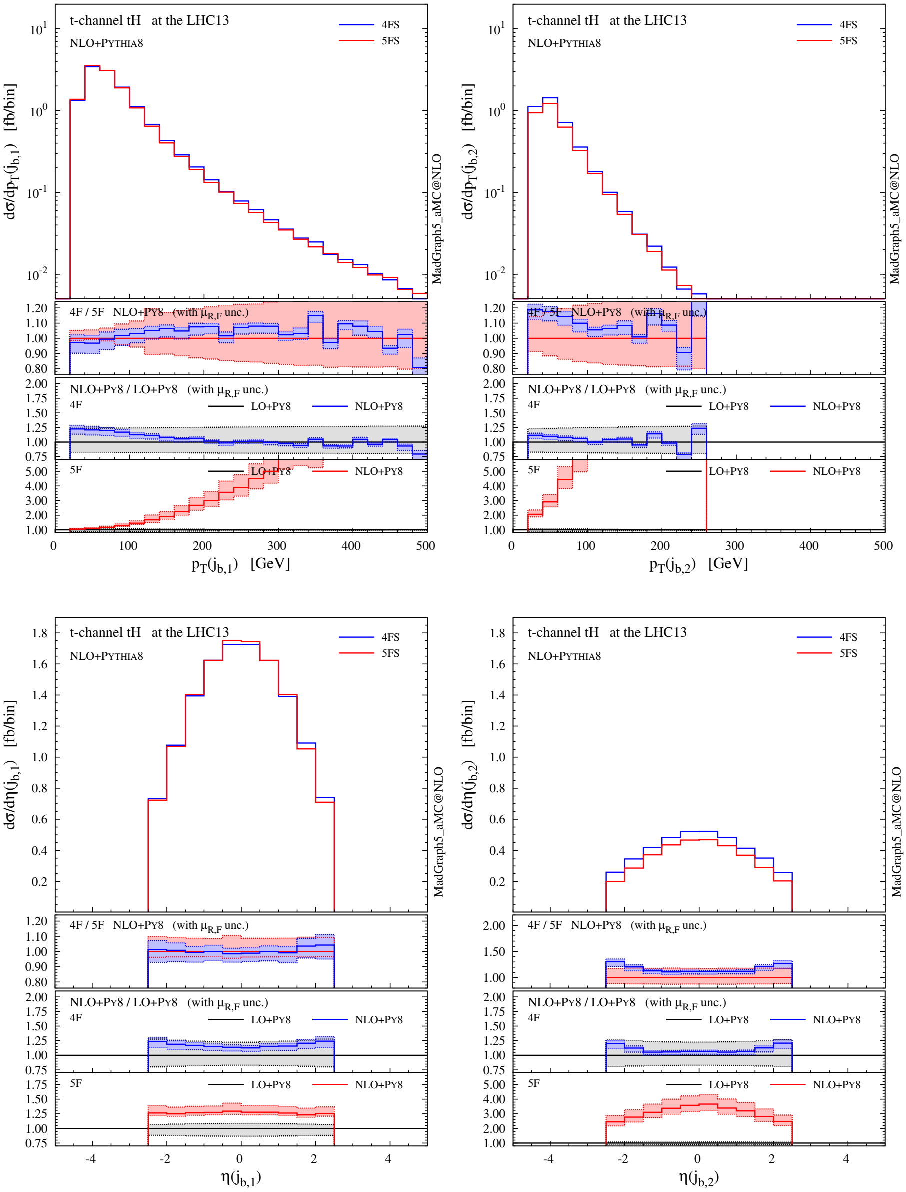

Figure 5.9: Same as Fig. 5.6, but for the b-tagged jets.

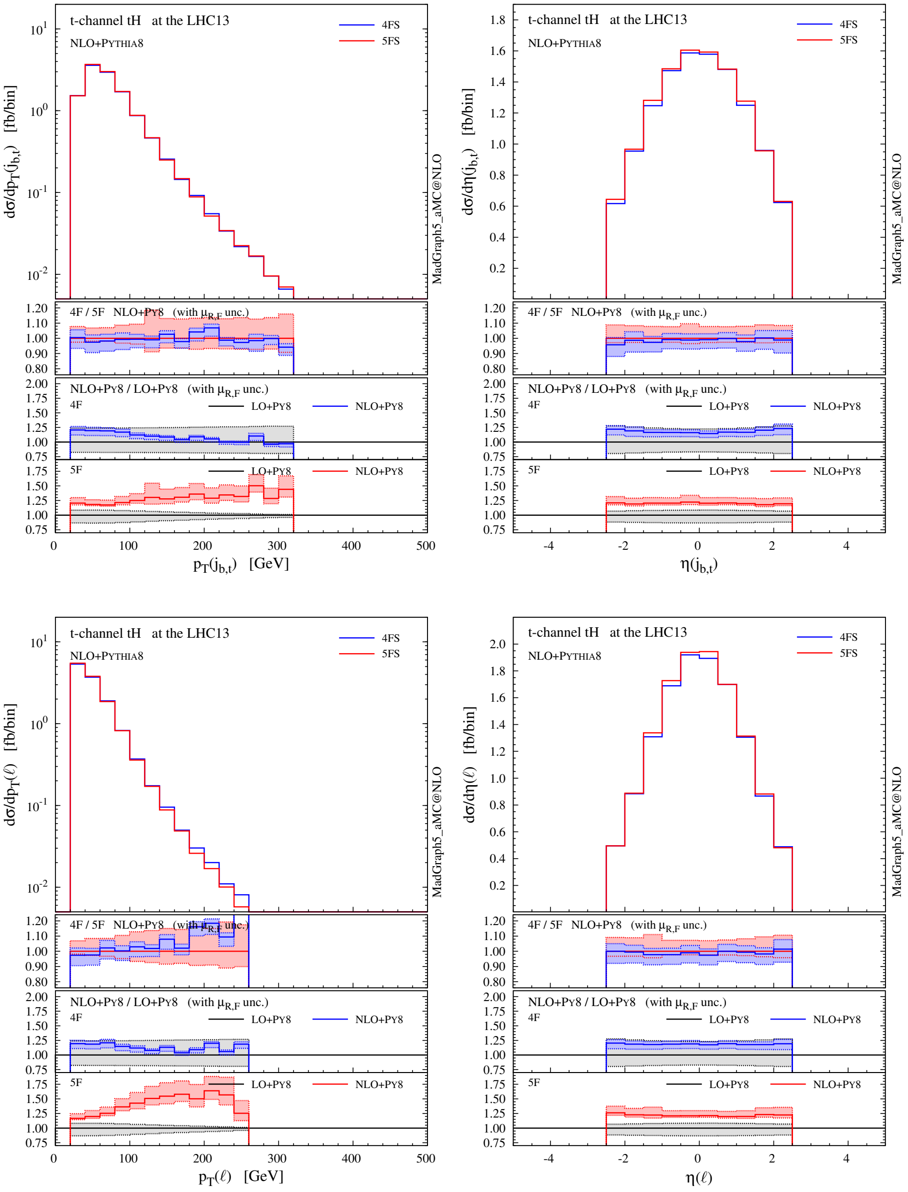

Figure 5.10: Same as Fig. 5.6, but for the top-quark decay products (the b jet and the charged lepton) selected by using Monte Carlo information.

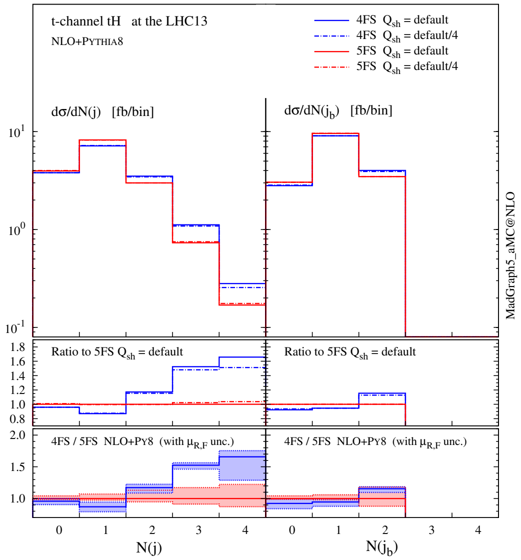

Figure 5.11: Jet (left) and b-jet (right) multiplicities at NLO+PS accuracy, in the 4FS and 5FS, with two different choices of the shower scale $Q_{\rm sh}$.

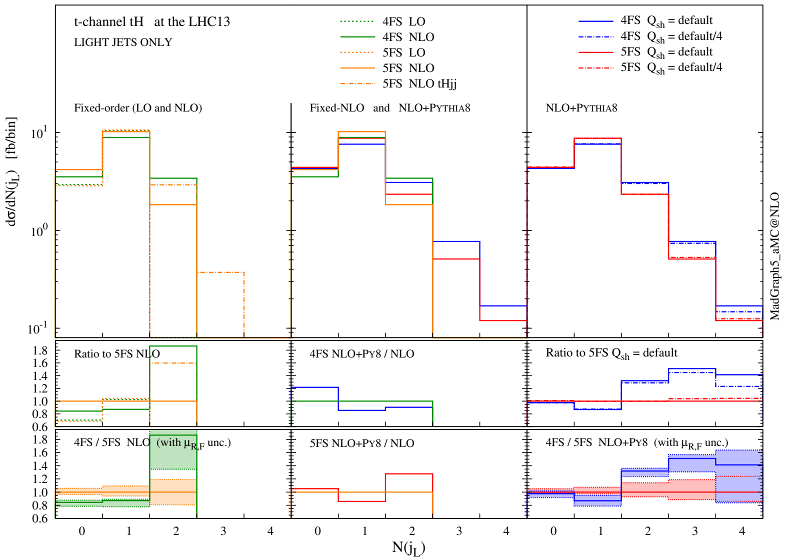

Figure 5.12: Multiplicity rates for the light jets only, both at fixed order and matched to a parton shower, in the 4FS and 5FS, and with two different choices of the shower scale $Q_{\rm sh}$.

the flavour scheme. For the b-tagged jets (right panel in Fig. 5.11), differences between the two schemes are rather mild ($\sim 15\%$ in the 2-jet bin, and less for 0 and 1 jet) and always compatible within the scale uncertainty, which is much larger in the 5FS for the 2-jet bin (the accuracy being only at LO). For non-b-tagged jets (left panel in Fig. 5.11), on the other hand, a higher jet multiplicity is clearly observed in the 4FS, which implies that harder QCD radiation is favoured in this scheme. Interestingly, the difference is visible already in the 1-jet bin, which is described at NLO accuracy at the matrix-element level.

These differences cannot arise from the small component of forward, non-taggable heavy jets; on the contrary, they can be understood by considering jets that come from genuinely light QCD radiation. In Fig. 5.12 we show explicitly the multiplicity of light jets only (tagged by using Monte Carlo information), both at fixed order in QCD and at NLO matched to parton shower. Our first observation is that results in the 4FS and 5FS are almost identical at fixed LO (where only the zero and one jet bins are filled). The difference is therefore an effect of higher-order corrections, as it is confirmed by observing the fixed-NLO histograms. We recall that the fixed-order matrix element has a different colour structure in different schemes; in particular, the 4FS at LO features a gluon in the initial state (compared to the b-quark in the 5FS) and an extra b in the final state. The radiation of extra light QCD partons from the $g \to b\bar{b}$ splitting is therefore favoured in the 4FS (*e.g.* an extra gluon can either attach to the initial-state gluon or to one of the b's, while in the 5FS it can attach only to the initial-state b). This is indeed what we observe at fixed NLO.

If the origin of the jet-rate discrepancy can be traced back to the difference between the 4FS and 5FS colour structures at LO, then one would also expect this discrepancy to be mitigated once higher-order corrections are included. To this aim, we have performed a fixed-order computation of the 2-jet bin in the 5FS at NLO accuracy, *i.e.* simulated $tHjj$ at NLO, finding indeed that the rate is significantly enhanced (by $\sim 60\%$) and lies much closer to the 4FS result. A further hint that the scheme difference is indeed mitigated at higher orders is given by the NLO+PS results, which show that the 2-jet bin in the 4FS is reduced by just $\sim 10\%$ after the shower, while the corresponding 5FS one is enhanced by $\sim 30\%$ over the fixed-order result. Finally, we have checked that the same results we have found for single top plus Higgs, occur also in the case of single top production alone. In conclusion, our results suggest that the inclusion of the $g \to b\bar{b}$ splitting in the matrix-element description at the lowest order, *i.e.* using the four-flavour scheme, allows a wider range of observables relevant for the analyses to be described more accurately.

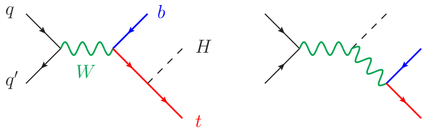

Figure 5.13: LO Feynman diagrams for s-channel tH production.

5.3 SM results in the s-channel

Higgs-top quark associated production at hadron colliders can also be mediated by s-channel diagrams, see Fig. 5.13. Compared to t-channel production, the s-channel mechanism is naturally suppressed by the higher virtuality of the intermediate W boson and features a much smaller cross section at the LHC. In this section we calculate the NLO cross section, evaluating the corresponding uncertainties, and compare some s-channel distributions at NLO+PS accuracy to the corresponding ones from t-channel production.

At LO, s-channel production proceeds through $q\bar{q}$ annihilation into a virtual W boson, which can either emit a Higgs boson and then split to a tb final state, or first split to tb with the subsequent emission of a Higgs from the top quark. It turns out that in this case the interference between these two diagrams is positive and its effect are much less relevant than in t-channel production [162], since their impact on the total cross section amounts to roughly +15%. At NLO, extra radiation can take place from either initial or final state, with no interference between the two due to colour conservation. For the same reason, no interference between the s-channel and t-channel processes is present in the five-flavour scheme, and the separation between channels is still exact at NLO accuracy. In this production mode, bottom quarks are directly produced in the hard scattering via electroweak interaction and appear only in the final state. Thus, at variance with the t-channel and W-associated production, the flavour scheme is not a key source of uncertainties for s-channel production.

In the MadGraph5_aMC@NLO framework the code and the events for s-channel production at hadron colliders can be automatically generated by typing the following commands:

```
> import model loop_sm(-no_b_mass)
> generate p p > w+ > h t b~ [QCD]
> add process p p > w- > h t~ b [QCD]
> output
> launch
```

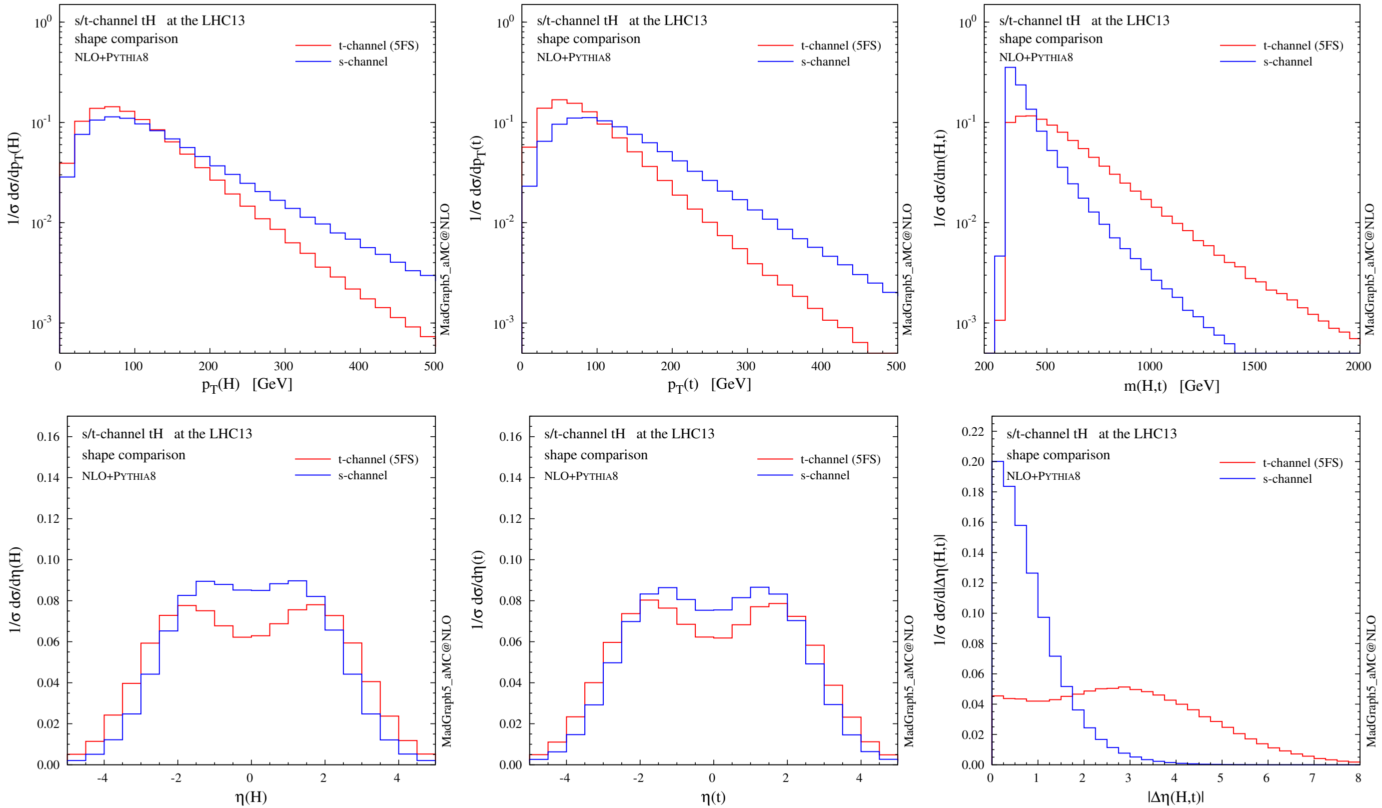

Figure 5.14: Shape comparison between s- and t-channel distributions for the Higgs boson and the top quark at NLO+PS accuracy.

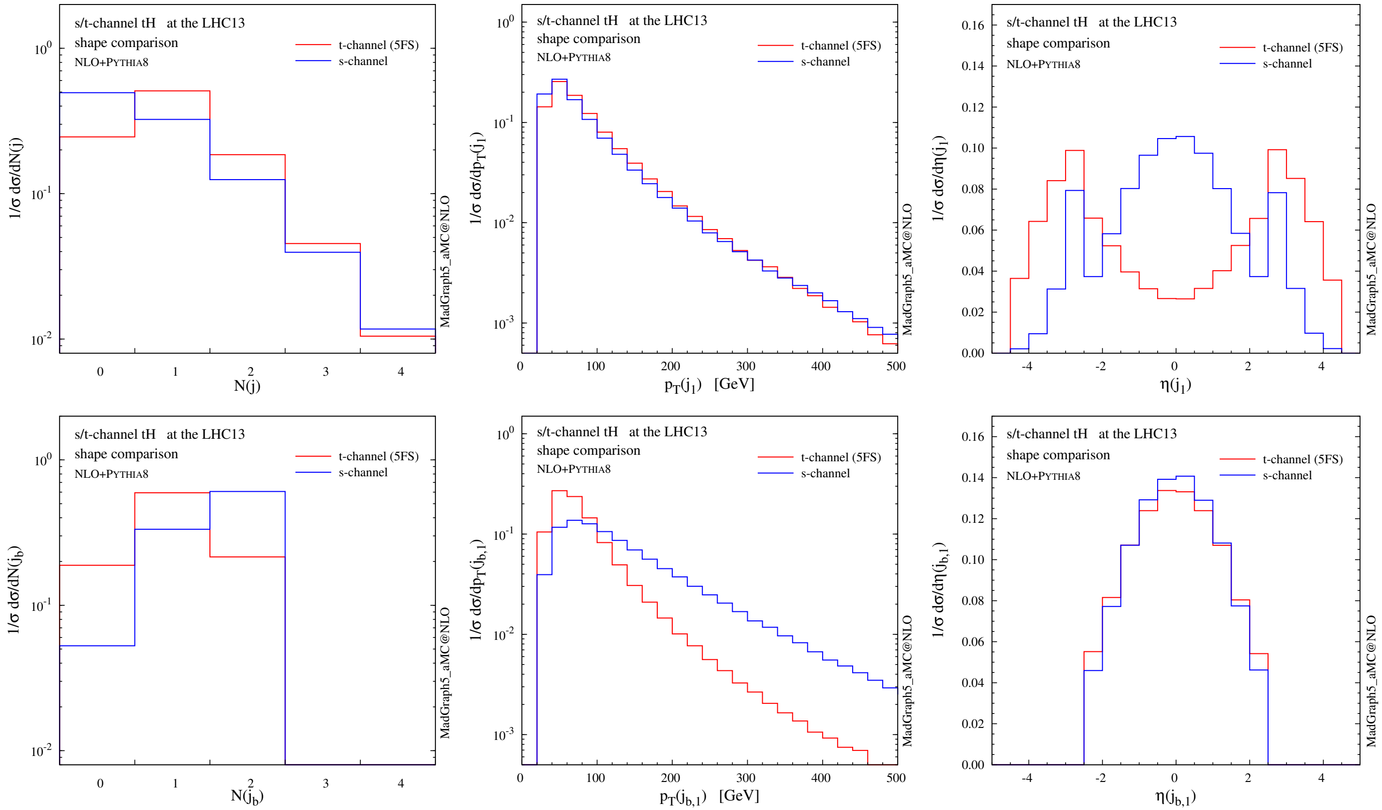

Figure 5.15: In the top row: shape comparison between s- and t-channel distributions for jet rates (left), p_T (centre) and η (right) spectra for the hardest jet at NLO+PS accuracy. In the bottom row: corresponding plots for b-tagged jets.

s-channel	σ_{NLO} [fb]	$\delta^{\%}_{\mu}$	$\delta^{\%}_{\mathrm{PDF}}$	$\delta^{\%}_{\alpha_s}$
$tH+\bar{t}H$	2.812(3)	$^{+1.6}_{-1.2}$	$^{+1.4}_{-1.4}$	$^{+0.3}_{-0.5}$

Table 5.8: NLO total cross section for the processes $pp \to tH\bar{b}+\bar{t}Hb$ via an s-channel W-boson exchange at the LHC with $\sqrt{s}=13$ TeV. NNPDF2.3 PDFs have been used. The integration uncertainty in the last digit (in parentheses), the fractional scale dependence and the PDF and α_s uncertainties (in %) are also reported.

In Table 5.8 we show the total cross section at NLO. Reference values for the factorisation and renormalisation scales are set to $\mu_0 = H_T/2 = \sum m_T/2$. Being a pure EW process at LO, s-channel production exhibits very low scale and α_s uncertainties up to NLO. In the SM, the total rate amounts to about 3 fb, *i.e.* less than 5% of the t-channel cross section.

In Figs. 5.14 and 5.15 we compare the shape of some distributions between the s-channel and t-channel production modes at NLO+PS accuracy. We can see that most of the observables related to s-channel events display a significantly different shape. Even though the total cross section in s-channel production is tiny and deviations from a t-channel-only simulation would probably fall inside the uncertainty band, the s-channel simulation can be included with little extra computing cost when precision is needed (it is also extremely fast at NLO).

5.4 Official SM predictions for *tH* production at the LHC Run II

In this section we report the recommended values for the t- and s-channel tH cross sections at the LHC Run II. They are a result of the discussions and efforts within the LHC Higgs Cross Section Working Group (LHCHXSWG), aimed at providing an official reference to the whole LHC experimental community, to be consistently used in the various analyses during Run II. All these results have been published in the fourth LHCHXSWG technical report [19].

The recipe to compute these numbers, especially for the t-channel process, is based on the key lessons we have learned earlier in this chapter. However, in some aspects it is quite simpler than the procedure followed for the results in Fig. 5.5. In fact, after the publication of [17], the 2015 update of the PDF4LHC recommendations has been released [183]. Not only it is based on the last-generation PDF fits of the CT14 [184], MMHT14 [33] and NNPDF3 [185] families, but also it provides a unique PDF set that automatically encompasses both the usual PDF uncertainty (propagated from fitted data) and the differences in fitting procedures adopted by the three groups. Therefore, it is sufficient to use just this PDF4LHC15 set to compute official predictions. Moreover, the 5FS has been employed to obtain both the reference cross section and the PDF+α_s uncertainty, while the 4FS has been used just to compute the combined scale and flavour-scheme uncertainty. On the other hand, the scale dependence is estimated on six different points, some of which do not lie on the diagonal $\mu_R = \mu_F$. Some input parameters have also been changed to comply with the LHCHXSWG recommendations [186]; in particular, the bottom-mass uncertainty is effectively halved with respect to Eq. (5.3), and discussed separately from the PDF+α_s uncertainty.

In Figs. 5.16 and 5.17 we can see the result of the theoretical efforts during the last years to improve the predictions for the Higgs cross section at the LHC. Notably, Higgs plus single top production has been included for the first time among the various processes. In Fig. 5.18 we plot the t-channel (on the left) and s-channel (on the right) SM cross sections as a function of the LHC energy, together with the total theoretical uncertainty (shown as a blue band), and also the separate single-top and anti-top contributions. The total uncertainty is the sum of the scale (plus flavour-scheme, for the t-channel process) uncertainty on the one hand, and the PDF+α_s uncertainty on the other hand. In the insets we show the NLO-QCD K factor and the separate sources of uncertainty. In Figs. 5.19 and 5.20 we plot the SM cross sections as a function of the Higgs-boson mass, at four different LHC energies (7, 8, 13 and 14 TeV).

Finally, in Figs. 5.21 and 5.22, we extend our results to Higgs masses in the range $m_H = 10-3000$ GeV, keeping the Higgs boson as stable particle and neglecting Higgs-width effects. They might provide a useful reference for BSM Higgs searches, as requested by the LHCHXSWG. However, we stress that these results should be taken with care: an hypothetical BSM Higgs boson may contribute to the tH process through different interactions than the ones described by SM-like diagrams, and also finite-width effects may become important at large masses. It is interesting to note the change of slope in the cross section around $m_H \sim 100$ GeV. This region marks the transition from small Higgs masses, where the cross section is dominated by the $t^* \to tH$ splitting diagrams, to large Higgs masses, where instead the diagrams featuring the WWH vertex are numerically more important, since $t^* \to tH$ suffers from s-channel suppression.

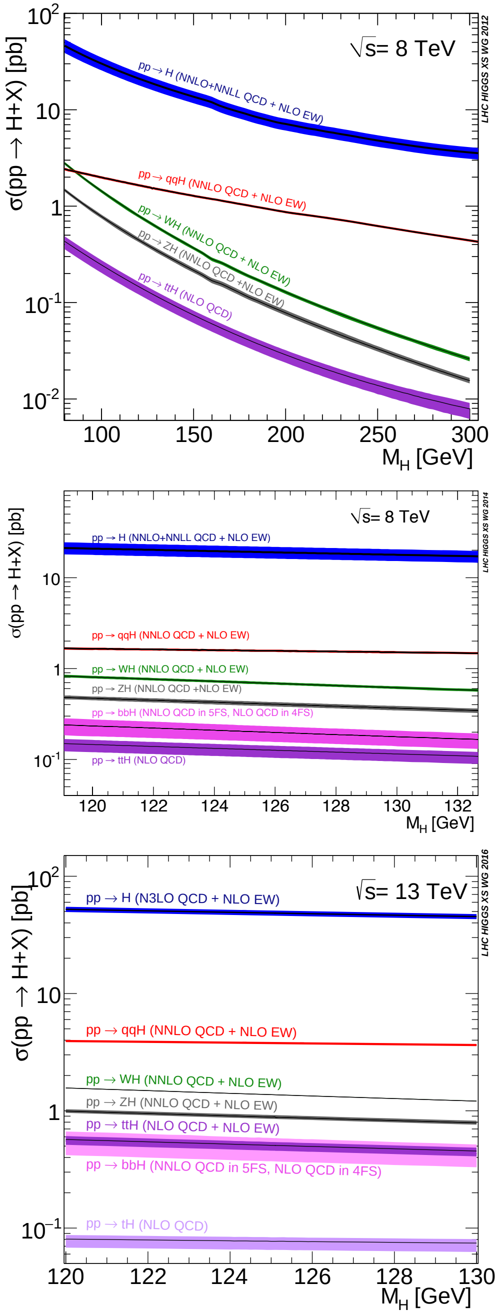

Figure 5.16: Reference cross sections for single-Higgs processes at the LHC, as a function of m_H, provided by the LHCHXSWG at different years: 2012 (top), 2014 (centre) and 2016 (bottom). Taken from the CERN TWiki [88].

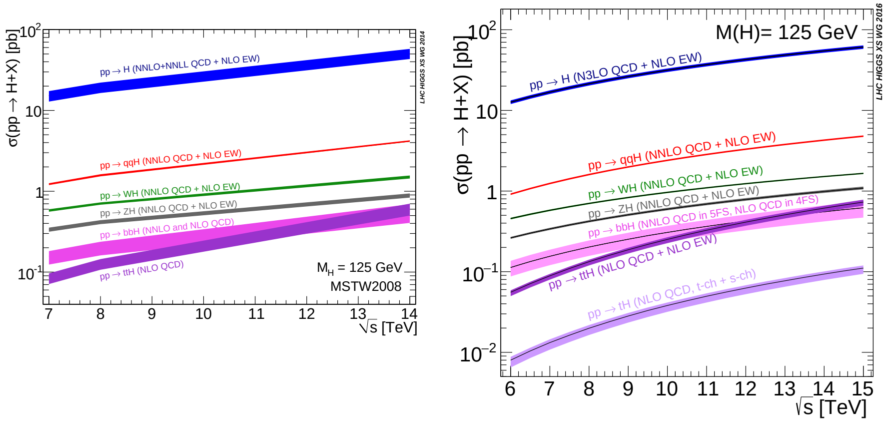

Figure 5.17: Reference cross sections for single-Higgs processes at the LHC, as a function of the collider energy, provided by the LHCHXSWG at different years: 2014 (left) and 2016 (right). Taken from the CERN TWiki [88].

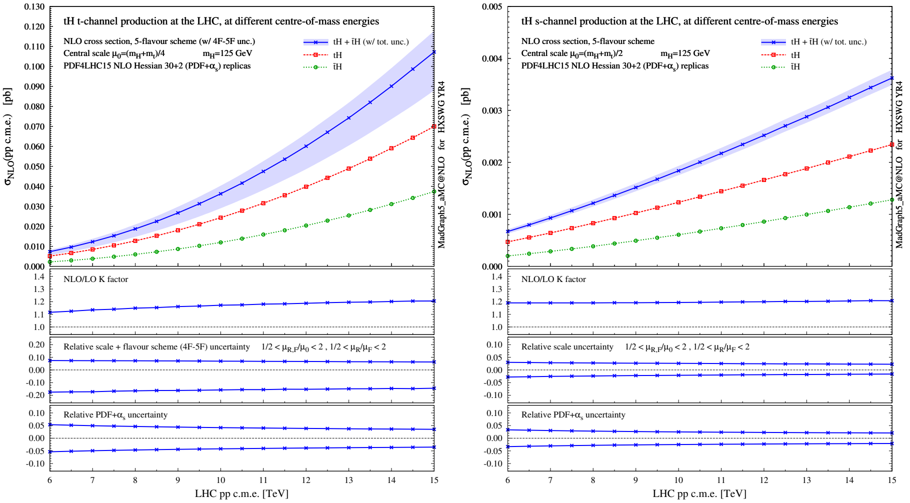

Figure 5.18: Cross sections for t-channel (left) and s-channel (right) tH and $\bar{t}H$ production at different LHC energies.

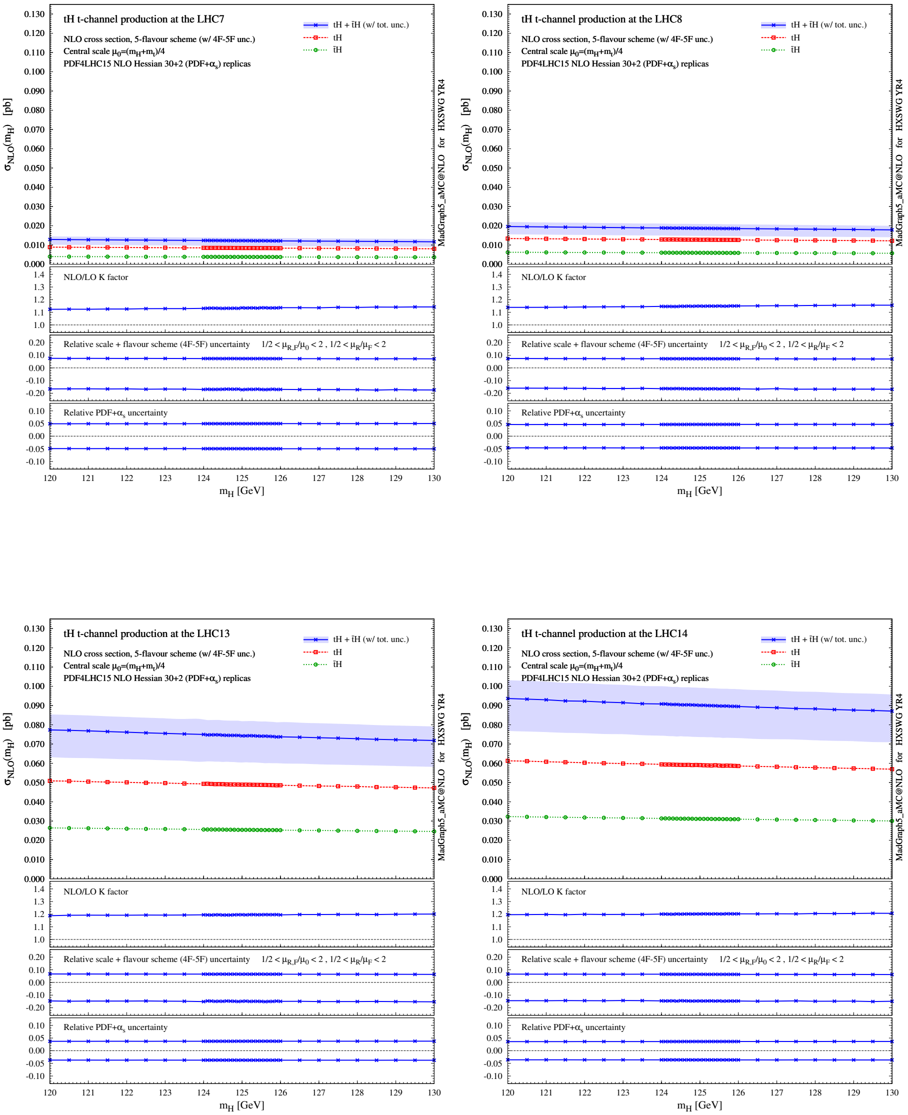

Figure 5.19: Cross sections for t-channel tH and $\bar{t}H$ production.

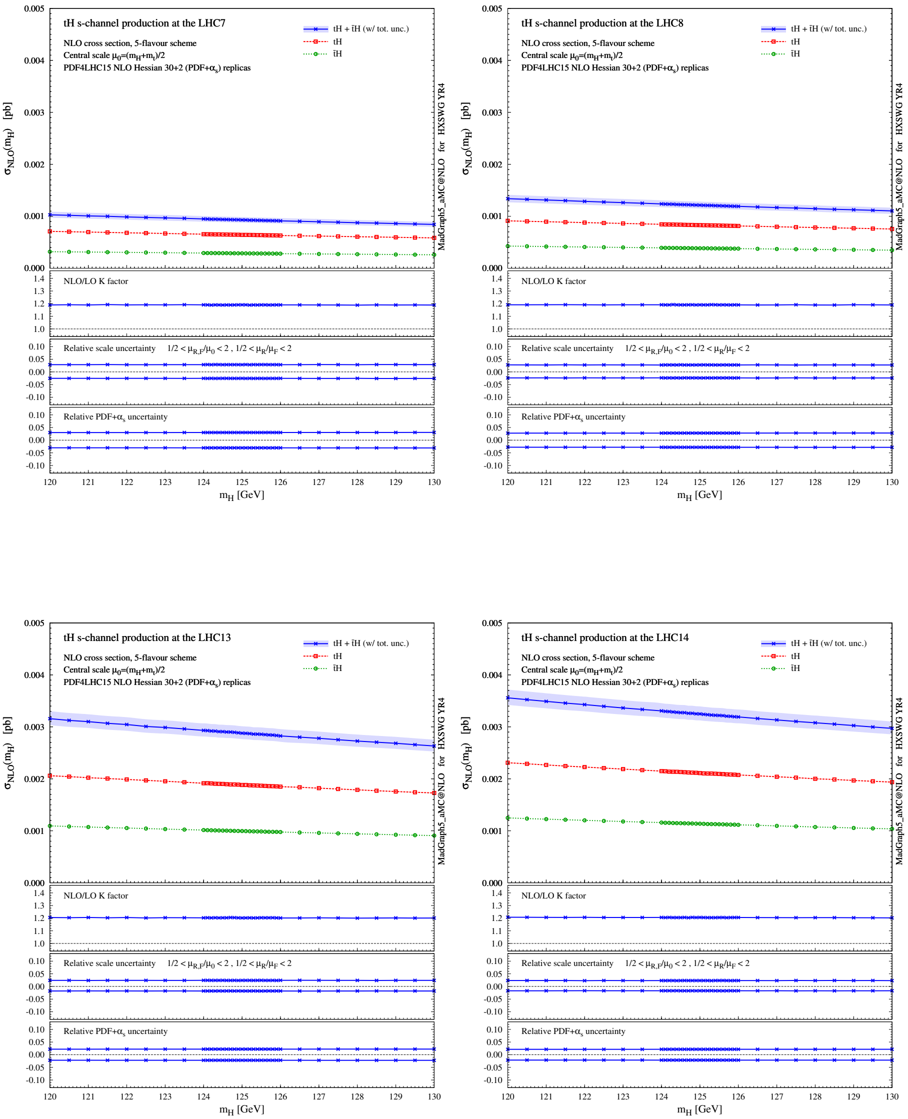

Figure 5.20: Cross sections for s-channel tH and $\bar{t}H$ production.

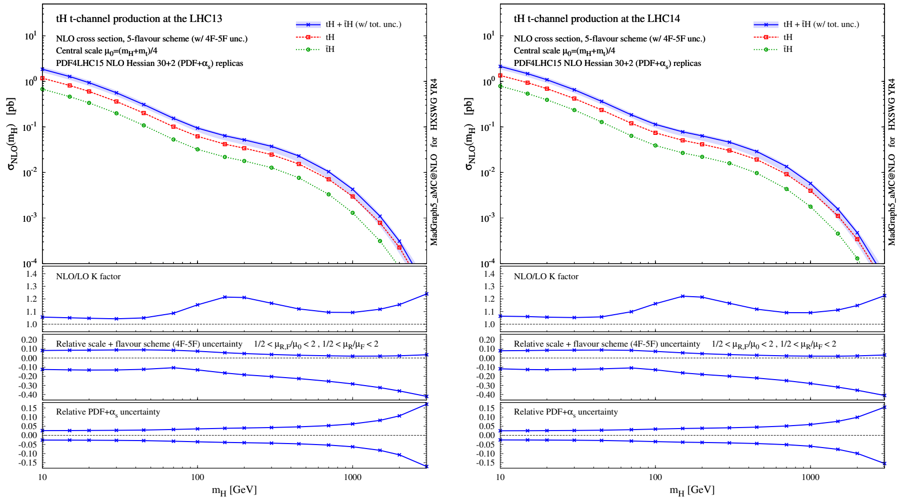

Figure 5.21: Cross sections for t-channel tH and $\bar{t}H$ production in the extended Higgs-mass range.

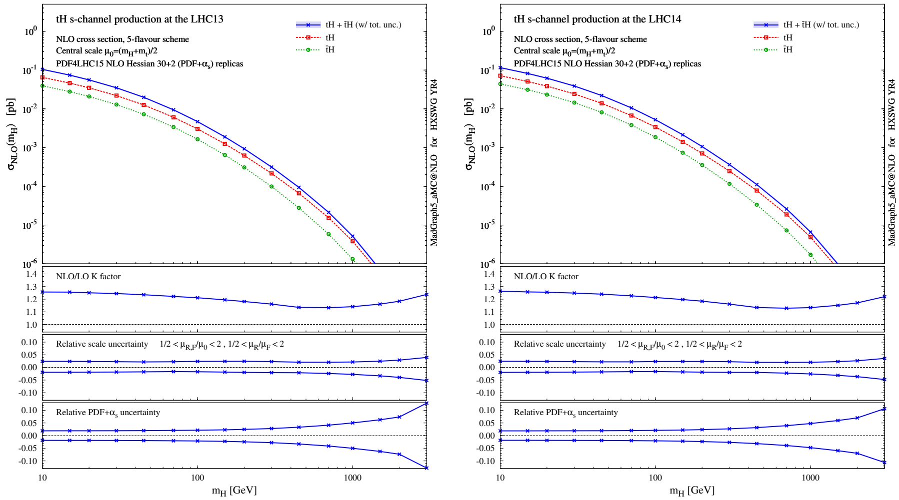

Figure 5.22: Cross sections for s-channel tH and $\bar{t}H$ production in the extended Higgs-mass range.

More details about the input parameters and the procedure followed to compute tH cross sections can be found in Appendix E, together with the tables containing all the official numbers used to generate the plots in Figs. 5.18 to 5.22.

5.5 Higgs Characterisation in the t-channel

In this section we go beyond the SM and explore the sensitivity of t-channel Higgs associated production with single top to a Yukawa interaction between the Higgs boson and the top quark that does not conserve CP. Before [17], several phenomenological studies on anomalous Higgs couplings that took advantage of this process have appeared [142,187–193], using just LO predictions for tH. Current experimental constraints on the Higgs-boson couplings favour the SM, and in particular the magnitude of the top-quark Yukawa is consistent with the expectations, even though an opposite sign with respect to the SM one is not yet excluded [12].

Moreover, although the scenario of a purely pseudoscalar Higgs is practically excluded [11,194], no stringent constraint has been put on a CP-violating $H-t$ coupling. In fact, even if current results are fully compatible with the SM hypothesis, some analyses on public LHC data seem to favour a non-zero phase in the top quark Yukawa interaction [190, 195–198]. The bottom line is that current constraints are not very stringent, due to the small cross sections of processes directly sensitive to the top Yukawa, such as $t\bar{t}H$ and tH production, and the relatively low amount of data collected during the LHC Run I. The larger cross sections and the anticipated integrated luminosity at Run II and beyond will certainly change this picture.

Here we consider the (simplified) case of a spin-0 particle with a general CP-violating Yukawa interaction with the top quark, which couples both to scalar and pseudoscalar fermionic densities. On the other hand, we assume the interaction with the W bosons to be the SM one. We note that this assumption does not correspond to a typical realisation of CP-violation in a two-Higgs-doublet model (2HDM), where the mass eigenstates are CP-mixed states and their coupling to the vector bosons is reduced. Our setup, however, corresponds to considering the effective HC Lagrangian of Eq. (2.6), implemented in the HC_NLO_X0 model [22][4], which we report again here for the sake of

---

[4] For the code and event generation, one can simply issue the command '`> import model HC_NLO_X0`' and replace '`h`' with '`x0`' in the MadGraph5_aMC@NLO shell.

the upcoming discussion

$$\mathcal{L}_0^t = -\bar{\psi}_t\big(c_\alpha \kappa_{Htt} g_{Htt} \, + \, i s_\alpha \kappa_{Att} g_{Att} \, \gamma_5\big)\psi_t \, X_0 \, . \tag{5.14}$$

We also recall that while the EFT hypothesis is satisfied if deviations from the SM are not too large, *i.e.* $c_\alpha \kappa_{Htt} \simeq 1$ and $s_\alpha \kappa_{Att} \simeq 0$, the parametrisation given above actually allows to explore a wider range of scenarios, such as the reversed-sign top Yukawa coupling when $\alpha = 0$ and $\kappa_{Htt} = -1$ (strictly speaking, this cannot be realised in the SM EFT extension).

The nature of the top quark Yukawa coupling directly affects the loop-induced Higgs coupling to gluons in Eq. (2.8)

$$\mathcal{L}_0^g = -\frac{1}{4}\left(c_\alpha \kappa_{Hgg} g_{Hgg} \, G^a_{\mu\nu} G^{a,\mu\nu} \, + \, s_\alpha \kappa_{Agg} g_{Agg} \, G^a_{\mu\nu} \widetilde{G}^{a,\mu\nu}\right) X_0 \, , \tag{5.15}$$

where $g_{Hgg} = -\alpha_s/(3\pi v)$ and $g_{Agg} = \alpha_s/(2\pi v)$. Assuming that the top quark dominates the gluon-fusion (GF) process at the LHC energies, then $\kappa_{Hgg} \to \kappa_{Htt}$, $\kappa_{Agg} \to \kappa_{Att}$. In so doing, the ratio between the actual cross section for GF at NLO QCD and the corresponding SM prediction can be written as

$$\frac{\sigma^{gg\to X_0}_{\text{NLO}}}{\sigma^{gg\to H}_{\text{NLO,SM}}} = c_\alpha^2 \, \kappa_{Htt}^2 \, + \, s_\alpha^2 \left(\kappa_{Att} \, \frac{g_{Agg}}{g_{Hgg}}\right)^2 , \tag{5.16}$$

because there is no interference between the scalar and pseudoscalar components in the amplitudes for Higgs plus up to three external partons, see *e.g.* [16]. In particular, if the rescaling parameters are set to

$$\kappa_{Htt} = 1 \, , \qquad \kappa_{Att} = |\, g_{Hgg}/g_{Agg} \,| = 2/3 \, , \tag{5.17}$$

the SM GF cross section is reproduced for every value of the CP-mixing phase α. Given that current measurements are compatible with the expected SM GF production rate, one can consider the simplified scenario where the condition in Eq. (5.17) is imposed and the CP-mixing phase α is only loosely constrained using Run I data (given the insufficient sensitivity to $t\bar{t}H$ production at Run I, only the $\gamma\gamma$ decay channel can be employed to constrain the CP-mixing angle).

Fig. 5.23 shows the total cross section for t-channel tX_0 production as a function of the CP-mixing angle α. We also show the $t\bar{t}X_0$ cross section, which is not only another process sensitive to the modifications of the top quark Yukawa coupling, but also a background to t-channel production. The uncertainty band represents the envelope defined in sect. 5.2.2, *i.e.* the combined scale and flavour-scheme dependence. The $t\bar{t}X_0$ uncertainty band represents the scale dependence only, when the scale is varied by a factor two around the central value $\mu_0 = \sqrt[3]{m_T(t)\, m_T(\bar{t})\, m_T(X_0)}$, see Eq. (4.1).

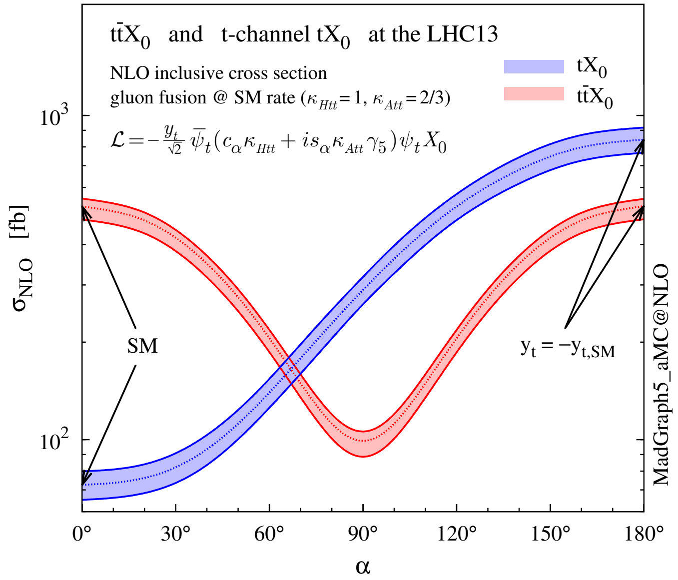

Figure 5.23: NLO cross sections (with scale uncertainties) for $t\bar{t}X_0$ and t-channel tX_0 productions at the 13-TeV LHC as a function of the CP-mixing angle α. The factors κ_{Htt} and κ_{Att} are set according to Eq. (5.17), in order to reproduce the SM GF cross section for any value of α.

The first important observation is that while the GF and $t\bar{t}H$ cross sections are degenerate under $y_t \to -y_t$ (depending quadratically from the top quark Yukawa coupling), in t-channel production this degeneracy is clearly lifted by the interference between diagrams where the Higgs couples to the top quark and to the W boson. In [187,188] it was shown that the t-channel cross section is enhanced by more than one order of magnitude when the strength of the top Yukawa coupling is changed in sign with respect to the SM value. Here we can see how the same enhancement can take place also in the presence a continuous rotation in the scalar-pseudoscalar plane. While not affecting GF (by construction), such a rotation has an impact also on the $t\bar{t}X_0$ rate, which is in general lower for a pseudoscalar or CP-mixed state [16]. Higgs plus single top t-channel production lifts another degeneracy present in GF and $t\bar{t}X_0$, namely $\alpha \to \pi - \alpha$. Given the partial compensation between the t-channel and $t\bar{t}X_0$ cross sections at different values of α, an analysis which could well separate between the two production mechanisms would be needed to put stringent constraints on a CP-violating Higgs coupling to the top quark.

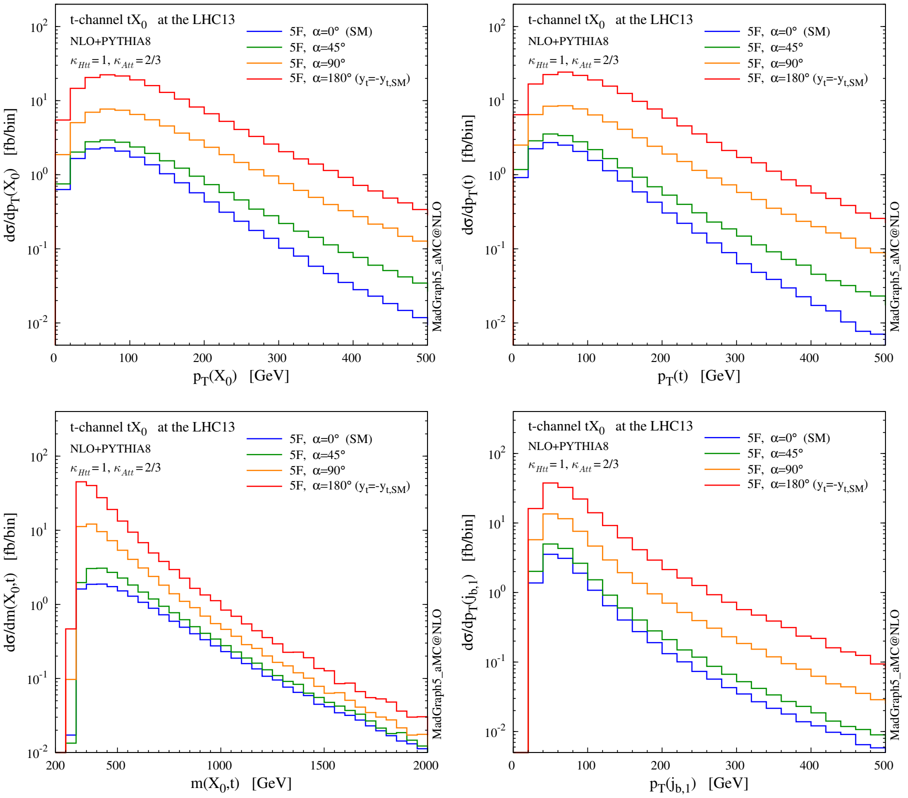

Figure 5.24: Sample differential distributions for the Higgs boson, the top quark and the hardest b jet at NLO+PS accuracy in t-channel tX_0 associated production at the 13-TeV LHC, at different values of the CP-mixing angle α. The factors κ_{Htt} and κ_{Att} are set according to Eq. (5.17).

We remind that the enhancement of the t-channel cross section takes place mostly at threshold, as one can clearly see in the upper left plot of Fig. 5.24. This means that one should not be concerned by violations of perturbative unitarity at the LHC, as they do not appear for partonic centre-of-mass energies lower than $\sim$ 10 TeV [188]. In Fig. 5.24 we also show the transverse momentum distributions for the Higgs, the top quark and the hardest b-tagged jet. The distributions are well behaved in this case too: albeit some exhibit slightly harder high-p_T tails than in the SM case, none of them displays any strong trend that could suggest a violation of unitarity.

Finally, in Fig. 5.25 we plot the pseudorapidity separation between the Higgs and the top quark (left) and the opening angle between the hardest jet and the

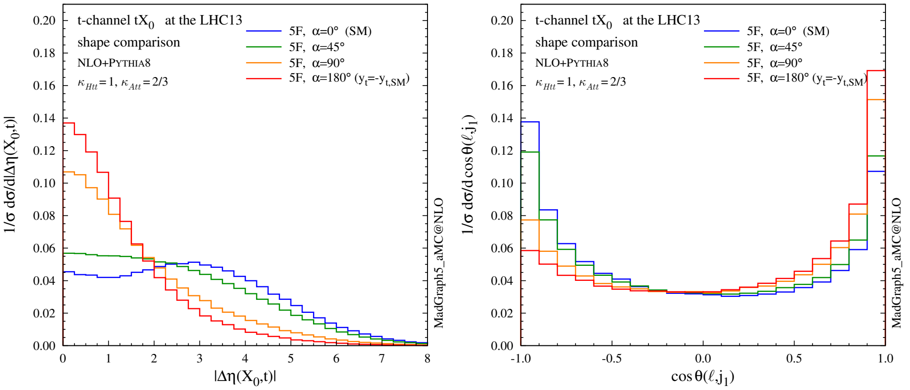

Figure 5.25: Shape comparison among different values of the CP-mixing angles. We show the pseudorapidity separation between the Higgs and the top quark (left), and the opening angle between the hardest jet and the lepton from the top quark in the lab frame (right).

lepton from the top quark in the lab frame (right), showing that the shape of these variables have a discriminating power on α, too. For this last observable, the lepton is required to satisfy the following selection criteria

$$p_T(\ell) > 20 \text{ GeV}\,, \quad |\eta(\ell)| < 2.5\,. \tag{5.18}$$

5.6 Summary

In this chapter we have studied the production of a Higgs boson in association with a single top quark at the LHC.

Our first aim has been to carefully consider the effects of NLO corrections in QCD on total cross sections and differential distributions for t-channel production. We have scrutinised a wide range of theoretical uncertainties, and in particular those arising from the choice of the heavy-quark scheme, four-flavour or five-flavour. We recall that higher-order QCD corrections are crucial in order to reduce this flavour-scheme dependence. We have found that at the level of total cross sections a comfortable consistency between the two schemes exists when physically motivated choices for the renormalisation and factorisation scales are made, with similar resulting uncertainties. For differential distributions, on the other hand, the situation is slightly more involved. While sizeable differences between the two schemes arise at LO, they are considerably milder at NLO and NLO+PS, in line with expectations. In this case, we have shown that both flavour schemes provide fully consistent and similarly precise predictions for differential distributions related to the Higgs boson, the top quark, and the forward jet. On the other hand, the four-flavour scheme is in general able to provide accurate predictions for a wider set of observables, including those related to the spectator b quark and the extra light QCD radiation.

In addition to t-channel production in the SM, we have also briefly presented the results for the subdominant s-channel production, highlighting the differences in the most important distributions with respect to the corresponding ones of t-channel production.

These results, published in [17], have provided the foundations for including, for the first time, Higgs plus single top production among the various processes addressed by the LHC Higgs Cross Section Working Group. We have provided official predictions for the total cross sections of t- and s-channel tH production, to be used as a reference by the HEP community at the LHC Run II. The numbers have been collected and published in the fourth technical report of the LHCHXSWG [19], together with instructions and recommendations for generating event samples.

Finally, we have shown results (total cross sections as well as a few representative distributions) for the case where an explicit CP mixing is present in the coupling between the top quark and the Higgs boson, making it clear that in this case the t-channel Higgs production in association with a single top can provide complementary and very valuable information to the one extracted from $t\bar{t}H$, thereby promoting the study of tH in fully-fledged experimental analyses. This process will play a key role during Run II and beyond to exclude the (CP-conserving) case of a flipped-sign top Yukawa coupling, and to constrain CP mixing in the same interaction.

Chapter 6

Higgs, single top and W boson associated production

In this chapter we study Higgs boson production in association with a top quark and a W boson at the LHC, at NLO accuracy in QCD, and also matching short-distance events to a parton shower (NLO+PS). First we present results in the SM, and then we study the sensitivity to a non-Standard-Model relative phase between the Higgs couplings to the top quark and to the W boson.

At NLO in QCD, tWH interferes with $t\bar{t}H$ and a procedure to meaningfully separate the two processes needs to be employed. In order to define tWH production for both total rates and differential distributions, we consider the *diagram removal* (DR) and *diagram subtraction* (DS) techniques that have been previously proposed for treating intermediate resonances at NLO, in particular in the context of tW production. These techniques feature approximations that need to be carefully taken into account when theoretical predictions are compared to experimental measurements. To this aim, we first critically revisit the tW process, for which an extensive literature exists and where an analogous interference with $t\bar{t}$ production takes place. We then provide robust results for total and differential cross sections for both tW and tWH at 13 TeV. We formulate a reliable prescription to estimate the theoretical uncertainties, including those associated to the very definition of the process at NLO.

The chapter is organised as follows: in section 6.1 we introduce the main features of the processes under study; in particular, we discuss the problem of overlap with top-pair production, and the common approaches and techniques that can be employed to tackle it. In section 6.2 we review the definition of the techniques that can be employed to produce results in the five-flavour scheme (5FS) at NLO, notably the local DR and DS techniques used to generate events. At the end of this section, we also summarise the rationale we use to validate the results obtained with these techniques. In section 6.3 we describe the setup and input parameters for NLO simulations, including parton-shower matching. In section 6.4 we discuss total rates and differential distributions for the SM tW process at the LHC; first at the inclusive level, and then after applying fiducial cuts to isolate tW from $t\bar{t}$. In section 6.5 we discuss analogous results for the SM tWH process at the LHC; then, we also study the effects of a BSM CP-mixing top Yukawa coupling. In section 6.6 we summarise the main results presented in this chapter.

The results collected in this chapter are based on the work published in [18], which provides the first study of tWH hadroproduction at NLO-QCD accuracy in the 5FS. Accurate predictions for tWH are not only important for the measurement of tWH itself, but also as a possible background to tH production, and in view of the observation of $t\bar{t}H$ and of the consequent extraction of Higgs couplings.

6.1 Approaches to compute *tWH* at NLO

Exactly as when no Higgs is present in the final state, top quark and Higgs boson associated production can proceed either via a top pair production mediated by QCD interactions, or as a single top (anti-)quark process mediated by electroweak interactions, as we have already remarked in Chapter 5. There we have already shown that EW tH production, despite being characterised by much smaller cross sections with respect to the QCD production, displays a richness and peculiarities that make it phenomenologically very interesting. We recall that single-top production (in association with a Higgs boson) can be conveniently classified in three main channels: t-channel, s-channel (depending on the virtuality of the intermediate W boson) and $tW(H)$ associated production. For the first two channels, this classification is unambiguous only up to NLO accuracy in the 5FS; beyond NLO, the two processes interfere and cannot be uniquely separated. The associated $tW(H)$ production, on the other hand, can easily be defined only at LO accuracy and in the 5FS, *i.e.* through the partonic process $gb \to tW(H)$. At NLO, real corrections of the type $gg \to tWb(H)$

arise that can feature a resonant $\bar{t}$ in the intermediate state and therefore overlap with $gg \to t\bar{t}(H)$, *i.e.* with $t\bar{t}(H)$ production at LO. This would not be necessarily a problem per se, were it not for the fact that the cross section of $t\bar{t}(H)$ is one order of magnitude larger than $tW(H)$, and usually it is generated separately in the on-shell approximation. Therefore, the $t\bar{t}(H)$ contribution needs not to be double counted in the $tW(H)$ process; however, its subtraction – which can only be achieved within some approximation – leads to ambiguities that have to be carefully estimated, and entails both conceptual issues and practical complications.

A fully consistent and theoretically satisfying treatment of resonant contributions can be achieved by starting from the complete final state $WbWb(H)$ in the four-flavour scheme (4FS), including all contributions, *i.e.* doubly, singly and non-resonant diagrams. Employing the complex-mass scheme [199,200] to deal with the finite width of the top quark guarantees the gauge invariance of the amplitude and the possibility of consistently going to NLO accuracy in QCD. This approach has been followed already for $WbWb$ and other processes calculations at NLO [201–206]. Recent advances have also proven that these calculations can be consistently matched to parton showers (PS) [207–209]. However, from the practical point of view, such calculations are computationally very expensive and would entail the generation of large samples with resonant and non-resonant contributions, as well as their interference. This approach does not allow to distinguish between top-pair and single-top production in the event generation. One would then need to generate signal and background together in the same sample (a procedure that entails complications from the experimental point of view, for example in data-driven analyses) and communicate experimental results and their comparison with theory only via fiducial cross sections measurements. In any case, results for $WbWbH$ are currently available at NLO accuracy only with massless b quarks [210], and therefore cannot be used for studying tWH.

A more pragmatic solution is to adopt a 5FS, define final states in terms of on-shell top quarks and remove overlapping contributions; the last point needs to be achieved by controlling the ambiguities to a level such that the NLO accuracy of the computation is not spoiled, and total cross section as well as differential distributions can be meaningfully defined. To this aim, several techniques have been developed with a different degree of flexibility, some being suitable only to evaluate total cross sections, others being employable in event generators. They have been applied to tW production and to the production of particles in SUSY or in other extensions of the SM, where the problem of resonances appearing in higher-order corrections is recurrent. Two main classes of such techniques exist for event generation, and they are generally dubbed diagram removal (DR) and diagram subtraction (DS). Unavoidably, all these approaches have their own shortcomings, some of them of more theoretical nature, such as possible violation of gauge invariance (which, however, turns out not to be worrisome), or ambiguities in the far off-shell regions which need to be kept into account and studied on a process-by-process basis. An important point of the 5FS approach is that the combination of the separate $t\bar{t}(H)$ and $tW(H)$ results ought not to depend on the technical details used to define the $tW(H)$ contribution, in the limit where overlapping is correctly removed and possible theoretical ambiguities are under control. In practice, the most common approach is to organise the perturbative expansion in poles of the top propagator, where $t\bar{t}(H)$ production is computed with on-shell top quarks (this approach can also be used in the 4FS [201–203, 205]). In this case, the complementary $tW(H)$ contribution should encompass all the remaining effects, *e.g.* including the missing interference with $t\bar{t}(H)$ if that is not negligible. We are interested in finding a practical and reliable procedure to generate $tW(H)$ events under this scenario.

At this point, we stress that even though our first aim is to address tWH hadroproduction at NLO in the 5FS, a preliminary critical review of the tW process is certainly useful. The relevance of which approach ought to be used to describe tW production is far from being only of academic interest: already during the Run I, single-top production has been measured by both ATLAS and CMS in the t-channel [211–214], s-channel [215, 216] and tW [217–219] modes. In particular, in tW analyses the difference between the two aforementioned methods, DR and DS (without including the $t\bar{t}$–tW interference), has been added to the theoretical uncertainties. In view of the more precise measurements at the Run II, a better understanding of the $t\bar{t}$–tW overlap is desirable, in order to avoid any mismodelling of the process and incorrect estimates of the associated theoretical uncertainties, both in the total cross section and in the shape of distributions. Furthermore, given the large amount of data expected at Run II and beyond, a measurement aimed at studying the details of the $t\bar{t}$–tW interference may become feasible, and this gives a further motivation to study the best modelling strategy. Finally, a sound understanding of tW production will also be beneficial for the numerous analyses which involve $t\bar{t}$ production as a signal or as background. This is particularly true in analyses looking for a large number of jets in the final state, which typically employ Monte Carlo samples based on NLO merged [220–222] events, where stable top quarks are produced together with extra jets ($t\bar{t} + nj$). In this case, all kinds of non-top-pair contributions, like tW, need to be generated separately. While these effects are expected to be subdominant, their importance has still to be assessed and may become relevant after specific cuts, given also

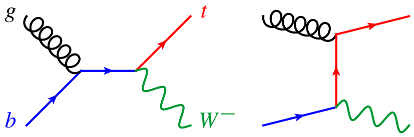

Figure 6.1: LO Feynman diagrams for tW^- production in the 5FS.

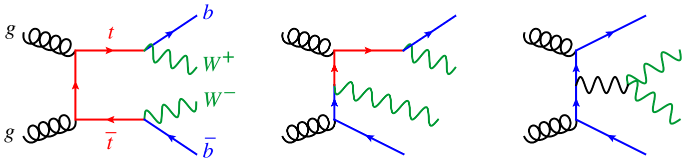

($\mathcal{A}_{2t}$) ($\mathcal{A}_{1t}$) ($\mathcal{A}_{0t}$)

Figure 6.2: Examples of doubly resonant (left), singly resonant (centre) and non-resonant (right) diagrams contributing to $WbWb$ production. The first two diagrams on the left (with the t line cut) describe the NLO real-emission contribution to the tW^- process.

the plethora of analyses; an example can be the background modelling in $t\bar{t}H$ or tH searches. Note that results for $WbWb$ plus one jet have been recently published [223, 224], but the inclusion of extra radiation in merged samples is much more demanding if one starts from the $WbWb$ final state, and thus may be impractical. Last but not least, a reliable 5FS description of tW is desirable in order to assess residual flavour-scheme dependence between the 4FS ($WbWb$) and the 5FS ($t\bar{t} + tW$) modelling of this process. Such a comparison can offer insights on the relevance of initial-state logarithms resummed in the bottom-quark PDF, which are an important source of theoretical uncertainty.

6.2 Subtraction of the top quark pair contribution

As discussed in the introduction, the computation of higher-order corrections to $tW(H)$ requires the isolation of the $t\bar{t}(H)$ process, and its consequent subtraction. In this section we review the techniques to remove such a resonant contribution which appears in the NLO real emissions of the $tW(H)$ process.

In the case of fixed-order calculations, and in particular when only the total cross section is computed, a *global subtraction* (GS) of the on-shell top quark can be employed, which just amounts to the subtraction of the total cross section for $t\bar{t}(H)$ production times the $t \to bW$ branching ratio [225, 226]:

$$\sigma^{\mathrm{GS}}_{\mathrm{NLO}}(tW(H)) = \lim_{\Gamma_t \to 0} \left[\sigma_{\mathrm{NLO}}(tW(H)) - \sigma_{\mathrm{LO}}(t\bar{t}(H)) \frac{\Gamma(t \to Wb)}{\Gamma_t} \right] , \tag{6.1}$$

where $\Gamma(t \to Wb)$ is the physical width, while Γ_t is merely a regulator introduced in the resonant top-quark propagator, and gauge invariance is ensured in the $\Gamma_t \to 0$ limit. A conceptually equivalent version, that can be applied *locally* in the virtuality of the resonant particle and in an analytic form,[1] has been employed in the NLO computations for pair production of supersymmetric particles [227, 228] and for charged Higgs boson production [229, 230].

On the other hand, NLO+PS simulations require a subtraction which is *fully local* in the phase space. In order to achieve such a local subtraction, two main schemes have been developed, known as *diagram removal* (DR) and *diagram subtraction* (DS) [231]. These subtraction schemes have been studied in detail for tW production matched to parton shower in MC@NLO [231, 232] and in POWHEG [233], as well as in the case of tH^- [234] and for supersymmetric particle pair production [235–238].

To keep the discussion as compact as possible, we focus on tW production (see Fig. 6.1 for the LO diagrams) and consider the specific case of the $tW^-\bar{b}$ real emission and of its overlap with $t\bar{t}$ production. The extension to the process with an extra Higgs boson is straightforward. Strictly speaking, one should consider $t\bar{t}$ and $tW^-\bar{b}$ ($\bar{t}W^+b$) processes as doubly resonant and singly resonant contributions to $WbWb$ production, which also contains the set of non-resonant diagrams as shown in Fig. 6.2. However, as discussed in detail in Appendix F, the contribution from non-resonant $WbWb$ production and off-shell effects for the final-state top quark are tiny, as well as possible gauge-dependent effects due to the introduction of a finite top width. Therefore, we will treat one top quark as a final-state particle with zero width, so that the only intermediate resonance appears in top-pair amplitudes. The squared matrix element for producing a $tW^-\bar{b}$ final state can be written as

$$\begin{aligned} |\mathcal{A}_{tWb}|^2 &= |\mathcal{A}_{1t} + \mathcal{A}_{2t}|^2 \\ &= |\mathcal{A}_{1t}|^2 + 2\mathrm{Re}(\mathcal{A}_{1t}\mathcal{A}^*_{2t}) + |\mathcal{A}_{2t}|^2 , \end{aligned} \tag{6.2}$$

where $\mathcal{A}_{1t}$ denotes the single-top amplitudes, considered as the real-emission corrections to the tW process, while $\mathcal{A}_{2t}$ represents the resonant top-pair amplitudes describing $t\bar{t}$ production, where the intermediate $\bar{t}$ can go on-shell. The corresponding representative Feynman diagrams are shown in Fig. 6.2. In the following, we will discuss the DR and DS techniques in detail.

---

[1] It differs only by tiny boundary effects, see [227].

DR (diagram removal): Two different version of DR have been proposed in the literature:

- **DR1 (without interference):** This was firstly proposed in [231] for tW production and its implementation in MC@NLO. One simply sets $\mathcal{A}_{2t} = 0$, removing not only $|\mathcal{A}_{2t}|^2$, which can be identified with $t\bar{t}$ production, but also the interference term $2\mathrm{Re}(\mathcal{A}_{1t}\mathcal{A}^*_{2t})$, so that the only contribution left is

  $$|\mathcal{A}_{tWb}|^2_{\mathrm{DR1}} = |\mathcal{A}_{1t}|^2 \,. \tag{6.3}$$

  This technique is the simplest from the implementation point of view and, since diagrams with intermediate top quarks are completely removed from the calculation, it does not need the introduction of any regulator.

- **DR2 (with interference):** This second version of DR was firstly proposed in [227] for squark-pair production. In this case, one removes only $|\mathcal{A}_{2t}|^2$, keeping the contribution of the interference between singly and doubly resonant diagrams

  $$|\mathcal{A}_{tWb}|^2_{\mathrm{DR2}} = |\mathcal{A}_{1t}|^2 + 2\mathrm{Re}(\mathcal{A}_{1t}\mathcal{A}^*_{2t}) \,. \tag{6.4}$$

  Note that the DR2 matrix element is not positive-definite, at variance with DR1. In this case, while the integral is finite even with $\Gamma_t \to 0$, in practice one has to introduce a finite Γ_t in the amplitude $\mathcal{A}_{2t}$ in order to improve the numerical stability of the phase-space integration.

An important remark concerning the DR schemes is that, as they are based on removing contributions all over the phase space, they are not gauge invariant. However, for tW the issue was investigated in detail in [231], and effects due to gauge dependence have been found to be negligible. We have confirmed this finding for both tW and tWH in a different way, and we discuss the details in Appendix F, where we show that gauge dependence is not an issue if one uses a covariant gauge, such as the Feynman gauge implemented in MadGraph5_aMC@NLO.

DS (diagram subtraction): DS methods, firstly proposed for the MC@NLO tW implementation, have been developed explicitly to avoid the problem of gauge dependence, which, at least in principle, affects the DR techniques. The DS matrix element is written as

$$|\mathcal{A}_{tWb}|^2_{\mathrm{DS}} = |\mathcal{A}_{1t} + \mathcal{A}_{2t}|^2 - \mathcal{C}_{2t} \,, \tag{6.5}$$

where the local subtraction term $\mathcal{C}_{2t}$, by definition, must [231, 233]:

1. cancel exactly the resonant matrix element $|\mathcal{A}_{2t}|^2$ when the kinematics is exactly on top of the resonant pole;
2. be gauge invariant;
3. decrease quickly away from the resonant region.

Given the above conditions, a subtraction term can be written as

$$\mathcal{C}_{2t}(\{p_i\}) = f(p_{Wb}^2)\left|\mathcal{A}_{2t}(\{q_i\})\right|^2, \tag{6.6}$$

where $p_{Wb} = (p_W + p_b)$, and $\{p_i\}$ is the set of momenta of the external particles (*i.e.* the phase-space point), while $\{q_i\}$ are the external momenta after a reshuffling that puts the internal anti-top quark on mass-shell, *i.e.*

$$\{q_i\} \ : \ q_{Wb}^2 \equiv (q_W + q_b)^2 = m_t^2 \, . \tag{6.7}$$

Such a reshuffling is needed in order to satisfy gauge invariance of $\mathcal{C}_{2t}$, which in turn implies gauge invariance of the DS matrix element of Eq. (6.5) in the $\Gamma_t \to 0$ limit. There is freedom to choose the prefactor $f(p_{Wb}^2)$, and the Breit–Wigner profile is a natural option to satisfy the third condition. Here, we consider two slightly different Breit–Wigner distributions:

- **DS1:**

  $$f_1(s) = \frac{(m_t\Gamma_t)^2}{(s-m_t^2)^2 + (m_t\Gamma_t)^2}\,, \tag{6.8}$$

  which is just the ratio between the two Breit–Wigner functions for the top quark computed before and after the momenta reshuffling, as implemented in MC@NLO and POWHEG for tW [231, 233].

- **DS2:**

  $$f_2(s) = \frac{(\sqrt{s}\,\Gamma_t)^2}{(s-m_t^2)^2 + (\sqrt{s}\,\Gamma_t)^2}\,. \tag{6.9}$$

  This off-shell profile of the resonance differs from DS1 by the replacement $m_t\Gamma_t \to \sqrt{s}\,\Gamma_t$ [24, 239]. The exact shape of a resonance may be process-dependent, and in the specific case of $tW(H)$ we find that this profile is in better agreement than DS1 with the off-shell lineshape of the amplitudes $|\mathcal{A}_{2t}|^2$ (away from Wb threshold), as can be seen in Fig. 6.3. In particular, we have checked that the agreement between the $|\mathcal{A}_{2t}|^2$ profile and the $\mathcal{C}_{2t}$ subtraction term in DS2 holds for the separate $q\bar{q}$ and gg channels; at least

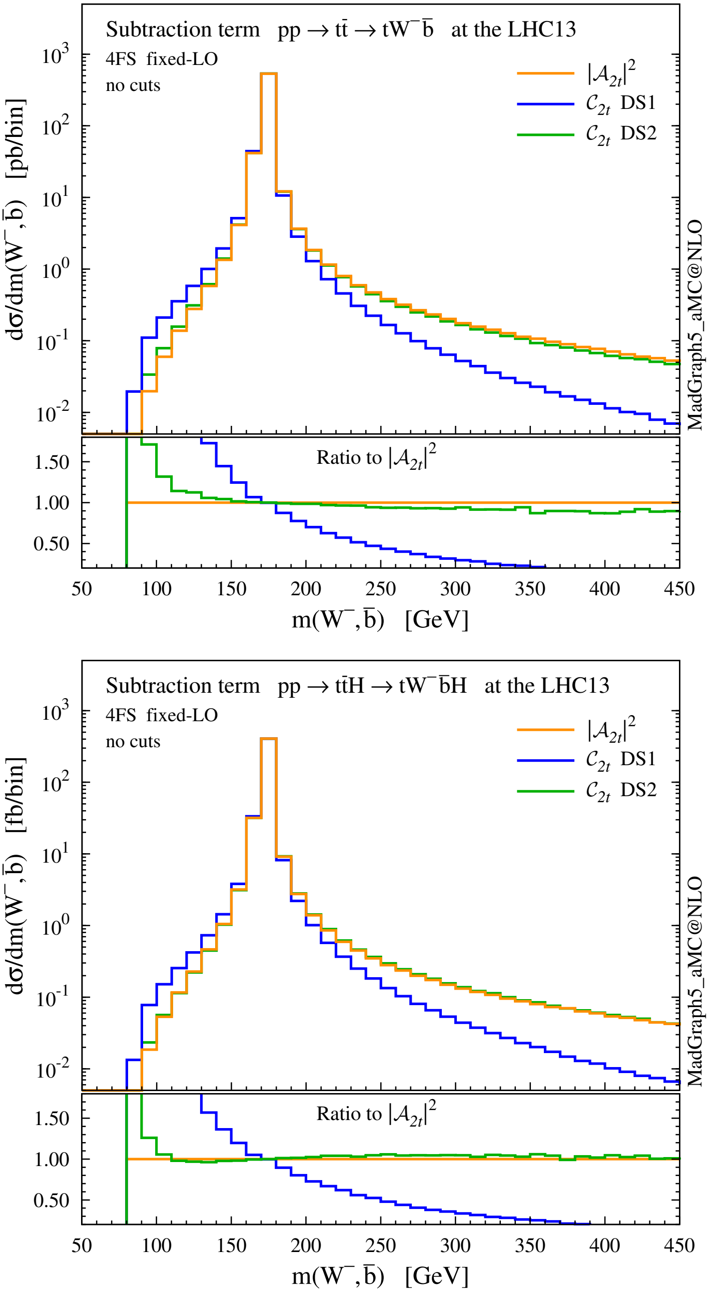

Figure 6.3: Invariant mass $m(W^-,\bar{b})$ distributions in the $pp \to tW^-\bar{b}$ process (top) and in the $pp \to tW^-\bar{b}H$ process (bottom), for comparison between $|\mathcal{A}_{2t}|^2$ and $\mathcal{C}_{2t}$ with two different Breit–Wigner forms, DS1 and DS2.

> in the $q\bar{q}$ channel there is no gauge-related issue, off-shell effects in top-pair production are correctly described by $|\mathcal{A}_{2t}|^2$, and DS2 captures these effects better. As it will be shown later, this modification in the resonance profile leads to appreciable differences between the two DS methods at the level of total cross sections as well as differential distributions.

Apart from the different resonance lineshapes, another important remark on DS is about the reshuffling of the momenta. Such a reshuffling is not a Lorentz transformation, since it changes the mass of the Wb system, therefore different momenta transformations could result in different subtraction terms. Actually, there is an intrinsic arbitrariness in defining the on-shell reshuffling, potentially leading to different counterterms and effects. Thus, on the one hand DS ensures that gauge invariance is preserved in the $\Gamma_t \to 0$ limit, at variance with DR. On the other hand, it introduces a possible dependence on how the on-shell reshuffling is implemented, which is not present in the DR approach and needs to be carefully assessed. To our knowledge, this problem has not been discussed in depth in the literature. Here, we adopt the reshuffling employed by MC@NLO and POWHEG [231,233], where the recoil is shared democratically among the initial-state particles, also rescaling by the difference in parton luminosities due to the change of the partonic centre-of-mass energy.

Finally, we comment on the introduction of a non-zero top-quark width in the DR2 and DS methods. In order to regularise the singularity of $\mathcal{A}_{2t}$, we have to modify the denominator of the resonant top-quark propagators as

$$\frac{1}{p_{Wb}^2 - m_t^2} \to \frac{1}{p_{Wb}^2 - m_t^2 + i m_t \Gamma_t} \,. \tag{6.10}$$

At variance with the case of a physical resonance, here Γ_t is just a mathematical regulator that does not necessarily need to be equal to the physical top-quark width.[2] In fact, one can set it to any number that satisfies $\Gamma_t/m_t \ll 1$ without affecting the numerical result in a significant way [235, 237]. We have checked that the NLO DR2 and DS codes provide stable results with Γ_t in the interval between 1.48 GeV and 0.001 GeV.[3]

After all the technical details exposed in this section, we summarise the key points that illustrate our rationale in assessing the results in the next sections:

---

[2] A modified version of DS (DS*), which requires to know the analytic structure of the poles over each integration channel, was proposed in [237] to guarantee gauge invariance already with a finite width. In practice, there is no difference between DS and DS* if Γ_t is small enough.

[3] However, the computational time does depend on this regulator, because the smaller is Γ_t the larger are the numerical instabilities, resulting in a slower convergence of the integration. For this reason, the results presented in the paper have been generated setting this regulator close to the physical value of the top width at LO, $\Gamma_t \simeq 1.48$ GeV.

- Our starting point is to assume the (common) case where results for $t\bar{t}(H)$ production are generated with on-shell top quarks. Resonance profile and correlation among production and decay are partially recovered from the off-shell LO amplitudes with decayed top quarks, following the procedure illustrated in [60]. In particular, after this procedure the on-shell production cross section is not changed.
- The GS procedure is gauge invariant and ensures that all and just the on-shell $t\bar{t}(H)$ contribution is subtracted. Thus, under the working assumptions in the previous point, GS provides a consistent definition of the missing $tW(H)$ cross section, that can be combined with $t\bar{t}(H)$ without any double counting and including all the remaining effects, such as interference. A local subtraction scheme should return a cross section close to the GS result *if off-shell and gauge-dependent effects are small.*
- DS is gauge invariant by construction. The difference between the GS and DS cross sections can thus quantify off-shell effects in the decayed $t\bar{t}(H)$ amplitudes. From Fig. 6.3 and the related discussion, we already find DS2 to provide a better treatment than DS1 in the subtraction of the off-shell $t\bar{t}(H)$ contribution; the difference between DS1 and DS2 quantifies the impact of different off-shell profiles.
- DR is in general gauge dependent. The difference between GS and DR2 amounts to the impact of possible gauge-dependent contributions and off-shell effects. As it will be shown, for the tW and tWH processes this difference is tiny. Finally, the difference between DR2 and DR1 amounts to the interference effects between $t\bar{t}(H)$ and $tW(H)$; the single-top process is well defined *per se* only if the impact of interference is small.

As a last comment, we already argue that in practice gauge dependence in DR should not be an issue in our case. When using a covariant gauge and only transverse external gluons, any gauge-dependent term decouples from the $gg \to tWb$ amplitudes [231], and this remains valid also after adding a Higgs. An independent constraint on gauge-dependent effects comes also from the off-shell profiles in Fig. 6.3. In the $q\bar{q}$ channel, $|\mathcal{A}_{2t}|^2$ is free from gauge dependence and validates the $\mathcal{C}_{2t}$ DS2 off-shell profile for $tW(H)$; the gauge-invariant DS2 counterterm continues to agree with $|\mathcal{A}_{2t}|^2$ also in the gg channel, which in turn limits the size of alleged gauge-dependent effects in DR2. Moreover, even in the case of a significant gauge dependence, its effects should cancel out in a consistent combination of $t\bar{t}(H)$ and $tW(H)$ events, if the off-shell amplitudes used to decay $t\bar{t}(H)$ have been computed in the same gauge as $tW(H)$.

6.3 Setup of the NLO+PS simulation

The code and events for tW production at hadron colliders at NLO-QCD accuracy can be generated in the MadGraph5_aMC@NLO framework by issuing the following commands:

```
> import model loop_sm-no_b_mass
> generate p p > t w- [QCD]
> add process p p > t~ w+ [QCD]
> output
> launch
```

and analogous ones for tWH production (`p p > t w- h`, `p p > t~ w+ h`).

The output of these commands contains, among the NLO real emissions, the tWb amplitudes that have to be treated with DR or DS. The technical implementation of DR1 (no interference) in the NLO code simply amounts to edit the relevant `matrix_*.f` files, setting to zero the top-pair amplitudes. To implement DR2, on the other hand, one subtracts the square of the top-pair amplitudes from the full matrix element. A subtlety is that the top-pair amplitudes (and only those) need to be regularised by introducing a non-zero width in the top-quark propagator. Note that, as we have already remarked in sec. 6.2, this width is just a mathematical regulator. The DS is more complicated, since it also requires the implementation of the momenta reshuffling to put the top quark on-shell before computing the subtraction term $\mathcal{C}_{2t}$.

In our numerical simulations we set the Higgs mass to $m_H = 125.0$ GeV and the mass of the top quark to $m_t = 172.5$ GeV, which are the reference values used by the ATLAS and CMS collaborations at the present time in Monte Carlo generations. We renormalise the top Yukawa coupling on-shell by setting it to $y_t/\sqrt{2} = m_t/v$, where $v \simeq 246$ GeV is the electroweak vacuum expectation value, computed from the Fermi constant $G_F = 1.16639 \cdot 10^{-5}$ GeV^{-2}; the electromagnetic coupling is also fixed to $\alpha = 1/132.507$. The W and Z boson masses are set to $m_W = 80.419$ GeV and $m_Z = 91.188$ GeV. In the 5FS the bottom-quark mass is set to zero in the matrix element, while $m_b = 4.75$ GeV determines the threshold of the bottom-quark parton distribution function (PDF), which affects the parton luminosities.[4] We have found the contributions proportional to the bottom Yukawa coupling to be negligible, therefore we have set $y_b = 0$ as well.

---

[4] In the 4FS simulations presented in Appendix F m_b enters the calculation of the hard-scattering matrix elements and the phase space.

The proton PDFs and their uncertainties are evaluated employing reference sets and error replicas from the NNPDF3.0 global fit [185], at LO or NLO as well as in the 5FS or 4FS (4FS numbers are shown in Appendix F). The value of the strong coupling constant at LO and NLO is set to $\alpha_s^{(5\mathrm{F},\mathrm{LO})}(m_Z) = 0.130$ and, respectively, $\alpha_s^{(5\mathrm{F},\mathrm{NLO})}(m_Z) = 0.118$.

The factorisation and renormalisation scales (μ_F and μ_R) are computed dynamically on an event-by-event basis, by setting them equal to the reference scale $\mu_0^d = H_T/4$, where H_T is the sum of the transverse masses of all outgoing particles in the matrix element. The scale uncertainty in the results is estimated varying μ_F and μ_R independently by a factor two around μ_0. Additionally, we also show total cross sections computed with a static scale, which we fix to $\mu_0^s = (m_t + m_W)/2$ for tW production and to $\mu_0^s = (m_t + m_W + m_H)/2$ for tWH.

We use a diagonal CKM matrix with $V_{tb} = 1$, ignoring any mixing between the third generation and the first two. In particular, this means that the top quark always decays to a bottom quark and a W boson, $\mathrm{BR}(t \to bW) = 1$, with a width computed at LO in the 5FS equal to $\Gamma_t = 1.4803$ GeV.[5] Spin correlations can be preserved by decaying the events with MadSpin [61], following the procedure presented in [60]. We choose to leave the W bosons stable, because we focus on the behaviour of the b jets stemming either from the top decay or from the initial-state gluon splitting.

Short-distance events are matched to the Pythia8 parton shower [177] by using the MC@NLO method [55]. Jets are defined using the anti-k_T algorithm [40] implemented in FastJet [120], with radius $R = 0.4$, and required to have

$$p_T(j) > 20\,\mathrm{GeV}\,, \quad |\eta(j)| < 4.5\,. \tag{6.11}$$

A jet is b-tagged if a b hadron is found among its constituents (we ideally assume 100% b-tagging efficiency in our studies). The same kinematic cuts are applied for b jets as for light flavour jets in the inclusive study. In the fiducial phase space, on the other hand, a requirement on the pseudorapidity of

$$|\eta(j_b)| < 2.5 \tag{6.12}$$

is imposed, resembling acceptances of b-tagging methods employed by the experiments.

---

[5] In the 4FS, due to a non-zero bottom mass, the LO width is slightly reduced to $\Gamma_t = 1.4763$ GeV.

6.4 tW production

In this section we review NLO+PS results for tW production at the LHC, running with a centre-of-mass energy $\sqrt{s} = 13$ TeV. With the shorthand tW we mean the sum of the two processes $pp \to tW^-$ and $pp \to \bar{t}W^+$, which have the same rates and distributions at the LHC. We carefully quantify the impact of theoretical systematics in the event generation. Our discussion is split in two parts, focusing first on the inclusive event generation and the related theoretical issues, and then on what happens when fiducial cuts are applied.

6.4.1 Inclusive results

We start by showing in Fig. 6.4 the renormalisation and factorisation scale dependence of the $pp \to tW$ cross section, computed at LO and NLO accuracy, keeping the t stable. Results are obtained by employing the static and dynamic scales μ_0^s and μ_0^d (defined in sec.6.3) in the left and right plot respectively. We show results where we simultaneously vary the renormalisation and factorisation scales on the diagonal $\mu_R = \mu_F$; on top of this, for LO and NLO DR results, we also present two off-diagonal profiles where $\mu_R = \sqrt{2}\mu_F$ and $\mu_R = \mu_F/\sqrt{2}$. In the two plots we present predictions obtained employing both DR, neglecting (DR1, red) or taking into account (DR2, orange) the interference with $t\bar{t}$, and DS, with the two Breit–Wigner forms in Eq. (6.8) (DS1, blue) or in Eq. (6.9) (DS2, green). We also report results using global subtraction (GS, squares) for the static scale choice. The details for the various NLO schemes can be found in sec. 6.2. We remark that we have validated our NLO DR1 and DS1 codes against the MC@NLO code, finding very good agreement. The values of the total rate computed at the central scale μ_0 are also quoted in Table 6.1. Unlike in Fig. 6.4, in this case scale variations are computed by varying μ_F and μ_R independently by a factor two around μ_0.

As expected, NLO corrections visibly reduce the scale dependence with respect to LO predictions. Comparing DR1 and DR2, we see that interference effects are negative at this centre-of-mass energy, and reduce significantly the NLO cross section, by about 13%. Also, the cross section scale dependence is different, in particular for very small scales. This effect is driven by the LO scale dependence in $t\bar{t}$ amplitudes, which is larger at low scales. Moving to DS, we find that DS1 and DS2 predictions show a 8% difference. Therefore, the dependence on the subtraction scheme is large, being comparable to the scale uncertainty or even larger.

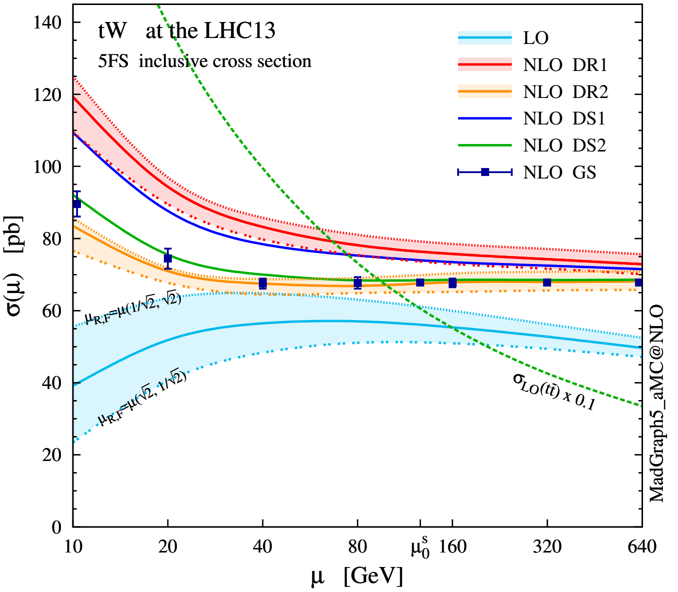

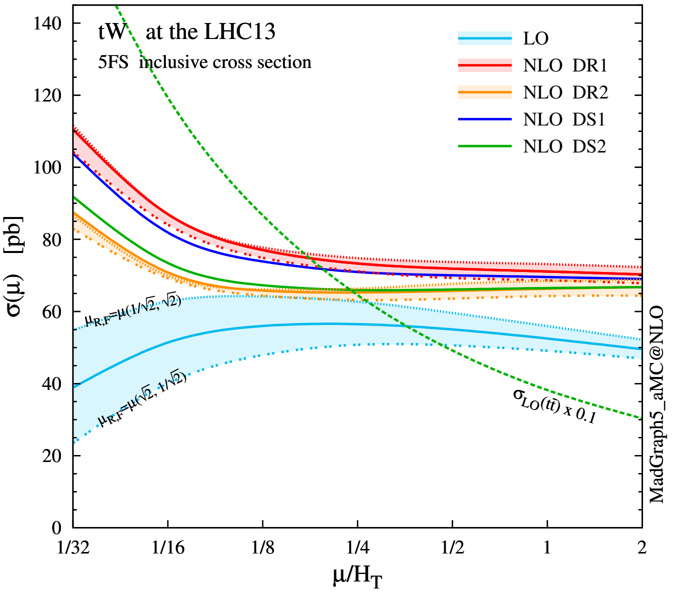

Figure 6.4: Scale dependence of the total $pp \to tW^-$ and $\bar{t}W^+$ cross section at the 13-TeV LHC, computed in the 5FS at LO and NLO. We present results for $\mu_F = \mu_R \equiv \mu$, using a static scale (top) and a dynamic one (bottom). The NLO tWb channels are treated with DR or DS. Furthermore, we show NLO GS results (only for the static scale), and two off-diagonal profiles for LO and NLO DR, ($\mu_R = \sqrt{2}\mu\,,\ \mu_F = \mu/\sqrt{2}$) and ($\mu_R = \mu/\sqrt{2}\,,\ \mu_F = \sqrt{2}\mu$). Finally, the scale dependence of $pp \to t\bar{t}$ at LO is also reported for comparison.

tW	$\sigma(\mu_0^s)$ [fb$\pm\delta_\mu^\%\pm\delta_{\rm PDF}^\%$]	K	$\sigma(\mu_0^d)$ [fb$\pm\delta_\mu^\%\pm\delta_{\rm PDF}^\%$]	K
LO	$56.07(3)\,^{+18.2}_{-17.4}\pm 8.4$	-	$56.50(6)\,^{+21.9}_{-20.9}\pm 8.4$	-
NLO DR1	$76.46(9)\,^{+6.9}_{-8.1}\pm 2.0$	1.36	$73.22(9)\,^{+5.1}_{-6.7}\pm 2.0$	1.30
NLO DR2	$67.49(9)\,^{+6.3}_{-8.1}\pm 2.0$	1.20	$65.12(9)\,^{+2.8}_{-6.8}\pm 2.0$	1.15
NLO DS1	$73.80(9)\,^{+6.7}_{-8.1}\pm 1.9$	1.32	$70.93(9)\,^{+4.0}_{-6.7}\pm 2.0$	1.26
NLO DS2	$68.28(8)\,^{+6.6}_{-8.3}\pm 2.1$	1.22	$66.09(9)\,^{+2.8}_{-6.8}\pm 1.9$	1.17
NLO GS	67.8(7)	1.21(1)		

Table 6.1: Total cross sections for $pp \to tW^-$ and $\bar{t}W^+$ at the 13-TeV LHC, in the 5FS at LO and NLO accuracy with different schemes, computed with a static scale $\mu_0^s = (m_t + m_W)/2$ and a dynamic scale $\mu_0^d = H_T/4$. We also report the scale and PDF uncertainties and the NLO-QCD K factors; the numerical uncertainty affecting the last digit is quoted in parentheses.

We note that the total rate predictions obtained with DR2 and DS2 agree rather well within uncertainties, especially at the reference scale choice, and also agree with the predictions from the GS scheme. This result is quite satisfactory because it supports some important observations. First, that the off-shell effects of the top-quark resonant diagrams are small, and indeed well described by the (gauge-invariant) parametrisation of Eq. (6.9). Second, that possible gauge dependence in DR2 is in practice not an issue if one uses a covariant gauge, where the subtraction of $|\mathcal{A}_{2t}|^2$ turns out to be very close to an on-shell gauge-invariant subtraction. On the other hand, DR1, which does not include the interference in the definition of the signal, and DS1, which has a different profile over the virtuality of the intermediate top quark, do not describe well the NLO effects and extrapolate to a biased total cross section, even in the $\Gamma_t \to 0$ limit. Thus, a third observation is that interference terms are not negligible, and it is mandatory to keep them in the definition of the tW process in order to have a complete simulation. Finally, a fourth point is that to include interference effects is not enough, but one also needs to subtract the top-pair process with an adequate profile over the phase space. This picture is confirmed at the level of differential distributions in the following discussion, and also at the total cross section level in the 4FS, see Appendix F.

We now turn to differential distributions, and we show some relevant observables in Figs. 6.5 and 6.6. Here, we employ a dynamical scale choice, $\mu_0 = H_T/4$ and we do not impose any cut on the final-state particles. Note that, for sim-

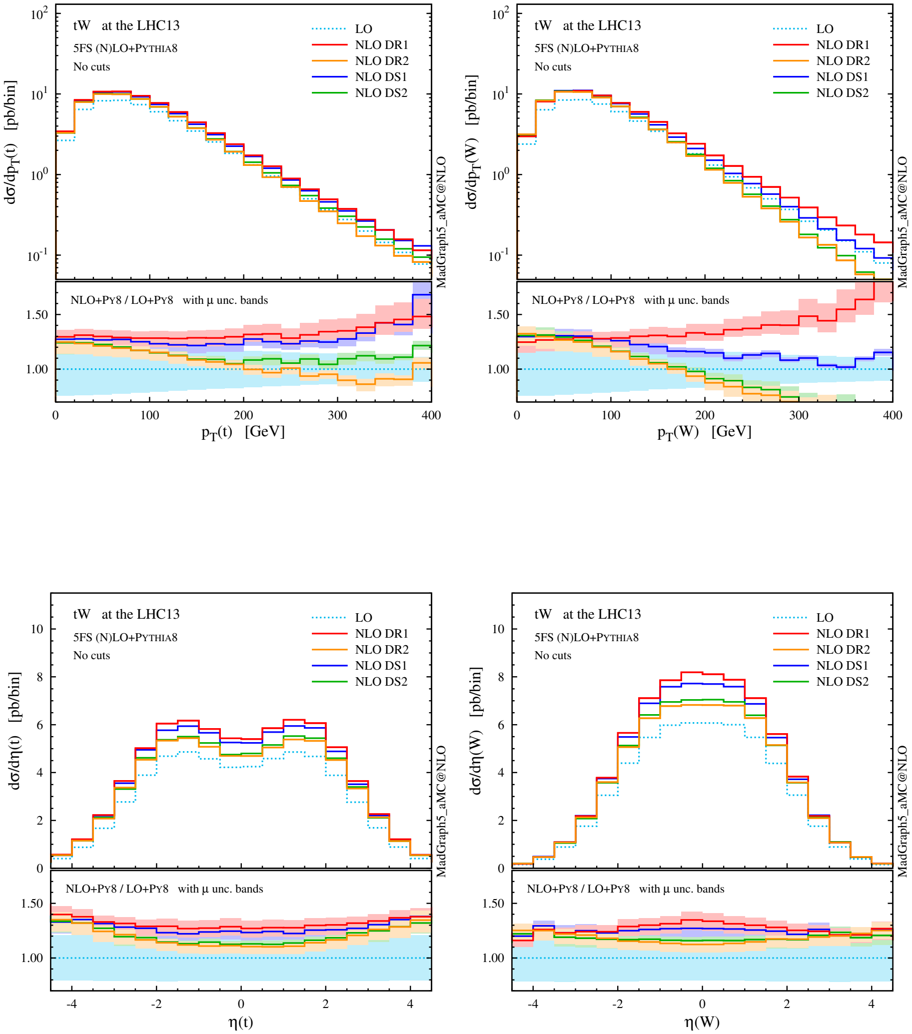

Figure 6.5: p_T and η distributions for the top quark and the W boson at NLO+PS accuracy in tW production at the 13-TeV LHC. The lower panels provide information on the differential K factors with the scale uncertainties.

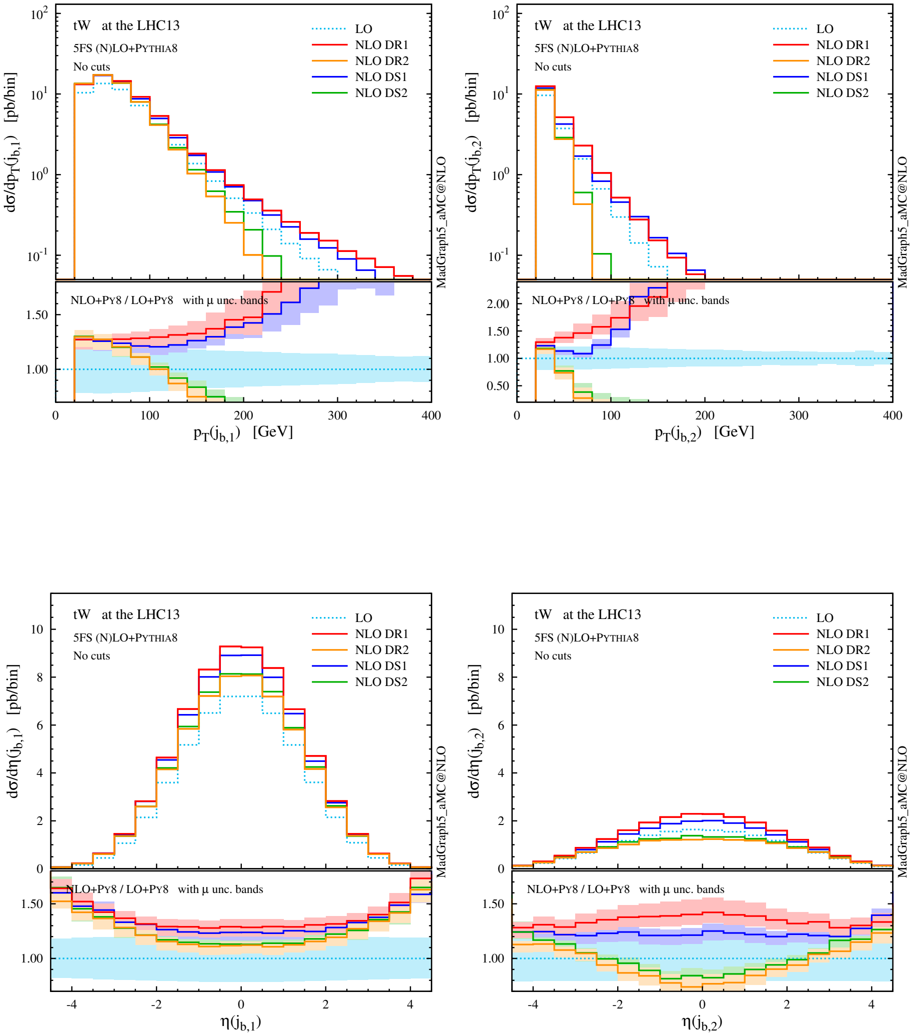

Figure 6.6: Same as Fig. 6.5, but for the b-tagged jets. Note that the second-hardest b jet is described by the parton shower at LO, while by the matrix element at NLO.

plicity and after the shorthand tW, we label as t both the undecayed top quark in tW^- production and the antitop in $\bar{t}W^+$; similarly, W indicates the W^- in the first process and W^+ in the second one, *i.e.* the boson produced in association with t, and not the one coming from the t decay. Particles (not) coming from the top decay are identified by using the event-record information. We see that the DR1 and DS1 simulations tend to produce harder and more central distributions, while the DR2 and DS2 results, very similar one another, tend to be softer and more forward. In any case, NLO corrections cannot be taken into account by the LO scale uncertainty, nor be described by a K factor, especially for the physics of b jets. The hardest b jet ($j_{b,1}$) dominantly comes from the top decay, while the second-hardest b jet is significantly softer due to the initial-state $g \to b\bar{b}$ splitting. As seen for DR2, the high-p_T W boson and b jets are highly suppressed due to the negative interference with the $t\bar{t}$ process. In fact, due to this interference the cross section can become negative in some corners of the phase space, for example in the high-p_T tail of the second b jet. We interpret this fact as a sign that tW cannot be separated from $t\bar{t}$ in this region, and the two contributions must be combined in order to obtain a physically observable (positive) cross section.

In summary, the tW–$t\bar{t}$ interference significantly affects the inclusive total rate as well as the shapes of various distributions at NLO. In particular, different schemes give rise to different NLO results, with ambiguities which in principle can be larger than the scale uncertainty. Such differences arise from two sources: the interference between resonant (top-pair) and non-resonant (single-top) diagrams, which is relevant and ought to be taken into account, and (in the case of DS) the treatment of the off-shell tails of the top-pair contribution. These ambiguities are intrinsically connected to the attempt of separating two processes that cannot be physically separated in the whole phase space. On the other hand, we have also found that two of such schemes, DR2 and DS2, give compatible results among themselves and integrate up to the total cross section defined in a gauge invariant way in the GS scheme. We are now ready to explore whether a region of phase space (possibly accessible from the experiments) exists where the two processes can be separated in a meaningful way.

6.4.2 Fiducial results

In this section we would like to investigate whether tW can be defined separately from $t\bar{t}$ at least in some fiducial region of the phase space, in the sense that in such a region interference terms between the two processes and thus theoretical ambiguities are suppressed. In practice, this goal can be achieved

$\sigma_{\rm NLO}$	No cuts	Fiducial cuts		Fiducial + top reco.	
	$[\,{\rm fb}\pm\delta_\mu^\% \pm\delta_{\rm PDF}^\%\,]$	$[\,{\rm fb}\pm\delta_\mu^\% \pm\delta_{\rm PDF}^\%\,]$	eff.	$[\,{\rm fb}\pm\delta_\mu^\% \pm\delta_{\rm PDF}^\%\,]$	eff.
$t\bar{t}$	$744.1(9)\,^{+4.8}_{-8.7}\pm1.7$	$44.9(3)\,^{+6.0}_{-9.5}\pm1.9$	0.06	$44.9(3)\,^{+6.0}_{-9.5}\pm1.9$	0.06
tW DR1	$73.22(9)\,^{+5.1}_{-6.7}\pm2.0$	$44.70(7)\,^{+4.0}_{-6.7}\pm1.9$	0.61	$41.70(7)\,^{+3.8}_{-6.8}\pm1.9$	0.57
tW DR2	$65.12(9)\,^{+2.8}_{-6.8}\pm2.0$	$43.88(8)\,^{+3.2}_{-7.0}\pm1.9$	0.67	$41.85(8)\,^{+3.7}_{-7.0}\pm1.9$	0.64
tW DS1	$70.93(9)\,^{+4.0}_{-6.7}\pm2.0$	$44.65(8)\,^{+3.8}_{-6.8}\pm1.9$	0.63	$41.90(8)\,^{+3.8}_{-6.8}\pm1.9$	0.59
tW DS2	$66.09(9)\,^{+2.8}_{-6.8}\pm1.9$	$44.05(8)\,^{+3.3}_{-6.9}\pm1.9$	0.67	$41.91(8)\,^{+3.8}_{-6.9}\pm1.9$	0.63

Table 6.2: Total cross sections in pb at the LHC 13 TeV for the $pp \to t\bar{t}$ and $pp \to tW$ processes, in the 5FS at NLO+PS accuracy. Results are presented before any cut (left), after fiducial cuts (centre), and also adding top reconstruction on the event sample (right). We also report the scale and PDF uncertainties, as well as the cut efficiency with respect to the case with no cuts. All numbers are computed with the reference dynamic scale $\mu_0 = H_T/4$, and the numerical uncertainty affecting the last digit is reported in parentheses.

by comparing results among different NLO schemes, since the difference among them provides a measure of interference effects and related theoretical systematics (gauge dependence in DR, subtraction term in DS). We remark that the following toy analysis is mainly for illustrative purposes, since the same procedure can be applied to any set of fiducial cuts defined in a real experimental analysis, also imposing a selection on specific decay products of the W bosons.

Motivated by the b-jet spectra in Fig. 6.5 and by experimental tW searches, a popular strategy to suppress the $t\bar{t}$ background as well as tW–$t\bar{t}$ interference is to select events with exactly one central b jet [217–219, 225, 232, 240]. We define our set of "fiducial cuts" for tW by selecting only events with

1. exactly one b jet with $\;p_T(j_b) > 20$ GeV $\;$ and $\;|\eta(j_b)| < 2.5\,,$
2. exactly two central W bosons with rapidity $\;|y(W)| < 2.5\,.$

In this regard we stress that the first selection is the key to suppress the contributions from $t\bar{t}$ amplitudes, hence both the pure $t\bar{t}$ "background" as well as the tW–$t\bar{t}$ interference (*i.e.* theoretical ambiguities). Note that we would like to draw general conclusions about the generation of tW events, therefore we have chosen to define a pseudo event category that does not depend on the particular decay channel of the W bosons. The second selection is added to mimic a good reconstructability of these bosons inside the detector regardless

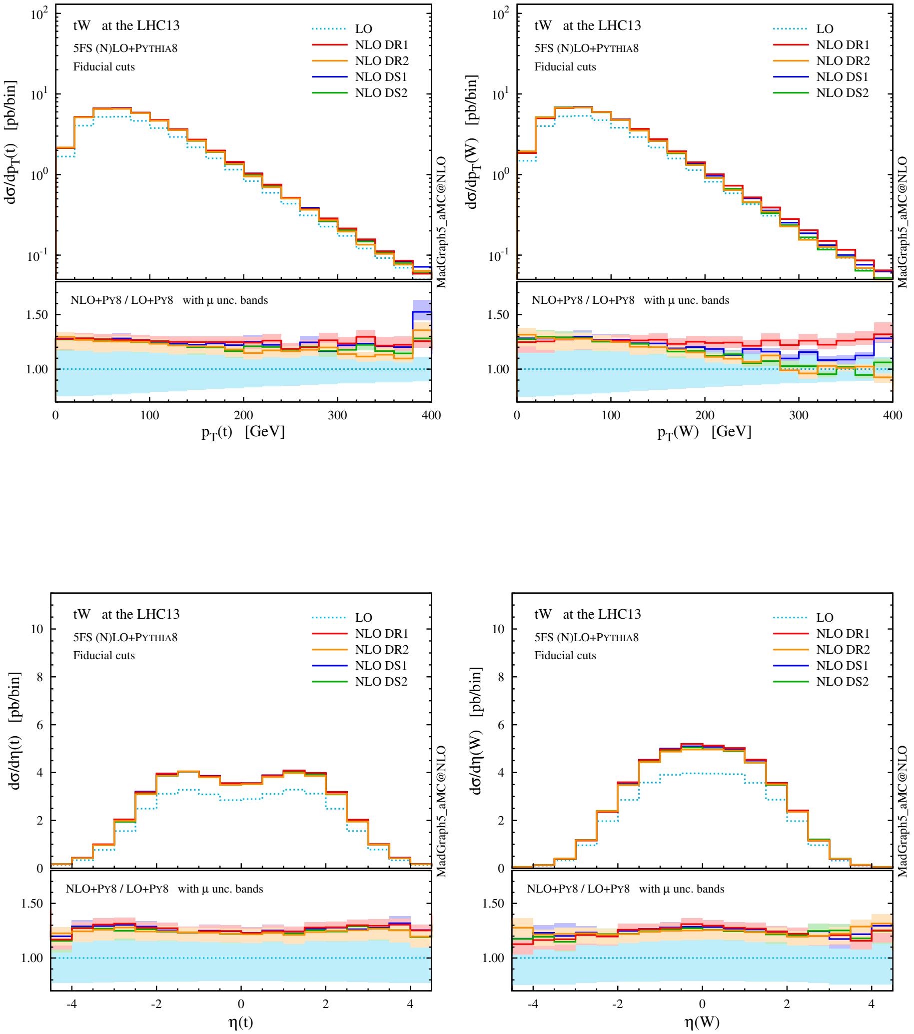

Figure 6.7: p_T and η distributions the top quark and the W boson as in Fig. 6.5, but after applying fiducial cuts to suppress the interference between tWb and $t\bar{t}$.

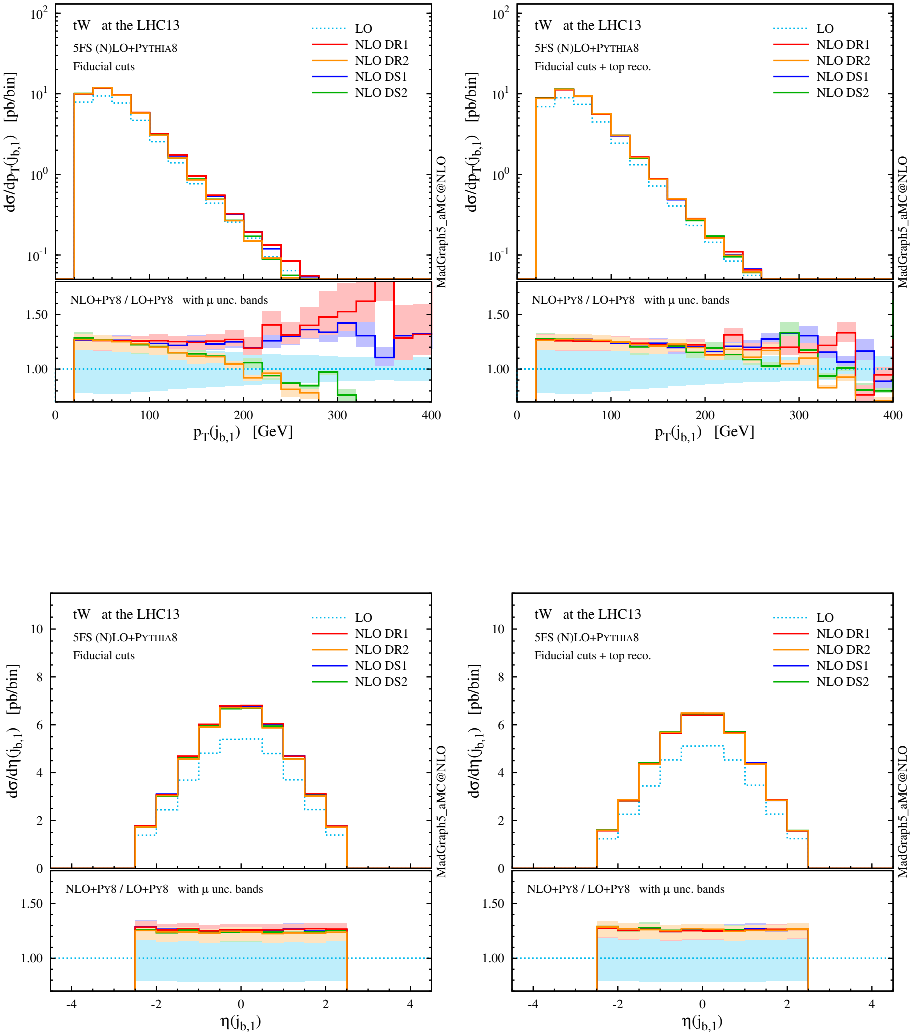

Figure 6.8: p_T and η distributions for the central b-tagged jet, after fiducial cuts are applied. In the right plots, in addition to fiducial cuts, top reconstruction is required.

of their final-state daughters; it affects less than 7% of the events surviving selection 1.

Looking at Table 6.2 we can see that, before any cut is applied, the event category is largely dominated by the $t\bar{t}$ contribution. Once the above fiducial cuts are applied, the $t\bar{t}$ contribution is reduced by more than a factor 16, while the tW rate shrinks by about just one third (for DR2 and DS2), bringing the signal-to-background ratio $\sigma(tW)/\sigma(t\bar{t})$ close to unity, which is exactly the aim of tW searches. The impact of interference has been clearly reduced by the cuts; The fiducial cross sections computed with the different NLO schemes agree much better with each other, than before selections are applied. Still, there is a minor residual difference in the rates, which amounts to about 2%.

From the distributions in Figs. 6.7 and 6.8 we can see once more an improved agreement among the different NLO schemes in the fiducial region. The lower panels show flatter and positive K factors and a lower scale dependence in the high-p_T tail than before the cuts, since we have suppressed the interference with LO $t\bar{t}$ amplitudes. Although considerably mitigated, some differences are still visible among the four schemes in the high-p_T region of the b-tagged jet $(j_{b,1})$. Monte Carlo information shows that the central b jet coincides with the one stemming from the top decay $(j_{b,t})$ for the vast majority of events. In the high-p_T region, however, the b jet can also originate from a hard initial-state $g \to b\bar{b}$ splitting, similar to the case of t-channel tH production [17].

This suggests that, if on top of the fiducial cuts we also demand the central b jet to unambiguously originate from the top quark, then we may be able to suppress even further the tW–$t\bar{t}$ interference and the related theoretical systematics. In fact, we can see from Table 6.2 and from the right plot in Fig. 6.8 that, after such a requirement is included in the event selection, the total rates as well as the distributions end up in almost perfect agreement, and one can effectively talk about tW and $t\bar{t}$ as separate processes in this region: interference effects have been suppressed at or below the level of numerical uncertainty in the predictions. A possible remark is that the top-reconstruction requirement shaves off another $\sim$ 2 pb of the cross section, *i.e.* more than the residual discrepancy between the different NLO schemes before this last selection is applied.

To summarise, a naturally identified region of phase space exists where tW is well defined, *i.e.* gauge invariant and basically independent of the scheme used (either DR1, DR2, DS1, DS2) to subtract the $t\bar{t}$ contribution. Given the fact that DS2 and DR2 also give consistent results outside the fiducial region and integrate to the same total cross section, equal to the GS one, they can both be used in MC simulations. In practice, given the fact that the gauge-dependent effects are practically small when employing a covariant gauge, and that the implementation in the code is rather easy, DR2 is certainly a very convenient scheme to use in simulations of tW production in the 5FS, including the effects of interference with the $t\bar{t}$ contribution. In addition, one can use the difference between DR1 and DR2 (*i.e.* the amount of tW–$t\bar{t}$ interference) to assess whether the fiducial region where the measurements are performed is such that the process-definition uncertainties are under control (smaller than the missing higher-order uncertainties), and to estimate the residual process-definition systematics. We have seen that requiring the presence of exactly one central b jet is a rather effective way to identify such a fiducial region. We have also found that, especially in DR2 and DS2 schemes, the perturbative series for the tW process is well behaved, NLO-QCD corrections mildly affect the shape of distributions but reduce the scale dependence considerably with respect to LO. A further handle to suppress process-definition systematics can be given by a reconstruction of the top quark, identifying the central b jet as coming from its decay. Top-tagging techniques are being developed (theoretical and experimental reviews can be found at [241] and [242, 243]), and may help to define a sharper fiducial region, although this may depend on the trade-off between the top-tagging efficiency and the amount of residual process-definition ambiguities to be suppressed.

6.5 tWH production

In this section we present novel NLO+PS results for tWH production in the 5FS at the 13-TeV LHC. Similar to what we have done for tW in the previous section, we address the theoretical systematics both at the inclusive level and with fiducial cuts. We anticipate that our findings for tWH are qualitatively similar to the ones for tW, but the larger numerical ratio between the top-pair and single-top contributions enhances the impact of interference effects and exacerbates theoretical systematics in the simulation, which are clearly visible in the t, W, H and b-jet observables. We will see that this can be alleviated after applying suitable cuts. Finally, we investigate the impact of non-SM couplings of the Higgs boson on this process.

6.5.1 Inclusive results

As for tW, we start by showing the renormalisation and factorisation scale dependence of the tWH cross section in Fig. 6.11, both at LO and NLO accuracy,

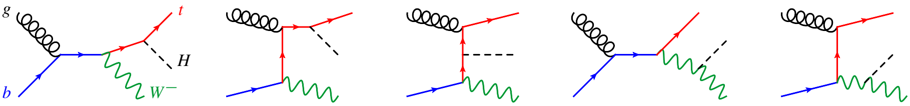

Figure 6.9: LO Feynman diagrams for tW^-H production in the 5FS.

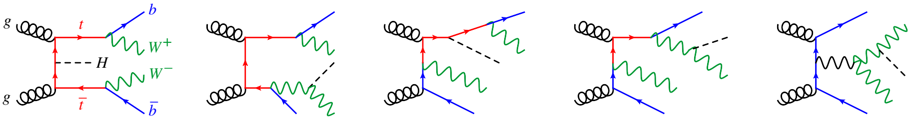

$(\mathcal{A}_{2t})$ $(\mathcal{A}_{1t})$ $(\mathcal{A}_{1t})$ $(\mathcal{A}_{0t})$ $(\mathcal{A}_{0t})$

Figure 6.10: Examples of doubly resonant (first on the left), singly resonant (second two) and non-resonant (last two) diagrams contributing to $WbWbH$ production. The first three diagrams (with the t line cut) describe the NLO real-emission contribution to the tW^-H process.

using different schemes to treat the $tWbH$ real-emission channels (the details for the various NLO schemes can be found in sec. 6.2). The values of the total rate computed at the central scale μ_0 are also quoted in Table 6.3. Unlike in Fig. 6.11, in this case scale variations are computed by varying μ_F and μ_R independently by a factor two around μ_0.

The same pattern we have found for tW is repeated. Comparing DR results obtained by neglecting (DR1, red) or taking into account (DR2, orange) interference with $t\bar{t}H$, we observe again that these interference effects are negative, but their relative impact on the cross section is even more sizeable. The interference reduces the NLO rate by about 5 fb, which amounts to a hefty -25%, leading to a K factor close to 1. Since interference effects are driven by the LO $t\bar{t}H$ contribution, they grow larger for lower scale choices. The cross sections obtained employing the two DS techniques, DS1 (blue) and DS2 (green), show large differences which go beyond the missing higher orders estimated by scale variations, and can be traced back to the different Breit-Wigner prefactor in the subtraction term $\mathcal{C}_{2t}$. As it has been the case for tW production, we find that DR2 and DS2 are in good agreement with GS.

In complete analogy with the case of the tWb channel in tW production at NLO, we perform a study of the theoretical systematics in the modelling of the $tWbH$ channel (employing the 4FS to isolate this contribution), which can be found in Appendix F.

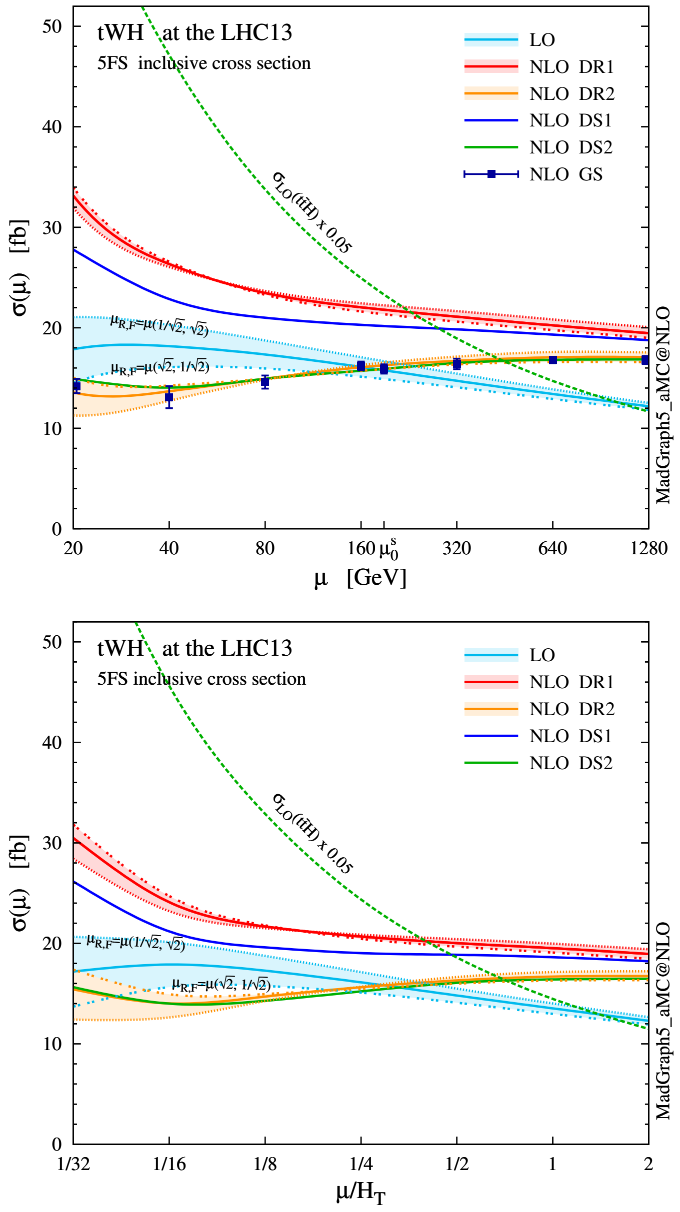

Figure 6.11: Scale dependence of the total $pp \to tW^-H$ and $\bar{t}W^+H$ cross section at the 13-TeV LHC, computed in the 5FS at LO and NLO. We present results for $\mu_F = \mu_R \equiv \mu$, using a static scale (top) and a dynamic one (bottom). The NLO $tWbH$ channels are treated with DR or DS. Furthermore, we show NLO GS results (only for the static scale), and two off-diagonal profiles for LO and NLO DR, ($\mu_R = \sqrt{2}\mu\,,\ \mu_F = \mu/\sqrt{2}$) and ($\mu_R = \mu/\sqrt{2}\,,\ \mu_F = \sqrt{2}\mu$). Finally, the scale dependence of $pp \to t\bar{t}H$ at LO is also reported for comparison.

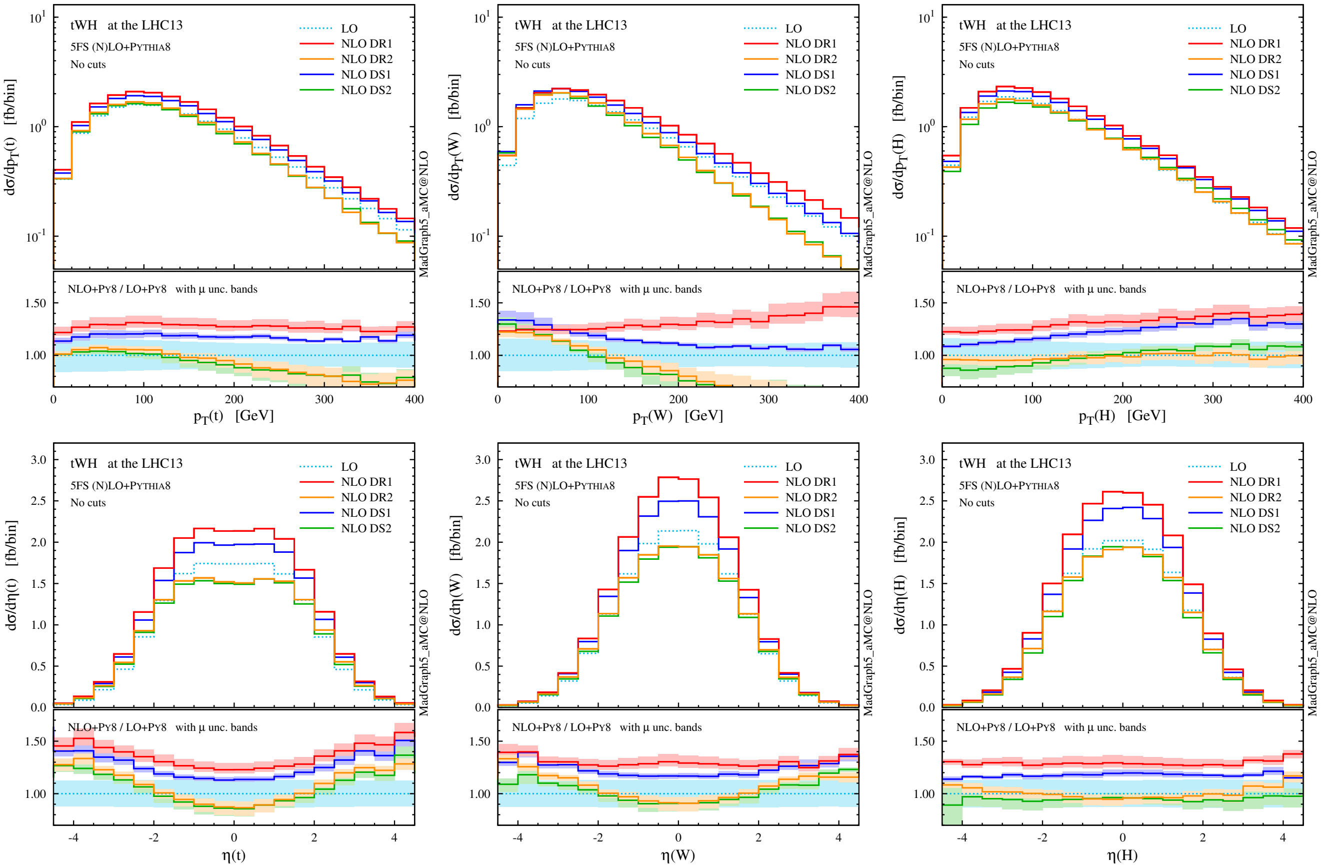

Figure 6.12: p_T and η distributions for the top quark, the W boson and the Higgs boson at NLO+PS accuracy in tWH production at the 13-TeV LHC. The lower panels provide information on the differential K factors with the scale uncertainties.

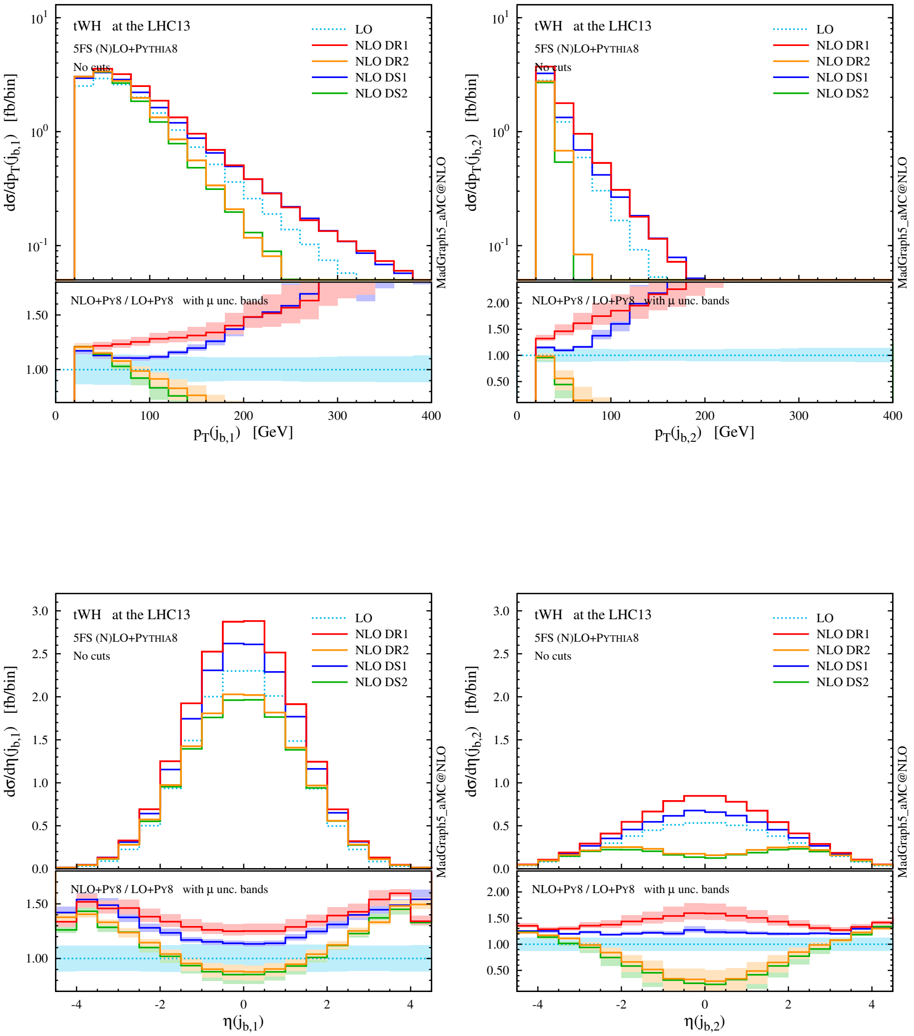

Figure 6.13: Same as Fig. 6.12, but for the b-tagged jets. Note that the second-hardest b jet is described by the parton shower at LO, while by the matrix element at NLO.

tWH	$\sigma(\mu_0^s)$ [fb$\pm\delta_\mu^\%\pm\delta_{\text{PDF}}^\%$]	K	$\sigma(\mu_0^d)$ [fb$\pm\delta_\mu^\%\pm\delta_{\text{PDF}}^\%$]	K
LO	$15.77(1)\,^{+11.3}_{-11.1}\pm11.2$	-	$16.14(2)\,^{+12.9}_{-12.8}\pm11.1$	-
NLO DR1	$21.72(2)\,^{+5.8}_{-4.3}\pm3.0$	1.38	$20.72(2)\,^{+5.0}_{-3.1}\pm3.0$	1.28
NLO DR2	$16.28(4)\,^{+4.6}_{-6.2}\pm2.7$	1.03	$15.68(3)\,^{+4.5}_{-5.9}\pm2.7$	0.97
NLO DS1	$20.17(3)\,^{+4.0}_{-3.9}\pm3.2$	1.28	$19.11(3)\,^{+2.3}_{-2.3}\pm2.9$	1.18
NLO DS2	$16.00(3)\,^{+4.8}_{-6.9}\pm2.5$	1.01	$15.31(3)\,^{+5.1}_{-6.7}\pm2.5$	0.95
NLO GS	15.9(5)	1.01(3)		

Table 6.3: Total cross sections for $pp \to tW^-H$ and $\bar{t}W^+H$ at the 13-TeV LHC, in the 5FS at LO and NLO accuracy with different schemes, computed with a static scale $\mu_0^s = (m_t + m_W + m_H)/2$ and a dynamic scale $\mu_0^d = H_T/4$. We also report the scale and PDF uncertainties and the NLO-QCD K factors; the numerical uncertainty affecting the last digit is quoted in parentheses.

In Figs. 6.12 and 6.13 we collect some differential distributions. Observables related to the Higgs boson can essentially be described by a constant K factor for each subtraction scheme. On the other hand, similar to the tW case, the NLO distributions for the top quark and the W boson are quite different among the four NLO techniques. As we know, these differences are driven essentially by whether the interference with $t\bar{t}H$ is included or not (in DR), and by the profile of the subtraction term (in DS). These NLO effects are quite remarkable for the b jets, since the negative interference with $t\bar{t}H$ drastically suppresses central hard b jets.

Summarising, in analogy with the tW process, effects due to the interference between $t\bar{t}H$ and tWH which appear in NLO corrections of the latter process are significant, and hence the details of how the $t\bar{t}H$ contribution is subtracted enormously affect the predictions for both the total rate and the shape of distributions. On the one hand, a LO description of tWH in the 5FS is apparently not sufficient. On the other hand, the NLO prediction strongly depends on the subtraction scheme employed. This last point is only a relative issue, if we take into account the fact that DR2 and DS2 results are quite consistent with each other and integrate to the same total cross section as GS, which suggests that they provide a better description of the physics not included in $t\bar{t}H$ than DR1 and DS1. Nevertheless, as in the case of tW production, it is clear that fiducial cuts are crucial to obtain a meaningful separation of tWH from $t\bar{t}H$, and their effects will be discussed in the next subsection.

6.5.2 Results with fiducial cuts

We now move to investigate whether the separation between tWH and $t\bar{t}H$ can become meaningful in a fiducial region, where interference between the two processes and theoretical systematics are suppressed. The problem is exactly analogous to the tW–$t\bar{t}$ separation. In practice, for any selection defined by suitable cuts, one needs to quantify the residual difference among different subtraction schemes and see if it is small enough.

Motivated by the same rationale behind our tW discussion, we define our set of "fiducial cuts" for tWH selecting only events with

1. exactly one b jet with $p_T(j_b) > 20$ GeV and $|\eta(j_b)| < 2.5\,,$
2. exactly two central W bosons with $|y(W)| < 2.5\,,$
3. exactly one central Higgs boson with $|y(H)| < 2.5\,.$

We recall that the first selection is the key to suppress the double-top amplitudes and hence tWH–$t\bar{t}H$ interference and theoretical ambiguities. We do not assume any particular decay channel for the heavy bosons and hence the second and third selections are added to mimic a good reconstructability of the W and H bosons in the detector. However, they are not crucial since they affect just 5% of the events after surviving selection 1. Our pseudo event category is defined mainly for illustrating the issues behind the simulation of the tWH signal, but the same procedure can be applied to any realistic set of fiducial cuts in experimental analyses, including a selection on specific decay products of the W and H bosons.

Looking at Table 6.4, we can see that the situation for tWH is very similar to the one we have already seen for tW. Before the fiducial cuts, the category is largely dominated by $t\bar{t}H$ events. Once the fiducial cuts are applied, the contribution from $t\bar{t}H$ is reduced by more than a factor 20, while the one from tWH just by about 1/4 (for DR2), enhancing the signal-to-background ratio ($tWH/t\bar{t}H$) to about 0.5, which is encouraging from the search point of view. The interference with LO $t\bar{t}H$ amplitudes has been visibly reduced, with fiducial cross sections among the four techniques agreeing much better than in the inclusive case; this is also apparent in the differential distributions of Figs. 6.14 and 6.15, and in particular in the much smaller scale dependence in the tails of tWH distributions at NLO.

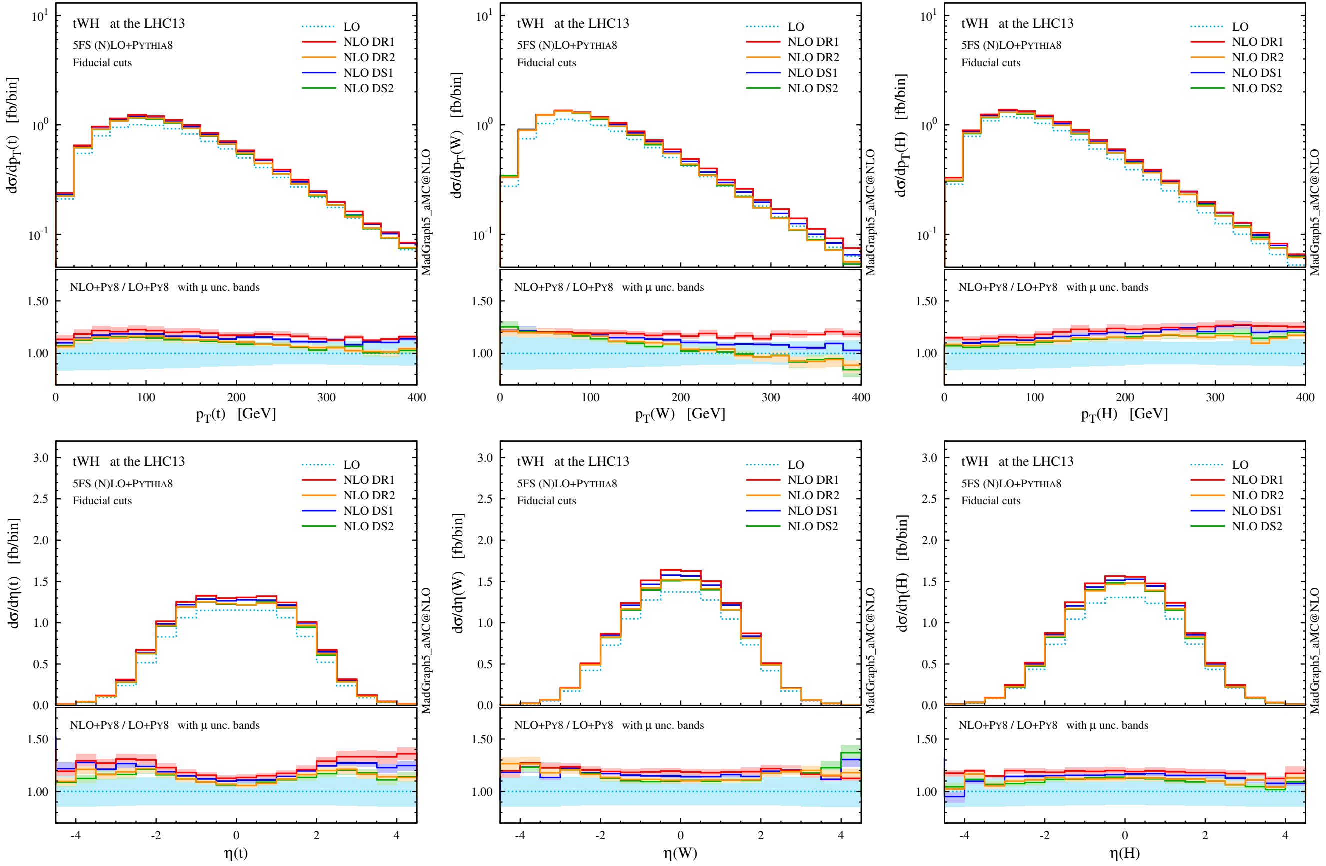

Figure 6.14: p_T and η distributions the top quark, the W boson and the Higgs boson as in Fig. 6.12, but after applying the fiducial cuts to suppress interference between $tWHb$ and $t\bar{t}H$.

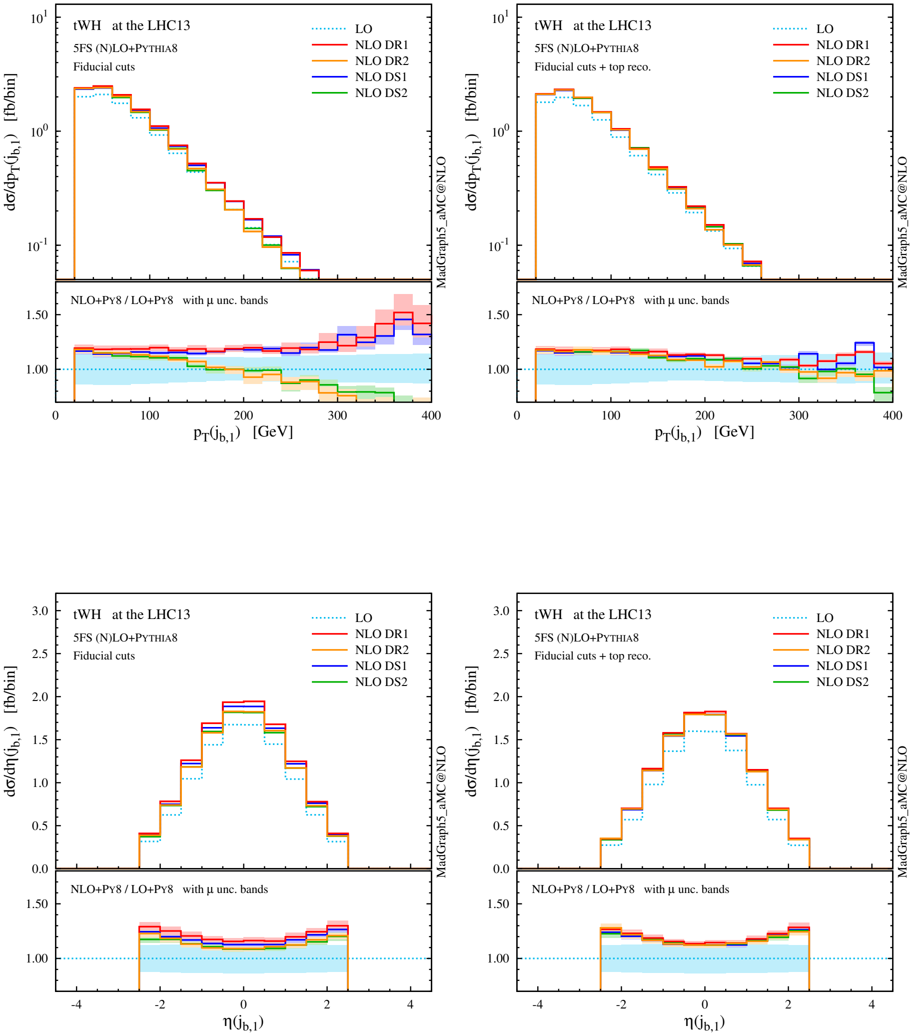

Figure 6.15: p_T and η distributions for the central b-tagged jet, after fiducial cuts are applied. In the right plots, in addition to fiducial cuts, top reconstruction is required.

σ_{NLO}	No cuts	Fiducial cuts		Fiducial + top reco.	
	[fb $\pm\delta_\mu^\% \pm\delta_{\text{PDF}}^\%$]	[fb $\pm\delta_\mu^\% \pm\delta_{\text{PDF}}^\%$]	eff.	[fb $\pm\delta_\mu^\% \pm\delta_{\text{PDF}}^\%$]	eff.
$t\bar{t}H$	485.0(9) $^{+1.3}_{-5.3}$ ±1.8	21.5(2) $^{+2.0}_{-6.8}$ ±2.7	0.04	21.5(2) $^{+2.0}_{-6.8}$ ±2.7	0.04
tWH DR1	20.72(2) $^{+5.0}_{-3.1}$ ±3.0	12.12(2) $^{+2.7}_{-2.3}$ ±2.5	0.58	11.18(2) $^{+2.2}_{-2.3}$ ±2.5	0.54
tWH DR2	15.68(3) $^{+4.5}_{-5.9}$ ±2.7	11.43(2) $^{+1.6}_{-2.4}$ ±2.4	0.73	11.04(2) $^{+1.8}_{-2.4}$ ±2.4	0.70
tWH DS1	19.11(3) $^{+2.3}_{-2.3}$ ±2.9	11.79(2) $^{+1.8}_{-2.3}$ ±2.5	0.62	11.02(2) $^{+1.7}_{-2.3}$ ±2.5	0.58
tWH DS2	15.31(3) $^{+5.1}_{-6.7}$ ±2.5	11.37(2) $^{+1.6}_{-2.3}$ ±2.4	0.74	11.05(2) $^{+1.8}_{-2.4}$ ±2.4	0.72

Table 6.4: Total cross sections in fb at the LHC 13 TeV for the processes $pp \to t\bar{t}H$ and $pp \to tWH$, in the 5FS at NLO+PS accuracy. Results are presented before any cut (left), after fiducial cuts (centre), and also adding top reconstruction on the event sample (right). We also report the scale and PDF uncertainties, as well as the cut efficiency with respect to the case with no cuts. All numbers are computed with the reference dynamic scale $\mu_0 = H_T/4$, and the numerical uncertainty affecting the last digit is reported in parentheses.

Nevertheless, a residual difference of about 6% (0.7 fb) is present between the DR1 and DR2 fiducial cross sections, and this discrepancy is also visible in the shape of some p_T distributions. Once again, if we use MC information to additionally require the central b jet to come unambiguously from the top quark, the residual interference effects are further reduced to less than 1% at a tiny cost on the signal efficiency. This brings the differential predictions in excellent agreement among the four schemes and with this selection one can effectively consider tWH and $t\bar{t}H$ as separate processes.

Finally, we briefly comment on the possibility to observe the tWH signal at the LHC. Naturally, one may wonder whether it will be possible to observe it over the (already quite rare) $t\bar{t}H$ process, in an experimental analysis that applies a selection similar to our fiducial cuts. For example, the LHC Run II is expected to deliver an integrated luminosity in the 100 fb^{-1} ballpark. In our pseudo event category (with top reconstruction), the difference between including or excluding the tWH contribution amounts to

$$t\bar{t}H \text{ only}: \quad 2147 \pm 46 \text{ (stat.) } {}^{+101}_{-204} \text{ (theo.) events,}$$

$$t\bar{t}H + tWH: \quad 3251 \pm 57 \text{ (stat.) } {}^{+147}_{-257} \text{ (theo.) events.}$$

Unfortunately, once branching ratios of the Higgs and W bosons and realistic efficiencies are taken into account, these numbers disfavour the possibility to observe tWH over $t\bar{t}H$ at the Run II. On top of that, there are many more background processes contributing to our event category than just $t\bar{t}H$. This makes the searches for the SM tWH signal extremely challenging, and the high-luminosity upgrade of the LHC is definitely needed in order to have a sufficient number of events.

On the other side, simulated tWH events should be taken into account in other searches for Higgs boson and top quark associated production, which are not necessarily going to apply tWH-specific fiducial cuts, in order to complete the MC modelling. In particular, this will be relevant in searches for the $t\bar{t}H$ signal, and also for the t-channel tH process (also called tHq by experiments) with Higgs decay into a pair of bottom quarks ($H \to b\bar{b}$), where semi-leptonic tWH events can lurk in the signal region defined by a large (b-)jet multiplicity. In fact, including the tWH simulation in the signal definition (as opposed to considering it a background) in the case of either $t\bar{t}H$ or t-channel tH searches will lead to a more comprehensive view on Higgs boson and top-quark associated production, *e.g.* being relevant when setting limits or measuring the signal strength.

6.5.3 Higgs Characterisation

In this section we explore the sensitivity of tWH production to BSM physics in the Higgs sector. Given the experimental constraints after the LHC Run I [12], we can reasonably fix the Higgs interaction with the EW bosons to be the SM one, and turn to study CP-mixing effects in the Higgs–fermion sector. In particular, we investigate a CP-mixed Yukawa interaction, in a way completely analogous to what we have done in Section 5.5 for t-channel tH production. This means that we consider the usual HC Lagrangian in Eq. (2.6), setting $\kappa_{Htt} = 1$ and $\kappa_{Att} = 2/3$. On the other hand, interactions between the Higgs and the EW vector bosons is described by the SM-like Lagrangian

$$\mathcal{L}_0^V = \left(\tfrac{1}{2} g_{HZZ}\, Z_\mu Z^\mu + g_{HWW}\, W^+_\mu W^{-\mu}\right) X_0 \,, \tag{6.13}$$

where $g_{HVV} = 2m_V^2/v$ ($V = W, Z$).

When using the HC_NLO_X0 model, the code and events for tWX_0 production at NLO can be generated in a way analogous to SM tWH:

```
> import model HC_NLO_X0-no_b_mass
> generate p p > t w- x0 [QCD]
> add process p p > t~ w+ x0 [QCD]
```

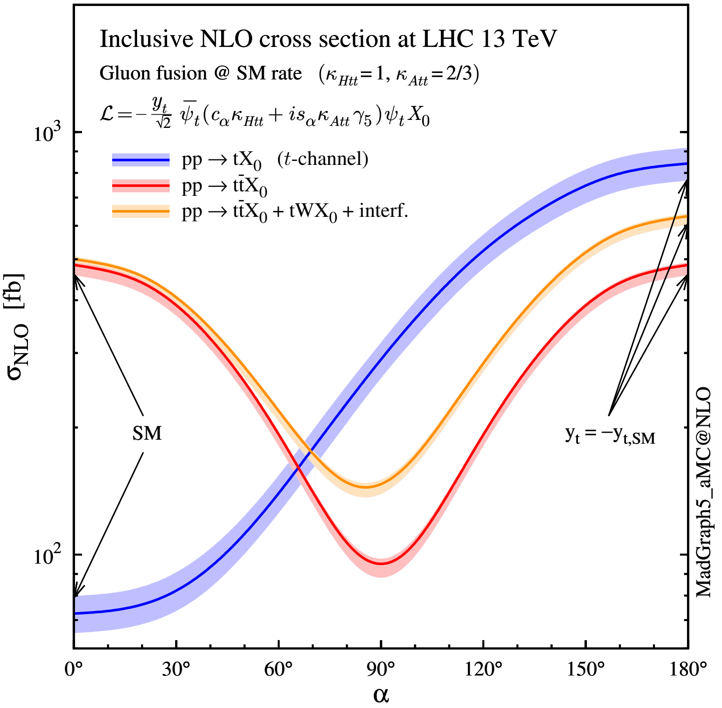

Figure 6.16: NLO cross sections (with scale uncertainties) for $pp \to t\bar{t}X_0$, $pp \to tWX_0$ (with DR2) and $pp \to tX_0$ (t-channel) at the 13-TeV LHC as a function of the CP-mixing angle α, where κ_{Htt} and κ_{Att} are set to reproduce the SM gluon-fusion cross section for every value of α. The $t\bar{t}X_0$ and tWX_0 processes have been computed using the dynamic scale $\mu_0 = H_T/4$, while tX_0 results are taken from Section 5.5.

In this section we show results obtained only with the DR techniques.

In Fig. 6.16 we plot the total NLO cross section for Higgs production in association with a top-quark pair $t\bar{t}X_0$ (red), and for the combined contribution of $t\bar{t}X_0$ and tWX_0 including their interference (orange), which is simply obtained by summing the tWX_0 DR2 cross section to the $t\bar{t}X_0$ one. We can immediately see that the inclusion of the tWX_0 process lifts the $y_t \to -y_t$ degeneracy that is present in $t\bar{t}X_0$ production. For a flipped-sign Yukawa coupling, the interference between single-top diagrams where the Higgs couples to the top and the ones where it couples to the W becomes constructive, and the total cross section is augmented from roughly 500 fb (SM, $\alpha = 0°$) to more than 600 fb ($\alpha = 180°$). This enhancement can help in a combined analysis of the

Higgs interactions, though it is less striking than the one which takes place in the t-channel Higgs plus single-top process (which is also reported in blue for comparison). For the sake of clarity we point out that, going along the α-axis in Fig. 6.16, the tWX_0 cross section includes in fact two different interference effects. On the one hand, there is the interference between single-top amplitudes with Higgs-to-fermion and Higgs-to-gauge-boson interactions, similar to the tH process. This is already present at LO, and it drives the growth of the cross section from the SM case (maximally destructive interference) to the case of a reversed-sign top Yukawa (maximally constructive). On the other hand, employing DR2 for the computation of the tWX_0 NLO cross section means that also the interference with $t\bar{t}H$ is included. This is an effect present only at NLO, and its size depends as well on the CP-mixing angle α (due to the different ratio between $t\bar{t}H$ and tWH amplitudes).

In Fig. 6.17 we compare some differential distributions for the SM hypothesis (blue), the purely CP-odd scenario (red) and the flipped-sign CP-even case (green), before any cuts. We can see that the interference between the doubly resonant $t\bar{t}H$ and the singly resonant tWH amplitudes is largest for the SM case. For the case of flipped Yukawa coupling the interference gives a minor contribution, while for the CP-odd case it is very tiny because the doubly resonant contribution is at its minimum. The W and Higgs transverse momentum distributions become harder when the mixing angle is larger. Once the fiducial cuts are applied (Fig. 6.18), the difference between DR1 and DR2 decreases as expected.

In conclusion, we find that the tWH process can help to lift the $y_t \to -y_t$ degeneracy for $t\bar{t}H$ and put constraint on BSM Yukawa interactions of the Higgs boson in a combined analysis, on top of the most sensitive t-channel tH production mode. Finally we recall that, if one also assumes a SM interaction between the Higgs and the W bosons, one can further include the $\gamma\gamma$ decay channel data to put limits on the CP-mixing phase α.

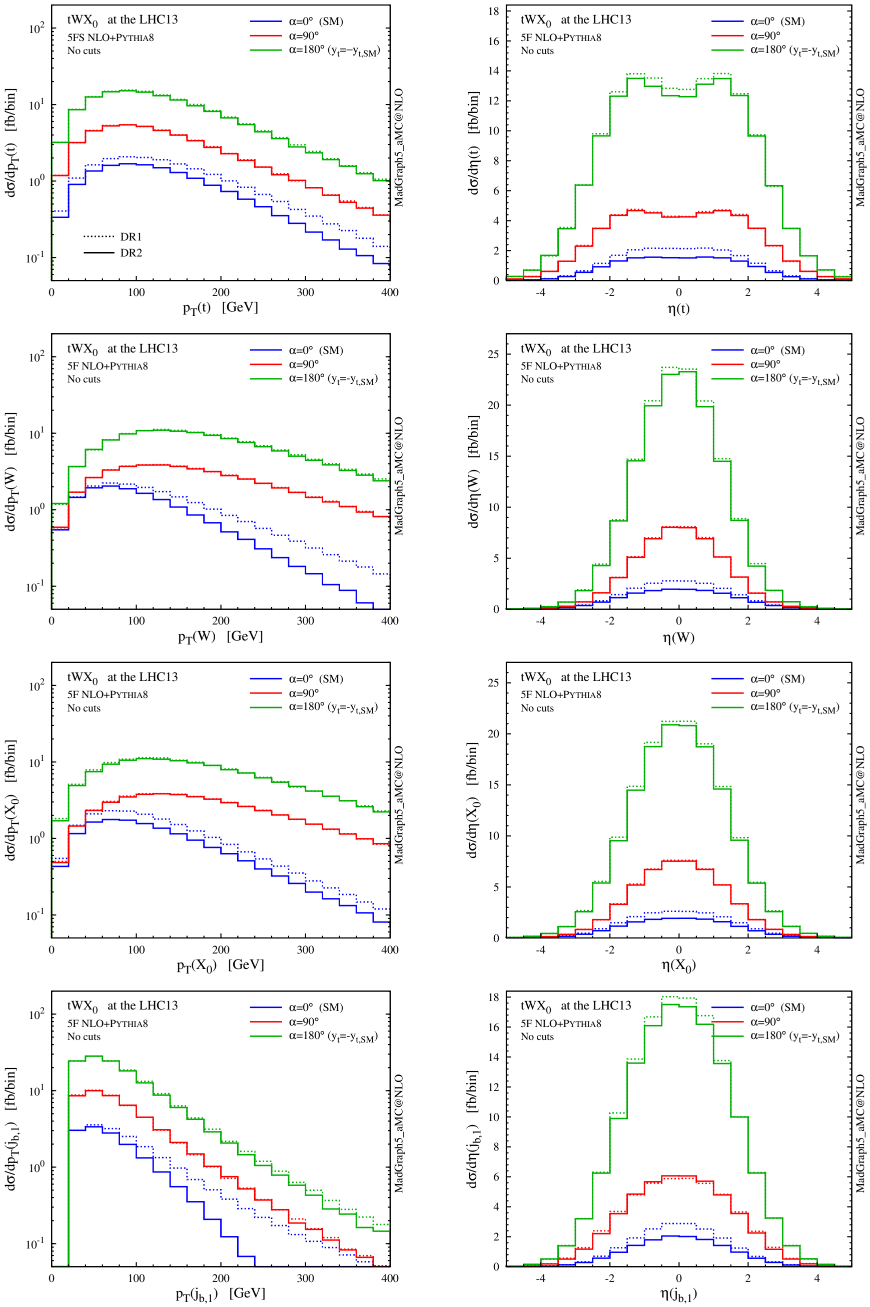

Figure 6.17: p_T and η distributions for the top quark, the W boson and the Higgs boson in tWH production at the 13-TeV LHC, with different CP-mixing angles in the top-Higgs Yukawa interaction. The results are obtained employing DR2 (solid) and DR1 (dashed), without any cut.

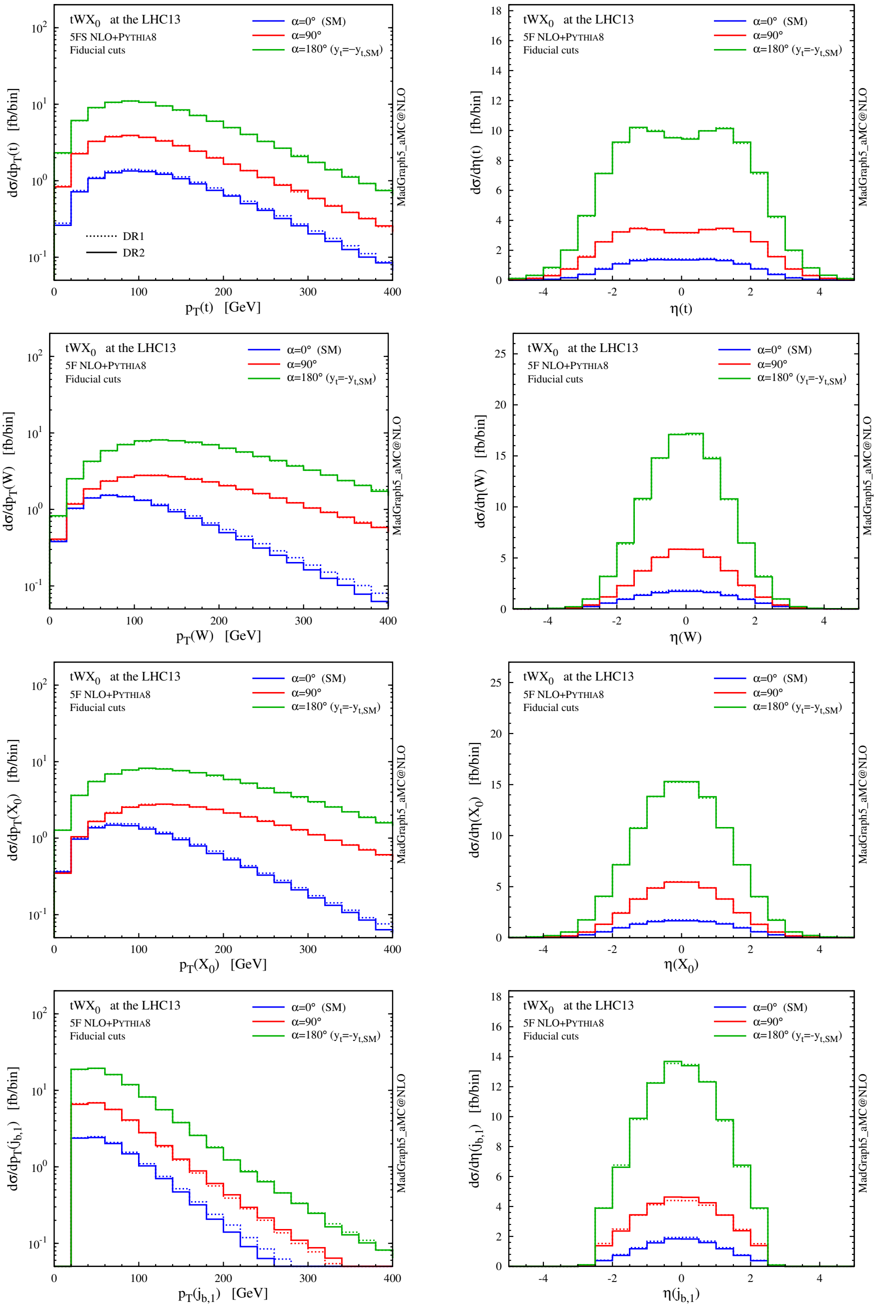

Figure 6.18: Same as in Fig. 6.17, but after applying the fiducial cuts.

6.6 Summary

In this Chapter we have discussed NLO-accurate predictions for the tWH process, including parton-shower effects. These are the first NLO results for tWH in the five-flavour scheme (5FS), and have been published in [18]. This process at NLO interferes with $t\bar{t}H$, therefore entails unavoidable ambiguities associated to its very definition. In order to achieve a clear understanding of these ambiguities, we have first revisited the currently available subtraction schemes in the case of tW production at NLO in the 5FS (also proposing the new DS2 scheme), and then we have proceeded in an analogous way for tWH. On the one hand, NLO corrections to these processes are crucial for a variety of reasons, ranging from a reliable description of the b-quark kinematics, to a better modelling of backgrounds in searches for Higgs production in association with the top. On the other hand, they introduce the aforementioned issue of interference with $t\bar{t}(H)$, which has a significant impact on the phenomenology of $tW(H)$ with respect to LO results.

Our first aim has been to study the pro's and con's of the various techniques available to subtract the resonant contributions appearing in the NLO corrections, which fall in the GS, DR and DS classes. At the inclusive level these techniques can deliver rather different results, with differences that often exceed the theoretical uncertainties at NLO (estimated via scale variations). These differences have been traced back to whether a given technique accounts for the interference between the $tW(H)$ and $t\bar{t}(H)$ processes, and to how the off-shell tails of the resonant diagrams are subtracted. They have a visible impact at the total cross section level as well as in distributions, particularly those involving b-jet related observables. We stress that the aim of this work is to provide a practical and reliable technique to simulate tW and tWH at NLO, when the corresponding $t\bar{t}$ and $t\bar{t}H$ process are generated separately in the on-shell approximation. In this sense, we find the DR2 and DS2 techniques to provide a more faithful description of the underlying physics in tW and tWH than that of DS1 and DR1, therefore we deem them as preferable to generate events for these two processes at NLO. Note that our results have no claim of generality, thus cannot be immediately extended to other SM or BSM processes. A study of subtraction techniques should be undertaken on a process-by-process basis, in particular for BSM physics, where different width-to-mass ratios and different amplitude structures (i.e. resonance profiles) can appear.

Our second aim has been to study what happens once event selections similar to those performed in experimental analyses are applied, and in general whether one can find a fiducial region where the single-top processes tW and

tWH can be considered well defined *per se*, and are stable under perturbative corrections. A simple cut as requiring exactly one b-tagged jet in the central detector (which becomes three b jets in the case of tWH if the Higgs decays to bottom quarks) can greatly reduce interference effects, and thus all the process-definition systematics of $tW(H)$ at NLO. In such a fiducial region, we find the perturbative description of $tW(H)$ to be well behaved, and the inclusion of NLO corrections significantly decreases the scale dependence; differences between the various DR and DS subtraction techniques are reduced much below the scale dependence, and the separation of the single-top and top-pair processes becomes meaningful. Given a generic set of cuts, we have provided a simple and robust recipe to estimate the left-over process-definition systematics: use the difference between the DR1 and DR2 predictions (which amounts to the impact of interference effects). In general, such approach provides a convenient way to quantify the limits in the separation of $t\bar{t}(H)$ and $tW(H)$ and the quality of fiducial regions. In particular, this is essential for a reliable extraction of the Higgs couplings in tWH production.

Finally, we have investigated the phenomenological consequences of a generic CP-mixed Yukawa interaction between the Higgs boson and the top quark in tWH production. While the SM cross section is tiny, due to maximally destructive interference between the H–t and H–W interactions, BSM Yukawa interaction tends to increase the production rate. For example, in the case of a reversed-sign Yukawa coupling with respect to the SM, the tWH cross section is enhanced by an order of magnitude, similar to what happens for the dominant single-top associated mode, *i.e.* the t-channel tH production.

Outlook

In this thesis we have promoted accurate and precise predictions for various single-Higgs production processes at the LHC, that are relevant to study the properties of the Yukawa interaction between the Higgs boson and the top quark. The processes that we have addressed are production of a Higgs boson with one and two extra jets via gluon fusion (GF $H + 1, 2j$), associated production of a Higgs boson with a top-quark pair ($t\bar{t}H$), and the three associated production modes of a Higgs boson with a single top quark: t-channel tH, s-channel tH, and tWH.

Gluon fusion has the largest cross section, and in the SM is dominated by top-quark loops, therefore it provides a useful indirect probe to the top Yukawa interaction. The $t\bar{t}H$ process, on the other hand, provides an important direct probe to the top Yukawa, that is rather independent from specific assumptions such as the intermediate virtual interactions (at variance with gluon fusion). The single-top modes are not only directly sensitive to the top Yukawa, but also to the relative phase between the Higgs interaction with the top quark and the one with the W boson. Therefore, despite the fact that their cross section in the SM is much smaller than $t\bar{t}H$, their peculiarities result in a rich and interesting phenomenology, that can provide as well important and complementary information on the Higgs properties, and to constrain deviations from the Standard Model.

A first major point of this thesis is that we have provided state-of-the-art predictions for the cross sections of the Higgs plus single top production channels in the SM, at next-to-leading-order (NLO) accuracy in QCD, addressing also various theoretical sources of systematic uncertainty. These results have been computed employing the MadGraph5_aMC@NLO framework.

Another major point is that we have developed and employed the HC_NLO_X0 UFO model, which greatly extends the reach of the MadGraph5_aMC@NLO default package when studying single-Higgs production processes. First, it allows to generate gluon-fusion events at NLO accuracy, also matched to parton showers (NLO+PS). This capability relies on the heavy-top approximation; despite some known limitations in the case of very hard QCD radiation, this approximation is very good for single-Higgs production at the LHC energies, and represents state-of-the-art accuracy for event generation of Higgs plus jets via gluon fusion. Second, it allows to pursue the Higgs Characterisation program at NLO; with this model, one can generate NLO+PS predictions for the production of a rather generic spin-0 particle, featuring CP-mixed interactions with the other SM particles. In general, the HC_NLO_X0 UFO model provides a convenient tool to study and constrain the Higgs properties at the ongoing LHC Run II, and at future runs with higher luminosity.

In our case, we have pointed out a variety of observables that can be sensitive to the top Yukawa properties and their deviations from the SM paradigm, in particular in the presence of CP mixing. The simplest observables are the total rates of processes proceeding through the Higgs-top interaction, which are summarised in Fig. O.1. Once we fix the rate of single Higgs production via gluon fusion, we can use the decay rate to two photons and the cross sections of Higgs production in association with a top-quark pair, with single top quarks, with Z bosons, or Higgs pair production, to tackle the scenario of a reversed-sign top Yukawa coupling and to constrain CP-mixing effects. It is important to design experimental analyses that can well separate the various production channels in order to maximise the sensitivity to the effects of new physics, especially if deviations from the SM in the Higgs-top interaction are small. For example, in the case of small CP-mixing angles, the reduced rate of $t\bar{t}H$ production is partly compensated by the larger tH and tWH cross sections, therefore it is important to disentangle these processes in analyses looking to Higgs production in association with top quarks. We have illustrated how many differential shapes can be sensitive to CP mixing as well, when looking at associated production of a Higgs boson with two jets, with a top-quark pair and with a single top. The wealth of information associated with these processes can be extracted in fully-fledged experimental analyses based on state-of-the-art multivariate techniques.

Finally, we have found that the inclusion of NLO corrections is very important for the processes that we have studied, and because of different reasons. The gluon-fusion and $t\bar{t}H$ processes proceed mainly through QCD interactions, therefore we expect NLO accuracy to provide substantial corrections to the LO predictions, and to be critical in order to bring under control the theoretical systematics associated with scale dependence. Indeed, we have confirmed this to be the case. On the other hand, the Higgs plus single-top processes proceed mainly via EW interactions. Nevertheless, for the main production mode

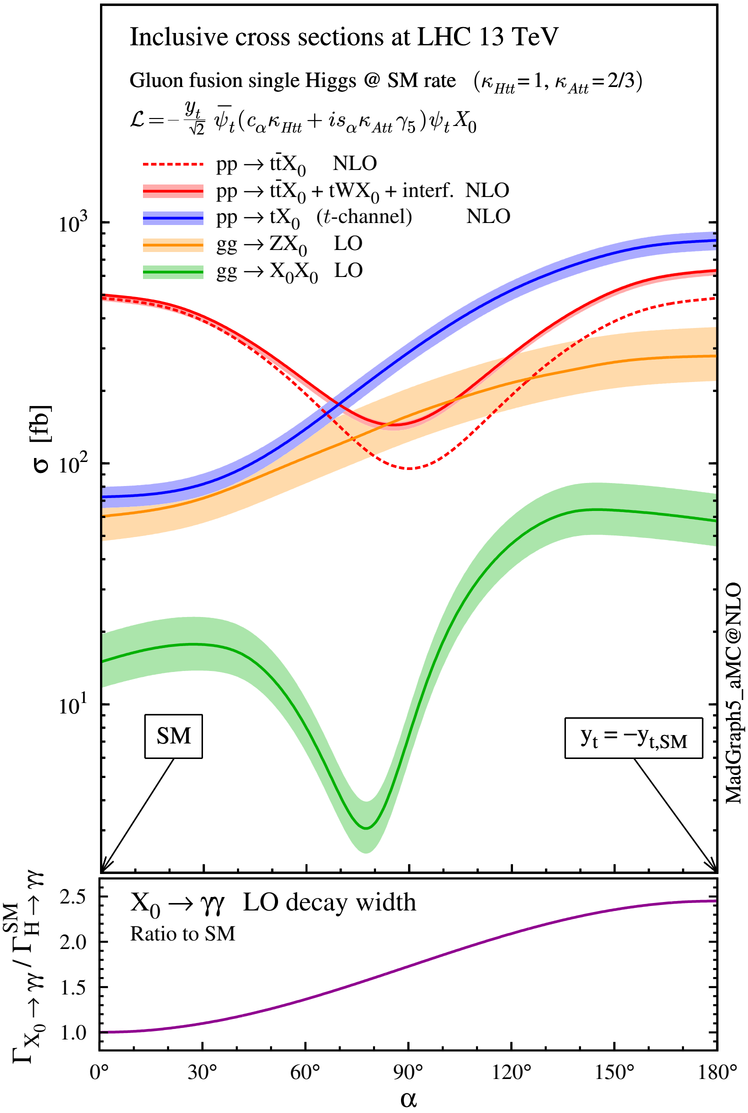

Figure O.1: Summary of the LHC processes sensitive to CP mixing in the interaction between the Higgs boson and the top quark. The SM single-Higgs cross section via gluon fusion is reproduced for any value of the CP-mixing angle α. In the upper plot we show the inclusive rates for Higgs production in association with a top pair and a single top quark (t-channel and tWH), the gg contribution to ZH production, and the gluon-fusion production of a Higgs pair, including the scale (and flavour-scheme) uncertainty bands. In the lower plot we show the partial decay width to two photons, divided by the SM value.

– t-channel tH – NLO corrections are paramount in order to reduce another type of theoretical systematic, the flavour-scheme dependence; notably, they greatly stabilise the inadequate LO predictions in the 5FS. In the case of tWH production, not only NLO corrections should help to reduce the flavour-scheme dependence, but we have also seen that in the 5FS they are needed to take into account the sizeable effects of interference with $t\bar{t}H$ production.

The original results of this research have been published in four scientific articles on peer-reviewed journals [15–18], in the fourth LHC Higgs Cross Section Working Group technical report [19], and in two conference proceedings [20,21]. The HC_NLO_X0 UFO model is publicly available online [22].

Appendix A

The Standard Model and the BEH mechanism

In this Appendix we review the so-called Standard Model (SM) of fundamental interactions, which is the currently-accepted paradigm in particle physics. The SM is in fact a fully fledged theory from the modern point of view: it is built on the fundamental principles of Lorentz and gauge invariance, it is consistent, and it is predictive ("renormalisable").

A.1 Fundamental principles

The Standard Model is a quantum gauge theory over the Minkowski spacetime. There are various fundamental principles that have been successfully employed to formulate physics theories and which lie behind the SM too.

The description of fundamental interactions through a covariant field theory on the Minkowski spacetime automatically embeds the *relativity principle*, one of the most important foundations of modern physics. This principle states that physics should be invariant under the Poincaré group of transformations that conserve the spacetime metric, also rephrased as being invariant for every observer in an "inertial" frame. In practice one define the physics in terms of local objects, the "fields", with definite properties under the proper orthochronous Lorentz subgroup of transformations; mathematically, they must be irreducible representation of this group. According to this classification, we can label each field depending on its spin, which assumes integer (for bosons) or half-integer (for fermions) values. In general, fields carry a Lorentz index associated with its representation (the trivial one is for the spin-0 case).

All the fundamental laws ruling a physical system are understood in terms of its action $\mathcal{S}$, a real (to conserve probability) and adimensional quantity. Equivalently, one can specify the Lagrangian $\mathcal{L}$ of the system, which is related to the action by

$$\mathcal{S} = \int d^4x\, \mathcal{L}\big(\phi(x),\, \partial_\mu \phi(x)\big)\,; \tag{A.1}$$

this can be regarded as the explicit formulation of the physical theory (for notation simplicity, we have considered the case of only one spin-0 field ϕ, but in general we can have a set of fields ϕ_i, and they carry Lorentz indices too). The Lagrangian $\mathcal{L}(x)$ is a function of one or more fields and their derivatives; we are mostly interested in theories where only first derivatives appear. Dimensional analysis and covariance of the theory imply that the Lagrangian must be Lorentz invariant and have dimensions of $[\text{lenght}]^{-4}$, which dictates what kind of field combinations can appear in it.

In a classical field theory, the *variational principle* (Hamilton) postulates that the evolution of a physical system takes place along a path in the space of field configurations where $\mathcal{S}$ is extremal, typically a minimum. Requiring the action to be invariant under arbitrary variations of the fields leads to the Euler-Lagrangian equations of motion, which determine the path in spacetime followed by each field.

In the quantum field theory formulation, fields are operator acting on some vacuum state $|0\rangle$ and the physics can be understood in terms of path integrals. In particular, one is interested in computing the correlation function between an initial and a final state of field configurations (asymptotically free in the distant past or future), by integrating over all the possible intermediate configurations, *i.e.* all the paths, each weighted with a factor that depends on the action corresponding to the path. An n-point time-ordered correlation function can be written as

$$\langle 0|\mathrm{T}\,\phi(x_1)\ldots\phi(x_n)|0\rangle = \int \mathcal{D}\phi\,\phi(x_1)\ldots\phi(x_n)\,\exp\left[\frac{i}{\hbar}\,\mathcal{S}(\phi)\right], \tag{A.2}$$

where $\mathcal{D}\phi$ denotes functional integration over all possible configurations $\phi(x)$, while $e^{i\mathcal{S}/\hbar}$ is the weight. The classical formulation of the theory, where only the extremal path is relevant for the physics, is recovered in the limit $\hbar \to 0$. These correlation functions are employed to calculate the results of any interaction, in general scattering probabilities, which are paramount in particle physics experiments. The Lehmann-Symanzik-Zimmermann (LSZ) theorem states how to compute the relevant scattering amplitudes in terms of connected field paths, and provided that the fields satisfy the conditions

$$\langle 0|\phi(x)|0\rangle = 0 \qquad \text{and} \qquad \langle p|\phi(x)|0\rangle = e^{-ip\cdot x}\,, \tag{A.3}$$

where $|p\rangle$ is the state with one ϕ particle with momentum p.

A convenient way to compute scattering amplitudes is to employ Feynman diagrams. One can derive the building blocks, called Feynman rules, from the Lagrangian of the theory, using functional derivatives. The Feynman rules represent free propagating fields and possible interaction vertices among them, and they can be assembled in all the allowed paths connecting the initial and final field configurations; as a result, one obtains the Feynman diagrams needed to compute the scattering amplitudes.

The *symmetries* of a theory play a fundamental role in modern physics. A relation between symmetries in the Lagrangian and conservation laws in physical processes is provided by Noether's theorem. Other than Lorentz symmetry, which implies conservation of the total angular momentum and the centre-of-mass velocity of an isolated system, and invariance under translations, which preserves the total four momentum p^μ, we are also interested in unitary transformations on the fields (these transformations do not affect the physical probabilities in quantum mechanics). For example, if the Lagrangian is invariant under a $U(1)$ transformation of a field, Noether's theorem implies conservation of the current and total charge associated to this field. This fact is employed to formulate the fundamental theory of electromagnetic interactions, quantum electrodynamics (QED). We shall see in the next section how interactions between charged fields and photons can arise simply requiring the $U(1)$ symmetry to be local in spacetime, as expected in a proper relativistic theory; in this case, we say that the Lagrangian exhibits a local gauge symmetry.

Gauge symmetries are also of paramount importance in quantum mechanics, to guarantee finite renormalisability of theories such as the Standard Model [244–247]. Renormalisability is needed if we want to use the parameters measured in one experiment to compute the results of another experiment, namely to guarantee predictability and usefulness of the theory. A final comment is due: one cannot have a finite renormalisation of operators in the Lagrangian that have a mass dimension higher than four. However, if a theory exhibits such higher-dimensional operators, it can be regarded as the low-energy limit of a more fundamental renormalisable theory; in this case we talk about effective field theories (EFTs). An EFT is still predictive, provided that the energy E of the experiments is small compared to the characteristic scale Λ of the underlying renormalisable theory (namely the masses of the new fields that do not appear in the EFT): effective interactions at higher orders will be more and more suppressed by higher powers of E/Λ, and can thus be kept under control. Moreover, if a subset of renormalisable gauge interactions is present in the EFT, one can systematically compute higher-order corrections in these interactions, as in a normal theory; for example, this is the case of QCD corrections to the SM EFT.

A thorough exposition of these principles and of the quantum gauge field formulation of modern theories of fundamental interactions can be found in standard textbooks, such as *Peskin & Schroeder* [74] or *Pokorski* [248].

A.2 The BEH mechanism

The mass generation mechanism in the classical Abelian theory has been formulated by Higgs, who at first invoked a gauge symmetry breaking with an explicit parametrisation of the vacuum state [4, 5], also pointing out the existence of the scalar H boson in the particle spectrum. Subsequently, Higgs published a manifestly gauge invariant treatment (as we do here) in [6]. The quantum mechanical formulation in the Abelian theory has been published by Brout and Englert [3], invoking again an explicit gauge symmetry breaking in the parametrisation of the vacuum state. Throughout this thesis, we collectively refer to this mass generation technique as the Brout-Englert-Higgs (BEH) mechanism, and to the resulting H particle as the Higgs boson.

In this section we present the BEH mechanism in classical field theory, following a manifestly gauge-invariant procedure. In particular, we discuss the Abelian theory, the non-Abelian theory and the bosonic sector of the electroweak theory. At the end, we briefly address what happens in the quantum theory.

Abelian theory

Consider the Lagrangian of a complex scalar field ϕ,

$$\mathcal{L} = |\partial_\mu \phi|^2 - V(|\phi|)\,, \tag{A.4}$$

where the potential V depends only on the field radius $|\phi|$. This Lagrangian is invariant under the global continuous $U(1)$ symmetry $\phi(x) \to U\phi(x) = e^{i\alpha}\phi(x)$ and the physics cannot depend on the choice of α; in a proper relativistic theory we need to require invariance under *local* $U(1)$ transformations

$$\phi(x) \to U(x)\phi(x) = e^{i\alpha(x)}\phi(x)\,. \tag{A.5}$$

To this purpose, we ought to add a minimal interaction with a *gauge* field b_μ (a real-valued vector field) via the covariant derivative

$$\partial_\mu \to D_\mu = \partial_\mu - ig\, b_\mu \,, \tag{A.6}$$

and the gauge field must transform as

$$b_\mu(x) \to b_\mu(x) + \frac{1}{g}\, \partial_\mu \alpha(x) \,. \tag{A.7}$$

The minimal gauge-invariant Lagrangian, including the free term for b_μ, is then

$$\mathcal{L}_{U(1)} = -\frac{1}{4}\big(b_{\mu\nu}\big)^2 + |D_\mu \phi|^2 - V(|\phi|) \,, \tag{A.8}$$

where we have introduced the field-strength tensor

$$b_{\mu\nu} = \partial_\mu b_\nu - \partial_\nu b_\mu \,. \tag{A.9}$$

The field b_μ must be massless, because a bilinear term $\frac{1}{2}m^2 b^\mu b_\mu$ is clearly not gauge invariant unless $m = 0$.

The apparent inevitability of massless gauge fields cannot be avoided if the minimum of the potential V is for $\phi = 0$; in the quantum mechanical version of the theory, this will mean that $\langle \phi \rangle = 0$ and ϕ can be directly associated with a particle of mass proportional to μ in scattering experiments. However, if we suppose that the potential has a minimum with $\phi \neq 0$ in the classical theory, then in the quantum version we have $\langle \phi \rangle \neq 0$, the LSZ conditions of Eq. (A.3) are not satisfied and the physical interpretation of ϕ is not straightforward. In order to extract the particle spectrum of the theory in this case, we first need to assume a specific form of the potential V; we shall consider the same potential realised in the standard EW theory, namely

$$V(|\phi|) = \lambda \left(|\phi|^2 + \frac{\mu^2}{\lambda} \right)^2 \,. \tag{A.10}$$

The potential $V(\phi)$ has a global minimum resulting in a stable vacuum state only for $\lambda > 0$, see Fig. A.1, so we assume this to be the case. If $\mu^2 > 0$ then the potential has a minimum at $|\phi| = 0$ and we are in the first scenario, namely ϕ can be interpreted as a physical field with mass proportional to μ. On the other hand, if $\mu^2 < 0$ then $|\phi| = 0$ is an unstable point and the potential has a stable minimum at

$$|\phi|^2 = -\frac{\mu^2}{\lambda} \equiv \frac{v^2}{2} > 0 \,; \tag{A.11}$$

in general, it will not be possible to directly associate the field ϕ to a physical particle (having imaginary mass, it would be a tachyon). In the Standard Model we are interested in the latter scenario, where $\langle\phi\rangle \neq 0$.

Wherever $\phi \neq 0$ we are allowed to make the following change of variables

$$\phi(x) = \frac{\rho(x)}{\sqrt{2}}\, e^{i\theta(x)}\,, \qquad B_\mu(x) = b_\mu(x) - \frac{1}{g}\,\partial_\mu\theta(x)\,, \tag{A.12}$$

where ρ and θ are real-valued fields.[1] After this convenient redefinition of the dynamical variables, the physical content of the theory becomes manifest. In fact, under the gauge transformations of Eqs. (A.5) and (A.7) we have

$$\phi \to \phi' = \frac{\rho}{\sqrt{2}}\, e^{i(\theta+\alpha)}\,, \tag{A.13}$$

namely

$$\rho' = \rho\,, \qquad \theta' = \theta + \alpha\,, \tag{A.14}$$

and also

$$B_\mu \to B'_\mu = b'_\mu - \frac{1}{g}\,\partial_\mu\theta' = b_\mu + \frac{1}{g}\,\partial_\mu\alpha - \frac{1}{g}\,\partial_\mu(\theta+\alpha)\,, \tag{A.15}$$

which immediately implies

$$B'_\mu = B_\mu\,. \tag{A.16}$$

We can clearly see that the fields ρ and B_μ are gauge invariant and therefore have a physical interpretation, while θ is a pure gauge degree of freedom without physical meaning. This will also mean that in the quantum version of the theory there is only one physically distinct vacuum state, defined by $\langle 0|\rho(x)|0\rangle = v$.

An even more convenient parametrisation to express the Lagrangian of Eq. (A.8) in terms of physical fields is given by

$$\rho(x) = v + H(x) \qquad \text{with } H(x) > -v\,, \tag{A.17}$$

$$\theta(x) = \xi(x)/v\,, \tag{A.18}$$

namely $H(x) = 0$ at the stable minimum of the classical theory, and it satisfies the LSZ condition $\langle H(x)\rangle = 0$ in the quantum mechanical formulation; from

---

[1] Note that Eq. (A.12) is *not* a gauge transformation, and also that $\rho(x)$ and $\theta(x)$ are dynamical field variables, not local constants.

this parametrisation we obtain

$$\begin{aligned}\mathcal{L}_{U(1)} &= -\frac{1}{4}\left(b_{\mu\nu}\right)^2 + |D_\mu\phi|^2 - V(|\phi|)\\ &= -\frac{1}{4}\left(B_{\mu\nu}\right)^2 + \frac{1}{2}\left|\left[\partial_\mu - ig\left(B_\mu + \frac{1}{gv}\left(\partial_\mu\xi\right)\right)\right]e^{i\xi/v}(v+H)\right|^2\\ &\quad - \lambda\left[\frac{(v+H)^2}{2} - \frac{v^2}{2}\right]^2\\ &= +\frac{1}{2}\left|\partial_\mu H + i\left(1+\frac{H}{v}\right)\left(\partial_\mu\xi\right) - igB_\mu(v+H) - i\left(1+\frac{H}{v}\right)\left(\partial_\mu\xi\right)\right|^2\\ &\quad - \frac{1}{4}\left(B_{\mu\nu}\right)^2 - \frac{\lambda}{4}\left(H^4 + 4vH^3 + 4v^2H^2\right)\\ &= -\frac{1}{4}\left(B_{\mu\nu}\right)^2 + \frac{1}{2}\left(\partial_\mu H\right)^2 + \frac{1}{2}(gv)^2\left(B_\mu\right)^2\left(1+\frac{H}{v}\right)^2\\ &\quad - (\lambda v^2)H^2 - (\lambda v)H^3 - \frac{\lambda}{4}H^4\,. \qquad (A.19)\end{aligned}$$

Eq. (A.19) describes a vector field B_μ with mass $m_B = gv$ and a scalar field H with mass $m_H = \sqrt{2\lambda}v = 2i\mu$. The scalar and the vector fields interact with each other, and the structure of this interaction is strictly connected with the mass m_B in the vector field bilinear term, as if we had made the substitution

$$m_B \to m_B\left(1+\frac{H}{v}\right)\,. \qquad (A.20)$$

The potential V results also in self-interaction terms for the H field. In summary, the hypothesis of $\phi(x) \neq 0$, corresponding to a vacuum expectation value $v > 0$, has these two important consequences:

1. the gauge boson B_μ and the scalar boson H have acquired masses proportional to the displacement v of the potential minimum from the $\phi = 0$ configuration, and
2. the $U(1)$ gauge symmetry has decoupled from the physical mass eigenstates, *i.e.* its action on the B_μ and ρ (or H) fields is trivial; the gauge-dependent field ξ, namely the would-be Goldstone boson[2], does not appear in the physical content of the theory.

To put it simply, if $\phi \neq 0$ then the gauge symmetry is hidden, in the sense that it is not manifest in the physical particle spectrum of the theory.

---

[2] According to the Nambu-Golstone theorem, after the breaking of a continuous global symmetry a massless physical particle ξ appears; however, the hypotheses of the theorem (covariance and absence of unphysical states) are not satisfied by a local gauge theory.

Note that analogous results for the physical eigenstates can be obtained with an explicit breaking of the gauge symmetry, setting $\theta = 0$ in Eq. (A.12); this choice is called unitary gauge, and it is a common procedure in textbooks to work out the physical content of the theory. However, it is important to stress that, as we have shown, explicitly breaking the gauge invariance with a gauge fixing is not needed in order to generate the boson masses. The key point of the mass generation mechanism is, instead, the non-zero vacuum expectation value of ϕ. Englert has in fact pointed out that "In contradistinction to the global symmetry case, [...] local gauge symmetry cannot be spontaneously broken" by the ground state [249], namely the Nambu-Goldstone theorem does not apply here; for further discussions, see e.g. [250] and references therein.

Yang-Mills theory

The same mass generation mechanism can also be invoked in a $SU(N)$ Yang-Mills theory [251], if certain conditions among the representations of the fields are satisfied. For example, consider an N-tuple ϕ of complex scalar fields that transforms under the fundamental representation of $SU(N)$

$$\phi(x) \to U(x)\phi(x) = e^{i\vec{T}\cdot\vec{\alpha}(x)}\phi(x) = e^{iT^a\alpha^a(x)}\phi(x)\,, \tag{A.21}$$

where T^a are the generators of the gauge group. In a way completely analogous to the Abelian theory, we introduce the covariant derivative

$$\partial_\mu \to D_\mu = \partial_\mu - ig\,\vec{T}\cdot\vec{b}_\mu = \partial_\mu - ig\,T^a b^a_\mu\,, \tag{A.22}$$

where the gauge fields $b^a_\mu(x)$ transform under the adjoint representation of $SU(N)$ as

$$\vec{T}\cdot\vec{b}_\mu(x) \to U(x)\,\vec{T}\cdot\vec{b}_\mu(x)\,U^\dagger(x) + \frac{i}{g}\,U(x)\big(\partial_\mu U^\dagger(x)\big)\,. \tag{A.23}$$

Once again we assume $|\phi| > 0$; in the case where the $2N-1$ unphysical directions of ϕ are equal to the N^2-1 gauge vectors, namely in the $SU(2)$ case, we can change dynamical variables to

$$\phi(x) = e^{i\vec{T}\cdot\vec{\theta}(x)}\begin{pmatrix} 0 \\ \frac{\rho(x)}{\sqrt{2}} \end{pmatrix}, \tag{A.24}$$

$$\vec{T}\cdot\vec{B}_\mu(x) = e^{-i\vec{T}\cdot\vec{\theta}(x)}\,\vec{T}\cdot\vec{b}_\mu(x)\,e^{i\vec{T}\cdot\vec{\theta}(x)} + \frac{i}{g}\,e^{-i\vec{T}\cdot\vec{\theta}(x)}\partial_\mu\left(e^{i\vec{T}\cdot\vec{\theta}(x)}\right), \tag{A.25}$$

where ρ and B^a_μ are gauge invariant, while the pure gauge modes transform as $\theta^a \to \theta^a + \alpha^a$. One ends up with three massive B^a_μ vector fields and one massive scalar H, while the $SU(2)$ gauge invariance decouples from the physical content of the theory.

The standard electroweak theory

The EW sector of the Standard Model is based on a composite $SU(2) \otimes U(1)_Y$ gauge group; the action of $SU(2)$ decouples from the mass eigenstates, and only the residual $U(1)_Q$ gauge invariance of QED is manifest in the theory (the photon remains massless). Following the previous examples, we consider the Lagrangian

$$\mathcal{L}_{SU(2)\otimes U(1)} = -\frac{1}{4}\big(B_{\mu\nu}\big)^2 - \frac{1}{4}\big(w^a_{\mu\nu}\big)^2 + |D_\mu \phi|^2 - V(|\phi|)\,, \tag{A.26}$$

where the scalar field ϕ is an $SU(2)$ complex doublet that transforms under the fundamental representation, while the gauge bosons w^a_μ and B_μ live the adjoint representation of their respective gauge group, $SU(2)$ and $U(1)_Y$. The corresponding Yang-Mills and Abelian field strengths are

$$I^a w^a_{\mu\nu} = I^a\big(\partial_\mu w^a_\nu - \partial_\nu w^a_\mu - g_W \epsilon^{abc} w^b_\mu w^c_\nu\big)\,, \tag{A.27}$$

$$B_{\mu\nu} = \partial_\mu B_\nu - \partial_\nu B_\mu\,, \tag{A.28}$$

where we have denoted with I^a (in lieu of T^a) the isospin generators of $SU(2)$ ($a = 1, 2, 3$), which can be expressed in terms of Pauli matrices as $I^a = \sigma^a/2$, and ϵ^{abc} returns the structure constants of the $SU(2)$ algebra. As usual, ϕ and the gauge bosons interact through the covariant derivative

$$D_\mu = \partial_\mu - i g_W I^a w^a_\mu - i g_B Y B_\mu = \partial_\mu - i g_W\, w_\mu - i g_B Y B_\mu\,, \tag{A.29}$$

where $w_\mu \equiv I^a w^a_\mu$ and Y is the charge under $U(1)$ transformations; ϕ has $Y = 1/2$, while the w^a_μ have no charge. According to Eqs. (A.7) and (A.23), the fields undergo the following gauge transformations, where $U(x) = e^{iI^a\alpha^a(x)}$

$$\begin{aligned}
(\phi)^{U(1)} &= e^{i\alpha/2}\phi\,, & (\phi)^{SU(2)} &= U\phi\,,\\
(w_\mu)^{U(1)} &= w_\mu\,, & (w_\mu)^{SU(2)} &= U w_\mu U^\dagger + \frac{i}{g_W}\,U\big(\partial_\mu U^\dagger\big)\,,\\
(B_\mu)^{U(1)} &= B_\mu + \frac{1}{g_B}\,\partial_\mu\alpha\,, & (B_\mu)^{SU(2)} &= B_\mu\,.
\end{aligned} \tag{A.30}$$

Once again, we suppose that $\phi \neq 0$ everywhere, and as in Eq. (A.24) we rewrite it in terms of new dynamical variables $\rho(x) = v + H(x)$ and $\theta^a(x) = \xi^a(x)/v$

$$\phi = U_\theta \begin{pmatrix} 0 \\ \frac{\rho}{\sqrt{2}} \end{pmatrix}, \tag{A.31}$$

$$W_\mu = U_\theta^\dagger w_\mu(x) U_\theta + \frac{i}{g_W}\,U_\theta^\dagger\big(\partial_\mu U_\theta\big)\,, \tag{A.32}$$

where ρ and each of the three W^a_μ are $SU(2)$ gauge invariant, and we have conveniently defined $U_\theta = e^{iI^a\theta^a(x)}$ to keep the notation compact (not to be confused with $U = e^{iI^a\alpha^a(x)}$). We can then use the inverse relation

$$w_\mu = U_\theta W_\mu(x) U_\theta^\dagger - \frac{i}{g_W}\, U_\theta^\dagger \big(\partial_\mu U_\theta\big) \tag{A.33}$$

to express the covariant derivative in terms of W_μ, obtaining

$$\begin{aligned}
|D_\mu\phi|^2 &= \frac{1}{2}\left|\Big(\partial_\mu \mathbb{1}_2 - i g_W\, U_\theta W_\mu U_\theta^\dagger - U_\theta^\dagger\big(\partial_\mu U_\theta\big) - i\frac{g_B}{2}\, B_\mu \mathbb{1}_2\Big) U_\theta \begin{pmatrix} 0 \\ v+H \end{pmatrix}\right|^2 \\
&= \frac{1}{2}\left| U_\theta \begin{pmatrix} 0 \\ 1 \end{pmatrix}\big(\partial_\mu H\big) \;+\; \big(\partial_\mu U_\theta\big)\begin{pmatrix} 0 \\ v+H \end{pmatrix}\right. \\
&\qquad \left. - \left[U_\theta\, i g_W\, W_\mu + \big(\partial_\mu U_\theta\big) + U_\theta\, i\frac{g_B}{2}\, B_\mu \mathbb{1}_2 \right] \begin{pmatrix} 0 \\ v+H \end{pmatrix}\right|^2 \\
&= \frac{1}{2}\,\big(\partial_\mu H\big)^2 \\
&\quad + \frac{1}{2}\left| \frac{1}{2} \begin{bmatrix} g_W W^3_\mu + g_B B_\mu & g_W(W^1_\mu - iW^2_\mu) \\ g_W(W^1_\mu + iW^2_\mu) & -g_W W^3_\mu + g_B B_\mu \end{bmatrix} \begin{pmatrix} 0 \\ v+H \end{pmatrix}\right|^2 ,
\end{aligned} \tag{A.34}$$

from which we can immediately see that the would-be $SU(2)$ Goldstone bosons $\xi^a = v\theta^a$ have decoupled from the theory, together with any action of this group: B_μ, W^a_μ, v and H are all invariant under $SU(2)$ transformations.

We now show that the theory contains a residual $U(1)_Q$ gauge invariance associated with the electric charge

$$Q = Y + I^3\,, \tag{A.35}$$

which can be interpreted as the usual electromagnetism. The action of a $U(1)_Q$ transformation $e^{iQ\alpha}$ on ϕ, which has $Y = +1/2$, is

$$(\phi)^{U(1)_Q} = \begin{pmatrix} e^{i\alpha} & 0 \\ 0 & 1 \end{pmatrix} U_\theta \begin{pmatrix} 0 \\ v+H \end{pmatrix} \tag{A.36}$$

from which we deduce that the Higgs field H and the vacuum expectation value v are invariant under electromagnetic gauge transformations

$$v \to v\,, \qquad\qquad H \to H\,. \tag{A.37}$$

The analogous action of $U(1)_Q$ on W_μ, which has $Y = 0$, is given by

$$
\begin{aligned}
(W_\mu)^{U(1)_Q} &= \begin{pmatrix} e^{i\alpha/2} & 0 \\ 0 & e^{-i\alpha/2} \end{pmatrix} \frac{1}{2} \begin{bmatrix} W_\mu^3 & \sqrt{2} W_\mu^+ \\ \sqrt{2} W_\mu^- & -W_\mu^3 \end{bmatrix} \begin{pmatrix} e^{-i\alpha/2} & 0 \\ 0 & e^{i\alpha/2} \end{pmatrix} \\
&\quad + \frac{i}{g_W} \begin{pmatrix} e^{i\alpha/2} & 0 \\ 0 & e^{-i\alpha/2} \end{pmatrix} \partial_\mu \begin{pmatrix} e^{-i\alpha/2} & 0 \\ 0 & e^{i\alpha/2} \end{pmatrix} \\
&= \frac{1}{2} \begin{bmatrix} W_\mu^3 + \frac{1}{g_W}\,\partial_\mu \alpha & e^{i\alpha}\sqrt{2} W_\mu^+ \\ e^{-i\alpha}\sqrt{2} W_\mu^- & -W_\mu^3 - \frac{1}{g_W}\,\partial_\mu\alpha \end{bmatrix}, \qquad \text{(A.38)}
\end{aligned}
$$

where we have defined

$$
\sqrt{2} W_\mu^\pm = W_\mu^1 \mp i W_\mu^2 \,. \qquad \text{(A.39)}
$$

In summary, including also the transformation of the gauge field B_μ, we have

$$
W_\mu^\pm \to e^{\pm i\alpha} W_\mu^\pm \,, \qquad \text{(A.40)}
$$

$$
W_\mu^3 \to W_\mu^3 + \frac{1}{g_W}\,\partial_\mu\alpha \,, \qquad B_\mu \to B_\mu + \frac{1}{g_B}\,\partial_\mu\alpha \,. \qquad \text{(A.41)}
$$

Note that $W_\mu^\pm$ transform under the fundamental representation of $U(1)_Q$ with charge $Q = \pm 1$, respectively, while W_μ^3 and B_μ transform as gauge fields, but with different couplings g_W and g_B. If we take a suitable linear combination, we end up with the proper gauge field of $U(1)_Q$. To this purpose, we define the Weinberg angle θ_W as

$$
c_W = \cos\theta_W = \frac{g_W}{\sqrt{g_W^2 + g_B^2}} \,, \qquad s_W = \sin\theta_W = \frac{g_B}{\sqrt{g_W^2 + g_B^2}} \,, \qquad \text{(A.42)}
$$

and the Z_μ and A_μ fields as

$$
Z_\mu = c_W W_\mu^3 - s_W B_\mu \,, \qquad A_\mu = s_W W_\mu^3 + c_W B_\mu \,. \qquad \text{(A.43)}
$$

Being a combination of the B_μ and W_μ^3 fields, A_μ and Z_μ are invariant under $SU(2)$ as well; under $U(1)_Q$ transformations we have instead

$$
\begin{aligned}
\left(Z_\mu\right)^{U(1)_Q} &= \frac{g_W}{\sqrt{g_W^2 + g_B^2}} \left(W_\mu^3 + \frac{1}{g_W}\,\partial_\mu\alpha \right) \\
&\quad - \frac{g_B}{\sqrt{g_W^2 + g_B^2}} \left(B_\mu + \frac{1}{g_B}\,\partial_\mu\alpha \right) = Z_\mu \,, \qquad \text{(A.44)}
\end{aligned}
$$

$$
\left(A_\mu\right)^{U(1)_Q} = A_\mu + \left(\frac{s_W}{g_W} + \frac{c_W^2}{g_W\, s_W} \right) \partial_\mu\alpha = A_\mu + \frac{1}{e}\,\partial_\mu\alpha \,, \qquad \text{(A.45)}
$$

where we have defined the electromagnetic coupling

$$e = g_W \sin\theta_W \,. \tag{A.46}$$

In the end, the electromagnetic field A_μ correctly transforms as a gauge field under $U(1)_Q$, while the orthogonal combination Z_μ is completely decoupled from electromagnetic interactions.

We are now ready to express the EW Lagrangian of Eq. (A.26) in terms of physical mass eigenstates. After inverting the relations between $(A_\mu,\, Z_\mu)$ and $(W^3_\mu,\, B_\mu)$, the covariant derivative becomes

$$D_\mu = \partial_\mu - i g_W \big(I^- W^+_\mu + I^+ W^-_\mu \big) - ieQA_\mu - i\frac{g_W}{c_W}\big(I^3 - s_W^2 Q\big) Z_\mu \,, \tag{A.47}$$

where, in analogy with $W^\pm_\mu$, we have defined $\sqrt{2} I^\pm = I^1 \mp i I^2$. The derivative of ϕ in Eq. (A.34) is then given by

$$\begin{aligned} |D_\mu\phi|^2 &= \\ &= \frac{1}{2}\left(\partial_\mu H\right)^2 + \frac{1}{2}\left|\frac{1}{2}\begin{bmatrix} eA_\mu + \frac{g_W}{c_W}(1-2s_W^2)Z_\mu & g_W\sqrt{2}W^+_\mu \\ g_W\sqrt{2}W^-_\mu & \frac{g_W}{c_W}Z_\mu \end{bmatrix}\begin{pmatrix} 0 \\ v+H \end{pmatrix}\right|^2 \\ &= \frac{1}{2}\left(\partial_\mu H\right)^2 + \frac{1}{2}\left(2m_W^2 W^{+,\mu}W^-_\mu + m_Z^2 Z^\mu Z_\mu\right)\left(1+\frac{H}{v}\right)^2 , \end{aligned} \tag{A.48}$$

where the $W^\pm_\mu$ and Z_μ bosons have acquired a mass proportional to v and the gauge couplings, namely

$$m_W = \frac{g_W v}{2} \qquad \text{and} \qquad m_Z = \frac{g_W v}{2c_W} = \frac{m_W}{c_W} \,, \tag{A.49}$$

while the electromagnetic field A_μ remains massless, since it does not interact with the $Q = 0$ component of ϕ that acquires the non-zero v.

The full Lagrangian of the BEH sector in the EW theory also contains the Higgs boson mass and interaction terms from the potential $V(|\phi|)$, which are identical to the last line of Eq. (A.19)

$$-V(|\phi|) = -\frac{1}{2}\, m_H^2 H^2 - (\lambda v) H^3 - \frac{\lambda}{4}\, H^4 \,. \tag{A.50}$$

On top of that, there is the part describing Abelian and Yang-Mills gauge bosons; we postpone rewriting these field strengths in terms of $W^\pm_\mu$, Z_μ and A_μ to Section A.3.2, where we discuss the full EW theory including fermions.

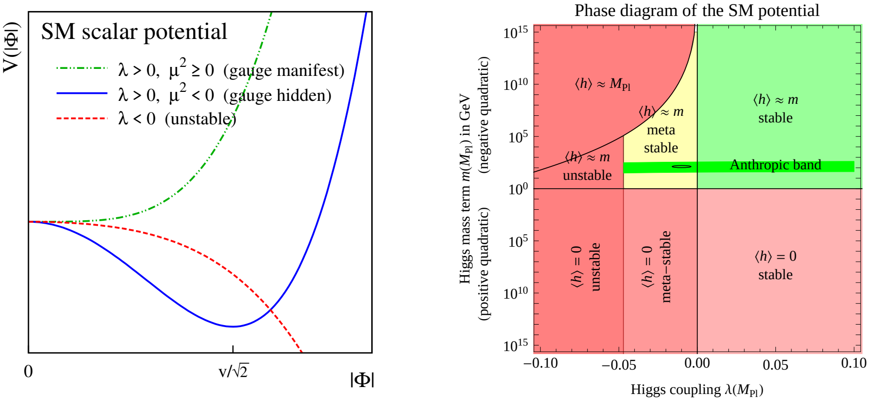

Figure A.1: Left plot: SM scalar potential, for different values of λ and μ^2. Right plot: SM phase diagram emerging from the scalar potential [73].

Quantum field theory

In the quantum version of the theory, one needs to eliminate redundant field configurations in order to solve the path integral. We have seen before that we can decouple the gauge symmetry from the physical content of the theory in a fully gauge-invariant way. An identical result can be obtained after an explicit breaking of gauge invariance, choosing the unitary gauge $\theta^a = 0$ ($i.e.$ $\xi^a = 0$). These equivalent choices are convenient for tree-level computations, since one can directly work with just the physical degrees of freedom.

This path is less straightforward as soon as we want to compute quantum corrections. In fact, renormalisability of theories featuring the BEH mechanism can be proven working with degrees of freedom where the original gauge symmetry of the theory is manifest, not hidden [245]. In practice, we still need a gauge fixing in order to solve the path integral, but we can employ a gauge different from the unitary one, for example a covariant R_ξ gauge. An important consequence is that the (would-be) Goldstone bosons ξ^a remain present among the fields, and one needs to work with these unphysical degrees of freedom, too.

The fact that some properties of the theory are more or less explicit depending on the choice of gauge is not a problem; on the contrary, it is a convenient way to use the symmetries of the theory in order to prove more easily its various aspects. The important point is that, since the gauge symmetry is just a redundancy in the description of the physical system, one is free to fix any gauge that may be more convenient to carry out the computation. In the end, gauge-dependent terms will cancel out in any physically meaningful quantity, since observables ought not to depend on the specific choice of gauge [252].

A.3 The Standard Model

The Standard Model is a gauge field theory based on the composite symmetry group $SU(3)_C \otimes SU(2)_L \otimes U(1)_Y$. It can be divided in two sectors: the QCD sector, associated to the $SU(3)_C$ symmetry, and the EW sector corresponding to $SU(2)_L \otimes U(1)_Y$. The EW sector undergoes the BEH mass generation mechanism presented in Section A.2, leaving only a manifest $U(1)_Q$ symmetry associated to QED. Therefore, the physical mass eigenstates of the SM exhibit a residual $SU(3)_C \otimes U(1)_Q$ gauge symmetry.

A.3.1 Quantum chromodynamics

Quantum chromodynamics (QCD) is a renormalisable gauge theory invariant under $SU(3)_C$ colour transformations[3], which describes the strong interactions of quarks and gluons. Quarks are spin-1/2 (spinor) objects which constitute the fermionic matter content of the theory, while gluons are spin-1 (vector) gauge bosons. Concerning their properties under gauge transformations, quarks q_j live in the 3-dimensional fundamental representation with colour basis $j = r, g, b$, while gluons live in the 8-dimensional adjoint representation generated by the $T^a_{jk} = \lambda^a_{jk}/2$, where λ^a_{jk} are the 3×3 Gell-Mann matrices ($a = 1, \ldots, 8$).

The classical QCD Lagrangian is given by two separate gauge-invariant pieces: the gauge boson part, describing the kinetic term and interactions of gluons in a Yang-Mills theory, and the fermionic matter part, describing the kinetic term of quarks and their interaction with gluons

$$\mathcal{L}^{cl}_{\mathrm{QCD}} = \mathcal{L}_{\mathrm{QCD:YM}} + \mathcal{L}_{\mathrm{QCD:f}} \,, \tag{A.51}$$

$$\mathcal{L}_{\mathrm{QCD:YM}} = -\frac{1}{2}\, G^{\mu\nu}_{jk} G_{\mu\nu,kj} \,, \tag{A.52}$$

$$\mathcal{L}_{\mathrm{QCD:f}} = \overline{q}_j \big(i\not{D}_{jk} - m_q \delta_{jk} \big) q_k \,, \tag{A.53}$$

where the gluon field strength $G_{\mu\nu}$ and the covariant derivative $\not{D} = \gamma^\mu D_\mu$ are given by

$$G_{\mu\nu,jk} = G^a_{\mu\nu} T^a_{jk} = \big(\partial_\mu G^a_\nu - \partial_\nu G^a_\mu - g_s f^{abc} G^b_\mu G^c_\nu \big)\, T^a_{jk} \,, \tag{A.54}$$

$$D_{\mu,jk} = \partial_\mu \delta_{jk} - i g_s G^a_\mu T^a_{jk} \,, \tag{A.55}$$

---

[3] There is no direct relation with the common meaning of colour; perhaps, it is just an analogy between the 3-dimensional basis of the quark polarisation states under the strong interactions and the RGB decomposition of colours as perceived by human eyes.

and f^{abc} are the structure constants of the algebra generating $SU(3)_C$. Note that the quark mass term $m_q\bar{q}q = m_q\big(\bar{q}_R q_L + \bar{q}_L q_R\big)$ does not break the $SU(3)_C$ gauge invariance of QCD. However, in the SM quarks also transform under the $SU(2)_L$ group of EW interactions, and a mass term would break such $SU(2)_L$ gauge invariance; therefore, we set the quark masses to zero for the moment[4]. In short, Eq. (A.51) is usually recast using the lighter notation

$$\mathcal{L}^{cl}_{\text{QCD}} = -\frac{1}{4}\,G^{a,\mu\nu}G^a_{\mu\nu} + \sum_{q=d,u,s,c,b,t} i\,\bar{q}\,\not{D}\,q\,, \tag{A.56}$$

where the fundamental j, k colour indices are implicit, we have made use of $\text{Tr}\left[T^a T^b\right] = \delta^{ab}/2$, and we have also summed over all the quark flavours.

The full quantum theory of QCD is obtained adding to the classical Lagrangian the gauge-fixing and the Faddeev-Popov ghost terms

$$\mathcal{L}_{\text{QCD}} = \mathcal{L}_{\text{QCD:YM}} + \mathcal{L}_{\text{QCD:f}} + \mathcal{L}_{\text{QCD:gfix}} + \mathcal{L}_{\text{QCD:gh}}\,, \tag{A.57}$$

which break the gauge invariance of $\mathcal{L}^{cl}_{\text{QCD}}$; of course, their explicit expressions depend on the choice of gauge. In the class of covariant R_ξ gauges, defined parametrically as

$$\mathcal{L}_{\text{QCD:gfix}} = -\frac{1}{2\xi}\left(\partial^\mu G^a_\mu\right)^2, \tag{A.58}$$

the ghost Lagrangian derived from the corresponding Faddeev-Popov functional determinant is

$$\mathcal{L}_{\text{QCD:gh}} = -\bar{c}^a D^{ab}_\mu \partial^\mu c^b = \left(\partial_\mu \bar{c}^a\right)\left(\partial^\mu c^a\right) - i g_s f^{abc} G^c_\mu \bar{c}^a \left(\partial^\mu c^b\right), \tag{A.59}$$

where $D^{ab}_\mu = \partial_\mu \delta^{ab} - i g_s G^c_\mu (T^c_A)^{ab} = \partial_\mu \delta^{ab} - i g_s f^{abc} G^c_\mu$ is the covariant derivative in the adjoint representation. Note that in an Abelian gauge theory the structure constant is null ($f = 0$) and thus the unphysical ghosts decouple from the physical fields and do not contribute to the scattering matrix, while in a Yang-Mills theory like QCD they must be taken into account (at least in internal loops) since they couple to gluons. The Feynman rules derived from the QCD Lagrangian Eq. (A.57) are collected in Table A.1.

When computing higher-order quantum corrections in g_s, the fields in the Lagrangian need to be renormalised in order to preserve the LSZ conditions of Eq. (A.3); this is achieved rescaling the fields by multiplicative factors Z_i. As a result, we will have further Feynman rules representing the renormalisation counterterms, see e.g. Appendix C in *Pokorski* [248].

---

[4] In Section A.3.2 we will generate quark masses via the gauge-invariant Yukawa interaction.

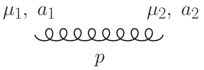

$$= \frac{i\delta^{a_1 a_2}}{p^2 + i0}\left[-g^{\mu\nu} + (1-\xi)\,\frac{p^{\mu_1}p^{\mu_2}}{p^2}\right]$$

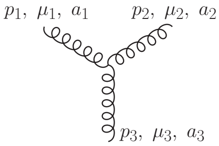

$$= -g_s\, f^{a_1 a_2 a_3}\Big[g^{\mu_1\mu_2}\,(p_1 - p_2)^{\mu_3} + g^{\mu_2\mu_3}\,(p_2 - p_3)^{\mu_1} + g^{\mu_3\mu_1}\,(p_3 - p_1)^{\mu_2} \Big]$$

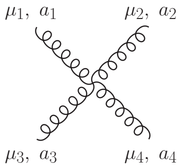

$$\begin{aligned} = -ig_s^2 \Big[& f^{a_1 a_2 b} f^{a_3 a_4 b}\big(g^{\mu_1\mu_3}g^{\mu_2\mu_4} - g^{\mu_1\mu_4}g^{\mu_2\mu_3}\big) \\ & + f^{a_1 a_3 b} f^{a_2 a_4 b}\big(g^{\mu_1\mu_2}g^{\mu_3\mu_4} - g^{\mu_1\mu_4}g^{\mu_2\mu_3}\big) \\ & + f^{a_1 a_4 b} f^{a_2 a_3 b}\big(g^{\mu_1\mu_2}g^{\mu_3\mu_4} - g^{\mu_1\mu_3}g^{\mu_2\mu_4}\big) \Big] \end{aligned}$$

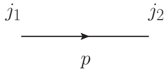

$$= \frac{i\big(\not{p} + m\big)\,\delta_{j_1 j_2}}{p^2 - m^2 + i0}$$

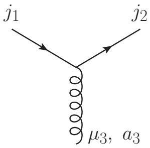

$$= ig_s\gamma^{\mu_3}T^{a_3}_{j_1 j_2}$$

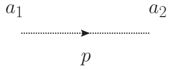

$$= \frac{i\delta^{a_1 a_2}}{p^2 + i0}$$

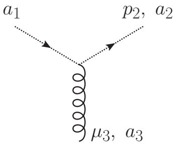

$$= -g_s f^{a_1 a_2 a_3} p_2^{\mu_3}$$

Table A.1: List of the Feynman rules derived from the QCD Lagrangian, in the covariant R_ξ gauge. Momenta are outgoing.

A.3.2 Electroweak theory

The second sector of the Standard Model is given by the theory of electroweak (EW) interactions, a renormalisable gauge theory that unifies the description of electromagnetic and weak nuclear interactions at high energies. It is based on the composite $SU(2)_L \otimes U(1)_Y$ group of weak isospin and hypercharge transformations, where the $SU(2)_L$ subgroup acts differently on the fermion chiralities: left-handed fermions transform under the fundamental representation, while there is no action on the right-handed components (trivial representation). Left- and right-handed fermions also have different charges under $U(1)_Y$. The gauge bosons couple to a scalar field with non-zero value in the ground state, and undergo the BEH mechanism described in Section A.2, which gives mass to the $W_\mu^\pm$ and Z_μ weak bosons. The theory's mass eigenstates retain a manifest residual QED gauge invariance $U(1)_Q$ associated with the massless photon A_μ.

Gauge invariance

The classical EW Lagrangian is given by four separately gauge-invariant pieces: the gauge boson part, describing the spin-1 Yang-Mills vector fields $W^{a,\mu}$ and the Abelian vector field B^μ; the BEH part, describing the kinetic and the potential terms of a spin-0 complex scalar field, and its interaction with the gauge bosons; the fermionic part, which describes the kinetic term of spin-1/2 fermions (quarks and leptons) plus their interaction with gauge bosons; and finally the Yukawa part, describing the interaction of fermions with the scalar field. These parts read

$$\mathcal{L}_{\text{EW}}^{cl} = \mathcal{L}_{\text{EW:gauge}} + \mathcal{L}_{\text{EW:BEH}} + \mathcal{L}_{\text{EW:f}} + \mathcal{L}_{\text{EW:Yu}} \,, \tag{A.60}$$

$$\mathcal{L}_{\text{EW:gauge}} = -\frac{1}{4}\, W^{a,\mu\nu} W^a_{\mu\nu} - \frac{1}{4}\, B^{\mu\nu} B_{\mu\nu} \,, \tag{A.61}$$

$$\mathcal{L}_{\text{EW:BEH}} = \left| D_\mu \phi \right|^2 - V(\phi) \,, \tag{A.62}$$

$$\begin{aligned} \mathcal{L}_{\text{EW:f}} = \sum_{m=1,2,3} i \Big[& \overline{Q}{}^m_L \not{D}\, Q^m_L \;\; + \overline{d}{}^m_R \not{D}^{(1)} d^m_R \;\; + \overline{u}{}^m_R \not{D}^{(1)} u^m_R \\ & + \overline{L}{}^m_L \not{D}\, L^m_L \;\; + \overline{e}{}^m_R \not{D}^{(1)} e^m_R \Big] \,, \end{aligned} \tag{A.63}$$

$$\begin{aligned} \mathcal{L}_{\text{EW:Yu}} = & -\lambda_d^{mn} \big(\overline{Q}{}^m_L \phi \big) d^n_R \;\; - \lambda_u^{mn} \big(\overline{Q}{}^m_L \widetilde{\phi}^\dagger \big) u^n_R \\ & - \lambda_e^{mn} \big(\overline{L}{}^m_L \phi \big) e^n_R \;\; + \text{h.c.} \,, \end{aligned} \tag{A.64}$$

where $\not{D} = D_\mu \gamma^\mu$, and the covariant derivative under the full group is

$$D_{\mu,jk} = \partial_\mu \delta_{jk} - i g_W I^a_{jk} W^a_\mu - i g_B Y B_\mu \delta_{jk} \,. \tag{A.65}$$

As usual, the gauge bosons live in the adjoint representation of their respective gauge group; the corresponding Yang-Mills and Abelian field strengths are

$$W^a_{\mu\nu} I^a_{jk} = \big(\partial_\mu W^a_\nu - \partial_\nu W^a_\mu - g_W \epsilon^{abc} W^b_\mu W^c_\nu\big) I^a_{jk}\,, \tag{A.66}$$

$$B_{\mu\nu} = \partial_\mu B_\nu - \partial_\nu B_\mu\,, \tag{A.67}$$

where $I^a_{jk} = \sigma^a_{jk}/2$ are the generators of $SU(2)_L$ ($a = 1, 2, 3$), and ϵ^{abc} the structure constants of the related algebra.

The gauge-invariant potential of the complex scalar field is completely analogous to the one presented in Section A.2

$$V(|\phi|) = \lambda \left(|\phi|^2 + \frac{\mu^2}{\lambda}\right)^2\,, \tag{A.68}$$

which triggers the BEH mechanism because we suppose $\mu^2 < 0$, thus $|\phi| > 0$.

Both the complex scalar field and left-handed fermion fields transforms under the fundamental representation of $SU(2)_L$, namely are isospin doublets ϕ_j and $\psi_{L,j}$, with u-type and d-type components. On the other hand, right-handed fermions do not transform under $SU(2)_L$, and thus their covariant derivative is limited to the $U(1)_Y$ group

$$D^{(1)}_\mu = \partial_\mu - i g_B Y B_\mu\,. \tag{A.69}$$

Fermions are divided in quarks (which undergo also QCD strong interactions) and leptons (which don't); the quark $SU(2)$ doublet consists of the up and down quarks, while the lepton doublet consists of the electron and its neutrino. Moreover, this is repeated for three identical generations of quarks and leptons, which we denote with the family index $m = 1, 2, 3$

$$Q^m_L = \begin{pmatrix} u^m_L \\ d^m_L \end{pmatrix}\,,\; u^m_R\,,\; d^m_R\,, \quad \text{where} \quad \begin{array}{lll} u^1 = u\,, & u^2 = c\,, & u^3 = t \\ d^1 = d\,, & d^2 = s\,, & d^3 = b \end{array}\,, \tag{A.70}$$

$$L^m_L = \begin{pmatrix} \nu^m_L \\ e^m_L \end{pmatrix}\,,\; e^m_R\,, \quad \text{where} \quad \begin{array}{lll} \nu^1 = \nu_e\,, & \nu^2 = \nu_\mu\,, & \nu^3 = \nu_\tau \\ e^1 = e\,, & e^2 = \mu\,, & e^3 = \tau \end{array}\,. \tag{A.71}$$

In Table A.2 we summarise the properties of the scalar and the fermionic matter fields under the SM gauge interactions: their representations in the two non-Abelian gauge groups, and their Abelian charge Y. Note that $Q = Y$ for right-handed fermions, and $U(1)$ chiral anomalies are avoided since the hypercharges in each fermionic generation m sum to zero (three coloured quarks exist for each uncoloured lepton). Also, there are no right-handed neutrinos in the minimal formulation of the Standard Model, being sterile under its gauge group.

spin-$\frac{1}{2}$	$SU(3)_C$	$SU(2)_L$	$U(1)_Y$	spin-1	$SU(3)_C$	$SU(2)_L$	$U(1)_Y$
Q_L	**3**	**2**	+1/6	G_μ	**8**	**1**	0
u_R	**3**	**1**	+2/3	W_μ	**1**	**3**	0
d_R	**3**	**1**	−1/3	B_μ	**1**	**1**	0
L_L	**1**	**2**	−1/2	spin-0			
e_R	**1**	**1**	−1	ϕ	**1**	**2**	+1/2

Table A.2: On the left: list of the spin-1/2 fermions in the Standard Model, together with their properties under the gauge groups. The $SU(3)_C$ and $SU(2)_L$ irreducible representations and the $U(1)_Y$ weak hypercharge are reported. A possible sterile ν_R (**1**, **1**, 0) field is not included. On the right: analogous table for the SM bosons (spin-1 gauge and spin-0 Higgs fields).

The last ingredient of the EW Lagrangian is the Yukawa sector, where λ^{mn} are in general complex-valued matrices that couple the left-handed and right-handed components of different generations of fermions, via the interaction with the scalar doublet. The structure of this interaction is slightly different for u-type and d-type Yukawa matrices; showing explicitly the $SU(2)_L$ indices we have $Q_L\phi = \delta_{jk}\overline{Q}_{L,j}\phi_k$ and $Q_L\widetilde{\phi}^\dagger = \epsilon_{jk}\overline{Q}_{L,j}\phi^*_k$. This will play an important role in the generation of fermion masses. Note that the SM Yukawa sector contains all the four-dimensional operators that can couple fermionic currents to the scalar field, and dimensional analysis shows that there cannot be such operators with dimension lower than four. Moreover, we need a field ϕ living in the same representation of Q_L and L_L, namely an $SU(2)_L$ doublet, and that has non-zero hypercharge too, in order to get a fully gauge-invariant operator (**1**,**1**,0) that can connect left-handed components of fermions to the right-handed ones, which live in different $SU(2)_L$ representations and have different $U(1)_Y$ charges.

As we already know, for the quantum version of the theory we need to choose a gauge, for example adding a covariant gauge-fixing term to the Lagrangian, and also the Faddeev-Popov ghosts related to the Yang-Mills part. As we have already discussed at the end of Section A.2, in a manifestly renormalisable procedure the (would-be) Goldstone bosons will appear; results can be found *e.g.* in *Pokorski* [248]. Since we are not interested in higher-order EW corrections throughout this thesis, we will just proceed to work out the physical mass eigenstates of the theory, ignoring Goldstone bosons and ghosts.

Physical bosons

We have seen in Section A.2 that, instead of following a gauge-invariant procedure, a convenient shortcut to compute the mass eigenstates of the theory is to fix the unitary gauge, as originally done by Weinberg in [8]. Here we shall proceed in the same way, setting from the beginning

$$\phi(x) = \frac{1}{\sqrt{2}} \begin{pmatrix} 0 \\ v + H(x) \end{pmatrix} , \tag{A.72}$$

which immediately implies

$$\begin{aligned} \mathcal{L}_{\mathrm{EW:BEH}} = {} & \frac{1}{2} \left(\partial_\mu H\right)^2 - \frac{1}{2}\, m_H^2 H^2 - (\lambda v) H^3 - \frac{\lambda}{4}\, H^4 \\ & + \left(m_W^2\, W^{+,\mu} W_\mu^- \, + \frac{1}{2}\, m_Z^2\, Z^\mu Z_\mu \right) \left(1 + \frac{H}{v} \right)^2 , \end{aligned} \tag{A.73}$$

where $m_H = \sqrt{2\lambda} v$, $m_W = \frac{g_W v}{2}$ and $m_Z = \frac{m_W}{c_W}$. The gauge bosons $W_\mu^\pm$, A_μ and Z_μ have been defined in Section A.2. The field-strength sector of these gauge bosons becomes

$$\mathcal{L}_{\mathrm{EW:gauge}} = \mathcal{L}_{\mathrm{kin}} + \mathcal{L}_{3\mathrm{V}} + \mathcal{L}_{4\mathrm{V}} \, , \tag{A.74}$$

where

$$\mathcal{L}_{\mathrm{kin}} = -\frac{1}{4} \left(A_{\mu\nu}\right)^2 - \frac{1}{4} \left(Z_{\mu\nu}\right)^2 - \frac{1}{2}\, W^{+,\mu\nu} W^-_{\mu\nu} \, , \tag{A.75}$$

$$\begin{aligned} & \mathcal{L}_{3\mathrm{V}} = \\ & = - ie\, \frac{c_W}{s_W} \left[Z^\mu \left(W^+_{\mu\nu} W^{-,\nu} - W^-_{\mu\nu} W^{+,\nu} \right) - \frac{1}{2}\, Z^{\mu\nu} \left(W^+_\mu W^-_\nu - W^-_\mu W^+_\nu \right) \right] \\ & \quad - ie \Big[A^\mu \left(W^+_{\mu\nu} W^{-,\nu} - W^-_{\mu\nu} W^{+,\nu} \right) - \frac{1}{2}\, A^{\mu\nu} \left(W^+_\mu W^-_\nu - W^-_\mu W^+_\nu \right) \Big] , \end{aligned} \tag{A.76}$$

$$\begin{aligned} \mathcal{L}_{4\mathrm{V}} = {} & e^2 \left[\frac{1}{2}\, A^\mu A^\nu \left(W^+_\mu W^-_\nu + W^-_\mu W^+_\nu \right) - \left(A_\mu\right)^2 W^{+,\nu} W^-_\nu \right] \\ & + e^2\, \frac{c_W}{s_W} \left[A^\mu Z^\nu \left(W^+_\mu W^-_\nu + W^-_\mu W^+_\nu \right) - A^\mu Z_\mu W^{+,\nu} W^-_\nu \right] \\ & + e^2\, \frac{c_W^2}{s_W^2} \left[\frac{1}{2}\, Z^\mu Z^\nu \left(W^+_\mu W^-_\nu + W^-_\mu W^+_\nu \right) - \left(Z_\mu\right)^2 W^{+,\nu} W^-_\nu \right] \\ & + e^2\, \frac{1}{s_W^2} \left[\frac{1}{2} \left(W^+_\mu\right)^2 \left(W^-_\nu\right)^2 - \frac{1}{4} \left(W^{+,\mu} W^-_\mu \right)^2 \right] . \end{aligned} \tag{A.77}$$

Physical fermions and mixing

We can work out the fermionic mass eigenstates from the Yukawa terms. For simplicity, start considering only one generation of quarks

$$\begin{aligned}\mathcal{L}^{d,u}_{\text{EW:Yu}} = &- \lambda_d \left(\bar{u}_L \;\; \bar{d}_L\right) \frac{1}{\sqrt{2}} \begin{pmatrix} 0 \\ v + H \end{pmatrix} d_R \\ &- \lambda_u \left(\bar{u}_L \;\; \bar{d}_L\right) \frac{1}{\sqrt{2}} \begin{pmatrix} v + H \\ 0 \end{pmatrix} u_R \;+ \text{h.c.}\,; \end{aligned} \tag{A.78}$$

if we also suppose λ to be real parameters, we immediately obtain

$$= - m_d\, \bar{d}d \left(1 + \frac{H}{v}\right) - m_u\, \bar{u}u \left(1 + \frac{H}{v}\right), \tag{A.79}$$

where $m_j = v\lambda_j/\sqrt{2}$ for $j = d, u$. If instead we consider the more general case of complex Yukawa couplings, they can always be written as $\lambda_j e^{i\alpha_j}$ with λ_j real; in this case we have

$$\begin{aligned}\mathcal{L}^{d,u}_{\text{EW:Yu}} = &- v \frac{\lambda_d}{\sqrt{2}} \left(e^{i\alpha_d} \bar{d}_L d_R + e^{-i\alpha_d} \bar{d}_R d_L\right) \left(1 + \frac{H}{v}\right) \\ &- v \frac{\lambda_u}{\sqrt{2}} \left(e^{i\alpha_u} \bar{u}_L u_R + e^{-i\alpha_u} \bar{u}_R u_L\right) \left(1 + \frac{H}{v}\right). \end{aligned} \tag{A.80}$$

Since, however, the overall phase of a fermion is not physically observable, we can always redefine the left- and right-handed quark components such that

$$\bar{d}_R d_L \to e^{i\alpha_d} \bar{d}_R d_L\,, \qquad \bar{u}_R u_L \to e^{i\alpha_u} \bar{u}_R u_L\,, \tag{A.81}$$

after which we obtain the same Lagrangian as in Eq. (A.79).

Consider now the case where many generations of particles are present. In general we have complex Yukawa matrices λ_d^{mn} and λ_u^{mn}; however, we can always take appropriate unitary transformations on the quark chiral fields

$$d_L^m \to \mathcal{U}_{d,L}^{mn}\, d_L^n\,, \qquad d_R^m \to \mathcal{U}_{d,R}^{mn}\, d_R^n\,, \tag{A.82}$$

$$u_L^m \to \mathcal{U}_{u,L}^{mn}\, u_L^n\,, \qquad u_R^m \to \mathcal{U}_{u,R}^{mn}\, u_R^n\,, \tag{A.83}$$

which diagonalise the Yukawa couplings

$$\tfrac{\sqrt{2}}{v}\, M_d = \mathcal{U}_{d,L}\, \lambda_d\, \mathcal{U}_{d,R}^\dagger\,, \qquad \tfrac{\sqrt{2}}{v}\, M_u = \mathcal{U}_{u,L}\, \lambda_u\, \mathcal{U}_{u,R}^\dagger\,, \tag{A.84}$$

into the mass matrices M_d and M_u. This results in quark mass terms and interactions with the Higgs boson, that are related once again by $m(1 + H/v)$

$$\mathcal{L}^{\text{quarks}}_{\text{EW:Yu}} = \sum_{q=d,u,s,c,b,t} - m_q\, q\bar{q} \left(1 + \frac{H}{v}\right). \tag{A.85}$$

An analogous treatment of charged (e-type) leptons yields

$$e_L^m \to \mathcal{U}_{e,L}^{mn}\, e_L^n\,, \qquad\qquad e_R^m \to \mathcal{U}_{e,R}^{mn}\, e_R^n\,, \tag{A.86}$$

$$\mathcal{L}_{\text{EW:Yu}}^{\text{leptons}} = \sum_{\ell=e,\mu,\tau} - m_\ell\, \ell\bar{\ell}\left(1+\frac{H}{v}\right), \tag{A.87}$$

while neutrinos remain massless since ν_R fields are not included in the SM.

Note that the possibility to diagonalise the Yukawa matrices means that any complex phase $e^{i\theta\gamma_5}$ in the masses of fermions is not physically observable, namely there are no pseudoscalar mass terms of the form $m\bar{\psi}\gamma_5\psi$, nor analogous pseudoscalar interactions with the Higgs boson. After having used our freedom to redefine the global phase of SM fermions and diagonalise their mass terms, pseudoscalar interactions between the Higgs and fermions can appear if we introduce further BSM "Yukawa-like" operators with complex couplings; an example can be the dimension-six operator in Eq. (2.7).

We now address the remaining sector of the EW Lagrangian, Eq. (A.63), which contains derivative terms for the fermions and their interactions with the EW bosons. After having diagonalised the mass terms in the Yukawa Lagrangian with the transformations in Eqs. (A.82), (A.83) and (A.86), we obtain

$$\begin{aligned}\mathcal{L}_{\text{EW:f}} = \sum_{m=1,2,3}\ \sum_{f=d,u,e,\nu} \Big\{ & i\bar{f}^m \partial\!\!\!/ f^m \ + \ e\,Q_f\, \bar{f}^m\gamma^\mu f^m A_\mu \\ & + \ \frac{e}{c_W s_W}\, \bar{f}^m\Big[I_f^3\gamma^\mu \tfrac{1}{2}(1-\gamma_5) - Q_f s_W^2\gamma^\mu\Big] f^m Z_\mu \Big\} \\ + \sum_{m=1,2,3} \frac{e}{s_W}\frac{1}{\sqrt{2}} \Big[& \bar{d}_L^m \big(V_{\text{CKM}}^\dagger\big)_{mn}\gamma^\mu u_L^n\, W_\mu^+ \ + \ \bar{u}_L^m\big(V_{\text{CKM}}\big)_{mn}\gamma^\mu d_L^n\, W_\mu^- \\ & + \ \bar{e}_L^m\gamma^\mu\nu_L^m\, W_\mu^+ \ + \ \bar{\nu}_L^m\gamma^\mu e_L^m\, W_\mu^- \Big]\,, \end{aligned} \tag{A.88}$$

where we have employed the leftover freedom to transform the ν_L fields in order to reabsorb $\mathcal{U}_{e,L}$, and we have defined the Cabibbo-Kobayashi-Maskawa (CKM) matrix as

$$V_{\text{CKM}} = \mathcal{U}_{u,L}\,\mathcal{U}_{d,L}^\dagger = \begin{pmatrix} V_{ud} & V_{us} & V_{ub} \\ V_{cd} & V_{cs} & V_{cb} \\ V_{td} & V_{ts} & V_{tb}\end{pmatrix}. \tag{A.89}$$

As we can see, after mass diagonalisation in the Yukawa Lagrangian, we can have *mixing* among quarks of different families. Thus, only the total baryon number is conserved, but not each separate quark flavour. In particular, mixing happens via the charged currents associated with the $W_\mu^\pm$ bosons; in other words, the eigenstates of charged weak interactions are a linear combination of the mass eigenstates. On the other hand, the remaining electroweak neutral currents mediated by A_μ and Z_μ are flavour diagonal. For N quark families, the CKM matrix allows to reabsorb $2N-1$ unobservable field phases, leaving $N(N-1)/2$ physical mixing angles among the quark families, and $(N-1)(N-2)/2$ observable complex phases. With two quark families, we have the Cabibbo mixing angle. With three quark families, as in the SM, there are three mixing angles and one complex phase; the latter allows for CP violation in the EW interactions, since a CP transformation on the Yukawa Lagrangian is equivalent to the substitution $\lambda_j \to \lambda_j^\dagger$.

In the case of leptons, on the other hand, the absence of neutrino masses results in solely flavour-diagonal interactions (both charged and neutral currents), namely in the conservation of each separate lepton flavour. If we extend the SM adding right-handed sterile neutrinos, and the neutrino Yukawa operators, then we can have mixing also among leptons, described by the Pontecorvo-Maki-Nakagawa-Sakata matrix.

A.4 Success and open problems

The Standard Model has been an incredibly successful theory of fundamental interactions. Nevertheless, we know from both theoretical and experimental arguments that it cannot be the ultimate model, but just an excellent approximation of a more general theory in the experimental regime tested so far.

For instance, the SM does not include gravity among the fundamental forces. Albeit this interaction is completely negligible in current and foreseeable particle experiments, the effects of quantum gravity are expected to be important approaching the Planck scale $\Lambda_\mathrm{P} \sim 10^{18-19}$ GeV. Moreover, the amount of CP violation in the EW sector seems insufficient to describe the observed asymmetry between matter and antimatter in our universe. A CP-violating term in the strong interactions $-\,\theta\,\frac{\alpha_s}{8\pi}\,G^{a,\mu\nu}\widetilde{G}^a_{\mu\nu}$ is not forbidden by the SM gauge symmetries, and can be observable if all quarks have non-zero masses. However, it is bound from experimental limits to be zero or highly suppressed ($\theta < 10^{-10}$); this is known as the strong CP problem. Compelling evidence of BSM physics is given by experimental results on neutrino mixing and oscillations, which point to non-zero neutrino masses. One could just make a minimal extension of the SM by adding sterile right-handed neutrinos, and parametrising their small masses in the respective Yukawa couplings. Majorana neutrino mass terms are

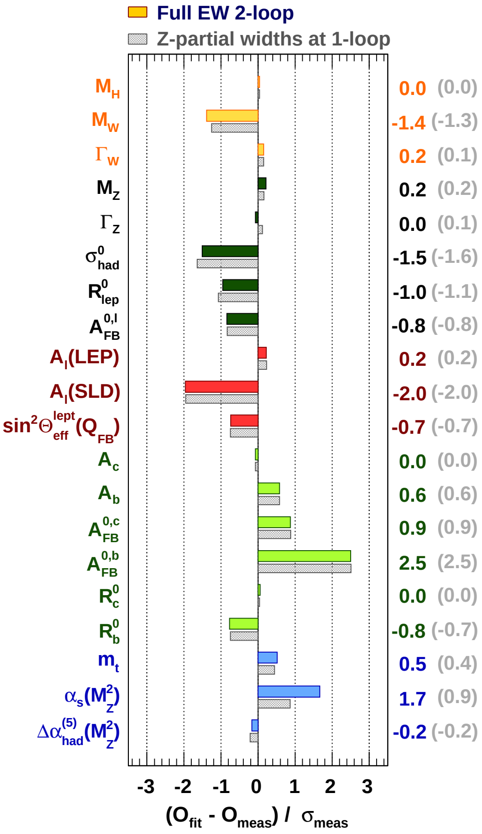

Figure A.2: Fit of the Standard Model to HEP data: deviations between experimental measurements and theoretical calculations, in units of the experimental uncertainty. Taken from [87].

also allowed without breaking the SM gauge invariance, and searched for in neutrinoless double beta decays.

A popular theoretical argument is the large separation between the EW scale v and the Planck scale Λ_{Planck}, which is known as the hierarchy problem. While many solutions have been proposed, ranging from supersymmetry to composite Higgs models, from extra dimensions to the multiverse and the anthropic principle, there is currently no consensus on how to solve it. Another example of hierarchy problem is why the electron and the top mass are so different (six orders of magnitude) if they are both generated by the same BEH mechanism; this is exacerbated if we introduce tiny neutrino masses.

Appendix B

The Higgs Characterisation model at NLO

In this Appendix we present the complete Higgs Characterisation (HC) model at NLO, which has been introduced in Ref. [15] and used to produce many results presented throughout this thesis. We recall that this model is relevant for the phenomenology of single-Higgs processes, and provides a flexible tool based on both the so-called κ framework and a simplified SM EFT (in particular, operators that do not directly affect Higgs processes are not included, as well as dimension-six contact interactions between the Higgs, a gauge boson and two fermions). For a mapping between the HC and other SM EFT basis, we refer to [19, 253].

The HC Lagrangian is expressed in terms of SM mass eigenstates, for a generic spin-0 boson X_0 with both scalar and pseudoscalar couplings. The interaction of such a boson with third generation fermions can be written as

$$\mathcal{L}_0^f = -\sum_{f=t,b,\tau} \frac{m_f}{v}\,\bar{\psi}_f \big(c_\alpha \kappa_{Hff} + i s_\alpha \kappa_{Aff}\,\gamma_5\big)\psi_f\, X_0\,, \tag{B.1}$$

where m_f is the fermion mass and $v = \big(\sqrt{2}G_\mu\big)^{-1/2}$ is the electroweak vacuum expectation value;

$$c_\alpha \equiv \cos\alpha \qquad \text{and} \qquad s_\alpha \equiv \sin\alpha \tag{B.2}$$

are interpreted as CP-mixing parameters, while $\kappa_{Htt,Att}$ are dimensionless and real rescaling factors. While obviously redundant (only two independent real quantities are needed to parametrise the most general CP-violating interaction between a spin-0 and two spin-1/2 particles at dimension four), this parametrisation has some practical advantages, among which the possibility of easily interpolating between the CP-even ($c_\alpha = 1, s_\alpha = 0$) and CP-odd ($c_\alpha = 0, s_\alpha = 1$) assignments, as well as easily recovering the SM case when $\alpha = 0$ and $\kappa_{Hff} = 1$.

The HC Lagrangian for the interactions with massive gauge bosons reads

$$\begin{aligned}\mathcal{L}_0^{Z,W} = \bigg\{ & c_\alpha \kappa_{\rm SM} \left[\frac{1}{2} g_{HZZ}\, Z_\mu Z^\mu + g_{HWW}\, W_\mu^+ W^{-\mu} \right] \\ & - \frac{1}{4}\frac{1}{\Lambda} \left[c_\alpha \kappa_{HZZ}\, Z_{\mu\nu} Z^{\mu\nu} + s_\alpha \kappa_{AZZ}\, Z_{\mu\nu} \widetilde{Z}^{\mu\nu} \right] \\ & - \frac{1}{2}\frac{1}{\Lambda} \left[c_\alpha \kappa_{HWW}\, W^+_{\mu\nu} W^{-\mu\nu} + s_\alpha \kappa_{AWW}\, W^+_{\mu\nu} \widetilde{W}^{-\mu\nu} \right] \\ & - \frac{1}{\Lambda} c_\alpha \left[\kappa_{H\partial Z}\, Z_\nu \partial_\mu Z^{\mu\nu} + \left(\kappa_{H\partial W} W_\nu^+ \partial_\mu W^{-\mu\nu} + \text{h.c.} \right) \right] \bigg\} X_0 \,, \end{aligned} \tag{B.3}$$

where $g_{HZZ} = 2m_Z^2/v$ and $g_{HWW} = 2m_W^2/v$ are the SM couplings, Λ is the cutoff scale for higher-dimensional interactions, and κ_i are dimensionless constants, which can be taken real without loss of generality, with the exception of $\kappa_{H\partial W}$. The (reduced) field strength tensors are defined as

$$V_{\mu\nu} = \partial_\mu V_\nu - \partial_\nu V_\mu \quad (V = A, Z, W^\pm)\,, \tag{B.4}$$

and the dual tensor is

$$\widetilde{V}_{\mu\nu} = \frac{1}{2}\epsilon_{\mu\nu\rho\sigma} V^{\rho\sigma}\,. \tag{B.5}$$

Finally, the Higgs interaction with the top quark and the W boson induces, in the limit where these particles are heavy, (non-decoupling) effective couplings to photons, gluons, and photon-Z bosons, through loop diagrams that are present already in the SM. In the HC framework, the effective Lagrangian for these loop-induced interactions reads

$$\begin{aligned}\mathcal{L}_0^{\rm loop} = \bigg\{ & - \frac{1}{4} \left[c_\alpha \kappa_{Hgg} g_{Hgg}\, G^a_{\mu\nu} G^{a,\mu\nu} + s_\alpha \kappa_{Agg} g_{Agg}\, G^a_{\mu\nu} \widetilde{G}^{a,\mu\nu} \right] \\ & - \frac{1}{4} \left[c_\alpha \kappa_{H\gamma\gamma} g_{H\gamma\gamma}\, A_{\mu\nu} A^{\mu\nu} + s_\alpha \kappa_{A\gamma\gamma} g_{A\gamma\gamma}\, A_{\mu\nu} \widetilde{A}^{\mu\nu} \right] \\ & - \frac{1}{2} \left[c_\alpha \kappa_{HZ\gamma} g_{HZ\gamma}\, Z_{\mu\nu} A^{\mu\nu} + s_\alpha \kappa_{AZ\gamma} g_{AZ\gamma}\, Z_{\mu\nu} \widetilde{A}^{\mu\nu} \right] \bigg\} X_0 \,, \end{aligned} \tag{B.6}$$

where

$$G^a_{\mu\nu} = \partial_\mu G^a_\nu - \partial_\nu G^a_\mu + g_s f^{abc} G^b_\mu G^c_\nu \,. \tag{B.7}$$

g_{Xvv}	gg	$\gamma\gamma$	$Z\gamma$
$X = H$	$-\alpha_s/3\pi v$	$47\alpha_{\rm EM}/18\pi v$	$C(94c_W^2 - 13)/9\pi v$
$X = A$	$\alpha_s/2\pi v$	$4\alpha_{\rm EM}/3\pi v$	$2C(8c_W^2 - 5)/3\pi v$

Table B.1: Loop-induced couplings $g_{Xyy'}$ in the Lagrangian (B.6). The shorthand $c_W = \cos\theta_W$ is the cosine of the Weinberg angle, and $C = \sqrt{\frac{\alpha_{\rm EM} G_F m_Z^2}{8\sqrt{2}\pi}}$.

parameter	description
Λ [GeV]	cutoff scale
c_α ($\equiv \cos\alpha$)	mixing between 0^+ and 0^-
κ_i	dimensionless rescaling parameter

Table B.2: HC model parameters.

We note that the gluonic operators provide not only the ggX_0, but also the $gggX_0$ and $ggggX_0$ effective vertices; for detailed information see Appendix C.[1] In the $X_0\gamma\gamma$ and $X_0Z\gamma$ interactions, in addition to the top-quark loop, a W-boson loop contributes for the CP-even case and in fact dominates. The dimensionful loop-induced couplings g_{Xvv} are shown in table B.1.

The LO Feynman rules derived from the HC Lagrangian have been automatically obtained by means of FeynRules, whose output in the UFO format [58, 254] can be directly passed to MadGraph5_aMC@NLO in order to obtain event simulations (at LO). The LO model actually contains also Lagrangian describing the interactions of a spin-1 or spin-2 boson; however, since these spin scenarios have been excluded by Run I data, we do not consider them here. As we mentioned in Chapter 2, we can consistently add NLO QCD corrections to the model, in order to automatically generate results at NLO accuracy, possibly matched with parton showers. The missing information needed for NLO computations has been coded by hand in the UFO model HC_NLO_X0, which is publicly available online [22]. In particular, the UV renormalisation counterterms, as well as the R_2 terms necessary for loop automatic computations with the OPP method [97], have been included. The interactions between X_0 and electroweak gauge bosons in the HC model feature QCD corrections that are completely analogous to the ones in the SM

---

[1] In the purely CP-odd case the four-gluon vertex is zero due to the anti-symmetric nature of the interaction.

(namely, QCD corrections are not directly connected with new-physics vertices). In this case, one simply needs to add the counterterms already present in the default LOOP_SM model that comes with the MADGRAPH5_AMC@NLO distribution. This procedure has been employed to obtain NLO predictions for VBF and VH processes in [121]. On the other hand, Higgs interactions with quarks and effective interactions with gluons are directly affected by QCD corrections (which are also expected to be more important than in the case of VBF or VH), thus need dedicated UV renormalisation of α_s and R_2 loop counterterms. UV renormalisation of the strong coupling is performed in the $\overline{\text{MS}}$ scheme; this is straightforward to implement, since it gives universal counterterms proportional to the LO vertices. Concerning the interaction with quarks described in Eq. (B.1), the relevant scalar and pseudoscalar R_2 counterterms can be found in [255]. The case of gluonic operators in Eq. (B.6) is described in more detail in Appendix C. Note that these gluonic operators allowed for the first time to generate automatic gluon-fusion events, including ones with many jets in the final state, at NLO-QCD accuracy in MADGRAPH5_AMC@NLO. With the default LOOP_SM model, gluon fusion can be generated only at LO (yet with full quark-mass dependence).

Appendix C

The Higgs–gluon EFT at NLO

In this Appendix we discuss the effective field theory where the Higgs boson couples directly to gluons, including NLO-accurate corrections in QCD and matching to the Standard Model. This effective theory is a key ingredient for automatic event generation at NLO with state-of-the-art tools, such as MG5_aMC@NLO, and have been used to obtain results for production of Higgs plus jets via gluon fusion in chapter 3. In particular, we present the Feynman rules, UV and R_2 terms necessary for NLO-QCD automatic computations. The LO rules have been obtained automatically by coding the effective Lagrangian in FeynRules [256], while the UV and R_2 terms have been coded by hand in the HC_NLO_X0 UFO model [22].

The SM Higgs boson can couple to gluons via loops of massive quarks. Despite being an indirect interaction, the Higgs–gluon coupling drives the main production mechanism of this boson at hadron colliders such as the LHC, and provides also a sizeable fraction (about 8%) of its decay modes. Since the intensity of the interaction is proportional to the quark mass, it is dominated by top-quark loops, while loops of lighter quarks can be added later as a correction (as for the bottom) or just completely neglected. Given that $m_H \simeq 125$ GeV, $m_t \simeq 173$ GeV and $m_q < 5$ GeV for $q = d, u, s, c, b$, the situation exhibits a mass hierarchy

$$\Lambda_{\mathrm{QCD}}\,,\ 2m_q \ \ll\ m_H \ <\ 2m_t\,, \tag{C.1}$$

where it is important to notice the factor two in front of the quark masses: $2m_q$ (and not just m_q) is the characteristic scale of the loops, below which these diagrams do not feature an imaginary part – in other words, it is impossible to physically produce the quarks running inside the loops below this energy.

Such a scale hierarchy justifies, if needed, the use of an effective theory in the limit of a heavy top quark, to simplify the description of processes where the external particles are only a Higgs and light partons [34, 62, 257]. The Lagrangian of this theory consists of the usual QCD sector in the SM given by Eq. (A.56), in the five-flavour scheme (5FS), plus the effective interaction term

$$\mathcal{L}_{GGH} = -\frac{1}{4}\, g_{_{Hgg}}\, G^{a}_{\mu\nu} G^{a,\mu\nu} H\,, \tag{C.2}$$

from which we obtain the Feynman rules listed in Table C.1. We want to match this theory to the full SM in the 5FS, of which it will provide an approximate description in the low-energy limit. To this purpose, we just need to match the Wilson coefficient $g_{_{Hgg}}$ by comparing the diagrams in Table C.1 to the corresponding ones in the SM, featuring the full dependence from the loop integral, in the limit $m_t \to \infty$. The simplest way to proceed is by computing the $H \to gg$ triangles in Fig. C.2a; the result is [62]

$$i\mathcal{A}^{H}_{\triangle} = -i\, \delta^{a_1 a_2}\, \frac{\alpha_s}{2\pi v} \left[\frac{1-\tau}{\tau^2}\, f(\tau) - \frac{1}{\tau} \right] \left(p_2^{\mu_1} p_1^{\mu_2} - g^{\mu_1 \mu_2}\, p_1 \!\cdot\! p_2 \right), \tag{C.3}$$

where

$$\tau = \frac{m_H^2}{4m_t^2} \qquad \text{and} \qquad f(\tau) = \arcsin^2 \sqrt{\tau} \quad \text{for} \quad \tau \leq 1\,. \tag{C.4}$$

In the limit $\tau \to 0$ the expression in Eq. (C.3) becomes

$$i\mathcal{A}^{H}_{\triangle} = +i\, \delta^{a_1 a_2}\, \frac{\alpha_s}{3\pi v} \left(p_2^{\mu_1} p_1^{\mu_2} - g^{\mu_1 \mu_2}\, p_1 \!\cdot\! p_2 \right), \tag{C.5}$$

and by comparing with the effective ggH vertex we immediately get

$$g_{_{Hgg}} = -\frac{\alpha_s}{3\pi v}\,. \tag{C.6}$$

It is interesting to note that this EFT provides a peculiar case where heavy particles do not completely decouple from the theory in the infinitely massive limit; instead, in some diagrams they can induce finite effective couplings at low energy. This is a distinctive trait of theories featuring the BEH mechanism, where the coupling of the Higgs to heavy states is not of $\mathcal{O}(1)$ in this limit, but grows with their masses, thereby compensating the propagator suppression.

As we said before, the GGH effective theory greatly simplifies SM calculations by reducing the number of loops that appear at a given perturbative order,

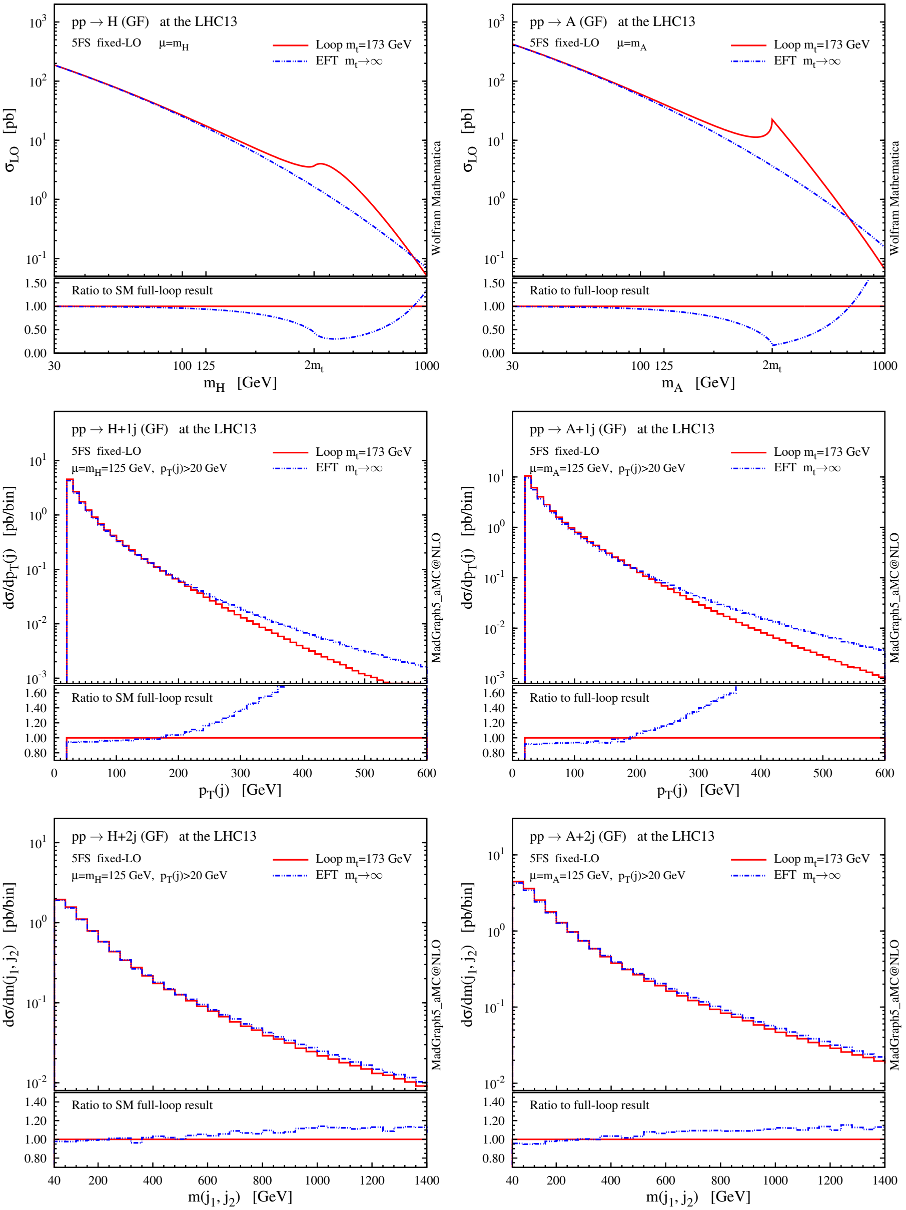

Figure C.1: Validity tests for gluon fusion in the EFT approximation, at LO. On the left column we show the inclusive $pp \to H$ cross section (top), the p_T of the recoiling jet in $pp \to H + 1j$ (centre), and the di-jet invariant mass in $pp \to H + 2j$ (bottom). On the right column, we show the analogous plots for the pseudoscalar A.

as shown in Fig. C.2. This allows us to employ automatic libraries for tree-level and one-loop amplitudes to carry out simulations at NLO accuracy. Since no equivalent tool exists for two-loop integrals at present, such an accuracy cannot be achieved in the full theory for a generic Higgs-plus-jets process. The price to pay is that we must pay attention to the regime in which this effective description is applicable.

In Fig. C.1 we show some tests which compare results from the Higgs–gluons EFT to the SM ones, where the full dependence from the top-quark loop is taken into account. Looking at the total cross section as a function of m_H, we can see that the EFT provides an approximation better than 10% for $m_H \lesssim m_t$, being about 6% at the actual value $m_H = 125$ GeV. It is also clear that $2m_t$ is the scale at which "new physics" appears: around this scale, the SM contribution gets enhanced by the top-quark resonance in the loop, while at even higher m_H the EFT outgrows the SM result, as expected. When one looks instead at differential observables in processes where the Higgs is produced together with jets, new scales such as transverse momenta enter the physics, thus the hierarchy picture is more complicated than Eq. (C.1). In particular, the EFT accuracy is better than 5% up to $p_T(j) \simeq 200$ GeV, where the bulk of events lies, while it rapidly becomes inadequate if the transverse momentum of the hardest jet is significantly larger than the top-quark mass [104,258]. Conversely, the EFT provides a valid description over a large invariant-mass range of the di-jet system in $H + 2j$ production [105], even for $m_{jj} \gg 2m_t$: the accuracy deteriorates slowly with increasing masses, and is better than 10% up to almost 1 TeV. In fact, we can argue that the scale of EFT breakdown is determined once again by the hardest transverse momentum, rather than by m_{jj}. Large di-jet masses predominantly emerge from quasi-collinear fragmentation of the colliding protons, therefore events with low to moderate $p_T(j)$ still dominate. In this regime, the Higgs production takes place mainly via the t-channel gluon exchange which, being soft enough in most events, ensures the EFT validity.

Our effective theory is invariant under $SU(3)_C$, so we can consistently add higher-order QCD corrections. Going to NLO, we match again the result from the effective theory to the corresponding one where the amplitude is induced by a top-quark loop. In the latter case, virtual corrections consist of two-loop diagrams; some of them appear explicitly in the effective theory as one-loop diagrams, while the other ones simply result in a correction to the value of the effective coupling, see Fig. C.2. This correction can be computed by means of a low-energy theorem [34] and amounts to

$$g_{Hgg} = -\frac{\alpha_s}{3\pi v}\Big(1 + \frac{11}{4}\,\frac{\alpha_s}{\pi} + \mathcal{O}\big(\alpha_s^2\big)\Big)\,. \tag{C.7}$$

Together with this finite contribution to the UV renormalisation of g_{Hgg}, we also need the UV polar terms that appear in $D = 4-2\epsilon$ dimensional regularisation. Such counterterms are simply obtained plugging into Eq. (C.2) the well known $\overline{\text{MS}}$ renormalisation of the strong coupling

$$\alpha_s \to \alpha_s\Big(1 - \frac{1}{\epsilon}\,\frac{\alpha_s}{2\pi}\,b_0 + \mathcal{O}\big(\alpha_s^2\big)\Big)\,, \tag{C.8}$$

where b_0 is the first coefficient of the QCD beta function

$$b_0 = \frac{11}{6}\,C_A - \frac{2}{3}\,T_F\,n_f\,. \tag{C.9}$$

Therefore, the UV counterterms have structures analogous to the tree-level Feynman rules in Table C.1.

To complete our set of rules, in Table C.3 we report the R_2 terms [259, 260] of our effective theory, needed for the automatic computation of one-loop amplitudes with the OPP method [97], which have firstly been published in [261] (with slightly different conventions).

An analogous effective theory can be used to describe the case of a pseudoscalar boson A which couples to the SM fermions accordingly to the CP-odd interaction in Eq. (B.1)

$$\mathcal{L}_{G\widetilde{G}A} = -\frac{1}{4}\,g_{Agg}\,G^a_{\mu\nu}\widetilde{G}^{a,\mu\nu}A\,, \tag{C.10}$$

where $\widetilde{G}^{a,\mu\nu} = \frac{1}{2}\,\epsilon^{\mu\nu\rho\sigma}G^a_{\rho\sigma}$, and the Wilson coefficient

$$g_{Agg} = \frac{\alpha_s}{2\pi v} \tag{C.11}$$

can be obtained by matching to the loop-induced amplitude in the full theory

$$i\mathcal{A}^A_\triangle = -i\,\delta^{a_1a_2}\,\frac{\alpha_s}{2\pi v}\,\frac{f(\tau)}{\tau}\,\epsilon^{\mu_1\mu_2\rho\sigma}\,p_{1\rho}\,p_{2\sigma} \tag{C.12}$$

in the limit $\tau \to 0$. At variance with the scalar case, the effective coupling g_{Agg} in Eq. (C.11) is exact to all orders in α_s [262]. On the other hand, when going to higher orders in QCD, the $G\widetilde{G}A$ operator in Eq. (C.10) is not closed under renormalisation; a closed set of operators is provided by [263]

$$\mathcal{L}_{G\widetilde{G}A} = g_{Agg}\Bigg[-\frac{1}{4}\,G^a_{\mu\nu}\widetilde{G}^{a,\mu\nu} + c_{\partial J5}\sum_{q=1}^{5}\partial_\mu\big(\bar{q}\gamma^\mu\gamma_5 q\big)\Bigg]A\,, \tag{C.13}$$

where the divergence of the axial-vector current, summed over the five active quarks ($q = d, u, s, c, b$), enters the physics only starting at NLO

$$c_{\partial J5} = \frac{\alpha_s}{4\pi}\,C_F\left(\frac{3}{4} - \frac{3}{2}\ln\frac{\mu_R^2}{m_t^2}\right) + \mathcal{O}\big(\alpha_s^2\big)\,. \tag{C.14}$$

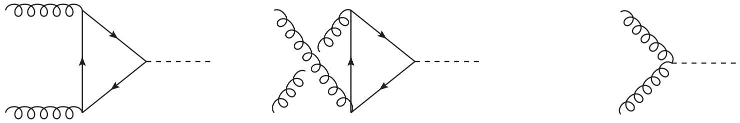

(a) one-loop in the SM (b) tree-level in the EFT

(c) two-loop in the SM (d) tree-level CT in the EFT

(e) two-loop in the SM (f) one-loop in the EFT

Figure C.2: Comparison of sample Feynman diagrams describing Higgs production via gluon fusion in the SM (left), and in the effective theory where heavy quarks have been integrated out (right). At LO, one-loop diagrams in the SM (a) are reduced to tree level in the EFT (b). At NLO, two-loop corrections to the vertex (c) appear as a tree-level correction to the effective coupling (d), while the remaining two-loop diagrams (e) are simplified to one loop (f).

Notwithstanding the formal need for this additional operator, its corresponding Feynman rule reported in Table C.2 has not been included in the public version of the HC_NLO_X0 model. In fact, we have checked with a private version of the model that, at NLO accuracy in QCD, the numerical impact of the $(\partial_\mu J_5^\mu)A$ operator is completely negligible in phenomenological simulations at the LHC: it gives a correction to the $A+1,2j$ cross sections which is 20 orders of magnitude smaller than the LO, thus it can be safely omitted for any practical purpose. The remaining $1/\epsilon$ UV counterterms at NLO can be found once again by inserting the expression of Eq. (C.8) into the tree-level Feynman rules of Table C.2. Finally, in Table C.4 we report the R_2 counterterms needed for automatic one-loop computations with the OPP method, which have been published for the first time in [16].

Looking again at Fig. C.1, we can see that the dependence on the top mass is different in the pseudoscalar case, resulting in a sharper peak around $m_A = 2m_t$ and more pronounced deviations from the EFT. Nevertheless, at 125 GeV the EFT provides an approximation better than 9% to the total cross section (compared to about 6% in the scalar case), and performs similarly well to the scalar case with respect to the $p_T(j)$ and m_{jj} scales.

We conclude this appendix reminding that the Higgs-gluon EFT is crucial not only to simulate single-Higgs production in association with jets at NLO+PS accuracy with modern event generators, but also to compute its inclusive cross section at higher orders in α_s. In fact, at present the full quark-loop dependence is known only up to NLO [34,264]. Instead, NNLO [265–268] and, very recently, also N^{3}LO corrections [101, 269] have been computed relying on this powerful approximation, for both the scalar and pseudoscalar case.

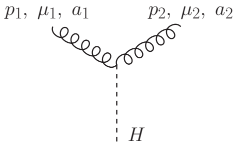

$$= -i\, g_{Hgg}\, \delta^{a_1 a_2} \left(p_2^{\mu_1} p_1^{\mu_2} - g^{\mu_1\mu_2}\, p_1 \cdot p_2 \right)$$

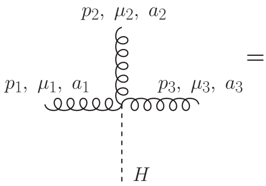

$$= -g_{Hgg}\, g_s\, f^{a_1 a_2 a_3} \Big[g^{\mu_1\mu_2} (p_1 - p_2)^{\mu_3} + g^{\mu_2\mu_3} (p_2 - p_3)^{\mu_1} + g^{\mu_3\mu_1} (p_3 - p_1)^{\mu_2} \Big]$$

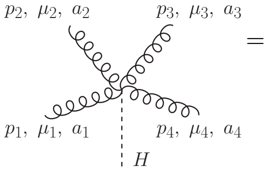

$$\begin{aligned} = -i\, g_{Hgg}\, g_s^2 \Big[\; & f^{a_1 a_2 b} f^{a_3 a_4 b} \left(g^{\mu_1\mu_3} g^{\mu_2\mu_4} - g^{\mu_1\mu_4} g^{\mu_2\mu_3} \right) \\ & + f^{a_1 a_3 b} f^{a_2 a_4 b} \left(g^{\mu_1\mu_2} g^{\mu_3\mu_4} - g^{\mu_1\mu_4} g^{\mu_2\mu_3} \right) \\ & + f^{a_1 a_4 b} f^{a_2 a_3 b} \left(g^{\mu_1\mu_2} g^{\mu_3\mu_4} - g^{\mu_1\mu_3} g^{\mu_2\mu_4} \right) \Big] \end{aligned}$$

Table C.1: Feynman rules derived from the Lagrangian (C.2).

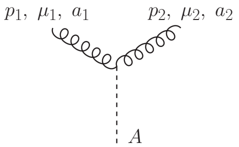

$$= -i\, g_{Agg}\, \delta^{a_1 a_2}\, \epsilon^{\mu_1\mu_2\rho\sigma}\, p_{1\rho}\, p_{2\sigma}$$

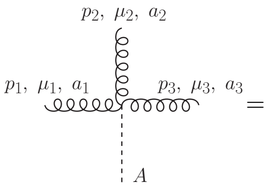

$$= -g_{Agg}\, g_s\, f^{a_1 a_2 a_3}\, \epsilon^{\mu_1\mu_2\mu_3\rho} \left(p_1 + p_2 + p_3 \right)_\rho$$

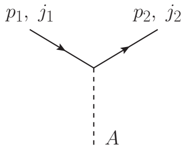

$$= -g_{Agg}\, c_{\partial J5}\, \delta_{j_1 j_2} \left(\not{p}_1 + \not{p}_2 \right) \gamma_5$$

Table C.2: Feynman rules derived from the Lagrangian (C.13). Note that there is no $ggggA$ vertex, and all the amplitudes above vanish when $p_A^\mu \to (0, \mathbf{0})$.

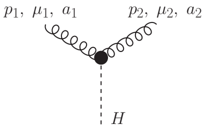

$$= i\, g_{Hgg}\, \frac{g_s^2 N_c}{384\pi^2}\, \delta^{a_1 a_2} \Big[-\big(17p_1^2 + 17p_2^2 + 93 p_1\cdot p_2\big)\, g^{\mu_1\mu_2} + p_1^{\mu_1} p_2^{\mu_2} + 89 p_2^{\mu_1} p_1^{\mu_2} + 14\big(p_1^{\mu_1} p_1^{\mu_2} + p_2^{\mu_1} p_2^{\mu_2}\big)\Big]$$

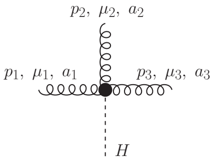

$$= g_{Hgg}\, \frac{15 g_s^3 N_c}{128\pi^2}\, f^{a_1 a_2 a_3} \Big[g^{\mu_1\mu_2}\, (p_1 - p_2)^{\mu_3} + g^{\mu_2\mu_3}\, (p_2 - p_3)^{\mu_1} + g^{\mu_3\mu_1}\, (p_3 - p_1)^{\mu_2} \Big]$$

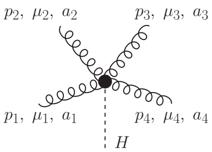

$$\begin{aligned} = i\, g_{Hgg}\, \frac{g_s^4}{128\pi} \Big[& f^{a_1 bc} f^{a_2 cd} f^{a_3 de} f^{a_4 eb} \big(21 g^{\mu_1\mu_2} g^{\mu_3\mu_4} - 41 g^{\mu_1\mu_3} g^{\mu_2\mu_4} + 21 g^{\mu_1\mu_4} g^{\mu_2\mu_3}\big) \\ & + f^{a_1 bc} f^{a_2 cd} f^{a_4 de} f^{a_3 eb} \big(21 g^{\mu_1\mu_2} g^{\mu_3\mu_4} + 21 g^{\mu_1\mu_3} g^{\mu_2\mu_4} - 41 g^{\mu_1\mu_4} g^{\mu_2\mu_3}\big) \\ & + f^{a_1 bc} f^{a_3 cd} f^{a_2 de} f^{a_4 eb} \big(- 41 g^{\mu_1\mu_2} g^{\mu_3\mu_4} + 21 g^{\mu_1\mu_3} g^{\mu_2\mu_4} + 21 g^{\mu_1\mu_4} g^{\mu_2\mu_3}\big) \Big] \end{aligned}$$

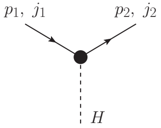

$$= i\, g_{Hgg}\, \frac{g_s^2}{32\pi^2}\, \frac{N_c^2 - 1}{2N_c}\, \lambda_{HV}\, \delta_{j_1 j_2} \big(\not{p}_2 - \not{p}_1\big)$$

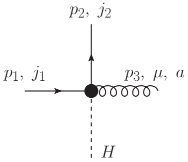

$$= -i\, g_{Hgg}\, \frac{g_s^3}{64\pi^2}\, t^a_{j_2 j_1} \gamma^\mu \left[\frac{2\lambda_{HV} + 1}{N_c} - \big(2\lambda_{HV} + 3\big) N_c \right]$$

Table C.3: R_2 counterterms for the Lagrangian (C.2). $\lambda_{HV} = 1$ is for dimensional regularisation, while $\lambda_{HV} = 0$ for dimensional reduction.

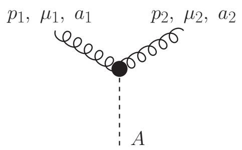

$$= i\, g_{Agg}\, \frac{g_s^2 N_c}{96\pi^2}\, \delta^{a_1 a_2}\, \epsilon^{\mu_1 \mu_2 \rho \sigma}\, p_{1\rho}\, p_{2\sigma}$$

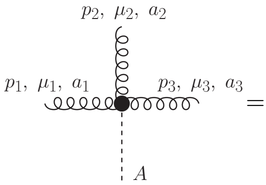

$$= g_{Agg}\, \frac{g_s^3 N_c}{64\pi^2}\, f^{a_1 a_2 a_3}\, \epsilon^{\mu_1 \mu_2 \mu_3 \rho}\, \left(p_1 + p_2 + p_3\right)_\rho$$

Table C.4: R_2 counterterms for the Lagrangian (C.10).

Appendix D

Additional tables with t-channel tH cross sections

In this Appendix we collect the t-channel tH cross sections obtained with the MSTW2008 and CT10 parton distributions, presented together with the NNPDF2.3 results in Fig. 5.5.

	t-channel	$\sigma_{\text{NLO}}(\mu_0^s)$ [fb]	$\delta_{\mu}^{\%}$	$\delta_{\text{PDF}+\alpha_s+m_b}^{\%}$	$\delta_{\text{PDF}}^{\%}$	$\delta_{\alpha_s}^{\%}$	$\delta_{m_b}^{\%}$
4FS	tH	45.91(9)	${}^{+3.7}_{-6.4}$	${}^{+2.1}_{-2.0}$	${}^{+1.1}_{-1.1}$	*n.a.*	${}^{+1.8}_{-1.7}$
	$\bar{t}H$	23.61(3)	${}^{+3.1}_{-7.9}$	${}^{+2.4}_{-2.5}$	${}^{+1.6}_{-1.9}$	*n.a.*	${}^{+1.7}_{-1.6}$
	$tH + \bar{t}H$	69.43(7)	${}^{+4.0}_{-5.8}$	${}^{+2.5}_{-1.9}$	${}^{+1.1}_{-1.2}$	*n.a.*	${}^{+2.2}_{-1.5}$
5FS	tH	48.28(6)	${}^{+7.0}_{-1.9}$	${}^{+2.6}_{-2.6}$	${}^{+1.2}_{-1.2}$	${}^{+1.2}_{-1.1}$	${}^{+2.1}_{-2.0}$
	$\bar{t}H$	24.99(3)	${}^{+6.4}_{-2.3}$	${}^{+2.7}_{-3.1}$	${}^{+1.7}_{-2.0}$	${}^{+0.9}_{-1.2}$	${}^{+2.0}_{-2.1}$
	$tH + \bar{t}H$	73.45(8)	${}^{+7.0}_{-2.3}$	${}^{+3.0}_{-2.6}$	${}^{+1.2}_{-1.3}$	${}^{+1.4}_{-1.4}$	${}^{+2.4}_{-1.8}$

Table D.1: Same as Table 5.3, but using the MSTW2008 parton distributions. Where the information is not available, *n.a.* is displayed.

	t-channel	$\sigma_{\mathrm{NLO}}(\mu_0^s)$ [fb]	$\delta^{\%}_{\mu}$	$\delta^{\%}_{\mathrm{PDF}+\alpha_s+m_b}$	$\delta^{\%}_{\mathrm{PDF}}$	$\delta^{\%}_{\alpha_s}$	$\delta^{\%}_{m_b}$
4FS	tH	47.00(7)	$^{+3.5}_{-6.7}$	$^{+1.9}_{-2.1}$	$^{+1.1}_{-1.1}$	*n.a.*	$^{+1.6}_{-1.8}$
	$\bar{t}H$	24.10(5)	$^{+4.6}_{-7.1}$	$^{+2.2}_{-2.5}$	$^{+1.6}_{-1.9}$	*n.a.*	$^{+1.5}_{-1.7}$
	$tH+\bar{t}H$	71.29(10)	$^{+3.8}_{-7.1}$	$^{+2.2}_{-2.3}$	$^{+1.1}_{-1.2}$	*n.a.*	$^{+1.9}_{-2.0}$
5FS	tH	47.17(6)	$^{+7.0}_{-2.6}$	$^{+2.9}_{-2.6}$	$^{+1.2}_{-1.2}$	$^{+1.9}_{-1.1}$	$^{+1.8}_{-2.0}$
	$\bar{t}H$	24.41(3)	$^{+7.1}_{-2.7}$	$^{+3.2}_{-2.8}$	$^{+1.7}_{-2.0}$	$^{+0.7}_{-1.7}$	$^{+2.6}_{-1.0}$
	$tH+\bar{t}H$	71.54(7)	$^{+7.3}_{-2.1}$	$^{+2.8}_{-2.6}$	$^{+1.2}_{-1.3}$	$^{+1.5}_{-1.1}$	$^{+2.1}_{-2.0}$

Table D.2: Same as Table D.1, but using the reference dynamic scale instead of the static one. Where the information is not available, *n.a.* is displayed.

	t-channel	$\sigma_{\mathrm{NLO}}(\mu_0^s)$ [fb]	$\delta^{\%}_{\mu+\mathrm{FS}}$	$\delta^{\%}_{\mathrm{PDF}+\alpha_s+m_b}$
4FS+5FS	tH	47.30(8)	±9.2	$^{+2.7}_{-2.0}$
	$\bar{t}H$	24.17(4)	±10.0	$^{+2.8}_{-2.4}$
	$tH+\bar{t}H$	71.99(11)	±9.2	$^{+3.1}_{-1.9}$

Table D.3: Flavour-scheme combined result, according to Eq. (5.10), using MSTW2008 PDFs.

	t-channel	$\sigma_{\mathrm{NLO}}(\mu_0^d)$ [fb]	$\delta^{\%}_{\mu+\mathrm{FS}}$	$\delta^{\%}_{\mathrm{PDF}+\alpha_s+m_b}$
4FS+5FS	tH	47.18(6)	±7.0	$^{+2.9}_{-2.1}$
	$\bar{t}H$	24.26(3)	±7.7	$^{+3.2}_{-2.5}$
	$tH+\bar{t}H$	71.48(9)	±7.3	$^{+2.8}_{-2.3}$

Table D.4: Same as Table D.3, but using the reference dynamic scale instead of the static one.

	t-channel	$\sigma_{\rm NLO}(\mu_0^s)$ [fb]	$\delta_\mu^\%$	$\delta_{{\rm PDF}+\alpha_s+m_b}^\%$	$\delta_{\rm PDF}^\%$	$\delta_{\alpha_s}^\%$	$\delta_{m_b}^\%$
4FS	tH	45.03(6)	$^{+3.4}_{-6.1}$	$^{+1.6}_{-2.1}$	$n.a.$	$n.a.$	$^{+1.6}_{-2.1}$
	$\bar{t}H$	22.78(2)	$^{+3.8}_{-6.5}$	$^{+1.4}_{-1.4}$	$n.a.$	$n.a.$	$^{+1.4}_{-1.4}$
	$tH+\bar{t}H$	67.69(8)	$^{+3.9}_{-6.3}$	$^{+1.7}_{-1.5}$	$n.a.$	$n.a.$	$^{+1.7}_{-1.5}$
5FS	tH	47.91(6)	$^{+7.0}_{-2.2}$	$^{+2.7}_{-2.5}$	$^{+2.3}_{-2.1}$	$^{+1.4}_{-1.4}$	$n.a.$
	$\bar{t}H$	24.53(2)	$^{+6.5}_{-2.5}$	$^{+3.7}_{-3.3}$	$^{+3.5}_{-2.9}$	$^{+1.2}_{-1.6}$	$n.a.$
	$tH+\bar{t}H$	72.36(9)	$^{+6.6}_{-2.4}$	$^{+2.9}_{-2.3}$	$^{+2.4}_{-2.0}$	$^{+1.6}_{-1.1}$	$n.a.$

Table D.5: Same as Table 5.3, but using the CT10 parton distributions. Where the information is not available, $n.a.$ is displayed.

	t-channel	$\sigma_{\rm NLO}(\mu_0^s)$ [fb]	$\delta_\mu^\%$	$\delta_{{\rm PDF}+\alpha_s+m_b}^\%$	$\delta_{\rm PDF}^\%$	$\delta_{\alpha_s}^\%$	$\delta_{m_b}^\%$
4FS	tH	46.00(8)	$^{+3.3}_{-6.5}$	$^{+1.3}_{-1.7}$	$n.a.$	$n.a.$	$^{+1.3}_{-1.7}$
	$\bar{t}H$	23.34(4)	$^{+3.8}_{-7.0}$	$^{+1.2}_{-2.2}$	$n.a.$	$n.a.$	$^{+1.2}_{-2.2}$
	$tH+\bar{t}H$	69.02(10)	$^{+4.5}_{-6.3}$	$^{+1.9}_{-1.8}$	$n.a.$	$n.a.$	$^{+1.9}_{-1.8}$
5FS	tH	46.76(6)	$^{+7.1}_{-2.0}$	$^{+2.5}_{-2.4}$	$^{+2.3}_{-2.1}$	$^{+0.8}_{-1.3}$	$n.a.$
	$\bar{t}H$	23.94(3)	$^{+7.3}_{-2.7}$	$^{+3.7}_{-3.2}$	$^{+3.5}_{-2.9}$	$^{+1.1}_{-1.2}$	$n.a.$
	$tH+\bar{t}H$	70.71(8)	$^{+7.1}_{-2.5}$	$^{+2.7}_{-2.4}$	$^{+2.4}_{-2.0}$	$^{+1.2}_{-1.3}$	$n.a.$

Table D.6: Same as Table D.5, but using the reference dynamic scale instead of the static one. Where the information is not available, $n.a.$ is displayed.

	t-channel	$\sigma_{\rm NLO}(\mu_0^s)$ [fb]	$\delta^{\%}_{\mu+{\rm FS}}$	$\delta^{\%}_{{\rm PDF}+\alpha_s+m_b}$
4FS+5FS	tH	46.78(6)	± 9.6	${}^{+2.8}_{-2.0}$
	$\bar{t}H$	23.71(4)	± 10.2	${}^{+3.9}_{-1.3}$
	$tH+\bar{t}H$	70.29(11)	± 9.8	${}^{+3.0}_{-1.5}$

Table D.7: Flavour-scheme combined result, according to Eq. (5.10), using CT10 PDFs.

	t-channel	$\sigma_{\rm NLO}(\mu_0^d)$ [fb]	$\delta^{\%}_{\mu+{\rm FS}}$	$\delta^{\%}_{{\rm PDF}+\alpha_s+m_b}$
4FS+5FS	tH	46.54(6)	± 7.6	${}^{+2.5}_{-1.7}$
	$\bar{t}H$	23.70(3)	± 8.4	${}^{+3.8}_{-2.2}$
	$tH+\bar{t}H$	70.21(9)	± 7.9	${}^{+2.7}_{-1.8}$

Table D.8: Same as Table D.7, but using the reference dynamic scale instead of the static one.

Appendix E

tH results for the HXSWG

In this Appendix we report the results for t-channel tH and s-channel tH cross sections published in the fourth LHCHXSWG technical report [19]. We also describe the setup and inputs used to compute these numbers.

E.1 t-channel tH

In the following, we list all the input parameters used to compute the inclusive tH cross sections via the exchange of a t-channel W boson, at NLO accuracy in QCD.

The pole mass of the top quark and its Yukawa coupling (renormalised on shell) are

$$m_t = 172.5 \text{ GeV}\,, \qquad\qquad y_t = \frac{m_t}{v} = \left(\sqrt{2}\,G_\mu\right)^{1/2} m_t\,, \tag{E.1}$$

where $v \simeq 246$ GeV is the EW vacuum expectation value. The bottom-quark pole mass in the 4FS (left) and 5FS (right) is set to

$$m_b^{(4\text{FS})} = 4.92 \pm 0.13 \text{ GeV}\,, \qquad\qquad m_b^{(5\text{FS})} = 0\,, \tag{E.2}$$

while the bottom-quark Yukawa coupling is always set to zero, $y_b = 0$, because its impact on the total cross section amounts to less than 0.1%. Actually, to speed up the 4FS code, the corresponding diagrams are not even generated.

The EW parameters are

$$G_\mu = 1.166379 \cdot 10^{-5}\ \text{GeV}^{-2}\,, \tag{E.3}$$

$$m_Z = 91.1876\ \text{GeV}\,, \tag{E.4}$$

$$m_W = 80.385\ \text{GeV}\,, \tag{E.5}$$

which in turn fix the electromagnetic coupling (no running) and the on-shell weak mixing angle to

$$\alpha = \sqrt{2}\, G_\mu m_W^2 (1 - m_W^2/m_Z^2)/\pi \simeq 1/132.233\,, \tag{E.6}$$

$$\sin^2\theta_\text{W} = 1 - m_W^2/m_Z^2 \simeq 0.2229\,. \tag{E.7}$$

We assume $V_{tb} = 1$ and, for simplicity, the whole CKM matrix to be diagonal[1]

$$V_\text{CKM} = \text{diag}\big\{V_{ud}, V_{cs}, V_{tb}\big\} = \text{diag}\big\{1, 1, 1\big\}\,. \tag{E.8}$$

The proton content in terms of parton distribution functions (PDFs) is evaluated by using the NLO PDF4LHC15 sets in the corresponding flavour-number scheme. The PDFs also determine the reference value of the strong coupling used in the simulation, which then is automatically run at 2-loop accuracy. In the 5FS this value and its uncertainty are

$$\alpha_s^{(5\text{FS})}(m_Z) = 0.1180 \pm 0.0015\,, \tag{E.9}$$

while in the 4FS $\alpha_s(m_Z)$ is slightly smaller and consistent with a four-flavour running [183]. The combined PDF+α_s uncertainty is computed from the Hessian set with 30 (PDF) + 2 (α_s) members, accordingly to Eq. (28) in Ref. [183]. The renormalisation μ_R and factorisation μ_F scales are both set equal to the reference value

$$\mu_0^{(t-\text{channel})} = (m_H + m_t)/4\,, \tag{E.10}$$

while the scale dependence in each flavour scheme is estimated from the maximum and minimum variations of the cross section among the seven scale points (central one plus six variations) given by

$$\frac{(\mu_R\,, \mu_F)}{\mu_0} = (0.5,\, 0.5),\ (0.5,\, 1),\ (1,\, 0.5),\ (1,\, 1),\ (1,\, 2),\ (2,\, 1),\ (2,\, 2)\,. \tag{E.11}$$

---

[1] The only important assumption here is $V_{tb} = 1$; once the third generation is decoupled from the first two, and if one is inclusive over the first two generations, then the result doesn't depend on the mixing between the first two generations (i.e. the Cabibbo angle) due to unitarity.

The reference scale choice in Eq. (E.10) is motivated by physical arguments in the 4FS description [163]. In particular, it ensures that the discrepancy between the 4FS and 5FS results is not unreasonably large, and that the 5FS uncertainty is not underestimated, which might happen when using a very high scale, see Fig. 5.4.

In Tables E.1, E.2, E.3 and E.4 we collect the results for the combined t-channel $pp \to tH + \bar{t}H$ production at the LHC, at centre-of-mass energies of $\sqrt{s} = 7, 8, 13$, and 14 TeV, respectively, and for various Higgs-boson masses in the range 120−130 GeV. In the third column we report the reference cross section (in fb), $\sigma_{tH+\bar{t}H}$, computed at NLO and in the 5FS, while in the fourth column we report the NLO K_{QCD} factor, defined as

$$K_{\mathrm{QCD}} = \sigma^{\mathrm{NLO\ QCD}}_{tH+\bar{t}H} / \sigma^{\mathrm{LO}}_{tH+\bar{t}H} \,, \tag{E.12}$$

where both the LO and NLO cross sections are computed with the same inputs. In the fifth column we report the combined scale plus flavour-scheme (FS) uncertainty, expressed as upper and lower percent variations with respect to the reference 5FS prediction. The combined scale+FS uncertainty band is the largest source of theoretical uncertainty, and it is computed from the maximum and minimum variations of the cross section among the 7+7 scale points, according to Eq. (E.11), in the two flavour schemes. This translates into the following equations

$$\sigma^{+} = \max_{\substack{(\mu_R,\mu_F)\ \text{points} \\ \text{4FS, 5FS}}} \sigma^{(\mathrm{FS})}_{tH+\bar{t}H}(\mu_R, \mu_F) \,, \tag{E.13}$$

$$\sigma^{-} = \min_{\substack{(\mu_R,\mu_F)\ \text{points} \\ \text{4FS, 5FS}}} \sigma^{(\mathrm{FS})}_{tH+\bar{t}H}(\mu_R, \mu_F) \,, \tag{E.14}$$

$$\text{Scale} + \text{FS}\ [\%] = 100 \left(\sigma^{+} / \sigma^{(\mathrm{5FS})}_{tH+\bar{t}H} - 1 \right) \,, \quad 100 \left(\sigma^{-} / \sigma^{(\mathrm{5FS})}_{tH+\bar{t}H} - 1 \right) \,. \tag{E.15}$$

In the sixth, seventh, and eighth columns we report the α_s, PDF, and combined PDF+α_s uncertainty in the 5FS, which is the second-largest source of theoretical uncertainty, since it also encompasses the differences in PDF-fitting procedures. We recall that it is computed employing the PDF4LHC15 Hessian set with 30 (PDF) + 2 (α_s) members, with the α_s uncertainty given in Eq. (E.9), and combining the two uncertainties in quadrature accordingly to the PDF4LHC15 prescription. Finally, in the last two columns we report the separate top (tH) and anti-top ($\bar{t}H$) contributions to the 5FS cross section (in fb). The numbers in tables from E.1 to E.4, relevant for the SM Higgs boson, are summarised in the plots of Fig. 5.19 where the blue uncertainty band is computed summing the scale+FS and PDF+α_s uncertainties. In Table E.5 we repeat the exercise, this time keeping the Higgs-boson mass fixed to $m_H = 125$ GeV and varying instead the collider energy in the range $\sqrt{s} = 6{-}15$ TeV, to show the gain in the cross section and the reduction of uncertainties. These numbers have been used for the plot in Fig. 5.18.

We conclude the discussion of results relevant for the SM Higgs boson by commenting on two minor uncertainties, namely the ones associated with the bottom-quark and top-quark masses. According to Eq. (E.2), we take the uncertainty on the bottom-quark mass according to be $m_b = 4.92 \pm 0.13$ GeV. At 13 TeV, and for a 125 GeV Higgs-boson mass, this translates into a 4FS cross section of $\sigma^{(4\mathrm{FS})}_{tH+\bar{t}H} = 67.4^{+0.7}_{-0.5}$ fb, which corresponds to an uncertainty of about 1%. Since no PDF4LHC15 set with heavy-quark mass variations has been published yet, we estimate the impact on the 5FS cross section using the numbers in [17], where previous-generation PDF sets have been used. The ±0.25 GeV bottom-mass uncertainty quoted in Ref. [17] returned an uncertainty in the 5FS cross section of about 2%. A crude rescaling to ±0.13 GeV results in an uncertainty of roughly 1%, comparable to the one in the 4FS.

Similarly, we consider a top-quark mass uncertainty of $m_t = 172.5 \pm 1.0$ GeV, which returns a 5FS cross section of $\sigma^{(5\mathrm{FS})}_{tH+\bar{t}H} = 74.3^{+0.4}_{-0.3}$ fb at 13 TeV. Thus, the m_t uncertainty in the total cross section is below 1%, since increasing the top-quark mass causes a reduction of the available phase space which is however partly compensated by the larger top-quark Yukawa coupling.

Associated tH production in the t-channel is known for having maximal destructive interference in the SM between $H - W$ interactions on the one hand, and $H - t$ interactions on the other hand: deviations from the SM top-quark Yukawa coupling can result in a large enhancement of the cross section. This has prompted the LHC experiments to perfom searches for the 125 GeV Higgs boson in this process [270,271] assuming that the sign of the top-quark Yukawa coupling is opposite to the SM coupling in Eq. (E.1),

$$y_t = -y_t^{(\mathrm{SM})} = -m_t/v\,, \tag{E.16}$$

which results in maximally constructive interference between the two subsets of diagrams. Given the interest in experimental searches, in Table E.6 we provide reference cross sections and uncertainties for this scenario at 13 and 14 TeV. For further applications of this process to constrain deviations from the SM interactions of the 125 GeV particle, see also section 5.5.

Finally, we extend our investigation to Higgs masses in the range $m_H = 10{-}3000$ GeV, but keeping the Higgs boson as a stable particle and neglecting Higgs-width effects, which might provide a useful reference for BSM Higgs searches. The results at 13 and 14 TeV are collected in Tables E.7 and E.8

respectively (analogous to Tables E.3 and E.4), and also plotted in Fig. 5.21. These results should be taken with care, since an hypothetical BSM Higgs boson may contribute to the same tH final state through different interactions than the ones described by SM-like diagrams.

$\sqrt{s}$ [TeV]	m_H [GeV]	$\sigma_{tH+\bar{t}H}$ [fb]	K_{QCD}	Scale+FS [%]		α_s [%]		PDF [%]		PDF+α_s [%]		σ_{tH} [fb]	$\sigma_{\bar{t}H}$ [fb]
7	120.0	12.89	1.12	+7.6	−16.6	+1.5	−1.5	+4.7	−4.7	+4.9	−4.9	8.88	4.00
7	120.5	12.81	1.12	+7.5	−16.5	+1.5	−1.5	+4.7	−4.7	+4.9	−4.9	8.83	3.97
7	121.0	12.73	1.12	+7.6	−16.5	+1.5	−1.5	+4.7	−4.7	+4.9	−4.9	8.78	3.95
7	121.5	12.67	1.13	+7.5	−16.6	+1.5	−1.5	+4.7	−4.7	+4.9	−4.9	8.73	3.93
7	122.0	12.60	1.13	+7.5	−16.6	+1.5	−1.5	+4.7	−4.7	+4.9	−4.9	8.69	3.92
7	122.5	12.54	1.13	+7.5	−16.8	+1.5	−1.5	+4.7	−4.7	+4.9	−4.9	8.63	3.89
7	123.0	12.47	1.13	+7.5	−16.7	+1.5	−1.5	+4.7	−4.7	+4.9	−4.9	8.60	3.88
7	123.5	12.41	1.13	+7.4	−16.8	+1.5	−1.5	+4.7	−4.7	+4.9	−4.9	8.55	3.86
7	124.0	12.36	1.13	+7.4	−17.0	+1.5	−1.5	+4.7	−4.7	+4.9	−4.9	8.51	3.84
7	124.1	12.35	1.13	+7.4	−16.9	+1.5	−1.5	+4.7	−4.7	+4.9	−4.9	8.51	3.84
7	124.2	12.35	1.13	+7.4	−17.0	+1.5	−1.5	+4.7	−4.7	+4.9	−4.9	8.50	3.83
7	124.3	12.33	1.13	+7.4	−17.0	+1.5	−1.5	+4.7	−4.7	+4.9	−4.9	8.50	3.83
7	124.4	12.31	1.13	+7.4	−17.0	+1.5	−1.5	+4.7	−4.7	+4.9	−4.9	8.50	3.83
7	124.5	12.28	1.13	+7.4	−16.9	+1.5	−1.5	+4.7	−4.7	+4.9	−4.9	8.46	3.82
7	124.6	12.28	1.13	+7.4	−16.8	+1.5	−1.5	+4.7	−4.7	+4.9	−4.9	8.47	3.82
7	124.7	12.26	1.13	+7.4	−16.8	+1.5	−1.5	+4.7	−4.7	+4.9	−4.9	8.47	3.81
7	124.8	12.25	1.13	+7.4	−16.8	+1.5	−1.5	+4.7	−4.7	+4.9	−4.9	8.44	3.81
7	124.9	12.23	1.13	+7.4	−16.8	+1.5	−1.5	+4.7	−4.7	+4.9	−4.9	8.43	3.80
7	125.0	12.26	1.14	+7.3	−17.2	+1.5	−1.5	+4.7	−4.7	+4.9	−4.9	8.43	3.80
7	125.09	12.23	1.13	+7.4	−17.0	+1.5	−1.5	+4.7	−4.7	+5.0	−5.0	8.42	3.80
7	125.1	12.23	1.13	+7.4	−17.0	+1.5	−1.5	+4.7	−4.7	+5.0	−5.0	8.42	3.80
7	125.2	12.22	1.13	+7.3	−16.9	+1.5	−1.5	+4.7	−4.7	+5.0	−5.0	8.41	3.80
7	125.3	12.21	1.13	+7.4	−16.9	+1.5	−1.5	+4.7	−4.7	+5.0	−5.0	8.41	3.79
7	125.4	12.17	1.13	+7.4	−16.8	+1.5	−1.5	+4.7	−4.7	+5.0	−5.0	8.40	3.79
7	125.5	12.19	1.14	+7.4	−17.0	+1.5	−1.5	+4.7	−4.7	+5.0	−5.0	8.40	3.79
7	125.6	12.18	1.14	+7.3	−17.1	+1.5	−1.5	+4.7	−4.7	+5.0	−5.0	8.39	3.78
7	125.7	12.16	1.13	+7.3	−17.0	+1.5	−1.5	+4.7	−4.7	+5.0	−5.0	8.38	3.78
7	125.8	12.14	1.13	+7.4	−16.8	+1.5	−1.5	+4.7	−4.7	+5.0	−5.0	8.36	3.78
7	125.9	12.13	1.13	+7.3	−17.0	+1.5	−1.5	+4.7	−4.7	+5.0	−5.0	8.35	3.77
7	126.0	12.13	1.14	+7.3	−17.0	+1.5	−1.5	+4.7	−4.7	+5.0	−5.0	8.34	3.77
7	126.5	12.07	1.14	+7.3	−17.1	+1.5	−1.5	+4.7	−4.7	+5.0	−5.0	8.32	3.75
7	127.0	11.99	1.14	+7.3	−17.1	+1.5	−1.5	+4.7	−4.7	+5.0	−5.0	8.27	3.74
7	127.5	11.97	1.14	+7.3	−17.1	+1.5	−1.5	+4.7	−4.7	+5.0	−5.0	8.24	3.72
7	128.0	11.90	1.14	+7.2	−17.2	+1.5	−1.5	+4.7	−4.7	+5.0	−5.0	8.20	3.70
7	128.5	11.85	1.14	+7.2	−17.5	+1.5	−1.5	+4.8	−4.8	+5.0	−5.0	8.16	3.69
7	129.0	11.78	1.14	+7.3	−17.2	+1.5	−1.5	+4.8	−4.8	+5.0	−5.0	8.12	3.67
7	129.5	11.74	1.14	+7.2	−17.4	+1.5	−1.5	+4.8	−4.8	+5.0	−5.0	8.08	3.66
7	130.0	11.67	1.14	+7.2	−17.4	+1.5	−1.5	+4.8	−4.8	+5.0	−5.0	8.04	3.65

Table E.1: Cross sections for t-channel tH and $\bar{t}H$ production at the 7 TeV.

$\sqrt{s}$ [TeV]	m_H [GeV]	$\sigma_{tH+\bar{t}H}$ [fb]	$K_{\rm QCD}$	Scale+FS [%]		α_s [%]		PDF [%]		PDF+α_s [%]		σ_{tH} [fb]	$\sigma_{\bar{t}H}$ [fb]
8	120.0	19.59	1.14	+7.4	−16.0	+1.4	−1.4	+4.4	−4.4	+4.6	−4.6	13.37	6.22
8	120.5	19.49	1.14	+7.4	−16.0	+1.4	−1.4	+4.4	−4.4	+4.6	−4.6	13.30	6.19
8	121.0	19.38	1.14	+7.4	−16.0	+1.4	−1.4	+4.4	−4.4	+4.6	−4.6	13.25	6.16
8	121.5	19.29	1.14	+7.4	−16.1	+1.4	−1.4	+4.4	−4.4	+4.6	−4.6	13.15	6.13
8	122.0	19.21	1.14	+7.4	−16.1	+1.4	−1.4	+4.4	−4.4	+4.6	−4.6	13.10	6.11
8	122.5	19.11	1.14	+7.4	−16.3	+1.4	−1.4	+4.4	−4.4	+4.6	−4.6	13.02	6.08
8	123.0	19.02	1.14	+7.3	−16.3	+1.4	−1.4	+4.4	−4.4	+4.6	−4.6	12.99	6.05
8	123.5	18.92	1.14	+7.3	−16.2	+1.4	−1.4	+4.4	−4.4	+4.6	−4.6	12.93	6.03
8	124.0	18.87	1.15	+7.3	−16.4	+1.4	−1.4	+4.4	−4.4	+4.6	−4.6	12.86	5.99
8	124.1	18.82	1.15	+7.3	−16.3	+1.4	−1.4	+4.4	−4.4	+4.6	−4.6	12.84	5.99
8	124.2	18.81	1.15	+7.3	−16.4	+1.4	−1.4	+4.4	−4.4	+4.6	−4.6	12.85	6.00
8	124.3	18.78	1.15	+7.3	−16.4	+1.4	−1.4	+4.4	−4.4	+4.6	−4.6	12.84	5.99
8	124.4	18.76	1.15	+7.3	−16.3	+1.4	−1.4	+4.4	−4.4	+4.6	−4.6	12.82	5.97
8	124.5	18.78	1.15	+7.2	−16.4	+1.4	−1.4	+4.4	−4.4	+4.6	−4.6	12.81	5.97
8	124.6	18.75	1.15	+7.3	−16.4	+1.4	−1.4	+4.4	−4.4	+4.6	−4.6	12.78	5.97
8	124.7	18.75	1.15	+7.3	−16.5	+1.4	−1.4	+4.4	−4.4	+4.6	−4.6	12.78	5.96
8	124.8	18.71	1.15	+7.2	−16.5	+1.4	−1.4	+4.4	−4.4	+4.6	−4.6	12.76	5.95
8	124.9	18.70	1.15	+7.2	−16.5	+1.4	−1.4	+4.4	−4.4	+4.6	−4.6	12.77	5.95
8	125.0	18.69	1.15	+7.3	−16.5	+1.4	−1.4	+4.4	−4.4	+4.6	−4.6	12.73	5.95
8	125.09	18.66	1.15	+7.3	−16.6	+1.4	−1.4	+4.4	−4.4	+4.6	−4.6	12.72	5.95
8	125.1	18.66	1.15	+7.3	−16.6	+1.4	−1.4	+4.4	−4.4	+4.6	−4.6	12.72	5.95
8	125.2	18.66	1.15	+7.3	−16.6	+1.4	−1.4	+4.4	−4.4	+4.6	−4.6	12.74	5.94
8	125.3	18.64	1.15	+7.2	−16.5	+1.4	−1.4	+4.4	−4.4	+4.6	−4.6	12.70	5.92
8	125.4	18.62	1.15	+7.2	−16.5	+1.4	−1.4	+4.4	−4.4	+4.6	−4.6	12.69	5.93
8	125.5	18.62	1.15	+7.2	−16.6	+1.4	−1.4	+4.4	−4.4	+4.6	−4.6	12.68	5.92
8	125.6	18.57	1.15	+7.2	−16.6	+1.4	−1.4	+4.4	−4.4	+4.6	−4.6	12.66	5.92
8	125.7	18.55	1.15	+7.2	−16.5	+1.4	−1.4	+4.4	−4.4	+4.6	−4.6	12.66	5.91
8	125.8	18.56	1.15	+7.2	−16.5	+1.4	−1.4	+4.4	−4.4	+4.6	−4.6	12.64	5.90
8	125.9	18.54	1.15	+7.2	−16.5	+1.4	−1.4	+4.4	−4.4	+4.6	−4.6	12.65	5.90
8	126.0	18.52	1.15	+7.2	−16.6	+1.4	−1.4	+4.4	−4.4	+4.7	−4.7	12.62	5.90
8	126.5	18.44	1.15	+7.2	−16.8	+1.4	−1.4	+4.4	−4.4	+4.7	−4.7	12.56	5.87
8	127.0	18.36	1.15	+7.2	−16.4	+1.4	−1.4	+4.4	−4.4	+4.7	−4.7	12.49	5.85
8	127.5	18.28	1.15	+7.1	−16.8	+1.4	−1.4	+4.4	−4.4	+4.7	−4.7	12.45	5.82
8	128.0	18.20	1.15	+7.1	−16.8	+1.4	−1.4	+4.4	−4.4	+4.7	−4.7	12.42	5.79
8	128.5	18.13	1.16	+7.1	−16.8	+1.4	−1.4	+4.5	−4.5	+4.7	−4.7	12.36	5.79
8	129.0	18.04	1.16	+7.1	−16.8	+1.4	−1.4	+4.5	−4.5	+4.7	−4.7	12.30	5.75
8	129.5	17.96	1.16	+7.1	−16.8	+1.4	−1.4	+4.5	−4.5	+4.7	−4.7	12.26	5.72
8	130.0	17.87	1.16	+7.1	−16.9	+1.4	−1.4	+4.5	−4.5	+4.7	−4.7	12.19	5.71

Table E.2: Cross sections for t-channel tH and $\bar{t}H$ production at the 8 TeV.

$\sqrt{s}$ [TeV]	m_H [GeV]	$\sigma_{tH+\bar{t}H}$ [fb]	K_{QCD}	Scale+FS [%]		α_s [%]		PDF [%]		PDF+α_s [%]		σ_{tH} [fb]	$\sigma_{\bar{t}H}$ [fb]
13	120.0	77.31	1.19	+6.7	−14.6	+1.2	−1.2	+3.5	−3.5	+3.7	−3.7	50.86	26.43
13	120.5	77.11	1.19	+6.7	−14.8	+1.2	−1.2	+3.5	−3.5	+3.7	−3.7	50.71	26.33
13	121.0	76.84	1.19	+6.7	−14.7	+1.2	−1.2	+3.5	−3.5	+3.7	−3.7	50.47	26.23
13	121.5	76.48	1.19	+6.6	−14.7	+1.2	−1.2	+3.5	−3.5	+3.7	−3.7	50.24	26.13
13	122.0	76.14	1.19	+6.7	−14.7	+1.2	−1.2	+3.5	−3.5	+3.7	−3.7	50.11	26.02
13	122.5	75.81	1.19	+6.6	−14.6	+1.2	−1.2	+3.5	−3.5	+3.7	−3.7	49.85	25.90
13	123.0	75.52	1.19	+6.6	−14.8	+1.2	−1.2	+3.5	−3.5	+3.7	−3.7	49.72	25.84
13	123.5	75.23	1.19	+6.6	−14.9	+1.2	−1.2	+3.5	−3.5	+3.7	−3.7	49.47	25.75
13	124.0	74.99	1.19	+6.6	−15.1	+1.2	−1.2	+3.5	−3.5	+3.7	−3.7	49.30	25.60
13	124.1	74.71	1.19	+6.6	−14.6	+1.2	−1.2	+3.5	−3.5	+3.7	−3.7	49.35	25.59
13	124.2	74.77	1.19	+6.6	−14.7	+1.2	−1.2	+3.5	−3.5	+3.7	−3.7	49.25	25.58
13	124.3	74.81	1.19	+6.5	−14.9	+1.2	−1.2	+3.5	−3.5	+3.7	−3.7	49.15	25.56
13	124.4	74.77	1.20	+6.6	−14.9	+1.2	−1.2	+3.5	−3.5	+3.7	−3.7	49.18	25.57
13	124.5	74.59	1.19	+6.6	−14.9	+1.2	−1.2	+3.5	−3.5	+3.7	−3.7	49.14	25.53
13	124.6	74.52	1.19	+6.6	−14.7	+1.2	−1.2	+3.5	−3.5	+3.7	−3.7	49.04	25.49
13	124.7	74.48	1.19	+6.6	−14.8	+1.2	−1.2	+3.5	−3.5	+3.7	−3.7	49.01	25.49
13	124.8	74.48	1.20	+6.6	−14.9	+1.2	−1.2	+3.5	−3.5	+3.7	−3.7	48.98	25.46
13	124.9	74.47	1.20	+6.6	−15.1	+1.2	−1.2	+3.6	−3.6	+3.7	−3.7	48.94	25.42
13	125.0	74.25	1.20	+6.5	−14.9	+1.2	−1.2	+3.5	−3.5	+3.7	−3.7	48.89	25.42
13	125.09	74.26	1.19	+6.5	−14.7	+1.2	−1.2	+3.5	−3.5	+3.7	−3.7	48.89	25.40
13	125.1	74.26	1.19	+6.5	−14.7	+1.2	−1.2	+3.5	−3.5	+3.7	−3.7	48.89	25.40
13	125.2	74.32	1.20	+6.5	−15.0	+1.2	−1.2	+3.5	−3.5	+3.7	−3.7	48.87	25.40
13	125.3	74.30	1.20	+6.6	−14.9	+1.2	−1.2	+3.6	−3.6	+3.8	−3.8	48.81	25.38
13	125.4	74.14	1.20	+6.6	−14.9	+1.2	−1.2	+3.6	−3.6	+3.7	−3.7	48.79	25.34
13	125.5	74.07	1.20	+6.6	−15.0	+1.2	−1.2	+3.5	−3.5	+3.7	−3.7	48.77	25.34
13	125.6	74.09	1.20	+6.5	−15.2	+1.2	−1.2	+3.6	−3.6	+3.7	−3.7	48.75	25.32
13	125.7	74.01	1.20	+6.5	−15.0	+1.2	−1.2	+3.6	−3.6	+3.7	−3.7	48.70	25.31
13	125.8	73.90	1.20	+6.5	−15.0	+1.2	−1.2	+3.6	−3.6	+3.7	−3.7	48.65	25.30
13	125.9	73.70	1.20	+6.6	−14.8	+1.2	−1.2	+3.5	−3.5	+3.7	−3.7	48.57	25.30
13	126.0	73.75	1.19	+6.5	−15.0	+1.2	−1.2	+3.6	−3.6	+3.7	−3.7	48.58	25.27
13	126.5	73.53	1.20	+6.5	−14.9	+1.2	−1.2	+3.6	−3.6	+3.8	−3.8	48.37	25.16
13	127.0	73.29	1.20	+6.5	−15.1	+1.2	−1.2	+3.6	−3.6	+3.8	−3.8	48.20	25.11
13	127.5	73.04	1.20	+6.5	−15.1	+1.2	−1.2	+3.6	−3.6	+3.8	−3.8	48.07	24.99
13	128.0	72.77	1.20	+6.5	−15.1	+1.2	−1.2	+3.6	−3.6	+3.8	−3.8	47.93	24.91
13	128.5	72.44	1.20	+6.4	−15.0	+1.2	−1.2	+3.6	−3.6	+3.8	−3.8	47.65	24.81
13	129.0	72.23	1.20	+6.4	−15.1	+1.2	−1.2	+3.6	−3.6	+3.8	−3.8	47.55	24.74
13	129.5	72.03	1.20	+6.4	−15.2	+1.2	−1.2	+3.6	−3.6	+3.8	−3.8	47.34	24.66
13	130.0	71.84	1.20	+6.4	−15.3	+1.2	−1.2	+3.6	−3.6	+3.8	−3.8	47.23	24.59

Table E.3: Cross sections for t-channel tH and $\bar{t}H$ production at 13 TeV.

$\sqrt{s}$ [TeV]	m_H [GeV]	$\sigma_{tH+\bar{t}H}$ [fb]	K_{QCD}	Scale+FS [%]		α_s [%]		PDF [%]		PDF+α_s [%]		σ_{tH} [fb]	$\sigma_{\bar{t}H}$ [fb]
14	120.0	93.64	1.20	+6.6	−14.4	+1.2	−1.2	+3.4	−3.4	+3.6	−3.6	61.29	32.31
14	120.5	93.30	1.20	+6.6	−14.4	+1.2	−1.2	+3.4	−3.4	+3.6	−3.6	61.10	32.17
14	121.0	92.98	1.20	+6.5	−14.4	+1.2	−1.2	+3.4	−3.4	+3.6	−3.6	60.80	32.07
14	121.5	92.39	1.20	+6.5	−14.3	+1.2	−1.2	+3.4	−3.4	+3.6	−3.6	60.56	31.92
14	122.0	92.26	1.20	+6.5	−14.4	+1.2	−1.2	+3.4	−3.4	+3.6	−3.6	60.28	31.83
14	122.5	91.78	1.20	+6.5	−14.4	+1.2	−1.2	+3.4	−3.4	+3.6	−3.6	60.04	31.69
14	123.0	91.48	1.20	+6.5	−14.3	+1.2	−1.2	+3.4	−3.4	+3.6	−3.6	59.86	31.60
14	123.5	90.94	1.20	+6.5	−14.4	+1.2	−1.2	+3.4	−3.4	+3.6	−3.6	59.72	31.49
14	124.0	90.83	1.20	+6.5	−14.6	+1.2	−1.2	+3.4	−3.4	+3.6	−3.6	59.43	31.34
14	124.1	90.81	1.20	+6.5	−14.6	+1.2	−1.2	+3.4	−3.4	+3.6	−3.6	59.34	31.35
14	124.2	90.62	1.20	+6.5	−14.6	+1.2	−1.2	+3.4	−3.4	+3.6	−3.6	59.35	31.33
14	124.3	90.54	1.20	+6.4	−14.6	+1.2	−1.2	+3.4	−3.4	+3.6	−3.6	59.27	31.30
14	124.4	90.55	1.20	+6.5	−14.8	+1.2	−1.2	+3.4	−3.4	+3.6	−3.6	59.23	31.24
14	124.5	90.38	1.20	+6.4	−14.4	+1.2	−1.2	+3.4	−3.4	+3.6	−3.6	59.18	31.22
14	124.6	90.35	1.20	+6.4	−14.6	+1.2	−1.2	+3.4	−3.4	+3.6	−3.6	59.15	31.21
14	124.7	90.38	1.20	+6.5	−14.6	+1.2	−1.2	+3.4	−3.4	+3.6	−3.6	59.17	31.20
14	124.8	90.29	1.20	+6.4	−14.7	+1.2	−1.2	+3.4	−3.4	+3.6	−3.6	59.07	31.17
14	124.9	90.21	1.20	+6.5	−14.7	+1.2	−1.2	+3.4	−3.4	+3.6	−3.6	59.11	31.11
14	125.0	90.10	1.20	+6.4	−14.7	+1.2	−1.2	+3.4	−3.4	+3.6	−3.6	59.07	31.12
14	125.09	90.12	1.20	+6.4	−14.7	+1.2	−1.2	+3.4	−3.4	+3.6	−3.6	58.96	31.11
14	125.1	90.12	1.20	+6.4	−14.7	+1.2	−1.2	+3.4	−3.4	+3.6	−3.6	58.96	31.11
14	125.2	89.98	1.20	+6.4	−14.6	+1.2	−1.2	+3.4	−3.4	+3.6	−3.6	58.92	31.09
14	125.3	89.94	1.20	+6.4	−14.6	+1.2	−1.2	+3.4	−3.4	+3.6	−3.6	58.83	31.07
14	125.4	89.88	1.20	+6.4	−14.7	+1.2	−1.2	+3.4	−3.4	+3.6	−3.6	58.98	31.02
14	125.5	89.76	1.20	+6.4	−14.6	+1.2	−1.2	+3.4	−3.4	+3.6	−3.6	58.81	31.04
14	125.6	89.72	1.20	+6.4	−14.8	+1.2	−1.2	+3.4	−3.4	+3.6	−3.6	58.70	31.00
14	125.7	89.73	1.20	+6.4	−14.7	+1.2	−1.2	+3.4	−3.4	+3.6	−3.6	58.78	30.99
14	125.8	89.62	1.20	+6.4	−14.7	+1.2	−1.2	+3.4	−3.4	+3.6	−3.6	58.72	30.93
14	125.9	89.58	1.20	+6.4	−14.7	+1.2	−1.2	+3.4	−3.4	+3.6	−3.6	58.66	30.96
14	126.0	89.50	1.20	+6.4	−14.7	+1.2	−1.2	+3.4	−3.4	+3.6	−3.6	58.59	30.95
14	126.5	89.11	1.20	+6.4	−14.8	+1.2	−1.2	+3.4	−3.4	+3.6	−3.6	58.38	30.83
14	127.0	88.86	1.20	+6.4	−14.8	+1.2	−1.2	+3.5	−3.5	+3.7	−3.7	58.19	30.72
14	127.5	88.44	1.20	+6.4	−14.5	+1.2	−1.2	+3.4	−3.4	+3.6	−3.6	57.94	30.62
14	128.0	88.28	1.20	+6.4	−14.9	+1.2	−1.2	+3.4	−3.4	+3.6	−3.6	57.76	30.51
14	128.5	87.91	1.20	+6.3	−14.8	+1.2	−1.2	+3.5	−3.5	+3.6	−3.6	57.52	30.42
14	129.0	87.62	1.21	+6.3	−14.8	+1.2	−1.2	+3.5	−3.5	+3.6	−3.6	57.35	30.28
14	129.5	87.44	1.21	+6.3	−15.1	+1.2	−1.2	+3.5	−3.5	+3.7	−3.7	57.17	30.17
14	130.0	87.10	1.21	+6.3	−14.9	+1.2	−1.2	+3.5	−3.5	+3.7	−3.7	56.92	30.06

Table E.4: Cross sections for t-channel tH and $\bar{t}H$ production at 14 TeV.

$\sqrt{s}$	m_H	$\sigma_{tH+\bar{t}H}$	K_{QCD}	Scale+FS		α_s		PDF		PDF+α_s		σ_{tH}	$\sigma_{\bar{t}H}$
[TeV]	[GeV]	[fb]		[%]		[%]		[%]		[%]		[fb]	[fb]
6.0	125.0	7.31	1.12	+7.5	−17.5	+1.6	−1.6	+5.1	−5.1	+5.4	−5.4	5.10	2.20
6.5	125.0	9.58	1.12	+7.4	−17.3	+1.5	−1.5	+4.9	−4.9	+5.1	−5.1	6.64	2.94
7.0	125.0	12.26	1.14	+7.3	−17.2	+1.5	−1.5	+4.7	−4.7	+4.9	−4.9	8.43	3.80
7.5	125.0	15.26	1.14	+7.3	−16.7	+1.4	−1.4	+4.6	−4.6	+4.8	−4.8	10.46	4.80
8.0	125.0	18.69	1.15	+7.3	−16.5	+1.4	−1.4	+4.4	−4.4	+4.6	−4.6	12.73	5.95
8.5	125.0	22.47	1.15	+7.2	−16.3	+1.4	−1.4	+4.3	−4.3	+4.5	−4.5	15.26	7.23
9.0	125.0	26.71	1.16	+7.1	−16.2	+1.3	−1.3	+4.2	−4.2	+4.4	−4.4	18.02	8.66
9.5	125.0	31.28	1.17	+7.1	−16.0	+1.3	−1.3	+4.1	−4.1	+4.3	−4.3	21.05	10.23
10.0	125.0	36.28	1.17	+6.9	−15.8	+1.3	−1.3	+4.0	−4.0	+4.2	−4.2	24.32	11.94
10.5	125.0	41.62	1.18	+6.9	−15.6	+1.3	−1.3	+3.9	−3.9	+4.1	−4.1	27.82	13.85
11.0	125.0	47.47	1.18	+6.8	−15.5	+1.2	−1.2	+3.8	−3.8	+4.0	−4.0	31.57	15.88
11.5	125.0	53.55	1.18	+6.8	−15.2	+1.2	−1.2	+3.7	−3.7	+3.9	−3.9	35.54	18.01
12.0	125.0	60.08	1.19	+6.7	−15.2	+1.2	−1.2	+3.7	−3.7	+3.9	−3.9	39.80	20.38
12.5	125.0	67.08	1.19	+6.6	−15.1	+1.2	−1.2	+3.6	−3.6	+3.8	−3.8	44.26	22.85
13.0	125.0	74.25	1.20	+6.5	−14.9	+1.2	−1.2	+3.5	−3.5	+3.7	−3.7	48.89	25.42
13.5	125.0	82.03	1.20	+6.5	−14.8	+1.2	−1.2	+3.5	−3.5	+3.7	−3.7	53.83	28.20
14.0	125.0	90.10	1.20	+6.4	−14.7	+1.2	−1.2	+3.4	−3.4	+3.6	−3.6	59.07	31.12
14.5	125.0	98.65	1.21	+6.4	−14.8	+1.2	−1.2	+3.4	−3.4	+3.6	−3.6	64.32	34.20
15.0	125.0	107.2	1.21	+6.3	−14.4	+1.1	−1.1	+3.3	−3.3	+3.5	−3.5	69.98	37.41

Table E.5: Cross sections for t-channel tH and $\bar{t}H$ production at the LHC, for 6 TeV $\leq \sqrt{s} \leq$ 15 TeV.

$\sqrt{s}$	m_H	$\sigma_{tH+\bar{t}H}$	K_{QCD}	Scale+FS		α_s		PDF		PDF+α_s		σ_{tH}	$\sigma_{\bar{t}H}$
[TeV]	[GeV]	[fb]		[%]		[%]		[%]		[%]		[fb]	[fb]
13	125.0	848.0	1.06	+6.6	−13.3	+1.1	−1.1	+3.1	−3.1	+3.3	−3.3	546.7	301.6
14	125.0	1011	1.07	+6.5	−13.0	+1.1	−1.1	+3.0	−3.0	+3.2	−3.2	649	363

Table E.6: Cross section for t-channel tH and $\bar{t}H$ production at the 13 and 14-TeV LHC, for $y_t = -y_t^{(\mathrm{SM})}$.

$\sqrt{s}$ [TeV]	m_H [GeV]	$\sigma_{tH+\bar{t}H}$ [fb]	K_{QCD}	Scale+FS [%]		α_s [%]		PDF [%]		PDF+α_s [%]		σ_{tH} [fb]	$\sigma_{\bar{t}H}$ [fb]
13	10	1848	1.06	+8.2	−12.5	+0.9	−0.9	+2.4	−2.4	+2.6	−2.6	1174	674
13	15	1274	1.05	+8.5	−13.0	+0.9	−0.9	+2.4	−2.4	+2.6	−2.6	813	462
13	20	935.0	1.05	+8.6	−13.2	+0.9	−0.9	+2.5	−2.5	+2.7	−2.7	599.8	336.8
13	30	561.3	1.04	+8.9	−13.1	+1.0	−1.0	+2.6	−2.6	+2.7	−2.7	361.6	199.3
13	45	309.5	1.05	+9.0	−12.4	+1.0	−1.0	+2.7	−2.7	+2.9	−2.9	201.3	108.1
13	70	154.2	1.09	+8.5	−10.6	+1.0	−1.0	+3.0	−3.0	+3.2	−3.2	101.3	52.9
13	100	94.14	1.15	+7.5	−13.0	+1.1	−1.1	+3.4	−3.4	+3.6	−3.6	62.11	32.16
13	150	63.89	1.21	+5.8	−16.4	+1.2	−1.2	+3.7	−3.7	+3.9	−3.9	41.85	21.90
13	200	51.91	1.21	+4.9	−18.3	+1.3	−1.3	+3.8	−3.8	+4.0	−4.0	34.09	17.87
13	300	37.43	1.17	+3.9	−20.4	+1.3	−1.3	+4.1	−4.1	+4.3	−4.3	24.70	12.75
13	450	23.01	1.12	+3.1	−22.6	+1.4	−1.4	+4.4	−4.4	+4.6	−4.6	15.35	7.64
13	700	10.41	1.09	+2.4	−25.5	+1.5	−1.5	+5.1	−5.1	+5.3	−5.3	7.09	3.31
13	1000	4.27	1.09	+2.1	−28.3	+1.6	−1.6	+6.0	−6.0	+6.3	−6.3	2.97	1.30
13	1500	1.10	1.12	+2.1	−32.4	+2.1	−2.1	+7.9	−7.9	+8.2	−8.2	0.78	0.31
13	2000	$3.11 \cdot 10^{-1}$	1.15	+2.4	−36.1	+2.7	−2.7	+10.4	−10.4	+10.7	−10.7	$2.27 \cdot 10^{-1}$	$0.84 \cdot 10^{-1}$
13	3000	$2.82 \cdot 10^{-2}$	1.24	+3.6	−42.0	+4.5	−4.5	+16.5	−16.5	+17.1	−17.1	$2.14 \cdot 10^{-2}$	$0.68 \cdot 10^{-2}$

Table E.7: Cross sections for t-channel tH and $\bar{t}H$ production at the 13-TeV LHC in the extended Higgs mass range.

$\sqrt{s}$ [TeV]	m_H [GeV]	$\sigma_{tH+\bar{t}H}$ [fb]	K_{QCD}	Scale+FS [%]		α_s [%]		PDF [%]		PDF+α_s [%]		σ_{tH} [fb]	$\sigma_{\bar{t}H}$ [fb]
14	10	2128	1.06	+8.0	−11.8	+0.9	−0.9	+2.3	−2.3	+2.5	−2.5	1347	789
14	15	1474	1.06	+8.2	−12.6	+0.9	−0.9	+2.4	−2.4	+2.5	−2.5	935	538
14	20	1084	1.06	+8.5	−12.8	+0.9	−0.9	+2.4	−2.4	+2.6	−2.6	690	393
14	30	654.3	1.05	+8.7	−12.5	+0.9	−0.9	+2.5	−2.5	+2.7	−2.7	419.8	234.7
14	45	363.2	1.06	+8.8	−11.9	+1.0	−1.0	+2.6	−2.6	+2.8	−2.8	235.2	128.1
14	70	183.7	1.10	+8.4	−10.9	+1.0	−1.0	+2.9	−2.9	+3.1	−3.1	112.0	63.7
14	100	113.5	1.16	+7.3	−12.9	+1.1	−1.1	+3.3	−3.3	+3.4	−3.4	74.3	39.1
14	150	77.81	1.22	+5.7	−16.3	+1.2	−1.2	+3.6	−3.6	+3.8	−3.8	50.74	26.89
14	200	63.63	1.21	+4.8	−18.0	+1.3	−1.3	+3.7	−3.7	+3.9	−3.9	41.56	22.05
14	300	46.22	1.17	+3.8	−19.9	+1.3	−1.3	+3.9	−3.9	+4.1	−4.1	30.36	15.94
14	450	28.89	1.12	+3.0	−21.9	+1.3	−1.3	+4.3	−4.3	+4.5	−4.5	19.21	9.69
14	700	13.49	1.09	+2.3	−24.8	+1.4	−1.4	+4.9	−4.9	+5.1	−5.1	9.15	4.34
14	1000	5.75	1.09	+2.0	−27.9	+1.6	−1.6	+5.7	−5.7	+6.0	−6.0	3.98	1.78
14	1500	1.57	1.11	+2.0	−31.9	+1.9	−1.9	+7.4	−7.4	+7.7	−7.7	1.12	0.46
14	2000	$4.76 \cdot 10^{-1}$	1.15	+2.3	−35.3	+2.4	−2.4	+9.6	−9.6	+9.9	−9.9	$3.45 \cdot 10^{-1}$	$1.30 \cdot 10^{-1}$
14	3000	$4.99 \cdot 10^{-2}$	1.23	+3.3	−41.0	+3.9	−3.9	+14.9	−14.9	+15.4	−15.4	$3.75 \cdot 10^{-2}$	$1.24 \cdot 10^{-2}$

Table E.8: Cross sections for t-channel tH and $\bar{t}H$ production at the 14-TeV LHC in the extended Higgs mass range.

E.2 *s*-channel *tH*

In the following, we list all the input parameters used to compute the inclusive tH cross sections proceeding via an s-channel off-shell W boson, at NLO accuracy in QCD, which have been published in the fourth LHCHXSWG technical report [19].

Since, at variance with the t-channel process, s-channel tH production is not affected by flavour-scheme ambiguities, we simply employ the 5FS for simulating this process. The same input parameters as for the t-channel process in the 5FS have been used, with the exception of the reference scale choice, which in this case is

$$\mu_0^{(s-\text{channel})} = (m_H + m_t)/2\,. \tag{E.17}$$

In Tables E.9, E.10, E.11 and E.12 we collect the results for the combined s-channel $pp \to tH + \bar{t}H$ production at the LHC, at centre-of-mass energies of $\sqrt{s} = 7, 8, 13$, and 14 TeV respectively, and for various Higgs-boson masses in the range 120−130 GeV. These tables are analogous to the ones presented in the previous section for the t-channel process: in the third column we report the reference cross section; in the fourth the QCD K factor, defined in Eq. (E.12); in the fifth the scale dependence, computed from the maximum and minimum variations of the cross section among the points listed in Eq. (E.11); in the sixth, seventh, and eight the α_s, PDF, and combined PDF+α_s uncertainty, computed employing the 30+2 PDF4LHC15 Hessian set; and finally, in the last two columns we report the separate top and anti-top contributions to the cross section. In Table E.13 we show the cross-section results obtained varying the LHC energy in the range $\sqrt{s} = 6{-}15$ TeV and keeping the Higgs-boson mass fixed to $m_H = 125$ GeV. All these numbers are summarised in the plots of Figs. 5.18 and 5.20.

We also collect the analogous cross-section results in the extended Higgs-boson mass range 10−3000 GeV, at 13 and 14 TeV, in Tables E.14 and E.15 respectively. These numbers are plotted in Fig. 5.22.

$\sqrt{s}$ [TeV]	m_H [GeV]	$\sigma_{tH+\bar{t}H}$ [fb]	K_{QCD}	Scale [%]		α_s [%]		PDF [%]		PDF+α_s [%]		σ_{tH} [fb]	$\sigma_{\bar{t}H}$ [fb]
7	120.0	1.028	1.19	+2.9	−2.5	+0.0	−0.0	+3.0	−3.0	+3.0	−3.0	0.709	0.319
7	120.5	1.018	1.19	+2.9	−2.5	+0.0	−0.0	+3.0	−3.0	+3.0	−3.0	0.703	0.315
7	121.0	1.008	1.19	+2.9	−2.5	+0.0	−0.0	+3.0	−3.0	+3.0	−3.0	0.696	0.311
7	121.5	1.000	1.19	+2.9	−2.6	+0.0	−0.0	+3.0	−3.0	+3.0	−3.0	0.689	0.309
7	122.0	0.987	1.19	+2.9	−2.5	+0.0	−0.0	+3.0	−3.0	+3.0	−3.0	0.682	0.305
7	122.5	0.978	1.19	+2.8	−2.5	+0.0	−0.0	+3.0	−3.0	+3.0	−3.0	0.676	0.302
7	123.0	0.969	1.19	+2.9	−2.5	+0.0	−0.0	+3.0	−3.0	+3.0	−3.0	0.669	0.299
7	123.5	0.960	1.19	+2.9	−2.5	+0.0	−0.0	+3.0	−3.0	+3.0	−3.0	0.663	0.296
7	124.0	0.949	1.19	+2.9	−2.5	+0.0	−0.0	+3.0	−3.0	+3.0	−3.0	0.655	0.293
7	124.1	0.947	1.19	+2.9	−2.6	+0.0	−0.0	+3.0	−3.0	+3.0	−3.0	0.654	0.292
7	124.2	0.943	1.19	+2.8	−2.5	+0.0	−0.0	+3.0	−3.0	+3.0	−3.0	0.653	0.291
7	124.3	0.943	1.19	+2.9	−2.6	+0.0	−0.0	+3.0	−3.0	+3.0	−3.0	0.652	0.291
7	124.4	0.941	1.19	+2.9	−2.6	+0.0	−0.0	+3.0	−3.0	+3.0	−3.0	0.651	0.290
7	124.5	0.939	1.19	+2.9	−2.5	+0.0	−0.0	+3.0	−3.0	+3.0	−3.0	0.650	0.290
7	124.6	0.937	1.19	+2.9	−2.5	+0.0	−0.0	+3.0	−3.0	+3.0	−3.0	0.648	0.289
7	124.7	0.935	1.19	+2.9	−2.6	+0.0	−0.0	+3.0	−3.0	+3.0	−3.0	0.647	0.288
7	124.8	0.934	1.19	+2.9	−2.5	+0.0	−0.0	+3.0	−3.0	+3.0	−3.0	0.645	0.288
7	124.9	0.933	1.19	+2.9	−2.6	+0.0	−0.0	+3.0	−3.0	+3.0	−3.0	0.644	0.287
7	125.0	0.930	1.19	+2.9	−2.5	+0.0	−0.0	+3.0	−3.0	+3.0	−3.0	0.642	0.287
7	125.09	0.929	1.19	+2.9	−2.6	+0.0	−0.0	+3.0	−3.0	+3.0	−3.0	0.642	0.286
7	125.1	0.929	1.19	+2.9	−2.6	+0.0	−0.0	+3.0	−3.0	+3.0	−3.0	0.642	0.286
7	125.2	0.925	1.19	+2.8	−2.5	+0.0	−0.0	+3.0	−3.0	+3.0	−3.0	0.641	0.285
7	125.3	0.925	1.19	+2.9	−2.6	+0.0	−0.0	+3.0	−3.0	+3.0	−3.0	0.640	0.285
7	125.4	0.922	1.19	+2.9	−2.6	+0.0	−0.0	+3.0	−3.0	+3.0	−3.0	0.638	0.284
7	125.5	0.921	1.19	+2.9	−2.6	+0.0	−0.0	+3.0	−3.0	+3.0	−3.0	0.638	0.284
7	125.6	0.919	1.19	+2.9	−2.6	+0.0	−0.0	+3.0	−3.0	+3.0	−3.0	0.636	0.283
7	125.7	0.917	1.19	+2.9	−2.6	+0.0	−0.0	+3.0	−3.0	+3.0	−3.0	0.634	0.283
7	125.8	0.916	1.19	+2.9	−2.5	+0.0	−0.0	+3.0	−3.0	+3.0	−3.0	0.633	0.282
7	125.9	0.914	1.19	+2.9	−2.6	+0.0	−0.0	+3.0	−3.0	+3.0	−3.0	0.632	0.281
7	126.0	0.912	1.19	+2.9	−2.5	+0.0	−0.0	+3.0	−3.0	+3.0	−3.0	0.630	0.280
7	126.5	0.903	1.19	+2.9	−2.6	+0.0	−0.0	+3.0	−3.0	+3.0	−3.0	0.625	0.278
7	127.0	0.894	1.19	+2.9	−2.6	+0.0	−0.0	+3.0	−3.0	+3.0	−3.0	0.619	0.275
7	127.5	0.885	1.19	+2.9	−2.6	+0.0	−0.0	+3.0	−3.0	+3.0	−3.0	0.613	0.272
7	128.0	0.875	1.19	+2.9	−2.5	+0.0	−0.0	+3.1	−3.1	+3.1	−3.1	0.607	0.270
7	128.5	0.869	1.19	+2.9	−2.6	+0.0	−0.0	+3.1	−3.1	+3.1	−3.1	0.601	0.267
7	129.0	0.860	1.19	+2.9	−2.6	+0.0	−0.0	+3.1	−3.1	+3.1	−3.1	0.595	0.264
7	129.5	0.852	1.19	+2.9	−2.6	+0.0	−0.0	+3.1	−3.1	+3.1	−3.1	0.589	0.262
7	130.0	0.843	1.19	+2.9	−2.6	+0.0	−0.0	+3.1	−3.1	+3.1	−3.1	0.585	0.259

Table E.9: Cross sections for s-channel tH and $\bar{t}H$ production at the 7 TeV.

$\sqrt{s}$ [TeV]	m_H [GeV]	$\sigma_{tH+\bar{t}H}$ [fb]	K_{QCD}	Scale [%]		α_s [%]		PDF [%]		PDF+α_s [%]		σ_{tH} [fb]	$\sigma_{\bar{t}H}$ [fb]
8	120.0	1.339	1.19	+2.8	−2.4	+0.1	−0.1	+2.8	−2.8	+2.8	−2.8	0.913	0.426
8	120.5	1.326	1.19	+2.8	−2.4	+0.0	−0.0	+2.8	−2.8	+2.8	−2.8	0.903	0.422
8	121.0	1.313	1.19	+2.8	−2.3	+0.0	−0.0	+2.8	−2.8	+2.8	−2.8	0.895	0.418
8	121.5	1.301	1.19	+2.8	−2.4	+0.0	−0.0	+2.8	−2.8	+2.8	−2.8	0.887	0.413
8	122.0	1.287	1.19	+2.8	−2.4	+0.0	−0.0	+2.8	−2.8	+2.8	−2.8	0.878	0.409
8	122.5	1.274	1.19	+2.8	−2.4	+0.0	−0.0	+2.8	−2.8	+2.8	−2.8	0.870	0.405
8	123.0	1.263	1.19	+2.8	−2.4	+0.0	−0.0	+2.8	−2.8	+2.8	−2.8	0.862	0.401
8	123.5	1.251	1.19	+2.8	−2.4	+0.0	−0.0	+2.8	−2.8	+2.8	−2.8	0.854	0.397
8	124.0	1.238	1.19	+2.7	−2.3	+0.0	−0.0	+2.8	−2.8	+2.8	−2.8	0.845	0.393
8	124.1	1.235	1.19	+2.8	−2.4	+0.0	−0.0	+2.8	−2.8	+2.8	−2.8	0.843	0.392
8	124.2	1.233	1.19	+2.8	−2.4	+0.0	−0.0	+2.8	−2.8	+2.8	−2.8	0.842	0.391
8	124.3	1.232	1.19	+2.8	−2.4	+0.0	−0.0	+2.8	−2.8	+2.8	−2.8	0.841	0.390
8	124.4	1.228	1.19	+2.8	−2.4	+0.0	−0.0	+2.8	−2.8	+2.8	−2.8	0.839	0.390
8	124.5	1.225	1.19	+2.8	−2.4	+0.0	−0.0	+2.8	−2.8	+2.8	−2.8	0.838	0.388
8	124.6	1.224	1.19	+2.7	−2.4	+0.0	−0.0	+2.8	−2.8	+2.8	−2.8	0.836	0.388
8	124.7	1.221	1.19	+2.8	−2.4	+0.0	−0.0	+2.8	−2.8	+2.8	−2.8	0.834	0.387
8	124.8	1.219	1.19	+2.8	−2.4	+0.0	−0.0	+2.8	−2.8	+2.8	−2.8	0.832	0.386
8	124.9	1.216	1.19	+2.8	−2.4	+0.0	−0.0	+2.8	−2.8	+2.8	−2.8	0.831	0.385
8	125.0	1.214	1.19	+2.8	−2.4	+0.0	−0.0	+2.8	−2.8	+2.8	−2.8	0.829	0.385
8	125.09	1.211	1.19	+2.8	−2.4	+0.0	−0.0	+2.8	−2.8	+2.8	−2.8	0.828	0.384
8	125.1	1.211	1.19	+2.8	−2.4	+0.0	−0.0	+2.8	−2.8	+2.8	−2.8	0.828	0.384
8	125.2	1.209	1.19	+2.8	−2.4	+0.0	−0.0	+2.8	−2.8	+2.8	−2.8	0.827	0.383
8	125.3	1.208	1.19	+2.8	−2.4	+0.0	−0.0	+2.8	−2.8	+2.8	−2.8	0.825	0.383
8	125.4	1.204	1.19	+2.8	−2.4	+0.0	−0.0	+2.8	−2.8	+2.8	−2.8	0.824	0.381
8	125.5	1.202	1.19	+2.8	−2.4	+0.0	−0.0	+2.8	−2.8	+2.8	−2.8	0.822	0.381
8	125.6	1.200	1.19	+2.8	−2.4	+0.0	−0.0	+2.8	−2.8	+2.8	−2.8	0.820	0.380
8	125.7	1.198	1.19	+2.8	−2.4	+0.0	−0.0	+2.8	−2.8	+2.8	−2.8	0.818	0.379
8	125.8	1.195	1.19	+2.8	−2.4	+0.0	−0.0	+2.8	−2.8	+2.8	−2.8	0.817	0.379
8	125.9	1.193	1.19	+2.8	−2.4	+0.0	−0.0	+2.8	−2.8	+2.8	−2.8	0.815	0.378
8	126.0	1.191	1.19	+2.8	−2.4	+0.0	−0.0	+2.8	−2.8	+2.8	−2.8	0.814	0.377
8	126.5	1.179	1.19	+2.8	−2.4	+0.0	−0.0	+2.8	−2.8	+2.8	−2.8	0.806	0.373
8	127.0	1.167	1.19	+2.8	−2.4	+0.0	−0.0	+2.8	−2.8	+2.8	−2.8	0.798	0.370
8	127.5	1.158	1.19	+2.7	−2.3	+0.0	−0.0	+2.8	−2.8	+2.8	−2.8	0.791	0.366
8	128.0	1.146	1.19	+2.8	−2.4	+0.0	−0.0	+2.8	−2.8	+2.8	−2.8	0.784	0.363
8	128.5	1.134	1.19	+2.8	−2.4	+0.0	−0.0	+2.8	−2.8	+2.8	−2.8	0.777	0.359
8	129.0	1.126	1.19	+2.8	−2.4	+0.0	−0.0	+2.8	−2.8	+2.8	−2.8	0.770	0.356
8	129.5	1.115	1.19	+2.8	−2.4	+0.0	−0.0	+2.8	−2.8	+2.8	−2.8	0.763	0.352
8	130.0	1.103	1.19	+2.8	−2.4	+0.0	−0.0	+2.8	−2.8	+2.8	−2.8	0.755	0.348

Table E.10: Cross sections for s-channel tH and $\bar{t}H$ production at the 8 TeV.

$\sqrt{s}$ [TeV]	m_H [GeV]	$\sigma_{tH+\bar{t}H}$ [fb]	K_{QCD}	Scale [%]		α_s [%]		PDF [%]		PDF+α_s [%]		σ_{tH} [fb]	$\sigma_{\bar{t}H}$ [fb]
13	120.0	3.158	1.21	+2.4	−1.8	+0.3	−0.3	+2.2	−2.2	+2.2	−2.2	2.060	1.095
13	120.5	3.124	1.20	+2.4	−1.8	+0.3	−0.3	+2.2	−2.2	+2.2	−2.2	2.042	1.083
13	121.0	3.101	1.21	+2.4	−1.8	+0.3	−0.3	+2.2	−2.2	+2.2	−2.2	2.022	1.073
13	121.5	3.068	1.20	+2.4	−1.8	+0.3	−0.3	+2.2	−2.2	+2.2	−2.2	2.006	1.063
13	122.0	3.045	1.21	+2.4	−1.8	+0.3	−0.3	+2.2	−2.2	+2.2	−2.2	1.989	1.052
13	122.5	3.007	1.20	+2.4	−1.8	+0.3	−0.3	+2.2	−2.2	+2.2	−2.2	1.971	1.043
13	123.0	2.988	1.20	+2.4	−1.8	+0.3	−0.3	+2.2	−2.2	+2.2	−2.2	1.953	1.033
13	123.5	2.960	1.20	+2.4	−1.8	+0.2	−0.2	+2.2	−2.2	+2.2	−2.2	1.935	1.023
13	124.0	2.932	1.20	+2.4	−1.8	+0.2	−0.2	+2.2	−2.2	+2.2	−2.2	1.915	1.014
13	124.1	2.928	1.20	+2.4	−1.8	+0.2	−0.2	+2.2	−2.2	+2.2	−2.2	1.916	1.012
13	124.2	2.920	1.20	+2.4	−1.8	+0.2	−0.2	+2.2	−2.2	+2.2	−2.2	1.912	1.010
13	124.3	2.918	1.20	+2.4	−1.8	+0.2	−0.2	+2.2	−2.2	+2.2	−2.2	1.906	1.008
13	124.4	2.908	1.20	+2.4	−1.8	+0.2	−0.2	+2.2	−2.2	+2.2	−2.2	1.904	1.006
13	124.5	2.907	1.20	+2.4	−1.8	+0.2	−0.2	+2.2	−2.2	+2.2	−2.2	1.902	1.004
13	124.6	2.901	1.20	+2.4	−1.8	+0.2	−0.2	+2.2	−2.2	+2.2	−2.2	1.897	1.003
13	124.7	2.900	1.21	+2.4	−1.8	+0.2	−0.2	+2.2	−2.2	+2.2	−2.2	1.892	1.000
13	124.8	2.895	1.20	+2.4	−1.8	+0.2	−0.2	+2.2	−2.2	+2.2	−2.2	1.891	0.998
13	124.9	2.886	1.20	+2.4	−1.8	+0.2	−0.2	+2.2	−2.2	+2.2	−2.2	1.888	0.996
13	125.0	2.879	1.20	+2.4	−1.8	+0.2	−0.2	+2.2	−2.2	+2.2	−2.2	1.882	0.996
13	125.09	2.875	1.20	+2.4	−1.8	+0.2	−0.2	+2.2	−2.2	+2.2	−2.2	1.881	0.993
13	125.1	2.875	1.20	+2.4	−1.8	+0.2	−0.2	+2.2	−2.2	+2.2	−2.2	1.881	0.993
13	125.2	2.871	1.20	+2.4	−1.8	+0.2	−0.2	+2.2	−2.2	+2.2	−2.2	1.876	0.991
13	125.3	2.861	1.20	+2.4	−1.8	+0.2	−0.2	+2.2	−2.2	+2.2	−2.2	1.874	0.989
13	125.4	2.860	1.20	+2.4	−1.8	+0.2	−0.2	+2.2	−2.2	+2.2	−2.2	1.871	0.988
13	125.5	2.857	1.20	+2.4	−1.8	+0.2	−0.2	+2.2	−2.2	+2.2	−2.2	1.868	0.987
13	125.6	2.851	1.20	+2.4	−1.8	+0.2	−0.2	+2.2	−2.2	+2.2	−2.2	1.863	0.983
13	125.7	2.845	1.20	+2.4	−1.8	+0.2	−0.2	+2.2	−2.2	+2.2	−2.2	1.859	0.982
13	125.8	2.842	1.20	+2.4	−1.8	+0.2	−0.2	+2.2	−2.2	+2.2	−2.2	1.858	0.980
13	125.9	2.835	1.20	+2.4	−1.8	+0.2	−0.2	+2.2	−2.2	+2.2	−2.2	1.855	0.979
13	126.0	2.826	1.20	+2.4	−1.8	+0.2	−0.2	+2.2	−2.2	+2.2	−2.2	1.849	0.977
13	126.5	2.802	1.20	+2.4	−1.8	+0.2	−0.2	+2.2	−2.2	+2.2	−2.2	1.837	0.967
13	127.0	2.780	1.20	+2.4	−1.8	+0.2	−0.2	+2.2	−2.2	+2.2	−2.2	1.820	0.959
13	127.5	2.752	1.20	+2.4	−1.8	+0.2	−0.2	+2.2	−2.2	+2.2	−2.2	1.804	0.950
13	128.0	2.726	1.20	+2.4	−1.8	+0.2	−0.2	+2.2	−2.2	+2.2	−2.2	1.788	0.941
13	128.5	2.705	1.20	+2.4	−1.8	+0.2	−0.2	+2.2	−2.2	+2.2	−2.2	1.771	0.933
13	129.0	2.683	1.20	+2.4	−1.8	+0.2	−0.2	+2.2	−2.2	+2.2	−2.2	1.755	0.924
13	129.5	2.657	1.20	+2.4	−1.8	+0.2	−0.2	+2.2	−2.2	+2.2	−2.2	1.742	0.916
13	130.0	2.633	1.20	+2.4	−1.8	+0.2	−0.2	+2.2	−2.2	+2.2	−2.2	1.728	0.908

Table E.11: Cross sections for s-channel tH and $\bar{t}H$ production at 13 TeV.

$\sqrt{s}$ [TeV]	m_H [GeV]	$\sigma_{tH+\bar{t}H}$ [fb]	K_{QCD}	Scale [%]		α_s [%]		PDF [%]		PDF+α_s [%]		σ_{tH} [fb]	$\sigma_{\bar{t}H}$ [fb]
14	120.0	3.558	1.21	+2.3	−1.7	+0.3	−0.3	+2.1	−2.1	+2.1	−2.1	2.310	1.248
14	120.5	3.523	1.21	+2.3	−1.7	+0.3	−0.3	+2.1	−2.1	+2.1	−2.1	2.289	1.235
14	121.0	3.490	1.21	+2.3	−1.7	+0.3	−0.3	+2.1	−2.1	+2.1	−2.1	2.267	1.225
14	121.5	3.457	1.21	+2.3	−1.7	+0.3	−0.3	+2.1	−2.1	+2.1	−2.1	2.246	1.213
14	122.0	3.429	1.21	+2.3	−1.7	+0.3	−0.3	+2.1	−2.1	+2.1	−2.1	2.226	1.201
14	122.5	3.395	1.21	+2.3	−1.7	+0.3	−0.3	+2.1	−2.1	+2.1	−2.1	2.206	1.190
14	123.0	3.363	1.21	+2.3	−1.7	+0.3	−0.3	+2.1	−2.1	+2.1	−2.1	2.188	1.179
14	123.5	3.335	1.21	+2.3	−1.7	+0.3	−0.3	+2.1	−2.1	+2.1	−2.1	2.168	1.168
14	124.0	3.307	1.21	+2.3	−1.7	+0.3	−0.3	+2.1	−2.1	+2.1	−2.1	2.148	1.159
14	124.1	3.298	1.20	+2.3	−1.7	+0.3	−0.3	+2.1	−2.1	+2.1	−2.1	2.146	1.154
14	124.2	3.294	1.21	+2.3	−1.7	+0.3	−0.3	+2.1	−2.1	+2.1	−2.1	2.138	1.153
14	124.3	3.286	1.20	+2.3	−1.7	+0.3	−0.3	+2.1	−2.1	+2.1	−2.1	2.136	1.149
14	124.4	3.280	1.20	+2.3	−1.7	+0.3	−0.3	+2.1	−2.1	+2.1	−2.1	2.136	1.148
14	124.5	3.274	1.20	+2.3	−1.7	+0.3	−0.3	+2.1	−2.1	+2.1	−2.1	2.131	1.147
14	124.6	3.273	1.21	+2.3	−1.7	+0.3	−0.3	+2.1	−2.1	+2.1	−2.1	2.128	1.145
14	124.7	3.261	1.20	+2.3	−1.7	+0.3	−0.3	+2.1	−2.1	+2.1	−2.1	2.122	1.143
14	124.8	3.261	1.21	+2.3	−1.7	+0.3	−0.3	+2.1	−2.1	+2.1	−2.1	2.119	1.141
14	124.9	3.251	1.21	+2.3	−1.7	+0.3	−0.3	+2.1	−2.1	+2.1	−2.1	2.117	1.138
14	125.0	3.249	1.21	+2.3	−1.7	+0.3	−0.3	+2.1	−2.1	+2.1	−2.1	2.110	1.137
14	125.09	3.240	1.20	+2.3	−1.7	+0.3	−0.3	+2.1	−2.1	+2.1	−2.1	2.104	1.134
14	125.1	3.240	1.20	+2.3	−1.7	+0.3	−0.3	+2.1	−2.1	+2.1	−2.1	2.104	1.134
14	125.2	3.234	1.20	+2.3	−1.7	+0.3	−0.3	+2.1	−2.1	+2.1	−2.1	2.102	1.130
14	125.3	3.227	1.20	+2.3	−1.7	+0.3	−0.3	+2.1	−2.1	+2.1	−2.1	2.102	1.129
14	125.4	3.222	1.20	+2.3	−1.7	+0.3	−0.3	+2.1	−2.1	+2.1	−2.1	2.098	1.128
14	125.5	3.219	1.21	+2.3	−1.7	+0.3	−0.3	+2.1	−2.1	+2.1	−2.1	2.094	1.126
14	125.6	3.215	1.21	+2.4	−1.7	+0.3	−0.3	+2.1	−2.1	+2.1	−2.1	2.091	1.124
14	125.7	3.205	1.20	+2.3	−1.7	+0.3	−0.3	+2.1	−2.1	+2.1	−2.1	2.086	1.122
14	125.8	3.202	1.21	+2.3	−1.7	+0.3	−0.3	+2.1	−2.1	+2.1	−2.1	2.083	1.119
14	125.9	3.195	1.21	+2.3	−1.7	+0.3	−0.3	+2.1	−2.1	+2.1	−2.1	2.080	1.118
14	126.0	3.191	1.21	+2.3	−1.7	+0.3	−0.3	+2.1	−2.1	+2.1	−2.1	2.074	1.115
14	126.5	3.160	1.20	+2.3	−1.7	+0.3	−0.3	+2.1	−2.1	+2.1	−2.1	2.058	1.106
14	127.0	3.133	1.20	+2.3	−1.7	+0.3	−0.3	+2.1	−2.1	+2.1	−2.1	2.040	1.095
14	127.5	3.104	1.20	+2.4	−1.7	+0.3	−0.3	+2.1	−2.1	+2.1	−2.1	2.023	1.085
14	128.0	3.079	1.20	+2.3	−1.7	+0.3	−0.3	+2.1	−2.1	+2.1	−2.1	2.001	1.073
14	128.5	3.053	1.20	+2.4	−1.7	+0.3	−0.3	+2.1	−2.1	+2.1	−2.1	1.987	1.065
14	129.0	3.025	1.20	+2.3	−1.7	+0.3	−0.3	+2.1	−2.1	+2.2	−2.2	1.969	1.054
14	129.5	2.998	1.20	+2.3	−1.7	+0.3	−0.3	+2.1	−2.1	+2.2	−2.2	1.953	1.047
14	130.0	2.971	1.20	+2.3	−1.7	+0.3	−0.3	+2.1	−2.1	+2.2	−2.2	1.937	1.037

Table E.12: Cross sections for s-channel tH and $\bar{t}H$ production at 14 TeV.

$\sqrt{s}$ [TeV]	m_H [GeV]	$\sigma_{tH+\bar{t}H}$ [fb]	K_{QCD}	Scale [%]		α_s [%]		PDF [%]		PDF+α_s [%]		σ_{tH} [fb]	$\sigma_{\bar{t}H}$ [fb]
6.0	125.0	0.669	1.19	+3.0	−2.8	+0.1	−0.1	+3.3	−3.3	+3.3	−3.3	0.470	0.200
6.5	125.0	0.796	1.19	+2.9	−2.7	+0.1	−0.1	+3.2	−3.2	+3.2	−3.2	0.555	0.242
7.0	125.0	0.930	1.19	+2.9	−2.5	+0.0	−0.0	+3.0	−3.0	+3.0	−3.0	0.642	0.287
7.5	125.0	1.070	1.19	+2.8	−2.5	+0.0	−0.0	+2.9	−2.9	+2.9	−2.9	0.735	0.334
8.0	125.0	1.214	1.19	+2.8	−2.4	+0.0	−0.0	+2.8	−2.8	+2.8	−2.8	0.829	0.385
8.5	125.0	1.363	1.19	+2.7	−2.3	+0.1	−0.1	+2.7	−2.7	+2.7	−2.7	0.927	0.437
9.0	125.0	1.517	1.19	+2.7	−2.2	+0.1	−0.1	+2.6	−2.6	+2.6	−2.6	1.025	0.492
9.5	125.0	1.676	1.19	+2.7	−2.2	+0.1	−0.1	+2.6	−2.6	+2.6	−2.6	1.127	0.549
10.0	125.0	1.838	1.19	+2.6	−2.1	+0.1	−0.1	+2.5	−2.5	+2.5	−2.5	1.231	0.608
10.5	125.0	2.004	1.19	+2.6	−2.0	+0.2	−0.2	+2.4	−2.4	+2.4	−2.4	1.338	0.668
11.0	125.0	2.173	1.20	+2.5	−2.0	+0.2	−0.2	+2.4	−2.4	+2.4	−2.4	1.444	0.731
11.5	125.0	2.345	1.20	+2.5	−1.9	+0.2	−0.2	+2.3	−2.3	+2.3	−2.3	1.550	0.794
12.0	125.0	2.519	1.20	+2.5	−1.9	+0.2	−0.2	+2.3	−2.3	+2.3	−2.3	1.661	0.859
12.5	125.0	2.703	1.20	+2.4	−1.8	+0.2	−0.2	+2.2	−2.2	+2.2	−2.2	1.772	0.928
13.0	125.0	2.879	1.20	+2.4	−1.8	+0.2	−0.2	+2.2	−2.2	+2.2	−2.2	1.882	0.996
13.5	125.0	3.060	1.20	+2.4	−1.7	+0.3	−0.3	+2.2	−2.2	+2.2	−2.2	1.997	1.065
14.0	125.0	3.249	1.21	+2.3	−1.7	+0.3	−0.3	+2.1	−2.1	+2.1	−2.1	2.110	1.137
14.5	125.0	3.439	1.21	+2.3	−1.7	+0.3	−0.3	+2.1	−2.1	+2.1	−2.1	2.227	1.207
15.0	125.0	3.623	1.21	+2.3	−1.6	+0.3	−0.3	+2.1	−2.1	+2.1	−2.1	2.343	1.281

Table E.13: Cross sections for s-channel tH and $\bar{t}H$ production at the LHC, for 6 TeV $\leq \sqrt{s} \leq$ 15 TeV.

$\sqrt{s}$ [TeV]	m_H [GeV]	$\sigma_{tH+\bar{t}H}$ [fb]	K_{QCD}	Scale [%]		α_s [%]		PDF [%]		PDF+α_s [%]		σ_{tH} [fb]	$\sigma_{\bar{t}H}$ [fb]
13	10	104.1	1.26	+2.4	−1.9	+0.5	−0.5	+1.8	−1.8	+1.9	−1.9	64.9	39.3
13	15	74.10	1.26	+2.4	−1.9	+0.5	−0.5	+1.8	−1.8	+1.9	−1.9	46.24	27.79
13	20	55.68	1.25	+2.3	−1.9	+0.5	−0.5	+1.9	−1.9	+1.9	−1.9	34.89	20.80
13	30	34.87	1.24	+2.3	−1.8	+0.5	−0.5	+1.9	−1.9	+1.9	−1.9	21.95	12.90
13	45	19.80	1.24	+2.2	−1.8	+0.4	−0.4	+1.9	−1.9	+2.0	−2.0	12.58	7.24
13	70	9.420	1.22	+2.2	−1.6	+0.4	−0.4	+2.0	−2.0	+2.0	−2.0	6.056	3.386
13	100	4.678	1.21	+2.4	−1.7	+0.3	−0.3	+2.1	−2.1	+2.1	−2.1	3.032	1.642
13	150	1.888	1.19	+2.4	−1.8	+0.2	−0.2	+2.3	−2.3	+2.3	−2.3	1.245	0.642
13	200	0.929	1.18	+2.4	−2.0	+0.1	−0.1	+2.5	−2.5	+2.5	−2.5	0.622	0.307
13	300	0.314	1.16	+2.3	−2.1	+0.0	−0.0	+2.8	−2.8	+2.8	−2.8	0.215	0.099
13	450	$9.39 \cdot 10^{-2}$	1.14	+2.1	−2.1	+0.2	−0.2	+3.3	−3.3	+3.3	−3.3	$6.61 \cdot 10^{-2}$	$2.79 \cdot 10^{-2}$
13	700	$2.13 \cdot 10^{-2}$	1.13	+2.0	−2.4	+0.5	−0.5	+4.1	−4.1	+4.1	−4.1	$1.54 \cdot 10^{-2}$	$0.58 \cdot 10^{-2}$
13	1000	$5.17 \cdot 10^{-3}$	1.14	+2.1	−2.8	+0.7	−0.7	+5.0	−5.0	+5.0	−5.0	$3.84 \cdot 10^{-3}$	$1.33 \cdot 10^{-3}$
13	1500	$7.14 \cdot 10^{-4}$	1.16	+2.5	−3.3	+1.0	−1.0	+6.2	−6.2	+6.3	−6.3	$5.42 \cdot 10^{-4}$	$1.71 \cdot 10^{-4}$
13	2000	$1.24 \cdot 10^{-4}$	1.18	+2.9	−3.9	+1.4	−1.4	+7.2	−7.2	+7.4	−7.4	$0.95 \cdot 10^{-4}$	$0.29 \cdot 10^{-4}$
13	3000	$4.80 \cdot 10^{-6}$	1.24	+3.9	−5.2	+2.3	−2.3	+12.8	−12.8	+12.8	−12.8	$3.59 \cdot 10^{-6}$	$1.21 \cdot 10^{-6}$

Table E.14: Cross sections for *s*-channel tH and $\bar{t}H$ production at the 13-TeV LHC in the extended Higgs mass range.

$\sqrt{s}$ [TeV]	m_H [GeV]	$\sigma_{tH+\bar{t}H}$ [fb]	K_{QCD}	Scale [%]		α_s [%]		PDF [%]		PDF+α_s [%]		σ_{tH} [fb]	$\sigma_{\bar{t}H}$ [fb]
14	10	115.3	1.26	+2.4	−2.0	+0.6	−0.6	+1.8	−1.8	+1.9	−1.9	71.4	43.8
14	15	81.83	1.26	+2.4	−1.9	+0.5	−0.5	+1.8	−1.8	+1.9	−1.9	50.82	31.05
14	20	61.75	1.26	+2.4	−1.9	+0.5	−0.5	+1.8	−1.8	+1.9	−1.9	38.47	23.24
14	30	38.70	1.25	+2.3	−1.9	+0.5	−0.5	+1.8	−1.8	+1.9	−1.9	24.26	14.46
14	45	22.05	1.24	+2.2	−1.8	+0.4	−0.4	+1.9	−1.9	+1.9	−1.9	13.90	8.13
14	70	10.54	1.23	+2.2	−1.7	+0.4	−0.4	+2.0	−2.0	+2.0	−2.0	6.716	3.820
14	100	5.248	1.21	+2.3	−1.6	+0.3	−0.3	+2.0	−2.0	+2.1	−2.1	3.389	1.865
14	150	2.139	1.20	+2.3	−1.8	+0.2	−0.2	+2.2	−2.2	+2.2	−2.2	1.403	0.737
14	200	1.062	1.18	+2.3	−1.9	+0.1	−0.1	+2.4	−2.4	+2.4	−2.4	0.705	0.355
14	300	0.363	1.16	+2.3	−2.0	+0.0	−0.0	+2.7	−2.7	+2.7	−2.7	0.247	0.116
14	450	0.111	1.13	+2.0	−2.0	+0.2	−0.2	+3.2	−3.2	+3.2	−3.2	0.078	0.034
14	700	$2.61 \cdot 10^{-2}$	1.13	+2.0	−2.3	+0.4	−0.4	+3.9	−3.9	+3.9	−3.9	$1.88 \cdot 10^{-2}$	$0.73 \cdot 10^{-2}$
14	1000	$6.59 \cdot 10^{-3}$	1.13	+2.0	−2.6	+0.6	−0.6	+4.7	−4.7	+4.8	−4.8	$4.88 \cdot 10^{-3}$	$1.72 \cdot 10^{-3}$
14	1500	$9.86 \cdot 10^{-4}$	1.15	+2.3	−3.1	+1.0	−1.0	+5.9	−5.9	+6.0	−6.0	$7.45 \cdot 10^{-4}$	$2.39 \cdot 10^{-4}$
14	2000	$1.85 \cdot 10^{-4}$	1.17	+2.6	−3.7	+1.3	−1.3	+6.9	−6.9	+7.0	−7.0	$1.42 \cdot 10^{-4}$	$0.44 \cdot 10^{-4}$
14	3000	$8.70 \cdot 10^{-6}$	1.22	+3.6	−4.8	+2.1	−2.1	+10.5	−10.5	+10.7	−10.7	$6.58 \cdot 10^{-6}$	$2.12 \cdot 10^{-6}$

Table E.15: Cross sections for s-channel tH and $\bar{t}H$ production at the 14-TeV LHC in the extended Higgs mass range.

Appendix F

The tWb and $tWbH$ channels in the 4FS

In this Appendix we perform a study of the various ways to treat the tWb channel in tW production at NLO In particular, we discuss the performance and shortcomings of the diagram removal and diagram subtraction techniques, which are used to eliminate the $t\bar{t}$ resonant contribution. Since the issue appears just in the matrix-element description, the study in this Appendix is simply performed at the partonic level. The tWb channel is more easily addressed in the 4FS, where it appears as a finite and independent LO contribution, thus it can be isolated from the other channels contributing to tW. The only difference from the 5FS is that bottom mass effects are included in the 4FS description, which act as an IR cutoff; the Feynman diagrams are the same ones describing the 5FS NLO real-emission channel, and the features and shortcomings of DR and DS are independent of the flavour scheme employed. An analogous study is then repeated for the $tWbH$ channel in the 4FS.

The problem of the LO $t\bar{t}$ contribution in the $tW^-\bar{b}$ channel has first been addressed in [225], where it is subtracted at the cross section level (see Eq. (4) in the reference). This *global subtraction* procedure (GS) is described in Section 6.2; an important point in the calculation is that the two pieces, $tW^-\bar{b}$ and $t\bar{t}$, are separately integrated before the subtraction is performed (since they belong to different phase spaces). The GS procedure ensures that the remainder of the subtraction converges to a well-defined limit $\Gamma_t \to 0$, where the result is fully gauge invariant, and exactly all and just the LO on-shell $t\bar{t}$ contribution is subtracted. Therefore, combining the $t\bar{t}$ simulation with the $tW^-\bar{b}$ obtained this way, one gets a well-defined total rate for producing the common physical final state, without double counting and also including interference effects; this procedure provides a consistent way to define the tW cross section.

Actually, the only way to perform a theoretically consistent simulation that encompasses both the top-pair and single-top contributions, that is gauge invariant and that includes interference and other finite-width effects, is to compute $pp \to W^+bW^-\bar{b}$ in the 4FS and using a complex top-quark mass. This $WbWb$ simulation will also contain the contribution from amplitudes without any resonant top propagator $\mathcal{A}_{0t}$, and also interference between single-top and single-antitop contributions $\mathcal{A}_{1t}\mathcal{A}^*_{1\bar{t}}$, which are not present in the tWb result

$$\begin{aligned}
|\mathcal{A}_{WbWb}|^2 &= |\mathcal{A}_{2t} + \mathcal{A}_{1t} + \mathcal{A}_{1\bar{t}} + \mathcal{A}_{0t}|^2 \\
&= |\mathcal{A}_{2t}|^2 + \Big[|\mathcal{A}_{1t}|^2 + 2\mathrm{Re}(\mathcal{A}_{2t}\mathcal{A}^*_{1t}) \Big] \\
&+ \Big[|\mathcal{A}_{1\bar{t}}|^2 + 2\mathrm{Re}(\mathcal{A}_{2t}\mathcal{A}^*_{1\bar{t}}) \Big] \\
&+ 2\mathrm{Re}(\mathcal{A}_{1t}\mathcal{A}^*_{1\bar{t}}) \\
&+ \Big[|\mathcal{A}_{0t}|^2 + 2\mathrm{Re}\big((\mathcal{A}_{2t} + \mathcal{A}_{1t} + \mathcal{A}_{1\bar{t}})\mathcal{A}^*_{0t}\big) \Big] ;
\end{aligned} \tag{F.1}$$

nonetheless, we expect the last two lines in Eq. (F.1) to be negligible compared to the previous two lines, which encompass top-pair $t\bar{t}$ and single-top tWb production. In the end, the reference result will be the difference between the $WbWb$ cross section (computed in the complex-mass scheme, with a physical Γ_t) and the $t\bar{t}$ cross section (computed with on-shell top's), which in general guarantees a correct description of tWb production. If the non resonant contributions $\mathcal{A}_{0t}$ to $WbWb$, the $\mathcal{A}_{1t}\mathcal{A}^*_{1\bar{t}}$ interference, and the off-shell effects related the single top kept stable in tWb simulations are small enough, this cross section will be close to the one obtained from GS.

The global subtraction schemes cannot be applied to event generation, where a fully *local subtraction* of the top-pair contribution must be performed in the $2 \to 3$ phase space; this is exactly the reason why alternative techniques such as DR and DS have been developed and implemented in MC@NLO and POWHEG for tW production. Nevertheless, a simple but powerful way to test the adequacy of DR and DS can be carried out by comparing their total cross section with the GS one, which is the number we expect to be returned from a consistent local subtraction scheme. We perform this comparison in Table F.1, where cross sections are computed with the static scale μ_0^s, also showing the cross section ratio R defined as

$$R = \frac{\sigma_{tWb}}{\sigma_{WbWb} - \sigma_{t\bar{t}}} \,. \tag{F.2}$$

process	σ_{LO} [pb]	R
$WbWb$ (complex t mass)	640.3(2)	-
$t\bar{t}$ (t stable)	609.0(1)	-
$WbWb - t\bar{t}$	31.3(2)	1
tWb GS	30.9(3)	0.99(1)
tWb DR1	40.79(1)	1.30(1)
tWb DR2	31.11(1)	0.99(1)
$WbWb - \|\mathcal{A}_{2t}\|^2$	31.81(1)	1.01(1)
tWb DS1	38.31(3)	1.22(1)
tWb DS2	31.56(2)	1.01(1)

Table F.1: LO cross sections in the 4FS at the 13-TeV LHC for the processes $pp \to W^+bW^-\bar{b}$ (complex-mass scheme), $pp \to t\bar{t}$ (t stable), and singly resonant $pp \to tW^-\bar{b}$ plus $pp \to \bar{t}W^+b$ computed using the GS, DR and DS prescriptions. For these tWb results we also report the ratio R defined in Eq. (F.2). All numbers are computed using the static scale $\mu_0^s = (m_t + m_W)/2$, and the numerical uncertainty affecting the last digit is reported in parentheses.

From the results in Table F.1 we first notice that the $WbWb - t\bar{t}$ cross section (computed with a physical Γ_t) is in good agreement with the tWb one computed with the GS prescription (which is independent on the actual value of Γ_t), thus either can be considered as the reference value. This also confirms that non resonant contributions from A_{0t} and $\mathcal{A}_{1t}\mathcal{A}_{1\bar{t}}^*$ interference are small, and justifies the 5FS treatment where one top is always on shell.

Among the two diagram removal techniques, the DR1 modelling does not capture the $\mathcal{A}_{2t}\mathcal{A}_{1t}^*$ interference, which amounts to more than 9 pb (this was evident already in Table 6.1). On the other hand, there is excellent agreement between the DR2 cross section and the desired one from $WbWb - t\bar{t}$, thus any possible violation of gauge invariance in the DR2 total rate must be negligible.[1] When we compute $|\mathcal{A}_{WbWb}|^2 - |\mathcal{A}_{2t}|^2$ (namely $WbWb - |\mathcal{A}_{2t}|^2$ in Table F.1), we can see that the difference with tWb DR2 is a modest 2%; this provides a further confirmation that effects related to A_{0t}, $\mathcal{A}_{1t}\mathcal{A}_{1\bar{t}}^*$ interference, and off-

---

[1] We recall that in our simulations we have included only transverse polarisations of initial-state gluons, and we have employed a covariant gauge for gluon propagators. A non-covariant gauge (axial) was shown to lead to differences at the level of permille in the case of tW production [231].

shell t are small; the subtraction of $|\mathcal{A}_{2t}|^2$ in a covariant gauge turns out to be almost equivalent to an on-shell $t\bar{t}$ subtraction (compare $WbWb - t\bar{t}$ and $WbWb - |\mathcal{A}_{2t}|^2$). Moving to diagram subtraction, we can see that DS2 is in rather good agreement with GS and DR2, while DS1 clearly overestimates the total rate, which tends to be much closer to DR1.

The situation can be understood also at the differential level by looking at the m_{Wb} distribution in Fig. F.1. The missing of interference in DR1 leads to an underestimate of the rate in the low-mass region $m_{Wb} < m_t$, and to an overestimate in the tail $m_{Wb} > m_t$; at the LHC energy, the latter region dominates, leading to a net overestimate of the total rate.[2] DR2 and DS2 nicely reproduce the peak-dip interference pattern, with small differences between the two curves; since DS2 is gauge invariant, this fact can be interpreted as that gauge effects in DR2, when employing a covariant gauge, are small also at the level of differential shapes. Finally, while DS1 includes interference effects as well, it also introduces a significant distortion in the profile of the subtraction term $\mathcal{C}_{2t}$, as already shown in Fig. 6.3; the net effect is an unreliable m_{Wb} profile, with an inverted dip-peak structure and a too large tail.

We now move on to studying the $tWbH$ channel in tWH production at NLO, which overlaps with LO $t\bar{t}H$. We follow a procedure completely analogous to the one employed for tWb, therefore we do not repeat all the details in the following discussion.

Our reference total rate is the difference between the $WbWbH$ cross section, computed in the complex top-quark mass scheme, and the $t\bar{t}H$ cross section computed in the approximation of stable final-state top quarks. Once again we find GS to be in very good agreement with this reference value, so both results can be taken as a reference for comparison with DR and DS, see Table F.2.

We can see that the ratio between top-pair and single-top amplitudes is even higher than for $t\bar{t}$ versus tW, and this exacerbates the same problems we have observed in that case. Interference effects are very large and neglecting them results in an error of $O(100\%)$ in DR1, where the cross section is more than twice that from GS. Once again, we find DR2 results to be in excellent agreement within the numerical accuracy. The impact of non resonant amplitudes and of interference between single-top and single-antitop contributions is very small, less than 2% of the DR2 rate in this channel. The rate obtained from DS1 is overestimated by more than a factor two, while DS2 looks again in

---

[2] We have verified that the net sum of interference effects in the total rate is positive at collider energies below ~ 2 TeV, while becomes more and more negative at higher energies, where the phase space for $m_{Wb} > m_t$ is larger.

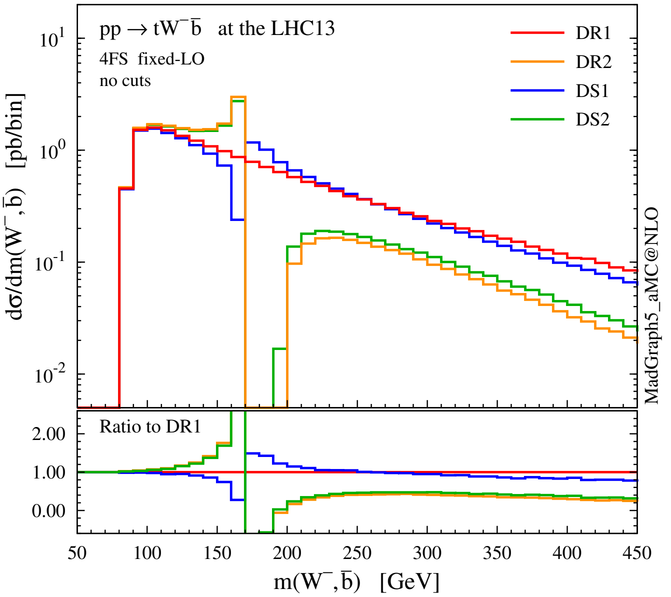

Figure F.1: Invariant mass $m(W^-, \bar{b})$ in the $pp \to tW^-\bar{b}$ process, computed with DR and DS.

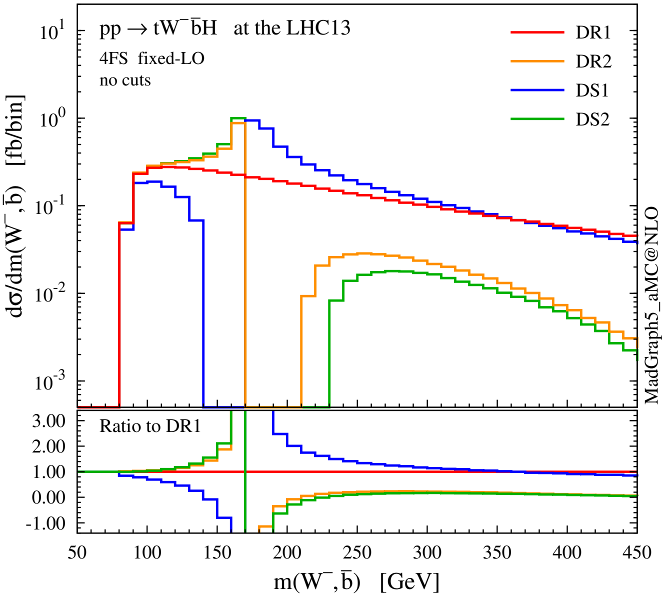

Figure F.2: Invariant mass $m(W^-, \bar{b})$ in the $pp \to tW^-\bar{b}H$ process, computed with DR and DS.

process	$\sigma_{\rm LO}$ [fb]	R
$WbWbH$ (complex t mass)	468.5(1)	-
$t\bar{t}H$ (t stable)	463.0(1)	-
$WbWbH - t\bar{t}H$	5.5(1)	1
$tWbH$ GS	5.7(2)	1.04(3)
$tWbH$ DR1	12.35(1)	2.27(5)
$tWbH$ DR2	5.49(1)	1.01(2)
$WbWbH - \lvert\mathcal{A}_{2t}\rvert^2$	5.59(2)	1.02(2)
$tWbH$ DS1	11.17(2)	2.05(4)
$tWbH$ DS2	4.80(2)	0.88(2)

Table F.2: LO cross sections in the 4FS at the LHC with $\sqrt{s} = 13$ TeV for the processes $pp \to W^+bW^-\bar{b}H$ (complex-mass scheme), $pp \to t\bar{t}H$ (t stable), and singly resonant $pp \to tW^-\bar{b}H$ plus $pp \to \bar{t}W^+bH$ computed using the GS, DR and DS prescriptions. For these $tWbH$ results we also report the ratio R, which is analogous to the one defined in Eq. (F.2). All numbers are computed using the static scale $\mu_0^s = (m_t + m_W + m_H)/2$, and the numerical uncertainty affecting the last digit is reported in parentheses.

better agreement with GS and DR2, although there is a residual difference of about 0.7 fb (slightly larger than the 0.3 fb in the 5FS scheme).

In Fig. F.2 we show the m_{Wb} differential distribution. A similar pattern of the one for tWb is repeated: interference effects are large and positive in the $m_{Wb} < m_t$ region, while negative for $m_{Wb} > m_t$, where DR1 clearly overestimates the event rate. The interference pattern is nicely reproduced by the DR2 and DS2 shapes, although there are some minor differences between the two methods; instead, DS1 fails to return a physical shape, due to the visibly distorted profile of the subtraction term $\mathcal{C}_{2t}$, see Fig. 6.3.

We would like to stress one final remark: the fact that gauge dependence is apparently not an issue in the DR2 procedure should be regarded as a peculiarity of the tWb and $tWbH$ channels, and not as a general result. We cannot exclude that gauge dependence could become a significant issue at higher perturbative orders (NNLO $tW(H)$), or in other processes with a more complex colour flow, or using a different (*i.e.* non-covariant) gauge.

Bibliography

[1] ATLAS collaboration, G. Aad et al., *Observation of a new particle in the search for the Standard Model Higgs boson with the ATLAS detector at the LHC*, *Phys. Lett.* **B716** (2012) 1–29, [`1207.7214`].

[2] CMS collaboration, S. Chatrchyan et al., *Observation of a new boson at a mass of 125 GeV with the CMS experiment at the LHC*, *Phys. Lett.* **B716** (2012) 30–61, [`1207.7235`].

[3] F. Englert and R. Brout, *Broken Symmetry and the Mass of Gauge Vector Mesons*, *Phys.Rev.Lett.* **13** (1964) 321–323.

[4] P. W. Higgs, *Broken symmetries, massless particles and gauge fields*, *Phys.Lett.* **12** (1964) 132–133.

[5] P. W. Higgs, *Broken Symmetries and the Masses of Gauge Bosons*, *Phys.Rev.Lett.* **13** (1964) 508–509.

[6] P. W. Higgs, *Spontaneous Symmetry Breakdown without Massless Bosons*, *Phys. Rev.* **145** (1966) 1156–1163.

[7] G. S. Guralnik, C. R. Hagen and T. W. B. Kibble, *Global Conservation Laws and Massless Particles*, *Phys. Rev. Lett.* **13** (1964) 585–587.

[8] S. Weinberg, *A Model of Leptons*, *Phys. Rev. Lett.* **19** (1967) 1264–1266.

[9] CMS collaboration, S. Chatrchyan et al., *Study of the Mass and Spin-Parity of the Higgs Boson Candidate Via Its Decays to Z Boson Pairs*, *Phys.Rev.Lett.* **110** (2013) 081803, [`1212.6639`].

[10] ATLAS collaboration, G. Aad et al., *Evidence for the spin-0 nature of the Higgs boson using ATLAS data*, *Phys.Lett.* **B726** (2013) 120–144, [`1307.1432`].

[11] CMS collaboration, V. Khachatryan et al., *Constraints on the spin-parity and anomalous HVV couplings of the Higgs boson in proton collisions at 7 and 8 TeV*, *Phys. Rev.* **D92** (2015) 012004, [`1411.3441`].

[12] ATLAS, CMS collaboration, G. Aad et al., *Measurements of the Higgs boson production and decay rates and constraints on its couplings from a combined ATLAS and CMS analysis of the LHC pp collision data at* $\sqrt{s} = 7$ *and 8 TeV*, *JHEP* **08** (2016) 045, [`1606.02266`].

[13] CDF collaboration, F. Abe et al., *Observation of top quark production in $\bar{p}p$ collisions*, *Phys. Rev. Lett.* **74** (1995) 2626–2631, [`hep-ex/9503002`].

[14] D0 collaboration, S. Abachi et al., *Observation of the top quark*, *Phys. Rev. Lett.* **74** (1995) 2632–2637, [`hep-ex/9503003`].

[15] P. Artoisenet, P. de Aquino, F. Demartin, R. Frederix, S. Frixione et al., *A framework for Higgs characterisation*, *JHEP* **1311** (2013) 043, [`1306.6464`].

[16] F. Demartin, F. Maltoni, K. Mawatari, B. Page and M. Zaro, *Higgs characterisation at NLO in QCD: CP properties of the top-quark Yukawa interaction*, *Eur.Phys.J.* **C74** (2014) 3065, [`1407.5089`].

[17] F. Demartin, F. Maltoni, K. Mawatari and M. Zaro, *Higgs production in association with a single top quark at the LHC*, *Eur. Phys. J.* **C75** (2015) 267, [`1504.00611`].

[18] F. Demartin, B. Maier, F. Maltoni, K. Mawatari and M. Zaro, *tWH associated production at the LHC*, *Eur. Phys. J.* **C77** (2017) 34, [`1607.05862`].

[19] LHC Higgs Cross Section Working Group collaboration, D. de Florian et al., *Handbook of LHC Higgs Cross Sections: 4. Deciphering the Nature of the Higgs Sector*, `1610.07922`.

[20] F. Demartin, E. Vryonidou, K. Mawatari and M. Zaro, *Higgs characterisation: NLO and parton-shower effects*, in *2nd Toyama International Workshop on Higgs as a Probe of New Physics (HPNP2015) Toyama, Japan, February 11-15, 2015*, 2015. `1505.07081`.

[21] F. Demartin and B. Maier, *Single top, W and Higgs associated production*, *PoS* **TOP2015** (2016) 080.

[22] The Higgs Characterisation model.
`http://feynrules.irmp.ucl.ac.be/wiki/HiggsCharacterisation`.

[23] R. K. Ellis, W. J. Stirling and B. R. Webber, *QCD and collider physics*, *Camb. Monogr. Part. Phys. Nucl. Phys. Cosmol.* **8** (1996) 1–435.

[24] Particle Data Group collaboration, C. Patrignani et al., *Review of Particle Physics*, *Chin. Phys.* **C40** (2016) 100001.

[25] D. J. Gross and F. Wilczek, *Ultraviolet Behavior of Nonabelian Gauge Theories*, *Phys. Rev. Lett.* **30** (1973) 1343–1346.

[26] H. D. Politzer, *Asymptotic Freedom: An Approach to Strong Interactions*, *Phys. Rept.* **14** (1974) 129–180.

[27] CMS collaboration, V. Khachatryan et al., *Measurement of the inclusive 3-jet production differential cross section in protonproton collisions at 7 TeV and determination of the strong coupling constant in the TeV range*, *Eur. Phys. J.* **C75** (2015) 186, [`1412.1633`].

[28] J. C. Collins, D. E. Soper and G. F. Sterman, *Factorization of Hard Processes in QCD*, *Adv. Ser. Direct. High Energy Phys.* **5** (1989) 1–91, [`hep-ph/0409313`].

[29] Y. L. Dokshitzer, *Calculation of the Structure Functions for Deep Inelastic Scattering and e+ e- Annihilation by Perturbation Theory in Quantum Chromodynamics.*, *Sov. Phys. JETP* **46** (1977) 641–653.

[30] V. N. Gribov and L. N. Lipatov, *Deep inelastic e p scattering in perturbation theory*, *Sov. J. Nucl. Phys.* **15** (1972) 438–450.

[31] G. Altarelli and G. Parisi, *Asymptotic Freedom in Parton Language*, *Nucl. Phys.* **B126** (1977) 298–318.

[32] H1 collaboration, F. D. Aaron et al., *Inclusive Deep Inelastic Scattering at High Q^2 with Longitudinally Polarised Lepton Beams at HERA*, *JHEP* **09** (2012) 061, [`1206.7007`].

[33] L. A. Harland-Lang, A. D. Martin, P. Motylinski and R. S. Thorne, *Parton distributions in the LHC era: MMHT 2014 PDFs*, *Eur. Phys. J.* **C75** (2015) 204, [`1412.3989`].

[34] M. Spira, A. Djouadi, D. Graudenz and P. Zerwas, *Higgs boson production at the LHC*, *Nucl.Phys.* **B453** (1995) 17–82, [`hep-ph/9504378`].

[35] S. Dawson, S. Dittmaier and M. Spira, *Neutral Higgs boson pair production at hadron colliders: QCD corrections*, *Phys. Rev.* **D58** (1998) 115012, [`hep-ph/9805244`].

[36] L. Altenkamp, S. Dittmaier, R. V. Harlander, H. Rzehak and T. J. E. Zirke, *Gluon-induced Higgs-strahlung at next-to-leading order QCD*, *JHEP* **02** (2013) 078, [`1211.5015`].

[37] S. Alioli, F. Caola, G. Luisoni and R. Rontsch, *ZZ production in gluon fusion at NLO matched to parton-shower*, `1609.09719`.

[38] T. Kinoshita, *Mass singularities of Feynman amplitudes*, *J. Math. Phys.* **3** (1962) 650–677.

[39] T. D. Lee and M. Nauenberg, *Degenerate Systems and Mass Singularities*, *Phys. Rev.* **133** (1964) B1549–B1562.

[40] M. Cacciari, G. P. Salam and G. Soyez, *The Anti-k(t) jet clustering algorithm*, *JHEP* **0804** (2008) 063, [`0802.1189`].

[41] S. Frixione, Z. Kunszt and A. Signer, *Three jet cross-sections to next-to-leading order*, *Nucl.Phys.* **B467** (1996) 399–442, [`hep-ph/9512328`].

[42] S. Catani and M. H. Seymour, *A General algorithm for calculating jet cross-sections in NLO QCD*, *Nucl. Phys.* **B485** (1997) 291–419, [`hep-ph/9605323`].

[43] D. A. Kosower, *Antenna factorization of gauge theory amplitudes*, *Phys. Rev.* **D57** (1998) 5410–5416, [`hep-ph/9710213`].

[44] J. M. Campbell, M. A. Cullen and E. W. N. Glover, *Four jet event shapes in electron - positron annihilation*, *Eur. Phys. J.* **C9** (1999) 245–265, [`hep-ph/9809429`].

[45] D. A. Kosower, *Antenna factorization in strongly ordered limits*, *Phys. Rev.* **D71** (2005) 045016, [`hep-ph/0311272`].

[46] OPAL event displays.
`https://opal.web.cern.ch/Opal/events/opalpics.html`.

[47] Sherpa. `https://sherpa.hepforge.org/trac/wiki`.

[48] T. Sjostrand, P. Eden, C. Friberg, L. Lonnblad, G. Miu, S. Mrenna et al., *High-energy physics event generation with PYTHIA 6.1*, *Comput. Phys. Commun.* **135** (2001) 238–259, [`hep-ph/0010017`].

[49] T. Sjostrand, S. Mrenna and P. Z. Skands, *PYTHIA 6.4 Physics and Manual*, *JHEP* **0605** (2006) 026, [`hep-ph/0603175`].

[50] T. Sjstrand, S. Ask, J. R. Christiansen, R. Corke, N. Desai, P. Ilten et al., *An Introduction to PYTHIA 8.2*, *Comput. Phys. Commun.* **191** (2015) 159–177, [`1410.3012`].

[51] G. Corcella, I. Knowles, G. Marchesini, S. Moretti, K. Odagiri et al., *HERWIG 6: An Event generator for hadron emission reactions with interfering gluons (including supersymmetric processes)*, *JHEP* **0101** (2001) 010, [`hep-ph/0011363`].

[52] M. Bahr, S. Gieseke, M. Gigg, D. Grellscheid, K. Hamilton et al., *Herwig++ Physics and Manual*, *Eur.Phys.J.* **C58** (2008) 639–707, [`0803.0883`].

[53] T. Gleisberg, S. Hoeche, F. Krauss, M. Schonherr, S. Schumann, F. Siegert et al., *Event generation with SHERPA 1.1*, *JHEP* **02** (2009) 007, [`0811.4622`].

[54] G. Bozzi, S. Catani, G. Ferrera, D. de Florian and M. Grazzini, *Production of Drell-Yan lepton pairs in hadron collisions: Transverse-momentum resummation at next-to-next-to-leading logarithmic accuracy*, *Phys. Lett.* **B696** (2011) 207–213, [`1007.2351`].

[55] S. Frixione and B. R. Webber, *Matching NLO QCD computations and parton shower simulations*, *JHEP* **0206** (2002) 029, [`hep-ph/0204244`].

[56] P. Nason, *A New method for combining NLO QCD with shower Monte Carlo algorithms*, *JHEP* **11** (2004) 040, [`hep-ph/0409146`].

[57] J. Alwall, R. Frederix, S. Frixione, V. Hirschi, F. Maltoni et al., *The automated computation of tree-level and next-to-leading order differential cross sections, and their matching to parton shower simulations*, *JHEP* **1407** (2014) 079, [`1405.0301`].

[58] C. Degrande, C. Duhr, B. Fuks, D. Grellscheid, O. Mattelaer et al., *UFO - The Universal FeynRules Output*, *Comput.Phys.Commun.* **183** (2012) 1201–1214, [`1108.2040`].

[59] R. Frederix, S. Frixione, F. Maltoni and T. Stelzer, *Automation of next-to-leading order computations in QCD: the FKS subtraction*, *JHEP* **10** (2009) 003, [`0908.4272`].

[60] S. Frixione, E. Laenen, P. Motylinski and B. R. Webber, *Angular correlations of lepton pairs from vector boson and top quark decays in Monte Carlo simulations*, *JHEP* **04** (2007) 081, [`hep-ph/0702198`].

[61] P. Artoisenet, R. Frederix, O. Mattelaer and R. Rietkerk, *Automatic spin-entangled decays of heavy resonances in Monte Carlo simulations*, *JHEP* **1303** (2013) 015, [`1212.3460`].

[62] A. Djouadi, *The Anatomy of electro-weak symmetry breaking. I: The Higgs boson in the standard model*, *Phys. Rept.* **457** (2008) 1–216, [`hep-ph/0503172`].

[63] LHC Higgs Cross Section Working Group collaboration, S. Dittmaier et al., *Handbook of LHC Higgs Cross Sections: 1. Inclusive Observables*, `1101.0593`.

[64] LHC Higgs Cross Section Working Group collaboration, S. Dittmaier et al., *Handbook of LHC Higgs Cross Sections: 2. Differential Distributions*, `1201.3084`.

[65] LHC Higgs Cross Section Working Group collaboration, J. R. Andersen et al., *Handbook of LHC Higgs Cross Sections: 3. Higgs Properties*, `1307.1347`.

[66] SLAC-SP-017 collaboration, J. E. Augustin et al., *Discovery of a Narrow Resonance in e+ e- Annihilation*, *Phys. Rev. Lett.* **33** (1974) 1406–1408.

[67] E598 collaboration, J. J. Aubert et al., *Experimental Observation of a Heavy Particle J*, *Phys. Rev. Lett.* **33** (1974) 1404–1406.

[68] M. Kobayashi and T. Maskawa, *CP Violation in the Renormalizable Theory of Weak Interaction*, *Prog. Theor. Phys.* **49** (1973) 652–657.

[69] M. L. Perl et al., *Evidence for Anomalous Lepton Production in e+ - e- Annihilation*, *Phys. Rev. Lett.* **35** (1975) 1489–1492.

[70] S. W. Herb et al., *Observation of a Dimuon Resonance at 9.5-GeV in 400-GeV Proton-Nucleus Collisions*, *Phys. Rev. Lett.* **39** (1977) 252–255.

[71] DONUT collaboration, K. Kodama et al., *Observation of tau neutrino interactions*, *Phys. Lett.* **B504** (2001) 218–224, [`hep-ex/0012035`].

[72] A. B. Galtieri, F. Margaroli and I. Volobouev, *Precision measurements of the top quark mass from the Tevatron in the pre-LHC era*, *Rept. Prog. Phys.* **75** (2012) 056201, [`1109.2163`].

[73] D. Buttazzo, G. Degrassi, P. P. Giardino, G. F. Giudice, F. Sala, A. Salvio et al., *Investigating the near-criticality of the Higgs boson*, *JHEP* **12** (2013) 089, [`1307.3536`].

[74] M. E. Peskin and D. V. Schroeder, *An Introduction to quantum field theory.* 1995.

[75] A. H. Hoang, A. V. Manohar, I. W. Stewart and T. Teubner, *The Threshold t anti-t cross-section at NNLL order*, *Phys. Rev.* **D65** (2002) 014014, [`hep-ph/0107144`].

[76] K. Hagiwara, Y. Sumino and H. Yokoya, *Bound-state Effects on Top Quark Production at Hadron Colliders*, *Phys. Lett.* **B666** (2008) 71–76, [`0804.1014`].

[77] A. H. Hoang and I. W. Stewart, *Top Mass Measurements from Jets and the Tevatron Top-Quark Mass*, *Nucl. Phys. Proc. Suppl.* **185** (2008) 220–226, [`0808.0222`].

[78] P. Nason, *Theory Summary*, *PoS* **TOP2015** (2016) 056, [`1602.00443`].

[79] K. Seidel, F. Simon, M. Tesar and S. Poss, *Top quark mass measurements at and above threshold at CLIC*, *Eur. Phys. J.* **C73** (2013) 2530, [`1303.3758`].

[80] G. 't Hooft, *Renormalizable Lagrangians for Massive Yang-Mills Fields*, *Nucl. Phys.* **B35** (1971) 167–188.

[81] G. 't Hooft and M. J. G. Veltman, *Regularization and Renormalization of Gauge Fields*, *Nucl. Phys.* **B44** (1972) 189–213.

[82] J. R. Ellis, M. K. Gaillard and D. V. Nanopoulos, *A Phenomenological Profile of the Higgs Boson*, *Nucl. Phys.* **B106** (1976) 292.

[83] Gargamelle Neutrino collaboration, F. J. Hasert et al., *Observation of Neutrino Like Interactions Without Muon Or Electron in the Gargamelle Neutrino Experiment*, *Phys. Lett.* **B46** (1973) 138–140.

[84] UA1 collaboration, G. Arnison et al., *Experimental Observation of Isolated Large Transverse Energy Electrons with Associated Missing Energy at s**(1/2) = 540-GeV*, *Phys. Lett.* **B122** (1983) 103–116.

[85] UA1 collaboration, G. Arnison et al., *Experimental Observation of Lepton Pairs of Invariant Mass Around 95-GeV/c**2 at the CERN SPS Collider*, *Phys. Lett.* **B126** (1983) 398–410.

[86] LEP Electroweak Working Group. `http://lepewwg.web.cern.ch/LEPEWWG/plots/winter2012/`.

[87] Gfitter Group collaboration, M. Baak, J. Cth, J. Haller, A. Hoecker, R. Kogler, K. Mnig et al., *The global electroweak fit at NNLO and prospects for the LHC and ILC*, *Eur. Phys. J.* **C74** (2014) 3046, [`1407.3792`].

[88] The LHC Higgs Cross Section Working Group. `https://twiki.cern.ch/twiki/bin/view/LHCPhysics/LHCHXSWG`.

[89] A. Kobakhidze, N. Liu, L. Wu and J. Yue, *Implications of CP-violating Top-Higgs Couplings at LHC and Higgs Factories*, *Phys. Rev.* **D95** (2017) 015016, [`1610.06676`].

[90] LHC Higgs Cross Section Working Group collaboration, A. David, A. Denner, M. Duehrssen, M. Grazzini, C. Grojean, G. Passarino et al., *LHC HXSWG interim recommendations to explore the coupling structure of a Higgs-like particle*, `1209.0040`.

[91] G. C. Branco, P. M. Ferreira, L. Lavoura, M. N. Rebelo, M. Sher and J. P. Silva, *Theory and phenomenology of two-Higgs-doublet models*, *Phys. Rept.* **516** (2012) 1–102, [`1106.0034`].

[92] P. M. Ferreira, J. F. Gunion, H. E. Haber and R. Santos, *Probing wrong-sign Yukawa couplings at the LHC and a future linear collider*, *Phys. Rev.* **D89** (2014) 115003, [`1403.4736`].

[93] P. M. Ferreira, R. Guedes, M. O. P. Sampaio and R. Santos, *Wrong sign and symmetric limits and non-decoupling in 2HDMs*, *JHEP* **12** (2014) 067, [`1409.6723`].

[94] T. D. Lee, *A Theory of Spontaneous T Violation*, *Phys. Rev.* **D8** (1973) 1226–1239.

[95] CMS collaboration, V. Khachatryan et al., *Searches for heavy Higgs bosons in two-Higgs-doublet models and for tch decay using multilepton and diphoton final states in pp collisions at 8 TeV*, *Phys. Rev.* **D90** (2014) 112013, [`1410.2751`].

[96] ATLAS collaboration, G. Aad et al., *Search for flavour-changing neutral current top quark decays $t \to Hq$ in pp collisions at $\sqrt{s} = 8$ TeV with the ATLAS detector*, *JHEP* **12** (2015) 061, [`1509.06047`].

[97] G. Ossola, C. G. Papadopoulos and R. Pittau, *Reducing full one-loop amplitudes to scalar integrals at the integrand level*, *Nucl.Phys.* **B763** (2007) 147–169, [`hep-ph/0609007`].

[98] S. M. Barr and A. Zee, *Electric Dipole Moment of the Electron and of the Neutron*, *Phys. Rev. Lett.* **65** (1990) 21–24.

[99] S. Weinberg, *Larger Higgs Exchange Terms in the Neutron Electric Dipole Moment*, *Phys. Rev. Lett.* **63** (1989) 2333.

[100] J. Brod, U. Haisch and J. Zupan, *Constraints on CP-violating Higgs couplings to the third generation*, *JHEP* **1311** (2013) 180, [`1310.1385`].

[101] C. Anastasiou, C. Duhr, F. Dulat, F. Herzog and B. Mistlberger, *Higgs Boson Gluon-Fusion Production in QCD at Three Loops*, *Phys. Rev. Lett.* **114** (2015) 212001, [`1503.06056`].

[102] X. Chen, J. Cruz-Martinez, T. Gehrmann, E. W. N. Glover and M. Jaquier, *NNLO QCD corrections to Higgs boson production at large transverse momentum*, *JHEP* **10** (2016) 066, [`1607.08817`].

[103] G. Cullen, H. van Deurzen, N. Greiner, G. Luisoni, P. Mastrolia et al., *Next-to-Leading-Order QCD Corrections to Higgs Boson Production Plus Three Jets in Gluon Fusion*, *Phys.Rev.Lett.* **111** (2013) 131801, [`1307.4737`].

[104] V. Del Duca, W. Kilgore, C. Oleari, C. Schmidt and D. Zeppenfeld, *Higgs + 2 jets via gluon fusion*, *Phys.Rev.Lett.* **87** (2001) 122001, [`hep-ph/0105129`].

[105] V. Del Duca, W. Kilgore, C. Oleari, C. Schmidt and D. Zeppenfeld, *Gluon fusion contributions to H + 2 jet production*, *Nucl.Phys.* **B616** (2001) 367–399, [`hep-ph/0108030`].

[106] F. Campanario and M. Kubocz, *Higgs boson production in association with three jets via gluon fusion at the LHC: Gluonic contributions*, *Phys.Rev.* **D88** (2013) 054021, [`1306.1830`].

[107] F. Campanario and M. Kubocz, *Higgs boson CP-properties of the gluonic contributions in Higgs plus three jet production via gluon fusion at the LHC*, *JHEP* **10** (2014) 173, [`1402.1154`].

[108] J. M. Campbell, R. K. Ellis and C. Williams, *Hadronic production of a Higgs boson and two jets at next-to-leading order*, *Phys.Rev.* **D81** (2010) 074023, [`1001.4495`].

[109] J. M. Campbell, R. K. Ellis, R. Frederix, P. Nason, C. Oleari et al., *NLO Higgs Boson Production Plus One and Two Jets Using the POWHEG BOX, MadGraph4 and MCFM*, *JHEP* **1207** (2012) 092, [`1202.5475`].

[110] S. Hoeche, F. Krauss and M. Schonherr, *Uncertainties in MEPS@NLO calculations of h+jets*, *Phys. Rev.* **D90** (2014) 014012, [`1401.7971`].

[111] H. van Deurzen, N. Greiner, G. Luisoni, P. Mastrolia, E. Mirabella et al., *NLO QCD corrections to the production of Higgs plus two jets at the LHC*, *Phys.Lett.* **B721** (2013) 74–81, [`1301.0493`].

[112] F. Campanario, M. Kubocz and D. Zeppenfeld, *Gluon-fusion contributions to Phi + 2 Jet production*, *Phys.Rev.* **D84** (2011) 095025, [`1011.3819`].

[113] R. D. Ball, V. Bertone, S. Carrazza, C. S. Deans, L. Del Debbio et al., *Parton distributions with LHC data*, *Nucl.Phys.* **B867** (2013) 244–289, [`1207.1303`].

[114] M. Whalley, D. Bourilkov and R. Group, *The Les Houches accord PDFs (LHAPDF) and LHAGLUE*, `hep-ph/0508110`.

[115] F. Demartin, S. Forte, E. Mariani, J. Rojo and A. Vicini, *The impact of PDF and alphas uncertainties on Higgs Production in gluon fusion at hadron colliders*, *Phys.Rev.* **D82** (2010) 014002, [`1004.0962`].

[116] S. Alekhin, S. Alioli, R. D. Ball, V. Bertone, J. Blumlein et al., *The PDF4LHC Working Group Interim Report*, `1101.0536`.

[117] M. Botje, J. Butterworth, A. Cooper-Sarkar, A. de Roeck, J. Feltesse et al., *The PDF4LHC Working Group Interim Recommendations*, `1101.0538`.

[118] NNPDF collaboration, R. D. Ball et al., *Unbiased global determination of parton distributions and their uncertainties at NNLO and at LO*, *Nucl.Phys.* **B855** (2012) 153–221, [`1107.2652`].

[119] A. Martin, W. Stirling, R. Thorne and G. Watt, *Parton distributions for the LHC*, *Eur.Phys.J.* **C63** (2009) 189–285, [`0901.0002`].

[120] M. Cacciari, G. P. Salam and G. Soyez, *FastJet User Manual*, *Eur.Phys.J.* **C72** (2012) 1896, [`1111.6097`].

[121] F. Maltoni, K. Mawatari and M. Zaro, *Higgs characterisation via vector-boson fusion and associated production: NLO and parton-shower effects*, *Eur.Phys.J.* **C74** (2014) 2710, [`1311.1829`].

[122] S. Frixione, P. Torrielli and M. Zaro, *Higgs production through vector-boson fusion at the NLO matched with parton showers*, *Phys.Lett.* **B726** (2013) 273–282, [`1304.7927`].

[123] R. P. Kauffman and S. V. Desai, *Production of a Higgs pseudoscalar plus two jets in hadronic collisions*, *Phys.Rev.* **D59** (1999) 057504, [`hep-ph/9808286`].

[124] G. Klamke and D. Zeppenfeld, *Higgs plus two jet production via gluon fusion as a signal at the CERN LHC*, *JHEP* **0704** (2007) 052, [`hep-ph/0703202`].

[125] K. Hagiwara, Q. Li and K. Mawatari, *Jet angular correlation in vector-boson fusion processes at hadron colliders*, *JHEP* **0907** (2009) 101, [`0905.4314`].

[126] J. R. Andersen, K. Arnold and D. Zeppenfeld, *Azimuthal Angle Correlations for Higgs Boson plus Multi-Jet Events*, *JHEP* **1006** (2010) 091, [`1001.3822`].

[127] C. Englert, M. Spannowsky and M. Takeuchi, *Measuring Higgs CP and couplings with hadronic event shapes*, *JHEP* **1206** (2012) 108, [`1203.5788`].

[128] C. Englert, D. Goncalves-Netto, K. Mawatari and T. Plehn, *Higgs Quantum Numbers in Weak Boson Fusion*, *JHEP* **1301** (2013) 148, [`1212.0843`].

[129] M. J. Dolan, P. Harris, M. Jankowiak and M. Spannowsky, *Constraining CP-violating Higgs Sectors at the LHC using gluon fusion*, *Phys. Rev.* **D90** (2014) 073008, [`1406.3322`].

[130] A. Djouadi, R. Godbole, B. Mellado and K. Mohan, *Probing the spin-parity of the Higgs boson via jet kinematics in vector boson fusion*, *Phys.Lett.* **B723** (2013) 307–313, [`1301.4965`].

[131] B. E. Cox, J. R. Forshaw and A. D. Pilkington, *Extracting Higgs boson couplings using a jet veto*, *Phys.Lett.* **B696** (2011) 87–91, [`1006.0986`].

[132] E. Gerwick, T. Plehn and S. Schumann, *Understanding Jet Scaling and Jet Vetos in Higgs Searches*, *Phys.Rev.Lett.* **108** (2012) 032003, [`1108.3335`].

[133] S. Gangal and F. J. Tackmann, *Next-to-leading-order uncertainties in Higgs+2 jets from gluon fusion*, *Phys.Rev.* **D87** (2013) 093008, [`1302.5437`].

[134] J. Andersen, T. Binoth, G. Heinrich and J. Smillie, *Loop induced interference effects in Higgs Boson plus two jet production at the LHC*, *JHEP* **0802** (2008) 057, [`0709.3513`].

[135] A. Bredenstein, K. Hagiwara and B. Jager, *Mixed QCD-electroweak contributions to Higgs-plus-dijet production at the LHC*, *Phys.Rev.* **D77** (2008) 073004, [`0801.4231`].

[136] CMS collaboration, *Search for* $\mathrm{t\bar{t}H}$ *production in the* $\mathrm{H} \to \mathrm{b\bar{b}}$ *decay channel with* $\sqrt{s} = 13$ TeV *pp collisions at the CMS experiment*, .

[137] W. Beenakker, S. Dittmaier, M. Kramer, B. Plumper, M. Spira et al., *Higgs radiation off top quarks at the Tevatron and the LHC*, *Phys.Rev.Lett.* **87** (2001) 201805, [`hep-ph/0107081`].

[138] S. Dawson, L. Orr, L. Reina and D. Wackeroth, *Associated top quark Higgs boson production at the LHC*, *Phys.Rev.* **D67** (2003) 071503, [`hep-ph/0211438`].

[139] R. Frederix, S. Frixione, V. Hirschi, F. Maltoni, R. Pittau and P. Torrielli, *Scalar and pseudoscalar Higgs production in association with a top-antitop pair*, *Phys.Lett.* **B701** (2011) 427–433, [`1104.5613`].

[140] M. Garzelli, A. Kardos, C. Papadopoulos and Z. Trocsanyi, *Standard Model Higgs boson production in association with a top anti-top pair at NLO with parton showering*, *Europhys.Lett.* **96** (2011) 11001, [`1108.0387`].

[141] S. Biswas, R. Frederix, E. Gabrielli and B. Mele, *Enhancing the $t\bar{t}H$ signal through top-quark spin polarization effects at the LHC*, *JHEP* **1407** (2014) 020, [`1403.1790`].

[142] J. Ellis, D. S. Hwang, K. Sakurai and M. Takeuchi, *Disentangling Higgs-Top Couplings in Associated Production*, *JHEP* **1404** (2014) 004, [`1312.5736`].

[143] S. Frixione, V. Hirschi, D. Pagani, H. S. Shao and M. Zaro, *Weak corrections to Higgs hadroproduction in association with a top-quark pair*, *JHEP* **1409** (2014) 065, [`1407.0823`].

[144] Y. Zhang, W.-G. Ma, R.-Y. Zhang, C. Chen and L. Guo, *QCD NLO and EW NLO corrections to $t\bar{t}H$ production with top quark decays at hadron collider*, *Phys. Lett.* **B738** (2014) 1–5, [`1407.1110`].

[145] S. Frixione, V. Hirschi, D. Pagani, H. S. Shao and M. Zaro, *Electroweak and QCD corrections to top-pair hadroproduction in association with heavy bosons*, *JHEP* **06** (2015) 184, [`1504.03446`].

[146] J. Aguilar-Saavedra, *A Minimal set of top-Higgs anomalous couplings*, *Nucl.Phys.* **B821** (2009) 215–227, [`0904.2387`].

[147] C. Zhang and S. Willenbrock, *Effective-Field-Theory Approach to Top-Quark Production and Decay*, *Phys.Rev.* **D83** (2011) 034006, [`1008.3869`].

[148] C. Zhang, N. Greiner and S. Willenbrock, *Constraints on Non-standard Top Quark Couplings*, *Phys.Rev.* **D86** (2012) 014024, [`1201.6670`].

[149] C. Degrande, J.-M. Gerard, C. Grojean, F. Maltoni and G. Servant, *Non-resonant New Physics in Top Pair Production at Hadron Colliders*, *JHEP* **1103** (2011) 125, [`1010.6304`].

[150] C. Degrande, J. Gerard, C. Grojean, F. Maltoni and G. Servant, *Probing Top-Higgs Non-Standard Interactions at the LHC*, *JHEP* **1207** (2012) 036, [`1205.1065`].

[151] C. Zhang and F. Maltoni, *Top-quark decay into Higgs boson and a light quark at next-to-leading order in QCD*, *Phys.Rev.* **D88** (2013) 054005, [`1305.7386`].

[152] C. Zhang, *Effective field theory approach to top-quark decay at next-to-leading order in QCD*, *Phys.Rev.* **D90** (2014) 014008, [`1404.1264`].

[153] J. Alwall, A. Ballestrero, P. Bartalini, S. Belov, E. Boos et al., *A Standard format for Les Houches event files*, *Comput.Phys.Commun.* **176** (2007) 300–304, [`hep-ph/0609017`].

[154] P. Artoisenet, P. de Aquino, F. Maltoni and O. Mattelaer, *Unravelling $t\bar{t}h$ via the Matrix Element Method*, *Phys.Rev.Lett.* **111** (2013) 091802, [`1304.6414`].

[155] J. M. Butterworth, A. R. Davison, M. Rubin and G. P. Salam, *Jet substructure as a new Higgs search channel at the LHC*, *Phys.Rev.Lett.* **100** (2008) 242001, [`0802.2470`].

[156] T. Plehn, G. P. Salam and M. Spannowsky, *Fat Jets for a Light Higgs*, *Phys.Rev.Lett.* **104** (2010) 111801, [`0910.5472`].

[157] M. R. Buckley, T. Plehn, T. Schell and M. Takeuchi, *Buckets of Higgs and Tops*, *JHEP* **1402** (2014) 130, [`1310.6034`].

[158] J. Bramante, A. Delgado and A. Martin, *Cornering a Hyper Higgs: Angular Kinematics for Boosted Higgs Bosons with Top Pairs*, *Phys.Rev.* **D89** (2014) 093006, [`1402.5985`].

[159] D. Contardo, M. Klute, J. Mans, L. Silvestris and J. Butler, *Technical Proposal for the Phase-II Upgrade of the CMS Detector*, Tech. Rep. CERN-LHCC-2015-010. LHCC-P-008. CMS-TDR-15-02, Geneva, Jun, 2015.

[160] S. Dawson and L. Reina, *QCD corrections to associated Higgs boson production*, *Phys.Rev.* **D57** (1998) 5851–5859, [`hep-ph/9712400`].

[161] S. Dittmaier, M. Kramer, Y. Liao, M. Spira and P. Zerwas, *Higgs radiation off quarks in supersymmetric theories at e^+e^- colliders*, *Phys.Lett.* **B478** (2000) 247–254, [`hep-ph/0002035`].

[162] F. Maltoni, K. Paul, T. Stelzer and S. Willenbrock, *Associated production of Higgs and single top at hadron colliders*, *Phys.Rev.* **D64** (2001) 094023, [`hep-ph/0106293`].

[163] F. Maltoni, G. Ridolfi and M. Ubiali, *b-initiated processes at the LHC: a reappraisal*, *JHEP* **1207** (2012) 022, [`1203.6393`].

[164] J. Campbell, R. K. Ellis and R. Rntsch, *Single top production in association with a Z boson at the LHC*, *Phys. Rev.* **D87** (2013) 114006, [`1302.3856`].

[165] M. Kramer, F. I. Olness and D. E. Soper, *Treatment of heavy quarks in deeply inelastic scattering*, *Phys.Rev.* **D62** (2000) 096007, [`hep-ph/0003035`].

[166] M. Cacciari, M. Greco and P. Nason, *The P(T) spectrum in heavy flavor hadroproduction*, *JHEP* **05** (1998) 007, [`hep-ph/9803400`].

[167] S. Forte, E. Laenen, P. Nason and J. Rojo, *Heavy quarks in deep-inelastic scattering*, *Nucl. Phys.* **B834** (2010) 116–162, [`1001.2312`].

[168] M. Brucherseifer, F. Caola and K. Melnikov, *On the NNLO QCD corrections to single-top production at the LHC*, *Phys.Lett.* **B736** (2014) 58–63, [`1404.7116`].

[169] J. M. Campbell, R. Frederix, F. Maltoni and F. Tramontano, *Next-to-Leading-Order Predictions for t-Channel Single-Top Production at Hadron Colliders*, *Phys.Rev.Lett.* **102** (2009) 182003, [`0903.0005`].

[170] M. Wiesemann, R. Frederix, S. Frixione, V. Hirschi, F. Maltoni et al., *Higgs production in association with bottom quarks*, *JHEP* **1502** (2015) 132, [`1409.5301`].

[171] A. Martin, W. Stirling, R. Thorne and G. Watt, *Heavy-quark mass dependence in global PDF analyses and 3- and 4-flavour parton distributions*, *Eur.Phys.J.* **C70** (2010) 51–72, [`1007.2624`].

[172] H.-L. Lai, M. Guzzi, J. Huston, Z. Li, P. M. Nadolsky et al., *New parton distributions for collider physics*, *Phys.Rev.* **D82** (2010) 074024, [`1007.2241`].

[173] PARTICLE DATA GROUP collaboration, K. Olive et al., *Review of Particle Physics*, *Chin.Phys.* **C38** (2014) 090001.

[174] A. Martin, W. Stirling, R. Thorne and G. Watt, *Uncertainties on alpha(S) in global PDF analyses and implications for predicted hadronic cross sections*, *Eur.Phys.J.* **C64** (2009) 653–680, [`0905.3531`].

[175] H.-L. Lai, J. Huston, Z. Li, P. Nadolsky, J. Pumplin et al., *Uncertainty induced by QCD coupling in the CTEQ global analysis of parton distributions*, *Phys.Rev.* **D82** (2010) 054021, [`1004.4624`].

[176] S. Lionetti, R. D. Ball, V. Bertone, F. Cerutti, L. Del Debbio et al., *Precision determination of α_s using an unbiased global NLO parton set*, *Phys.Lett.* **B701** (2011) 346–352, [`1103.2369`].

[177] T. Sjostrand, S. Mrenna and P. Z. Skands, *A Brief Introduction to PYTHIA 8.1*, *Comput.Phys.Commun.* **178** (2008) 852–867, [`0710.3820`].

[178] R. D. Ball, S. Carrazza, L. Del Debbio, S. Forte, J. Gao et al., *Parton Distribution Benchmarking with LHC Data*, *JHEP* **1304** (2013) 125, [`1211.5142`].

[179] ATLAS, CDF, CMS, D0 collaboration, *First combination of Tevatron and LHC measurements of the top-quark mass*, `1403.4427`.

[180] ATLAS collaboration, M. Aaboud et al., *Measurement of the top quark mass in the $t\bar{t} \rightarrow$ dilepton channel from $\sqrt{s} = 8$ TeV ATLAS data*, *Phys. Lett.* **B761** (2016) 350–371, [`1606.02179`].

[181] CMS collaboration, V. Khachatryan et al., *Measurement of the top quark mass using proton-proton data at $\sqrt{(s)} = 7$ and 8 TeV*, *Phys. Rev.* **D93** (2016) 072004, [`1509.04044`].

[182] ATLAS, CMS collaboration, G. Aad et al., *Combined Measurement of the Higgs Boson Mass in pp Collisions at $\sqrt{s} = 7$ and 8 TeV with the ATLAS and CMS Experiments*, *Phys. Rev. Lett.* **114** (2015) 191803, [`1503.07589`].

[183] J. Butterworth et al., *PDF4LHC recommendations for LHC Run II*, *J. Phys.* **G43** (2016) 023001, [`1510.03865`].

[184] S. Dulat, T.-J. Hou, J. Gao, M. Guzzi, J. Huston, P. Nadolsky et al., *New parton distribution functions from a global analysis of quantum chromodynamics*, *Phys. Rev.* **D93** (2016) 033006, [`1506.07443`].

[185] NNPDF collaboration, R. D. Ball et al., *Parton distributions for the LHC Run II*, *JHEP* **04** (2015) 040, [`1410.8849`].

[186] A. Denner, S. Dittmaier, M. Grazzini, R. V. Harlander, R. S. Thorne, M. Spira et al., *Standard Model input parameters for Higgs physics*, .

[187] S. Biswas, E. Gabrielli and B. Mele, *Single top and Higgs associated production as a probe of the Htt coupling sign at the LHC*, *JHEP* **1301** (2013) 088, [`1211.0499`].

[188] M. Farina, C. Grojean, F. Maltoni, E. Salvioni and A. Thamm, *Lifting degeneracies in Higgs couplings using single top production in association with a Higgs boson*, *JHEP* **1305** (2013) 022, [`1211.3736`].

[189] J. Yue, *Enhanced thj signal at the LHC with $h \to \gamma\gamma$ decay and $\mathcal{CP}$-violating top-Higgs coupling*, *Phys. Lett.* **B744** (2015) 131–136, [`1410.2701`].

[190] A. Kobakhidze, L. Wu and J. Yue, *Anomalous Top-Higgs Couplings and Top Polarisation in Single Top and Higgs Associated Production at the LHC*, *JHEP* **1410** (2014) 100, [`1406.1961`].

[191] J. Chang, K. Cheung, J. S. Lee and C.-T. Lu, *Probing the Top-Yukawa Coupling in Associated Higgs production with a Single Top Quark*, *JHEP* **1405** (2014) 062, [`1403.2053`].

[192] C. Englert and E. Re, *Bounding the top Yukawa coupling with Higgs-associated single-top production*, *Phys.Rev.* **D89** (2014) 073020, [`1402.0445`].

[193] P. Agrawal, S. Mitra and A. Shivaji, *Effect of Anomalous Couplings on the Associated Production of a Single Top Quark and a Higgs Boson at the LHC*, *JHEP* **1312** (2013) 077, [`1211.4362`].

[194] ATLAS collaboration, G. Aad et al., *Study of the spin and parity of the Higgs boson in diboson decays with the ATLAS detector*, *Eur. Phys. J.* **C75** (2015) 476, [`1506.05669`].

[195] K. Cheung, J. S. Lee and P.-Y. Tseng, *Higgs Precision (Higgcision) Era begins*, *JHEP* **1305** (2013) 134, [`1302.3794`].

[196] A. Djouadi and G. Moreau, *The couplings of the Higgs boson and its CP properties from fits of the signal strengths and their ratios at the 7+8 TeV LHC*, *Eur.Phys.J.* **C73** (2013) 2512, [`1303.6591`].

[197] K. Nishiwaki, S. Niyogi and A. Shivaji, *ttH Anomalous Coupling in Double Higgs Production*, *JHEP* **1404** (2014) 011, [`1309.6907`].

[198] F. Boudjema, R. M. Godbole, D. Guadagnoli and K. A. Mohan, *Lab-frame observables for probing the top-Higgs interaction*, *Phys. Rev.* **D92** (2015) 015019, [`1501.03157`].

[199] A. Denner, S. Dittmaier, M. Roth and D. Wackeroth, *Predictions for all processes e+ e- $\to$ 4 fermions + gamma*, *Nucl. Phys.* **B560** (1999) 33–65, [`hep-ph/9904472`].

[200] A. Denner, S. Dittmaier, M. Roth and L. H. Wieders, *Electroweak corrections to charged-current e+ e- $\to$ 4 fermion processes: Technical details and further results*, *Nucl. Phys.* **B724** (2005) 247–294, [`hep-ph/0505042`].

[201] A. Denner, S. Dittmaier, S. Kallweit and S. Pozzorini, *NLO QCD corrections to WWbb production at hadron colliders*, *Phys. Rev. Lett.* **106** (2011) 052001, [`1012.3975`].

[202] G. Bevilacqua, M. Czakon, A. van Hameren, C. G. Papadopoulos and M. Worek, *Complete off-shell effects in top quark pair hadroproduction with leptonic decay at next-to-leading order*, *JHEP* **02** (2011) 083, [`1012.4230`].

[203] A. Denner, S. Dittmaier, S. Kallweit and S. Pozzorini, *NLO QCD corrections to off-shell top-antitop production with leptonic decays at hadron colliders*, *JHEP* **10** (2012) 110, [`1207.5018`].

[204] R. Frederix, *Top Quark Induced Backgrounds to Higgs Production in the $WW^{(*)} \to ll\nu\nu$ Decay Channel at Next-to-Leading-Order in QCD*, *Phys. Rev. Lett.* **112** (2014) 082002, [`1311.4893`].

[205] F. Cascioli, S. Kallweit, P. Maierhöfer and S. Pozzorini, *A unified NLO description of top-pair and associated Wt production*, *Eur. Phys. J.* **C74** (2014) 2783, [`1312.0546`].

[206] G. Heinrich, A. Maier, R. Nisius, J. Schlenk and J. Winter, *NLO QCD corrections to $W^+W^-b\bar{b}$ production with leptonic decays in the light of top quark mass and asymmetry measurements*, *JHEP* **06** (2014) 158, [`1312.6659`].

[207] T. Ježo and P. Nason, *On the Treatment of Resonances in Next-to-Leading Order Calculations Matched to a Parton Shower*, *JHEP* **12** (2015) 065, [`1509.09071`].

[208] R. Frederix, S. Frixione, A. S. Papanastasiou, S. Prestel and P. Torrielli, *Off-shell single-top production at NLO matched to parton showers*, *JHEP* **06** (2016) 027, [`1603.01178`].

[209] T. Jeo, J. M. Lindert, P. Nason, C. Oleari and S. Pozzorini, *An NLO+PS generator for $t\bar{t}$ and Wt production and decay including non-resonant and interference effects*, *Eur. Phys. J.* **C76** (2016) 691, [`1607.04538`].

[210] A. Denner and R. Feger, *NLO QCD corrections to off-shell top-antitop production with leptonic decays in association with a Higgs boson at the LHC*, *JHEP* **11** (2015) 209, [`1506.07448`].

[211] CMS collaboration, S. Chatrchyan et al., *Measurement of the t-channel single top quark production cross section in pp collisions at $\sqrt{s} = 7$ TeV*, *Phys. Rev. Lett.* **107** (2011) 091802, [`1106.3052`].

[212] CMS collaboration, S. Chatrchyan et al., *Measurement of the single-top-quark t-channel cross section in pp collisions at $\sqrt{s} = 7$ TeV*, *JHEP* **12** (2012) 035, [`1209.4533`].

[213] ATLAS collaboration, G. Aad et al., *Measurement of the t-channel single top-quark production cross section in pp collisions at $\sqrt{s} = 7$ TeV with the ATLAS detector*, *Phys. Lett.* **B717** (2012) 330–350, [`1205.3130`].

[214] CMS collaboration, V. Khachatryan et al., *Measurement of the t-channel single-top-quark production cross section and of the $\mid V_{tb} \mid$ CKM matrix element in pp collisions at $\sqrt{s}$= 8 TeV*, *JHEP* **06** (2014) 090, [`1403.7366`].

[215] ATLAS collaboration, G. Aad et al., *Evidence for single top-quark production in the s-channel in proton-proton collisions at $\sqrt{s}$ =8 TeV with the ATLAS detector using the Matrix Element Method*, *Phys. Lett.* **B756** (2016) 228–246, [`1511.05980`].

[216] CMS collaboration, V. Khachatryan et al., *Search for s channel single top quark production in pp collisions at* $\sqrt{s} = 7$ *and 8 TeV*, *JHEP* **09** (2016) 027, [`1603.02555`].

[217] CMS collaboration, S. Chatrchyan et al., *Evidence for associated production of a single top quark and W boson in pp collisions at* $\sqrt{s} = 7$ *TeV*, *Phys. Rev. Lett.* **110** (2013) 022003, [`1209.3489`].

[218] ATLAS collaboration, G. Aad et al., *Measurement of the production cross-section of a single top quark in association with a W boson at 8 TeV with the ATLAS experiment*, *JHEP* **01** (2016) 064, [`1510.03752`].

[219] CMS collaboration, S. Chatrchyan et al., *Observation of the associated production of a single top quark and a W boson in pp collisions at* $\sqrt{s} =8$ *TeV*, *Phys. Rev. Lett.* **112** (2014) 231802, [`1401.2942`].

[220] R. Frederix and S. Frixione, *Merging meets matching in MC@NLO*, *JHEP* **1212** (2012) 061, [`1209.6215`].

[221] L. Lönnblad and S. Prestel, *Merging Multi-leg NLO Matrix Elements with Parton Showers*, *JHEP* **03** (2013) 166, [`1211.7278`].

[222] S. Hoeche, F. Krauss, P. Maierhoefer, S. Pozzorini, M. Schonherr and F. Siegert, *Next-to-leading order QCD predictions for top-quark pair production with up to two jets merged with a parton shower*, *Phys. Lett.* **B748** (2015) 74–78, [`1402.6293`].

[223] G. Bevilacqua, H. B. Hartanto, M. Kraus and M. Worek, *Top Quark Pair Production in Association with a Jet with Next-to-Leading-Order QCD Off-Shell Effects at the Large Hadron Collider*, *Phys. Rev. Lett.* **116** (2016) 052003, [`1509.09242`].

[224] G. Bevilacqua, H. B. Hartanto, M. Kraus and M. Worek, *Off-shell Top Quarks with One Jet at the LHC: A comprehensive analysis at NLO QCD*, *JHEP* **11** (2016) 098, [`1609.01659`].

[225] T. M. P. Tait, *The* tW^- *mode of single top production*, *Phys. Rev.* **D61** (1999) 034001, [`hep-ph/9909352`].

[226] S. Zhu, *Next-to-leading order QCD corrections to b g* $\to$ *t W- at the CERN Large Hadron Collider*, *Phys. Lett.* **B524** (2002) 283–288.

[227] W. Hollik, J. M. Lindert and D. Pagani, *NLO corrections to squark-squark production and decay at the LHC*, *JHEP* **03** (2013) 139, [`1207.1071`].

[228] W. Beenakker, R. Hopker, M. Spira and P. M. Zerwas, *Squark and gluino production at hadron colliders*, *Nucl. Phys.* **B492** (1997) 51–103, [`hep-ph/9610490`].

[229] E. L. Berger, T. Han, J. Jiang and T. Plehn, *Associated production of a top quark and a charged Higgs boson*, *Phys. Rev.* **D71** (2005) 115012, [`hep-ph/0312286`].

[230] T. N. Dao, W. Hollik and D. N. Le, *W-+ H+- production and CP asymmetry at the LHC*, *Phys. Rev.* **D83** (2011) 075003, [`1011.4820`].

[231] S. Frixione, E. Laenen, P. Motylinski, B. R. Webber and C. D. White, *Single-top hadroproduction in association with a W boson*, *JHEP* **07** (2008) 029, [`0805.3067`].

[232] C. D. White, S. Frixione, E. Laenen and F. Maltoni, *Isolating Wt production at the LHC*, *JHEP* **11** (2009) 074, [`0908.0631`].

[233] E. Re, *Single-top Wt-channel production matched with parton showers using the POWHEG method*, *Eur. Phys. J.* **C71** (2011) 1547, [`1009.2450`].

[234] C. Weydert, S. Frixione, M. Herquet, M. Klasen, E. Laenen, T. Plehn et al., *Charged Higgs boson production in association with a top quark in MC@NLO*, *Eur. Phys. J.* **C67** (2010) 617–636, [`0912.3430`].

[235] T. Binoth, D. Goncalves Netto, D. Lopez-Val, K. Mawatari, T. Plehn and I. Wigmore, *Automized Squark-Neutralino Production to Next-to-Leading Order*, *Phys. Rev.* **D84** (2011) 075005, [`1108.1250`].

[236] D. Goncalves-Netto, D. Lopez-Val, K. Mawatari, T. Plehn and I. Wigmore, *Automated Squark and Gluino Production to Next-to-Leading Order*, *Phys. Rev.* **D87** (2013) 014002, [`1211.0286`].

[237] R. Gavin, C. Hangst, M. Kramer, M. Muhlleitner, M. Pellen, E. Popenda et al., *Matching Squark Pair Production at NLO with Parton Showers*, *JHEP* **10** (2013) 187, [`1305.4061`].

[238] R. Gavin, C. Hangst, M. Krmer, M. Mhlleitner, M. Pellen, E. Popenda et al., *Squark Production and Decay matched with Parton Showers at NLO*, *Eur. Phys. J.* **C75** (2015) 29, [`1407.7971`].

[239] M. A. Gigg and P. Richardson, *Simulation of Finite Width Effects in Physics Beyond the Standard Model*, `0805.3037`.

[240] J. M. Campbell and F. Tramontano, *Next-to-leading order corrections to Wt production and decay*, *Nucl. Phys.* **B726** (2005) 109–130, [`hep-ph/0506289`].

[241] T. Plehn and M. Spannowsky, *Top Tagging*, *J. Phys.* **G39** (2012) 083001, [`1112.4441`].

[242] J. Caudron, *Top tagging at ATLAS*, Tech. Rep. ATL-PHYS-PROC-2015-163, CERN, Geneva, Dec, 2015.

[243] CMS collaboration, *Boosted Top Jet Tagging at CMS*, Tech. Rep. CMS-PAS-JME-13-007, CERN, Geneva, 2014.

[244] G. 't Hooft, *Renormalization of Massless Yang-Mills Fields*, *Nucl. Phys.* **B33** (1971) 173–199.

[245] G. 't Hooft, *Renormalizable Lagrangians for Massive Yang-Mills Fields*, *Nucl. Phys.* **B35** (1971) 167–188.

[246] G. 't Hooft and M. J. G. Veltman, *Regularization and Renormalization of Gauge Fields*, *Nucl. Phys.* **B44** (1972) 189–213.

[247] G. 't Hooft, *Renormalization and gauge invariance*, *Prog. Theor. Phys. Suppl.* **170** (2007) 56–71.

[248] S. Pokorski, *GAUGE FIELD THEORIES.* Cambridge University Press, 2005.

[249] F. Englert, *Broken symmetry and Yang-Mills theory*, in *50 years of Yang-Mills theory* (G. 't Hooft, ed.), pp. 65–95. 2005. `hep-th/0406162`. DOI.

[250] W. Struyve, *Gauge invariant accounts of the Higgs mechanism*, *Stud. Hist. Phil. Sci.* **B42** (2011) 226–236, [`1102.0468`].

[251] T. W. B. Kibble, *Symmetry breaking in nonAbelian gauge theories*, *Phys. Rev.* **155** (1967) 1554–1561.

[252] G. 't Hooft and M. J. G. Veltman, *Combinatorics of gauge fields*, *Nucl. Phys.* **B50** (1972) 318–353.

[253] A. Falkowski, *Higgs Basis: Proposal for an EFT basis choice for LHC HXSWG*, .

[254] P. de Aquino, W. Link, F. Maltoni, O. Mattelaer and T. Stelzer, *ALOHA: Automatic Libraries Of Helicity Amplitudes for Feynman Diagram Computations*, *Comput.Phys.Commun.* **183** (2012) 2254–2263, [`1108.2041`].

[255] P. Draggiotis, M. Garzelli, C. Papadopoulos and R. Pittau, *Feynman Rules for the Rational Part of the QCD 1-loop amplitudes*, *JHEP* **0904** (2009) 072, [`0903.0356`].

[256] A. Alloul, N. D. Christensen, C. Degrande, C. Duhr and B. Fuks, *FeynRules 2.0 - A complete toolbox for tree-level phenomenology*, *Comput.Phys.Commun.* **185** (2014) 2250–2300, [`1310.1921`].

[257] M. A. Shifman, A. I. Vainshtein, M. B. Voloshin and V. I. Zakharov, *Low-Energy Theorems for Higgs Boson Couplings to Photons*, *Sov. J. Nucl. Phys.* **30** (1979) 711–716.

[258] V. Hirschi and O. Mattelaer, *Automated event generation for loop-induced processes*, *JHEP* **10** (2015) 146, [`1507.00020`].

[259] G. Ossola, C. G. Papadopoulos and R. Pittau, *On the Rational Terms of the one-loop amplitudes*, *JHEP* **0805** (2008) 004, [`0802.1876`].

[260] R. Pittau, *Primary Feynman rules to calculate the epsilon-dimensional integrand of any 1-loop amplitude*, *JHEP* **1202** (2012) 029, [`1111.4965`].

[261] B. Page and R. Pittau, *R_2 vertices for the effective ggH theory*, *JHEP* **1309** (2013) 078, [`1307.6142`].

[262] S. L. Adler and W. A. Bardeen, *Absence of higher order corrections in the anomalous axial vector divergence equation*, *Phys.Rev.* **182** (1969) 1517–1536.

[263] K. G. Chetyrkin, B. A. Kniehl, M. Steinhauser and W. A. Bardeen, *Effective QCD interactions of CP odd Higgs bosons at three loops*, *Nucl. Phys.* **B535** (1998) 3–18, [`hep-ph/9807241`].

[264] D. Graudenz, M. Spira and P. M. Zerwas, *QCD corrections to Higgs boson production at proton proton colliders*, *Phys. Rev. Lett.* **70** (1993) 1372–1375.

[265] R. V. Harlander and W. B. Kilgore, *Next-to-next-to-leading order Higgs production at hadron colliders*, *Phys. Rev. Lett.* **88** (2002) 201801, [`hep-ph/0201206`].

[266] C. Anastasiou and K. Melnikov, *Higgs boson production at hadron colliders in NNLO QCD*, *Nucl. Phys.* **B646** (2002) 220–256, [`hep-ph/0207004`].

[267] R. V. Harlander and W. B. Kilgore, *Production of a pseudoscalar Higgs boson at hadron colliders at next-to-next-to leading order*, *JHEP* **10** (2002) 017, [`hep-ph/0208096`].

[268] C. Anastasiou and K. Melnikov, *Pseudoscalar Higgs boson production at hadron colliders in NNLO QCD*, *Phys. Rev.* **D67** (2003) 037501, [`hep-ph/0208115`].

[269] T. Ahmed, M. C. Kumar, P. Mathews, N. Rana and V. Ravindran, *Pseudo-scalar Higgs boson production at threshold N^3LO and N^3LL QCD*, *Eur. Phys. J.* **C76** (2016) 355, [`1510.02235`].

[270] ATLAS collaboration, G. Aad et al., *Search for $H \to \gamma\gamma$ produced in association with top quarks and constraints on the Yukawa coupling between the top quark and the Higgs boson using data taken at 7 TeV and 8 TeV with the ATLAS detector*, *Phys. Lett.* **B740** (2015) 222–242, [`1409.3122`].

[271] CMS collaboration, V. Khachatryan et al., *Search for the associated production of a Higgs boson with a single top quark in proton-proton collisions at $\sqrt{s} = 8$ TeV*, *JHEP* **06** (2016) 177, [`1509.08159`].